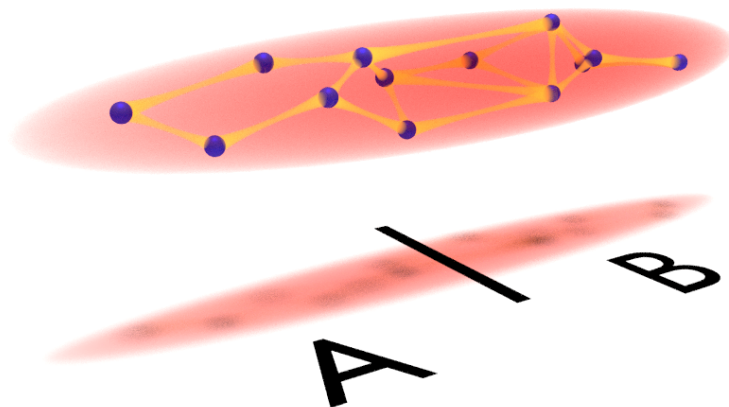


Splitting a Bose-Einstein condensate enables EPR steering and simultaneous readout of noncommuting observables



Philipp Kunkel
2019

Dissertation
submitted to the
Combined Faculties of the Natural Sciences and Mathematics
of the Ruperto-Carola-University of Heidelberg, Germany
for the degree of
Doctor of Natural Sciences

Put forward by

Philipp Kunkel

born in: Aschaffenburg, Germany

Oral examination: 03. December, 2019

Splitting a Bose-Einstein condensate enables EPR steering and simultaneous readout of noncommuting observables

Referees: Prof. Dr. Markus K. Oberthaler
 Prof. Dr. Selim Jochim

Abstract

Whether quantum correlations between identical particles can serve as a resource for quantum information protocols has often been questioned, since the constituent particles are not individually addressable. In this work, a scheme is presented that converts these correlations into entanglement between distinct spatial modes. Starting with a Bose-Einstein condensate (BEC) of ^{87}Rb in a tightly confining trap, we use spin-mixing to generate a quantum correlated state of indistinguishable particles in a single spatial mode. This entanglement is subsequently distributed in space by expanding the atomic cloud which can be viewed as splitting the BEC in the spatial degree of freedom. Using a spatially resolved spin readout we demonstrate a particularly strong form of entanglement known as Einstein-Podolsky-Rosen (EPR) steering between spatially distinct regions of the expanded BEC. This certifies that the prepared state is indeed a useful resource for quantum information protocols. Additionally, we developed a new readout technique based on coupling the spin state to initially unoccupied auxiliary modes. This splitting in the internal degree of freedom enables the simultaneous and spatially resolved extraction of multiple noncommuting observables. We show that this technique is capable of detecting quantum correlations by measuring fluctuations below the standard quantum limit. This results in a new method to characterize quantum states and together with the spatial resolution provides the possibility to detect entanglement in complex multimode settings. Combining these two results provides the prospect of studying the generation of cluster states, which are the crucial resource for one-way quantum computation. This renders BECs a new test bed for quantum information tasks.

Zusammenfassung

Ob Quantenkorrelationen zwischen identischen Teilchen als Ressource für Quanteninformationsprotokolle dienen können, wurde oft in Frage gestellt, da die einzelnen Bestandteile nicht individuell adressierbar sind. Innerhalb dieser Arbeit wird eine Methode vorgestellt, mit der diese Korrelationen in Verschränkung zwischen unterscheidbaren räumlichen Moden umgewandelt werden können. Als Ausgangspunkt dient ein Bose-Einstein Kondensat (BEC) aus ^{87}Rb Atomen in einer eng begrenzten Falle. Mittels Spin-Wechselwirkung wird ein quantenverschränkter Zustand zwischen ununterscheidbaren Teilchen in einer einzelnen räumlichen Mode erzeugt. Durch Expandieren der Atomwolke wird diese Verschränkung im Raum verteilt. Die Expansion kann dabei als Teilung des BECs im räumlichen Freiheitsgrad aufgefasst werden. Eine räumlich aufgelöste Detektion des Spinzustandes ermöglicht den Nachweis von Einstein-Podolsky-Rosen (EPR) Steering, einer besonders starken Form der Verschränkung zwischen räumlich getrennten Regionen im ausgebreiteten BEC. Damit wird zugleich gezeigt, dass der präparierte Zustand tatsächlich eine nützliche Ressource für Quanteninformationsprotokolle liefert. Darüberhinaus wurde eine neue Auslesemethode entwickelt, welche darauf beruht, den Spinzustand an anfangs unbesetzte Hilfsmoden zu koppeln. Diese Teilung im internen Freiheitsgrad ermöglicht die gleichzeitige und räumlich aufgelöste Extraktion mehrerer nichtkommutierender Observablen. Durch Messung von Fluktuationen unterhalb des Standard-Quantenlimits wird gezeigt, dass diese Technik in der Lage ist, Quantenkorrelationen nachzuweisen. Dies stellt eine neue Methode dar, Quantenzustände zu charakterisieren und bietet zusammen mit der räumlichen Auflösung die Möglichkeit, Verschränkung in komplexen Multimoden-Umgebungen zu detektieren. Beide Ergebnisse der Arbeit zusammen bieten die Aussicht, die Erzeugung von Cluster-Zuständen zu untersuchen, welche einen essentiellen Bestandteil messbasierter Quantencomputer bilden. Dadurch werden BECs zu einem neuen Testfeld für Quanteninformationsprotokolle.

Contents

1. Introduction	1
2. Theoretical background	5
2.1. From spin-1/2 to spin-1	5
2.1.1. Spin-1/2	5
2.1.2. Spin-1	7
2.1.3. Graphical representation on a spin-1 sphere	9
2.1.4. Additional SU(2) subspaces	10
2.1.5. The spin-nematic sphere	11
2.1.6. Spin-2	14
2.2. Collective spins	14
2.3. Projective measurements	15
2.4. Representation of many-body states	16
2.4.1. Coherent spin states	17
2.4.2. The Wigner distribution	18
2.4.3. The Husimi distribution	20
2.5. Quantum correlations	21
2.5.1. EPR-Steering	21
2.5.2. Steering criterion	23
2.5.3. Quantum information and LOCC	23
2.5.4. Entanglement	24
3. Experimental system and control	27
3.1. Bose-Einstein condensation and trapping configurations	27
3.2. Magnetic field shifts	28
3.3. Imaging and post-processing	29
3.4. Rf spin rotations	30
3.5. Microwave control	32
3.6. Magnetic field control sequence	33
4. Interactions and spin-mixing	37
4.1. Interaction Hamiltonian	37
4.2. Spin-mixing	38
4.3. Experimental control	40
4.4. Mean-field dynamics on the spin-nematic sphere	41
4.5. Truncated Wigner simulation	43
4.5.1. Short-time dynamics and spin-nematic squeezing	44
4.5.2. Long time dynamics and non-Gaussian states	44
4.6. Effective potential	44
4.7. Spectroscopy of spatial modes	48
4.8. Time evolution of spatial modes	49
4.9. Single mode addressing	51

4.10. Variance analysis	53
4.11. Spatially resolved fluctuation spectroscopy	53
4.12. Tomography of spatial modes	56
5. Spatially distributed entanglement and EPR steering	59
5.1. Surpassing the standard quantum limit	59
5.1.1. Shot noise limited detection	59
5.1.2. Spectroscopy control sequence	60
5.1.3. Spin-nematic squeezing	61
5.2. Steering between spatially distinct regions of the atomic cloud	62
5.2.1. Steering inequality	64
5.2.2. EPR Steering between spatially distinct atomic clouds	64
5.2.3. Monogamy of steering	66
5.2.4. Beamsplitter picture	67
5.2.5. Steering and entanglement in different experimental settings . .	68
5.2.6. Threeway EPR steering	69
5.3. Detection of genuine 5-partite entanglement	70
5.4. Experimental imperfections	71
5.5. Classical correlations induced by imaging	72
5.6. Undefined Larmor phase	74
6. Simultaneous readout of conjugate observables	77
6.1. Positive operator valued measures	77
6.1.1. Naimark's extension	79
6.1.2. Informationally complete measurements	79
6.2. Experimental implementation	80
6.2.1. Hyperfine selective spin rotations	81
6.2.2. Phase imprints	83
6.3. Simultaneous readout of all spin directions	84
6.3.1. Spin wave	85
6.3.2. Readout with conventional projective measurements	87
6.3.3. Calibration of the readout	88
6.3.4. Technical error contributions to this readout	91
6.4. Alternative readout sequence	93
6.4.1. Spin wave with spinor evolution	94
6.5. Detection of quantum correlations	94
6.5.1. Surpassing the shot-noise limit	97
6.6. Applicability to other systems	99
7. Entanglement detection using a simultaneous readout	101
7.1. Entanglement measures based on uncertainty relations	101
7.1.1. Duan entanglement criterion	102
7.1.2. Arthurs-Kelly uncertainty relation	103
7.1.3. Technical fluctuations	105
7.1.4. Stability of the mw transfers	107
7.1.5. Alternative readout sequence for \hat{S}_x and \hat{Q}_{yz}	107
7.2. Alternative entanglement detection schemes	109
7.2.1. Simultaneous measurement in two mutually unbiased bases . .	109
7.2.2. Experimental implementation of the quantum Fourier transform	110

8. State characterization using a simultaneous readout	113
8.1. Connection between the simultaneous readout and the Husimi function	113
8.2. Efficient detection of quantum state properties	116
8.3. Recording spin-mixing dynamics with a simultaneous readout	118
8.3.1. Single Mode dynamics	118
8.3.2. Corrections of phase imprint	120
8.3.3. Beyond single mode dynamics	120
9. Outlook	123
9.1. One-way quantum computation	123
9.2. Cluster state generation	125
9.2.1. Lattice potential	125
9.2.2. Multimode dynamics	126
9.3. Local control	126
A. Technical parameters and imaging calibration	129
A.1. Trap frequencies	129
A.2. Stability of the magnetic field	131
A.3. Imaging calibration	132
A.3.1. Imaging calibration for steering measurement	133
A.3.2. Imaging calibration for simultaneous readout	134
A.3.3. Buildup of correlations during expansion	135
A.4. Technical stability of the rf pulse	137
A.5. Technical stability of the mw pulse	138
B. Simultaneous readout of conjugate spin observables	141
B.1. Readout of all spin directions with arbitrary splitting ratio	141
B.2. Alternative readout sequence for \hat{S}_x and \hat{Q}_{yz}	142
B.2.1. Entanglement detection using this readout	143
B.3. Informationally complete sequence in a pseudo-spin-1/2	144
C. Spin-1 operators	145
C.1. SU(2) subspaces	147
C.2. Spin-nematic subspaces	147

List of Figures

2.1.	Bloch vs. spin sphere	6
2.2.	Representation of the polar and transverse polar state on a spin sphere .	10
2.3.	Spin-nematic and spin sphere	13
2.4.	Standard measurement scheme	16
2.5.	Coherent polar state for different atom numbers	17
2.6.	Comparision between Wigner and Husimi distribution	21
2.7.	The EPR paradox	22
2.8.	Sketch for the different entanglement definitions	25
3.1.	Experimental setup	28
3.2.	Rabi in $F = 1$ with long evolution times	32
3.3.	Control measurement magnetic field	34
3.4.	Compensation of the magnetic field gradient	34
4.1.	Energy scales for spin-mixing	40
4.2.	Mean-field trajectories	42
4.3.	Truncated Wigner simulation	45
4.4.	Effective potential	47
4.5.	Spin-mixing spectroscopy	48
4.6.	Time evolution for different spatial modes	50
4.7.	Spectroscopy of different atom numbers and trapping frequencies	51
4.8.	Spectroscopy signal with reduces heating	52
4.9.	Spin readout for spatially excited modes	54
4.10.	Fluctuation spectroscopy	56
4.11.	Tomography of fluctuations	57
4.12.	Mode spacing; theory vs. experiment	58
5.1.	Spectrsocopy control measurement	60
5.2.	Spin-nematic squeezing	61
5.3.	Scheme for spatial distribution of entanglement	62
5.4.	Evaluation regions	63
5.5.	Einstein-Podolsky-Rosen steering	65
5.6.	Threeway EPR steering	69
5.7.	Genuine multipartite entanglement	70
5.8.	Comparison theory vs. experiment	72
5.9.	Classical correlations after absorption imaging	73
6.1.	POVM measurement scheme	78
6.2.	Rabi oscillations with a single rf coil	81
6.3.	Selective spin rotations	82
6.4.	Readout sequence for the simultaneous readout of all three spin directions	84
6.5.	Absorption image of the atomic densities for a spin wave	86

6.6.	Spin wave evaluation	87
6.7.	Calibration of spin readout	89
6.8.	Effects of residual coupling and wrong pulse times	92
6.9.	Alternative readout sequence for all three spin directions	93
6.10.	Spinor phase evolution of a spin wave	95
6.11.	Pulse sequence for the simultaneous readout of S_x and Q_{yz}	96
6.12.	Evaluation of spin-nematic squeezing	97
6.13.	Spin-nematic squeezing	98
7.1.	Noise analysis of the readout sequence	105
7.2.	Alternative readout sequence for \hat{S}_x and \hat{Q}_{yz}	107
7.3.	Comparison between old and new readout sequence	108
7.4.	Experimental sequence for the quantum Fourier transform	110
8.1.	Uncertainties Wigner Vs. Husimi sampling	117
8.2.	Single mode dynamics of spin-mixing	119
8.3.	Multimode dynamics of spin-mixing	121
9.1.	Circuit vs. measurement based quantum computation	124
9.2.	Generation of cluster states in a lattice potential	126
9.3.	Generation of cluster states via multimode dynamics	127
A.1.	Longitudinal trap frequencies	130
A.2.	Transversal trap frequencies	130
A.3.	Magnetic field measurement	131
A.4.	Imaging calibration steering	133
A.5.	Imaging calibration for simultaneous readout	134
A.6.	Correlations during expansion	135
A.7.	Correlation lengths after expansion	137
A.8.	Technical stability of the rf pulse	138
A.9.	Technical stability of the mw pulse	139

1. Introduction

While entanglement is nowadays widely accepted as a key ingredient for future quantum technologies, its meaning in the context of identical particles has remained somewhat elusive. Stating that two or more systems are correlated implicitly assumes that it is possible to assign to each of them a distinct label, for example system A and system B. In classical physics, this appears like a needless remark, since there two systems, e.g. two particles, are in principle always distinguishable via a list of distinct properties [1]. In quantum mechanics, however, the notion of indistinguishable particles exists [2]. Thus, the statement that two identical particles A and B are correlated or rather entangled, is conceptually difficult as the labeling is artificial and fundamentally meaningless. Moreover, such a labeling directly leads to an entangled state as the mathematical description requires the quantum state to be (anti-) symmetrized under the exchange of two bosons (fermions) [3, 4, 5]. In this way, entanglement between identical particles has sometimes been argued to be merely a mathematical artifact [6].

This debate has been fueled by experimental results with Bose-Einstein condensates (BECs) which consist of hundreds to thousands of indistinguishable bosons. In these systems spin squeezed states have been generated which provide an enhancement in precision for metrological tasks [7, 8, 9]. This metrological gain is attributed to quantum correlations between the constituent spins and in a particle basis one indeed finds that the particles are highly entangled [10, 11]. The correlations are even strong enough to certify steering [12] and Bell correlations [13] which are especially strong forms of entanglement. Thus, in these systems entanglement between identical particles is not just a mathematical statement but can, in fact, be measured.

To resolve this confusion, an operational definition of entanglement has been proposed. Specifically in quantum information theory, entanglement is only considered to be “real” if it can somehow be exploited for quantum enhanced protocols via local manipulations [14]. However, since the entangled subsystems in a BEC are not individually addressable, the question remains, whether such correlations can be used as a resource for quantum information applications. In this context, it has been argued that the particles in a BEC can in principle be made distinguishable by expanding the atomic cloud until it is dilute enough, that each atom can be identified by its position [15]. Moreover, it has been theoretically shown that entanglement between identical particles can be transformed into entanglement between distinguishable modes via basic beamsplitter operations which themselves do not introduce entanglement [16].

In this thesis, we experimentally demonstrate that it is indeed possible to convert quantum correlations between indistinguishable particles into quantum informationally useful entanglement. In the experiment, we use the interatomic interactions in a BEC to generate a quantum correlated state of identical particles. After expanding the atomic cloud, we use spatially resolved absorption imaging to record the spin state of the atoms. The expansion can be modeled as a beamsplitter operation in the spatial degree of freedom and enables the definition of subsystems via distinct spatial regions on the absorption images. With this, we reveal Einstein-Podolsky-Rosen (EPR) steering between spatially

separated parts of the expanded condensate. EPR steering certifies that the generated state is a useful resource for quantum information protocols such as quantum teleportation [17] and quantum cryptography [18]. This has already triggered renewed theoretical efforts to incorporate entanglement between identical particles into the framework of quantum information theory [19].

The hallmark of EPR steering is that the measurement results in one system, say B, can be used to estimate the results in system A better than predicted by the local uncertainty relation [20]. To reveal these correlations, both systems have to be probed in the same measurement basis. Experimentally, this means that it is sufficient to set the measurement basis globally. However, one could also consider different types of correlations, where one has to measure system A in a conjugate measurement basis. This is, for example, the case for cluster states, which are the essential resource for one-way quantum computation [21]. Thus, a measurement in a single global measurement basis might not be enough to fully assess the usefulness of an experimentally generated state for quantum information protocols. In this case a local control of the measurement basis is required. In an experimental multimode setting however, it is often challenging to predict exactly the correlated measurement bases. Thus, experimentally, one would need to try out different combinations which becomes very time consuming.

In this context, we developed a new readout technique based on coupling the spin state to initially unoccupied auxiliary modes. Unitary transformations combined with a projective measurement in this enlarged Hilbert space enable the simultaneous and spatially resolved measurement of multiple noncommuting spin observables. This constitutes an experimental implementation of a generalized measurement scheme which can be formulated in the framework of positive operator valued measures (POVMs). On a fundamental level this simultaneous readout is possible because the coupling to empty modes reduces the measurement precision in each observable to make it consistent with the uncertainty relation. Yet, by measuring fluctuations below the shot-noise limit, we demonstrate that this method is still capable of detecting quantum correlations. Combining this result with the spatial resolution, we demonstrate that this readout is in principle able to verify entanglement between spatially distinct modes. We also show that a simultaneous detection scheme is closely connected to a special representation of a many-body state, namely the Husimi function. Therefore, this readout provides a new tool for the characterization of quantum states. The application of this readout method is not limited to the detection of entanglement, but can in general be used to reveal correlations between conjugate observables in spatially extended systems. As such it also provides a new tool for the study of multimode BECs, for example, for the investigation of spin dynamics far from equilibrium [22].

Organization of this thesis

- Chapter 2 provides the theoretical basics for this work. Our experimental platform is a spinor BEC of ^{87}Rb occupying the $F = 1$ hyperfine manifold. Therefore, starting from the well-known spin-1/2 system, the first part introduces the relevant operators to describe spin-1 particles. Within this operator basis, two SU(2) subspaces, the spin sphere and the spin-nematic sphere, are presented which provide a convenient illustration of the state and the relevant dynamics. After a short review of projective measurements, the Wigner and the Husimi quasiprobability distributions are introduced as a representation of a many-body quantum state. The last part focuses on entanglement. Particularly, we will introduce steering and different entanglement definitions in multipartite systems.
- In chapter 3 we will present the experimental system. After a short overview over the condensation process, we describe the imaging scheme with which we implement a projective measurement of the spin state. We will give details about the experimental control of the spin state via microwave and radiofrequency fields.
- Chapter 4 provides details about the spin-mixing process which we use to generate entangled many-particle states. We first provide a theoretical description within the single-mode approximation before we extend the treatment to include the interactions of the condensate in the external potential. This leads to an effective potential for the particle excitations where spin-mixing allows the coupling to the spatially excited modes. By exploiting the symmetry of the corresponding wavefunction we are able to selectively analyze each spatial mode. With this we extract the energy spectrum of this potential which agrees well with our theoretical description.
- Chapter 5 builds on the understanding of the spin-mixing process developed in the preceding chapter to generate a spin-nematic squeezed state in a single spatial mode. Starting from a tightly confining crossed dipole trap we expand the atomic cloud in space by switching off one dipole beam. This distributes the generated entanglement in space. After a spatially resolved spin readout we verify EPR steering between spatially distinct parts of the expanded condensate. Based on steering we develop an entanglement witness with which we certify up to genuine 5-partite entanglement.
- In chapter 6 we introduce the generalized measurement concept of POVMs and its experimental implementation. This enables the simultaneous readout of conjugate collective spin-1 observables. We demonstrate this technique by analyzing two different types of spin-waves where this new readout together with our spatial resolution allows extracting all three spin directions in a single experimental realization. This provides a direct visualization of the generated states on a spin sphere. Moreover, we will show that this readout is capable of detecting quantum correlations by measuring fluctuations below the shot-noise limit.
- In chapter 7 we discuss in more detail how a simultaneous readout scheme could be employed to detect entanglement between distinct spatial regions. For this we introduce the Arthurs-Kelly uncertainty relation which provides a bound for the simultaneous measurement of two conjugate observables. In the end alternative

entanglement detection schemes are discussed based on measurements in mutually unbiased bases. In this context, we provide an experimental sequence to implement the quantum Fourier transformation, which corresponds to a transformation into a mutually unbiased basis.

- Chapter 8 provides further insight into the connection between a simultaneous readout and the representation of many-body states via the Husimi quasiprobability distribution. This represents an alternative to standard tomographic methods to reconstruct the Wigner distribution. Summarizing the results obtained in optical systems, the sampling of the Husimi function is in many cases more efficient to estimate the first and second moment of a given quantum state. Finally, we use the simultaneous readout to directly track the spin-mixing dynamics in the spin-nematic phase space beyond the initial squeezing dynamics. If the spin-mixing process is in resonance with a single spatial mode we find coherent dynamics. Tuning this process simultaneously into resonance with two spatial modes we find indications for a relaxation of the dynamics towards the minimum of the mean-field energy.
- In the last part we give a short outlook towards combining the results of this thesis for studying the generation of cluster states in a BEC.

2. Theoretical background

This chapter introduces the key theoretical concepts that are relevant throughout this thesis. For the experiments we employ a spinor Bose-Einstein condensate of ^{87}Rb which, in its electronic groundstate, features two hyperfine manifolds, $F = 1$ and $F = 2$. As most of the experiments are performed in the $F = 1$ manifold, we start with a treatment of a spin-1 system and provide a complete operator basis to describe the dynamics and coherent couplings. After a short introduction to quantum measurements and many-body systems we will give an overview of quantum correlations and entanglement which are deemed essential for future quantum technologies. The aim of this chapter is to provide a basic understanding of the concepts on which we will elaborate further in the following chapters.

2.1. From spin-1/2 to spin-1

Starting from a single-particle description, the well-known spin-1/2 system serves as a basis which we will expand to incorporate the additional degrees of freedom inherent to a spin-1 system. A special focus will be put on developing a graphical representation of the quantum state and its dynamics.

2.1.1. Spin-1/2

The spin-1/2 formalism provides a complete description of a single-particle two-level system, often referred to as a qubit in quantum information, and is therefore extensively discussed in literature [23]. We will here review the basic concepts and the visualization of a spin-1/2 state, which will prove useful later for an intuitive understanding of the spin-1 system. We will denote the two basis states as

$$|\uparrow\rangle = \begin{pmatrix} 1 \\ 0 \end{pmatrix} \quad \text{and} \quad |\downarrow\rangle = \begin{pmatrix} 0 \\ 1 \end{pmatrix}. \quad (2.1)$$

Any pure single-particle state $|\psi\rangle$ can then be written, up to a global phase, as a coherent superposition of these two states

$$\begin{aligned} |\psi\rangle &= e^{i\phi_L/2} \cos \frac{\theta}{2} |\uparrow\rangle + e^{-i\phi_L/2} \sin \frac{\theta}{2} |\downarrow\rangle \\ &= \begin{pmatrix} e^{i\phi_L/2} \cos \frac{\theta}{2} \\ e^{-i\phi_L/2} \sin \frac{\theta}{2} \end{pmatrix}. \end{aligned} \quad (2.2)$$

This state is characterized by the two angles $\theta \in [0, \pi]$ and $\phi_L \in [0, 2\pi]$. In the following, the phase $\phi_L = \phi_\uparrow - \phi_\downarrow$ will be referred to Larmor phase which describes the phase difference between the two basis states. With these two degrees of freedom, the state is conveniently represented on the surface of a sphere as shown in Fig. 2.1, the so-called

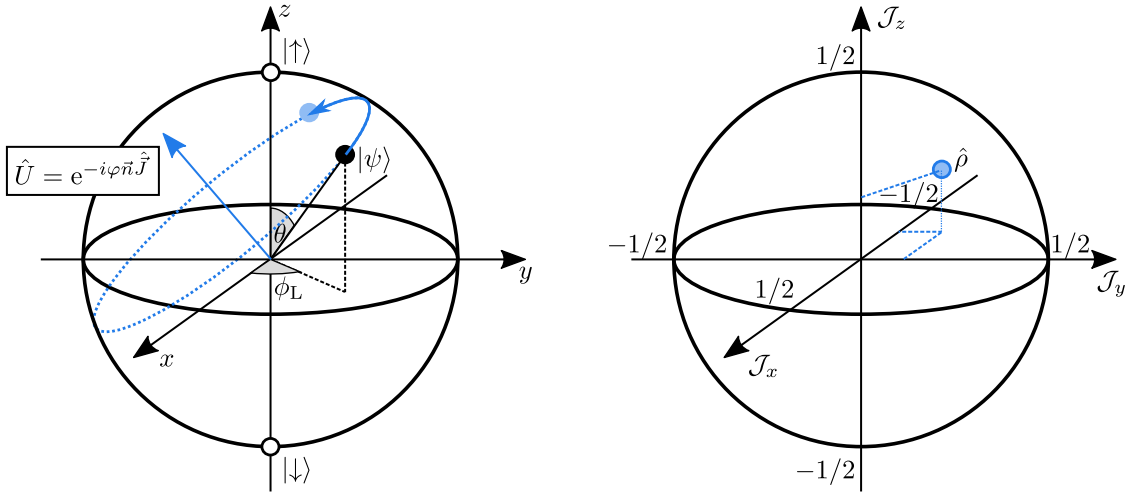


Figure 2.1.: **Bloch vs. spin sphere:** A general pure spin-1/2 state $|\psi\rangle$ is characterized by two angles and can therefore be represented as point on the surface of a sphere, the so-called Bloch sphere (left). The unitary $\hat{U} = \exp(-i\varphi\vec{n}\cdot\hat{\mathcal{J}})$ corresponds to rotations of the state around the unit vector \vec{n} (blue vector) by the angle φ . In comparison, a general mixed state is characterized by the expectation value of the three spin directions, which yields a point inside a spin sphere (right). Also on this sphere the spin operators are the generators of rotations.

Bloch sphere, where the poles correspond to the two basis states. Any unitary transformation of the state can then be mapped on rotations of the state on the Bloch sphere. To parameterize these rotations one defines the three Hermitian spin operators which, in matrix notation, are given by

$$\hat{\mathcal{J}}_x = \frac{1}{2} \begin{pmatrix} 0 & 1 \\ 1 & 0 \end{pmatrix}, \quad \hat{\mathcal{J}}_y = \frac{1}{2} \begin{pmatrix} 0 & -i \\ i & 0 \end{pmatrix}, \quad \hat{\mathcal{J}}_z = \frac{1}{2} \begin{pmatrix} 1 & 0 \\ 0 & -1 \end{pmatrix}. \quad (2.3)$$

These operators fulfill the defining SU(2) commutation relations $[\hat{\mathcal{J}}_i, \hat{\mathcal{J}}_j] = \epsilon_{ijk}i\hat{\mathcal{J}}_k$ with $i, j, k \in \{x, y, z\}$ and ϵ_{ijk} being the Levi-Civita symbol with $\epsilon_{xyz} = 1$. They are, thus, generators of rotations, meaning that the unitary $\hat{U} = \exp(-i\varphi\vec{n}\cdot\hat{\mathcal{J}})$ with $\hat{\mathcal{J}} = (\hat{\mathcal{J}}_x, \hat{\mathcal{J}}_y, \hat{\mathcal{J}}_z)^T$ generates rotations of the state on the Bloch sphere around the unit vector \vec{n} by the angle φ . Especially, a change of the Larmor phase corresponds to a rotation around the z -direction.

The spin operators form a basis of the $\mathfrak{su}(2)$ Lie algebra and together with the unity operator $\mathbb{1}_2$ provide a decomposition of any Hermitian operator in the Hilbert space \mathbb{C}^2 . Importantly the density matrix

$$\hat{\rho} = \sum_i P_i |\psi_i\rangle \langle\psi_i| \quad \text{with} \quad \sum_i P_i = 1 \quad (2.4)$$

used for the description of general mixed states, is also an Hermitian operator within this Hilbert space and can, therefore, be expressed as

$$\hat{\rho} = \frac{1}{2}\mathbb{1}_2 + \vec{r}\hat{\mathcal{J}}. \quad (2.5)$$

Together with the condition $\det \hat{\rho}^2 \leq 1$ we get $|\vec{r}|^2 \leq 1$, where equality only holds for pure states. This means, a general mixed state can be expressed as a vector \vec{r} inside a unit sphere, while any pure state is represented on the surface of this sphere. To distinguish this sphere from the Bloch sphere, which was introduced for pure states, this object will be denoted as *spin sphere*. In this representation the mixed state is completely determined by the expectation value of the three spin operators. Analogously to pure states, unitary transformations can be described by rotations on the spin sphere.

Representing the unitary transformation by a rotation of the state on the spin sphere corresponds to the Schrödinger picture for describing the quantum evolution. Equivalently, we could use the Heisenberg picture where the position of the state is fixed and the axes are rotated. To further highlight the connection between the SU(2) commutation relations and the rotations on the spin sphere, let us calculate how the axis \hat{J}_i is changed by a rotation generated by \hat{J}_j with $i \neq j$

$$\begin{aligned} e^{i\varphi \hat{J}_j} \hat{J}_i e^{-i\varphi \hat{J}_j} &= \underbrace{e^{i\varphi \hat{J}_j} e^{-i\varphi \hat{J}_j}}_{=1} \left(\hat{J}_i - i\varphi [\hat{J}_i, \hat{J}_j] - \frac{\varphi^2}{2} [[\hat{J}_i, \hat{J}_j], \hat{J}_j] + \dots \right) \\ &= \cos(\varphi) \hat{J}_i + \sin(\varphi) \epsilon_{ijk} \hat{J}_k. \end{aligned} \quad (2.6)$$

In practice, we will often employ a mixture of the Schrödinger and Heisenberg picture where the former is used to describe the dynamics and the latter for a description of the readout sequence.

For the single-particle spin-1/2 case the distinction between the Bloch and the spin sphere seems a bit pedantic. It is, however, important to discriminate between an exact representation of a pure state (Bloch sphere) and a representation in terms of mean spin values which connects to experimental measurement results.

2.1.2. Spin-1

A spin-1 state consists of three levels, where we use the three magnetic substates $|m_F\rangle$ with $m_F \in \{-1, 0, +1\}$ of the $F = 1$ hyperfine manifold as basis states. In this basis a pure single-particle state is, up to a global phase, given by

$$\begin{aligned} |\psi\rangle &= r_{+1} e^{i\phi_L/2} |+1\rangle + r_0 e^{i\phi_S} |0\rangle + r_{-1} e^{-i\phi_L/2} |-1\rangle \\ &= \begin{pmatrix} r_{+1} e^{i\phi_L/2} \\ r_0 e^{i\phi_S} \\ r_{-1} e^{-i\phi_L/2} \end{pmatrix} \end{aligned} \quad (2.7)$$

where the prefactors $r_{0,\pm 1}$ are chosen to be real numbers with $\sum_i r_i^2 = 1$, which give the probability r_i^2 to find the particle in the state $|i\rangle$. Analogously to the spin-1/2 case, we define the Larmor phase as $\phi_L = \phi_{+1} - \phi_{-1}$, i.e. the phase difference between the states $|\pm 1\rangle$. Additionally, the state is characterized by a second phase, the so-called spinor phase defined here as $\phi_S = \phi_0 - (\phi_{+1} + \phi_{-1})/2$ which describes the relative phase of the state $|0\rangle$ compared to the states $|\pm 1\rangle$. Note, that sometimes an alternative definition of the spinor phase is used which deviates from the one given here by a factor of -2 , i.e. $\phi'_S = -2\phi_S$ [24]. However, the convention used here is directly connected to the geometrical representation of the state as shown later.

Using spin algebra, a spin-1 state can be thought of as a symmetric superposition of two spin-1/2 states. This makes it possible to represent a pure spin-1 state via two points on the Bloch sphere [25]. While this representation is convenient to study symmetries of a given spin-1 state [26] and to gain an intuitive understanding why the mean of the spin operators is not enough to unambiguously characterize a given state, it is not very useful to describe more general mixed states, let alone many-particle states. Therefore, similar to the spin-1/2 case, the aim is to find a complete set of operators which form a basis for hermitian operators acting on the spin-1 Hilbert space to completely describe the density matrix of a mixed state. As a start, we choose the spin-1 analog of the three spin operators which, in matrix notation, are given by

$$\hat{S}_x = \frac{1}{\sqrt{2}} \begin{pmatrix} 0 & 1 & 0 \\ 1 & 0 & 1 \\ 0 & 1 & 0 \end{pmatrix}, \quad \hat{S}_y = \frac{1}{\sqrt{2}} \begin{pmatrix} 0 & -i & 0 \\ i & 0 & -i \\ 0 & i & 0 \end{pmatrix}, \quad \hat{S}_z = \begin{pmatrix} 1 & 0 & 0 \\ 0 & 0 & 0 \\ 0 & 0 & -1 \end{pmatrix}, \quad (2.8)$$

which, as before, fulfill the SU(2) commutation relation $[\hat{S}_i, \hat{S}_j] = i\epsilon_{ijk}\hat{S}_k$. In contrast to the spin-1/2 case, the mean value of these three operators are, however, not sufficient to uniquely determine the quantum state. Take for example the two states

$$|\psi_p\rangle = \begin{pmatrix} 0 \\ 1 \\ 0 \end{pmatrix} \quad |\psi_{tp}\rangle(\phi_L) = \frac{1}{\sqrt{2}} \begin{pmatrix} e^{i\phi_L/2} \\ 0 \\ e^{-i\phi_L/2} \end{pmatrix}, \quad (2.9)$$

which are called polar and transverse polar state, respectively. Calculating the mean spin lengths for both states one finds, $\langle \psi_p | \hat{S}_i | \psi_p \rangle = \langle \psi_{tp} | \hat{S}_i | \psi_{tp} \rangle = 0$ for all $i \in \{x, y, z\}$. Thus, additional observables are required to unambiguously identify the spin state.

One choice are the so-called quadrupole operators, which are defined via [27, 28, 24]

$$\hat{Q}_{ij} = \hat{S}_i \hat{S}_j + \hat{S}_j \hat{S}_i - \frac{4}{3} \delta_{ij} \mathbb{1}_3 \quad (2.10)$$

with $i, j \in \{x, y, z\}$, the Kronecker delta δ_{ij} and the unity operator $\mathbb{1}_3$.

If we imagine again a spin-1 state in terms of two points on a Bloch sphere, we can intuitively think about these operators in the following way. If we draw a vector from the origin of the sphere to each of the two points, then the spin operators describe the total spin of this system by adding the two vectors up. This is not unique since for a given total spin, there exist many configurations of the two points that yield the same result. To distinguish these configurations we need quadrupole operators, which, if we interpret the vectors as dipole moments, describe the quadrupole moment of each configuration. This is also, historically, the origin of the quadrupole operators [29].

Together with the spin operators we get a total of 9 operators. However, as the density just has 8 independent entries this basis set is overcomplete and, thus, we select the

following five operators out of the six quadrupole operators

$$\begin{aligned}\hat{Q}_{xz} &= \frac{1}{\sqrt{2}} \begin{pmatrix} 0 & 1 & 0 \\ 1 & 0 & -1 \\ 0 & -1 & 0 \end{pmatrix}, \quad \hat{Q}_{yz} = \frac{1}{\sqrt{2}} \begin{pmatrix} 0 & -i & 0 \\ i & 0 & i \\ 0 & -i & 0 \end{pmatrix}, \quad \hat{Q}_{zz} = \begin{pmatrix} \frac{2}{3} & 0 & 0 \\ 0 & -\frac{4}{3} & 0 \\ 0 & 0 & \frac{2}{3} \end{pmatrix}, \\ \hat{\mathcal{V}}_x &= \frac{1}{2}(\hat{Q}_{xx} - \hat{Q}_{yy}) = \begin{pmatrix} 0 & 0 & 1 \\ 0 & 0 & 0 \\ 1 & 0 & 0 \end{pmatrix}, \quad \hat{\mathcal{V}}_y = \hat{Q}_{xy} = \begin{pmatrix} 0 & 0 & -i \\ 0 & 0 & 0 \\ i & 0 & 0 \end{pmatrix}\end{aligned}\tag{2.11}$$

With these operators a general spin-1 density matrix is parameterized as

$$\hat{\rho} = \frac{1}{3}\mathbb{1}_3 + \sum_i s_i \hat{S}_i + \sum_j q_j \hat{Q}_j + \sum_k v_k \hat{\mathcal{V}}_k.\tag{2.12}$$

The density matrix of a general single-particle mixed state is, thus, defined by the mean value of these eight operators. Using again the example of the polar and transverse polar state we find that the two have indeed a unique representation via these operators, explicitly given by

$$\begin{aligned}\hat{\rho}_p &= \frac{1}{3}\mathbb{1}_3 - 4/3\hat{Q}_{zz} \\ \hat{\rho}_{tp} &= \frac{1}{3}\mathbb{1}_3 + 4/3\hat{Q}_{zz} + \cos(2\phi_L)\hat{\mathcal{V}}_x + \sin(2\phi_L)\hat{\mathcal{V}}_y.\end{aligned}\tag{2.13}$$

There exist alternative choices to parameterize a spin-1 state for example in terms of so-called Gell-Mann matrices [30]. However, the parameterization in terms of spin and quadrupole operators is more suitable to describe the dynamics in our experimental system.

2.1.3. Graphical representation on a spin-1 sphere

As the spin operators $\{\hat{S}_x, \hat{S}_y, \hat{S}_z\}$ fulfill the defining SU(2) commutation relations, the mean spin of a given state can be represented on a sphere on which the spin operators generate rotations in the same way as in the spin-1/2 case. In contrast to spin-1/2 systems, even the state vector of a pure state given by the expectation value of the three spin observables can be inside the sphere as we have seen for the polar state. Additionally, it has been shown that the expectation value of the spin alone is not sufficient to represent the quantum state but the expectation value of the quadrupole operators are required as well.

Taking a closer look at the definition of the quadrupole operators in Eq. (2.10), we see that they are linked to the second moment of the spin, i.e. the covariance matrix which is defined as

$$\begin{aligned}T_{ij} &= \frac{1}{2}\langle \hat{S}_i \hat{S}_j + \hat{S}_j \hat{S}_i \rangle_Q - \langle \hat{S}_i \rangle_Q \langle \hat{S}_j \rangle_Q \\ &= \langle \frac{1}{2}\hat{Q}_{ij} + \frac{1}{3}\delta_{ij}\mathbb{1}_3 \rangle_Q - \langle \hat{S}_i \rangle_Q \langle \hat{S}_j \rangle_Q,\end{aligned}\tag{2.14}$$

where we denote with $\langle \cdot \rangle_Q$ the quantum mechanical expectation value $\text{tr}(\cdot \hat{\rho})$. As the quadrupole operators together with the spin operators completely identify a given state,

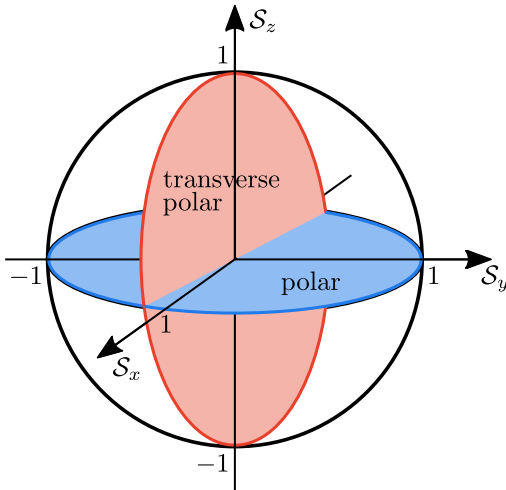


Figure 2.2.: Representation of the polar and transverse polar state on a spin sphere: Both, the polar and transverse polar state feature a vanishing expectation value for all three spin operators. To graphically distinguish these two states on a spin sphere, one has to include their second moments. The polar state has no fluctuations along the S_z direction but large fluctuations along the orthogonal spin directions resulting in a disk shape. As the transverse polar state is connected to the polar state via a $\pi/2$ spin rotation, the state features large fluctuations along the S_z direction and the orientation of the disk is determined by the Larmor phase.

any single-particle state can be characterized by its mean spin length and an ellipsoid representing the fluctuations of the state [31]. The major axes of this ellipsoid are determined by diagonalizing the covariance matrix. As such the state can be graphically represented in a spin sphere, similar to the spin-1/2 case. While for the spin-1/2 case the expectation values are enough, for the spin-1 case one has to additionally draw an ellipsoid to take into account the second moment of the state. Unitary transformations induced by the spin operators are still described by rotations on the spin sphere but one now has to rotate the whole state ellipsoid instead of just a single point.

As an example we take again the polar and the transverse polar state as defined before. We have seen that for both states the mean spin length vanishes along all directions. These states can, however, be distinguished by their fluctuations as shown in Fig. 2.2. The polar state features large fluctuation in the $S_x - S_y$ -plane but no fluctuations along S_z , since it is an eigenstate of the \hat{S}_z operator. In contrast, the transverse polar state has large fluctuations along the plane defined by the z -direction and one orthogonal direction $\cos(2\phi_L)S_x + \sin(2\phi_L)S_y$ determined by the Larmor phase ϕ_L .

2.1.4. Additional SU(2) subspaces

Here, we provide some additional connections between the spin-1 operators to make them more familiar to the reader. Besides the SU(2) subspace spanned by the three spin operators $\{\hat{S}_x, \hat{S}_y, \hat{S}_z\}$, there exist two other SU(2) subspaces, namely $\{\hat{Q}_{xz}, \hat{Q}_{yz}, \hat{S}_z\}$ and $\{\hat{V}_x, \hat{V}_y, \hat{S}_z\}$. In principle, these subspaces could also be used as a complimentary representation of a spin-1 state on the respective spheres. For describing the dynamics in the

experiments later these subspaces are however not very convenient. We just note that all three subspaces contain the operator \hat{S}_z and a rotation around the corresponding axis is equivalent to a change of the Larmor phase. Thus, in a Heisenberg picture the remaining two operators in each SU(2) subspace are connected via a change of the Larmor phase. With this, we define the “transversal” operators

$$\begin{aligned}\hat{S}_\perp(\phi_L) &:= \cos(\phi_L)\hat{S}_x + \sin(\phi_L)\hat{S}_y \\ \hat{Q}_\perp(\phi_L) &:= \cos(\phi_L)\hat{Q}_{yz} - \sin(\phi_L)\hat{Q}_{xz} \\ \hat{\mathcal{V}}_\perp(\phi_L) &:= \cos(2\phi_L)\hat{\mathcal{V}}_x + \sin(2\phi_L)\hat{\mathcal{V}}_y.\end{aligned}\tag{2.15}$$

Note that the minus sign in the second line is necessary for a consistent definition of these operators which will become clear in the following section.

Even though the operator $\hat{\mathcal{V}}_\perp$ will only play a minor role for the discussion of the experiments presented in this thesis, we will add a few remarks for completeness. In the definition of $\hat{\mathcal{V}}_\perp$ the factor of two originates from the commutation relations of this subspace which are $[\hat{\mathcal{V}}_x, \hat{\mathcal{V}}_y] = 2i\hat{S}_z$ and cyclic permutations thereof. This factor of two means that for example the unitary $e^{-i\phi_L\hat{S}_z}$ rotates the state on the sphere by $2 \cdot \phi_L$. Thus, $\hat{\mathcal{V}}_x$ and $\hat{\mathcal{V}}_y$ are connected by a change of the Larmor phase by only $\pi/4$. By looking at the definition of these three operators one finds that they effectively describe a spin-1/2 system consisting of the states $|\pm 1\rangle$. Canceling the second row and column in the matrix representation yields the spin-1/2 operators introduced before times a factor of two.

2.1.5. The spin-nematic sphere

Similar to the connection between the operator \hat{S}_z and the Larmor phase, the operator \hat{Q}_{zz} is connected to the spinor phase ϕ_S . Specifically, the unitary operation $e^{-i\varphi\hat{Q}_{zz}/2}$ will advance the spinor phase of the state by φ . In a Heisenberg picture, this unitary transformation connects the operators \hat{S}_\perp and \hat{Q}_\perp with $\hat{Q}_\perp \rightarrow \hat{S}_\perp$ for $\varphi = \pi/2$. This connection is the reason for the minus sign in Eq. (2.15) as the operator \hat{S}_y is connected to $-\hat{Q}_{xz}$ via the spinor phase.

Since the connection between the spinor phase and the quadrupole operator \hat{Q}_{zz} will be essential for many experimental sequences, it would be convenient to represent this unitary operation on some SU(2) sphere where the rotations are generated by \hat{Q}_{zz} . For this, we first define the operator

$$\hat{Q}_0 = -\frac{1}{3}\mathbb{1}_3 - \hat{Q}_{zz} = \begin{pmatrix} -1 & 0 & 0 \\ 0 & 1 & 0 \\ 0 & 0 & -1 \end{pmatrix}\tag{2.16}$$

to center the spectrum around zero. The rotation generated by this new operator will be the same just with a different orientation since the unity operator does not influence the unitary evolution. With this operator, we define the so-called spin-nematic subspace [24] consisting of $\{\hat{Q}_\perp(\phi_L), \hat{S}_\perp(\phi_L), \hat{Q}_0\}$ for each phase ϕ_L . Calculating the commutation rela-

tions for the three operators gives

$$\begin{aligned} [\hat{Q}_0, \hat{Q}_\perp(\phi_L)] &= 2i\hat{S}_\perp(\phi_L), \quad [\hat{S}_\perp(\phi_L), \hat{Q}_0] = 2i\hat{Q}_\perp(\phi_L), \\ [\hat{Q}_\perp(\phi_L), \hat{S}_\perp(\phi_L)] &= 2i\hat{Q}_0 + i \begin{pmatrix} 1 & 0 & -e^{-i2\phi_L} \\ 0 & 0 & 0 \\ -e^{i2\phi_L} & 0 & 1 \end{pmatrix} = 2i\hat{Q}_0 + i(\hat{\mathcal{N}}^+ - \hat{\mathcal{V}}_\perp(\phi_L)), \end{aligned} \quad (2.17)$$

where we introduced the operator $\hat{\mathcal{N}}^+ = (\mathbb{1}_3 - \hat{Q}_0)/2$ which measures the population in the states $|\pm 1\rangle$. The first two commutation relations are equivalent to the statement that the operators \hat{S}_\perp and \hat{Q}_\perp are connected via a change of the spinor phase. While this is true for any state, in general, the operators $\{\hat{Q}_\perp(\phi_L), \hat{S}_\perp(\phi_L), \hat{Q}_0\}$ do not fulfill the SU(2) commutation relation. This means that rotations generated by \hat{S}_\perp and \hat{Q}_\perp are generally not represented on such a sphere.

However, for states $|\psi_n\rangle$ with equal probabilities to find a particle in the state $|\pm 1\rangle$, one can find a value of ϕ_L with $\langle \hat{\mathcal{N}}^+ - \hat{\mathcal{V}}_\perp(\phi_L) \rangle_Q = 0$. The operators then fulfill the SU(2) permutation relation for the quantum mechanical expectation value with

$$\langle [\hat{Q}_\perp(\phi_L), \hat{S}_\perp(\phi_L)] \rangle_Q = 2i\langle \hat{Q}_0 \rangle_Q. \quad (2.18)$$

Since any unitary transformation that is generated by these three operators does not change the Larmor phase of a given state this permutation relation remains valid during the evolution. We can thus evaluate Eq. (2.6) in the mean and interpret these operators as generators for rotations on a sphere spanned by the expectation value of the operators $\{\hat{Q}_\perp(\phi_L), \hat{S}_\perp(\phi_L), \hat{Q}_0\}$. As before, the factor of 2 means that, for example, the unitary $\exp(-i\varphi\hat{S}_\perp(\phi_L))$ rotates the state by 2φ around $\hat{S}_\perp(\phi_L)$ on the spin-nematic sphere. It turns out that this spin-nematic sphere provides a convenient visualization for the quantum dynamics we are experimentally interested in. Especially the polar state, which is often used as an initial state for the experiments, is represented on the north pole of such a spin-nematic sphere. Even though the polar state has no defined Larmor phase and can consequently be represented on any spin-nematic sphere, a small rotation around S_\perp transforms the state consistently such that it stays on the surface of the corresponding spin-nematic sphere. We will therefore use this sphere in connection with the spin sphere to provide a complimentary representation of the quantum state (see Fig. 2.3).

The spin-nematic sphere also provides another insight about spin-1 operators. Assuming we start with a state with $\langle \hat{S}_x \rangle_Q = 1$, i.e. it has a maximal transversal spin length. Such a state is represented on the surface of the spin sphere as well as the corresponding spin-nematic sphere. A change of the spinor phase will then rotate the state on the spin nematic sphere around the Q_0 axis. After a rotation by $\pi/2$ the mean spin length has vanished and the state has a maximal transversal quadrupole moment. The resulting state is then no longer represented on the surface of the spin sphere as shown in Fig. 2.3. Similar for all states that can be represented on the surface of a spin-nematic sphere, one can find spinor phases for which the mean transversal spin vanishes and turns it into a quadrupole moment, i.e. one can change the spin length by tuning the spinor phase.

While the connection between the operators \hat{S}_\perp and \hat{Q}_\perp via the spinor phase is always true, it is not true that we can for every state reduce the transversal spin length to zero by changing the spinor phase. Consider, for example, a state with a vanishing population of the state $| -1 \rangle$, i.e. with a large mean spin length along the z -direction. In this case, we can for the calculation of the expectation value neglect the third row and column

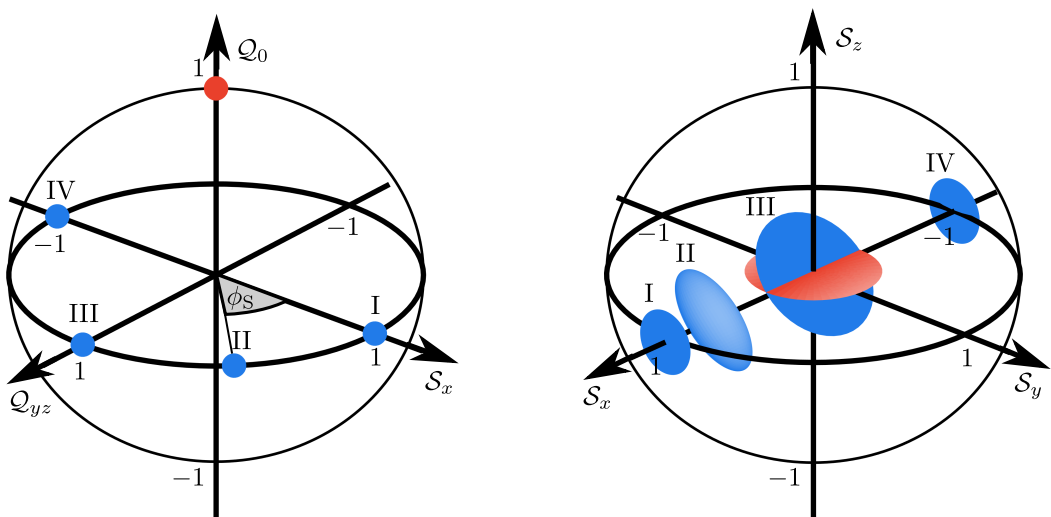


Figure 2.3.: Spin-nematic and spin sphere: We show here examples of states that are represented on the surface of the spin-nematic sphere (left) and their corresponding representations on the spin sphere (right). On the spin-nematic sphere the polar state (red) is represented as a point on the north pole. Starting with a state with $\langle \hat{S}_x \rangle_Q = 1$ (blue point I) we show its representation on both spheres for an evolution of the spinor phase (I - IV). Changing the spinor phase by $\pi/2$ results in a state with no mean spin length resembling a tilted polar state. For better visualization the covariance ellipsoid in the spin sphere has been scaled down by a factor of 5.

of the spin-1 observables. Within this approximation the operator $\hat{S}_\perp(\phi_L)$ is identical to $\hat{Q}_\perp(\phi_L - \pi/2)$. Let us, for example, start with a state for which the transversal spin is along the x -direction. In the Heisenberg picture a change of the spinor phase by $\pi/2$ will turn the operator $\hat{S}_x \rightarrow \hat{Q}_{yz}$. But in this limit \hat{Q}_{yz} is identical to \hat{S}_y . Thus, for such state a change of the spinor phase is identical to a change of the Larmor phase which we know does not reduce the transversal spin length.

2.1.6. Spin-2

Since in the experiment we will also employ spin rotations in the $F = 2$ manifold, we will briefly give the relevant spin operators without going into details of a spin-2 system. In matrix notation, the three spin operators are

$$\begin{aligned} \hat{S}_x^{F=2} &= \frac{1}{2} \begin{pmatrix} 0 & 2 & 0 & 0 & 0 \\ 2 & 0 & \sqrt{6} & 0 & 0 \\ 0 & \sqrt{6} & 0 & \sqrt{6} & 0 \\ 0 & 0 & \sqrt{6} & 0 & 2 \\ 0 & 0 & 0 & 2 & 0 \end{pmatrix}, & \hat{S}_y^{F=2} &= \frac{1}{2} \begin{pmatrix} 0 & -2i & 0 & 0 & 0 \\ 2i & 0 & -\sqrt{6}i & 0 & 0 \\ 0 & \sqrt{6}i & 0 & -\sqrt{6}i & 0 \\ 0 & 0 & \sqrt{6}i & 0 & -2i \\ 0 & 0 & 0 & 2i & 0 \end{pmatrix}, \\ \hat{S}_z^{F=2} &= \begin{pmatrix} 2 & 0 & 0 & 0 & 0 \\ 0 & 1 & 0 & 0 & 0 \\ 0 & 0 & 0 & 0 & 0 \\ 0 & 0 & 0 & -1 & 0 \\ 0 & 0 & 0 & 0 & -2 \end{pmatrix}, \end{aligned} \quad (2.19)$$

which fulfill the SU(2) commutation relation and with that generate spin rotations in the $F = 2$ hyperfine manifold.

2.2. Collective spins

So far, we have been discussing the spin-1 system on a single-particle level. In a single experimental realization, however, we deal with atom numbers on the order of $\sim 10^4$ spin-1 particles. Therefore, we have to extend our description from the single- to the many-particle case. As an example, we start with the operator \hat{S}_z . Experimentally, we do not resolve the atoms on a single-particle level, so it makes sense to define the collective operator $\hat{S}_{z,\text{coll.}} = \sum_{i=1}^N \hat{S}_{z,i}$ which is just the sum of the individual single-particle operators acting on the respective atom i for a total atom number N . In general, the Hilbert space dimension of N spin-1 particles is rather large with $d = 3^N$, if one uses the usual spin algebra for N individual spin-1 particles. In our case, we can use that the particles are part of a Bose-Einstein condensate. This means that they are fundamentally indistinguishable and the many-body state has to be symmetric under exchange of any two particles. This restricts the treatment of the collective spin to the fully symmetric subspace with $d = (N+2)(N+1)/2$. In this symmetric subspace the collective operators are conveniently

expressed in second quantization using the Jordan-Schwinger map [32, 33]

$$\begin{aligned}\hat{S}_z &= (\hat{a}_{+1}^\dagger, \hat{a}_0^\dagger, \hat{a}_{-1}^\dagger) \hat{S}_z \begin{pmatrix} \hat{a}_{+1} \\ \hat{a}_0 \\ \hat{a}_{-1} \end{pmatrix} \\ &= \hat{a}_{+1}^\dagger \hat{a}_{+1} - \hat{a}_{-1}^\dagger \hat{a}_{-1},\end{aligned}\quad (2.20)$$

where \hat{a}_m^\dagger (\hat{a}_m) is the creation (annihilation) operator in the magnetic substate m , obeying the bosonic commutation relation $[\hat{a}_m, \hat{a}_n^\dagger] = \delta_{mn}$. In second quantization, we denote the basis state of this Fock space by

$$|\psi\rangle = |N_{+1}, N_0, N_{-1}\rangle, \quad (2.21)$$

where N_{m_F} marks the atom number in the respective magnetic substate. Analogously, we define the collective pendants $\{\hat{S}_x, \hat{S}_y, \hat{Q}_{yz}, \hat{Q}_{xz}, \hat{Q}_{zz}, \hat{Q}_0, \hat{V}_x, \hat{V}_y\}$ to the corresponding single-particle operators described previously (for an explicit expression of the operators in terms of creation and annihilation operators see Appendix C).

Importantly, the commutation relations between the operators are unchanged under this mapping. Consequently, we can define a generalized spin sphere spanned by the operators $\{\hat{S}_x, \hat{S}_y, \hat{S}_z\}$ and generalized spin-nematic spheres spanned by the operators $\{\hat{Q}_\perp(\phi_L), \hat{S}_\perp(\phi_L), \hat{Q}_0\}$ on which these collective operators are generators of rotations. Here, we adopt the convention to normalize the axes by the total atom number N such that each sphere has a radius of one.

2.3. Projective measurements

Before we go into more detail about the visualization of a many-body state, we will discuss here shortly our experimental measurement procedure which is sketched in Fig. 2.4. Starting with an ensemble of N particles, we are measuring, in each experimental realization, the atom numbers in each magnetic substate to gain information about the state $\hat{\rho}$. In second quantization, this is described by the measurement operators

$$\begin{aligned}\hat{N}_{+1} &= \hat{a}_{+1}^\dagger \hat{a}_{+1} = \frac{1}{3} \hat{N} + \frac{1}{2} \hat{S}_z + \frac{1}{4} \hat{Q}_{zz} \\ \hat{N}_0 &= \hat{a}_0^\dagger \hat{a}_0 = \frac{1}{3} \hat{N} - \frac{1}{2} \hat{Q}_{zz} \\ \hat{N}_{-1} &= \hat{a}_{-1}^\dagger \hat{a}_{-1} = \frac{1}{3} \hat{N} - \frac{1}{2} \hat{S}_z + \frac{1}{4} \hat{Q}_{zz}\end{aligned}\quad (2.22)$$

which we decomposed here in the spin-1 operator basis given previously. We additionally introduced the operator for the total number $\hat{N} = \sum_{m=-1}^1 \hat{N}_m$ which is the second-quantized analog of the identity operator. Such a measurement constitutes a standard projective measurement [34], meaning that a successive measurement within the same experimental realization would give the same outcome for the particle numbers in each substate. In each realization, one will then measure in each substate a random atom number $N_m = \langle \hat{N}_m \rangle_{\text{Exp}}$, where the statistics is determined by the quantum state. Here, we introduced the notation $\langle \cdot \rangle_{\text{Exp}}$ to distinguish the result of a single measurement from the quantum mechanical expectation value. One can use a linear combination of the measured atom numbers to extract the value S_z and Q_{zz} within this single realization.

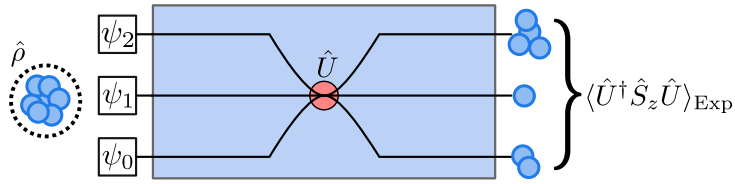


Figure 2.4.: **Sketch of a standard projective measurement scheme:** Measuring an ensemble of particles (blue dots) in a projective measurement yields in each realization a random distribution of particles over the basis states of the corresponding Hilbert space. The statistics of the measurement is determined by the state $\hat{\rho}$. Using a linear combination of the measured populations, we can extract in each experimental realization the value of at least two commuting spin-1 observables, for example S_z and Q_{zz} . To gain information about conjugate observables, one has to change the measurement basis by applying a unitary transformation \hat{U} prior to the projective measurement. In a Heisenberg picture, this means that, for example, the measurement outcome S_z is changed to $\langle \hat{U}^\dagger \hat{S}_z \hat{U} \rangle_{\text{Exp}}$, where $\langle \cdot \rangle_{\text{Exp}}$ denotes the result of a single realization.

For example, the spin in z -direction is given via $S_z = N^- = N_{+1} - N_{-1}$. In a spin sphere, this defines the readout axis as the S_z -axis along which we measure a given quantum state. Equivalently, in a spin-nematic sphere, the readout axis with this measurement is given by the Q_0 axis.

Because we can measure in principle all populations with single-particle resolution, the measurement operators in Eq. (2.22) and all linear combinations thereof must commute. Thus, each projective measurement in a $d = 3$ dimensional Hilbert space can only give us information about $d-1 = 2$ commuting spin-1 operators, like in this case S_z and Q_{zz} , since one piece of information is always reserved for the total atom number [35]. If we want to measure additional observables, we have to apply unitary transformations \hat{U} prior to the readout where the measured atom number is then determined by $N'_m = \langle \hat{U}^\dagger \hat{N}_m \hat{U} \rangle_{\text{Exp}}$. For example, a $\pi/2$ spin rotation around S_x changes the readout axis in the spin sphere from S_z to S_y .

Suppose, that the N particles are in a product state. Then such a measurement is equivalent to N independent measurements on identically prepared particles. In the single-particle case, the state is determined by the expectation value of the basis set of spin-1 observables. Then each measurement gives us an estimate of this value, where the precision is determined by the total number of atoms used for the estimation. If the preparation of the state is reproducible, one can also increase the statistic by averaging over multiple realizations. After measurements in at least $d+1 = 4$ different measurement bases we can estimate the full single-particle density matrix [35].

2.4. Representation of many-body states

After this short detour to recapitulate the basic properties of projective measurements, we now come back to consider in more detail the representation of many-body states. We recall that for the representation of a spin-1 system, which is basically the symmetric subspace of two spin-1/2 particles, we could either define additional quadrupole operators and describe the state by its quantum mechanical mean given a complete set of operators,

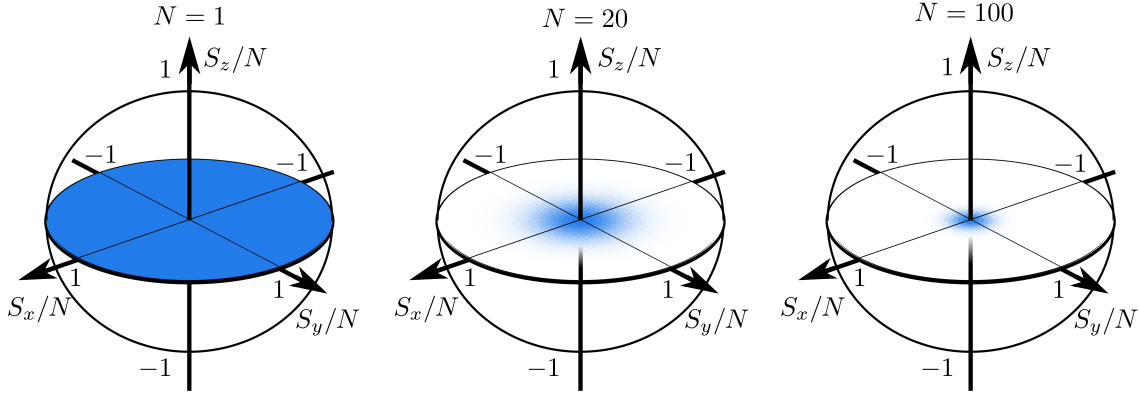


Figure 2.5.: Coherent polar state for different atom numbers: Here, the graphical representation of the coherent polar state for different atom numbers is shown. On a generalized spin sphere, we represent the state via a two-dimensional probability distribution which corresponds to the measurement statistics along the respective direction. For higher atom numbers this results in a two dimensional Gaussian distribution. As we normalize the spin to the total number, the width of this distribution decreases as $1/\sqrt{N}$.

or we could use the mean of the spin operators together with their covariance for visualization. The same now applies to the representation of a many-body state consisting of N spin-1 particle. We could either define additional spin- N operators to describe the state, which is not feasible, or we use the collective operators together with all higher moments and their correlations. This will result in the Wigner and Husimi distribution which are routinely used in quantum optics for the representation of many-body states.

2.4.1. Coherent spin states

We start with the important class of coherent spin states, which are usually the starting point of our experiments. These states are classical in the sense that each particle is in the same single-particle state and, thus, features no quantum correlations. We have already discussed such a state in the context of projective measurements, but we will now take a many-body point of view and look at the measurement statistics that is expected from such a state. As an example, we take a coherent polar state, where the quantum state is given by $|\alpha\rangle = (|0\rangle)^{\otimes N}$. We have seen that this state has a vanishing mean spin length in all spin directions as well as vanishing fluctuations in the z -direction. But it features fluctuations in the transversal spin direction. To measure the transversal spin in a projective measurement scheme as described above, one would first employ a $\pi/2$ spin rotation, which transform the initial state into a transverse polar state and then evaluate the atom number difference $N^- = N_{+1} - N_{-1}$. The measurement statistics of N^- is described by a binomial distribution

$$P(N^-) = \binom{N}{\frac{N}{2} + N^-} p_{+1}^{\frac{N}{2} + N^-} p_{-1}^{\frac{N}{2} - N^-} \quad (2.23)$$

where $p_{\pm 1}$ denotes the probability to find a particle in the state $|\pm 1\rangle$. For the transverse polar state we have an equal probability of $p_{+1} = p_{-1} = 0.5$ to measure a particle in $|+1\rangle$ or $|{-1}\rangle$ and, thus, for large N the distribution becomes Gaussian with mean $\langle N^- \rangle = \langle \hat{S}_\perp \rangle_Q =$

0 and variance $\Delta^2 N^- = \Delta^2 S_\perp = N$ along each transversal spin direction. Consequently, we represent the state by a two dimensional distribution in a generalized spin sphere as shown in Fig. 2.5. As explained before, we normalize the spin to the total atom number N and as a consequence the standard deviation of the plotted distribution decreases as $1/\sqrt{N}$ for higher atom numbers. These fluctuations are the reason for the standard quantum limit in precision measurements. Similarly, we can represent this coherent state on a generalized spin nematic sphere. While the state has no fluctuations along \hat{Q}_0 , it has Gaussian fluctuations along \hat{S}_\perp and \hat{Q}_\perp . Thus, the state is represented by a Gaussian distribution at the north pole of the spin-nematic sphere.

An important feature of coherent states is that they are minimal uncertainty states. That is, given the state can be represented on the surface of an SU(2) subspace, their variances saturate the uncertainty limit of two conjugate observables. For example, the polar state can be represented on the pole of the spin nematic sphere. The variances of the two conjugate observables \hat{S}_\perp and \hat{Q}_\perp obey the uncertainty relation [36]

$$\Delta^2 S_\perp \Delta^2 Q_\perp \geq \frac{1}{4} |\langle [\hat{S}_\perp, \hat{Q}_\perp] \rangle_Q|^2 \stackrel{\text{polar}}{=} N^2 \quad (2.24)$$

which is exactly satisfied by the coherent polar state.

2.4.2. The Wigner distribution

For the coherent polar state we have calculated explicitly its probability distribution and used it to represent the state on a given SU(2) subspace. Since the distribution is Gaussian and the fluctuations are uncorrelated between different measurement directions, the calculation could be carried out using classical statistics. Even though this two-dimensional distribution can never be directly measured, because one cannot simultaneously measure two noncommuting observables with arbitrary precision, the marginals of this distribution give the correct prediction for the probability distribution in the corresponding measurement basis. To generalize this representation via probability distributions to general quantum states, we need a way to calculate it directly from a given density matrix. For later purposes we focus this discussion on the observables \hat{S}_x and \hat{Q}_{yz} , but the treatment can be generalized to any observables.

Even though one cannot measure both observables simultaneously, we can always measure a linear combination of the observables, i.e. $k_1 \hat{S}_x + k_2 \hat{Q}_{yz}$. A single experimental realization gives us then a random number $k_1 S_x + k_2 Q_{yz}$ drawn from the corresponding marginal probability distribution. After acquiring sufficient measurement statistics for a given pair of k_1 and k_2 , one can estimate the characteristic function known from statistics as the expectation value of [37]

$$\chi(k_1, k_2) = \langle e^{i(k_1 S_x + k_2 Q_{yz})} \rangle. \quad (2.25)$$

In classical statistics, this characteristic function is calculated starting from a two-dimensional probability distribution $p(S_x, Q_{yz})$ with

$$\chi(k_1, k_2) = \int dS_x dQ_{yz} e^{i(k_1 S_x + k_2 Q_{yz})} p(S_x, Q_{yz}). \quad (2.26)$$

Thus, the characteristic function is the Fourier transform of $p(S_x, Q_{yz})$. Therefore, applying an inverse Fourier transform on the characteristic function will yield the original two-dimensional probability distribution.

Similarly in quantum mechanics, one can use the density matrix to calculate the characteristic function, i.e.

$$\chi_Q(k_1, k_2) = \langle e^{i(k_1 \hat{S}_x + k_2 \hat{Q}_{yz})} \rangle_Q. \quad (2.27)$$

One now applies the inverse Fourier transform to this quantum mechanical version of the characteristic function to get, in analogy to the classical case, a two-dimensional distribution

$$W(S_x, Q_{yz}) = \frac{1}{4\pi^2} \int dk_1 dk_2 e^{-i(k_1 S_x + k_2 Q_{yz})} \chi_Q(k_1, k_2). \quad (2.28)$$

This is the famous Wigner function or quasiprobability distribution, originally introduced in analogy to a classical phase space distribution [38]. It is widely used in quantum optics for representing the quantum state of light in terms of the two electromagnetic field quadratures. Note that the definition of the Wigner function presented here does not take into account that the underlying phase space is spherical. However, using spherical approaches such as in [39] is anyway problematic since a spin-1 state is not constrained to the surface of the sphere. Our definition rather yields the projection of the Wigner function to a two-dimensional surface. This is still a valid approach as the definition of the Wigner function just involves that its marginals provide the correct measurement statistics in the respective measurement basis [37]. Thus, the notation used here is also slightly different to what is commonly found in quantum optics literature, for example in [40]. To recover the standard notation one needs to define the complex parameter $\beta = (k_1 + ik_2)/\sqrt{2}$ and employ a Holstein-Primakoff approximation [41]. This means that the Wigner distribution has to be localized enough on the surface of the spin-nematic sphere such that the surface can be approximated by a flat phase space.

With Eq. (2.28), the Wigner function provides a representation of the quantum state as a two-dimensional quasiprobability distribution in a phase space spanned by the two observables \hat{S}_x and \hat{Q}_{yz} . In general, for a complete description of the state one would need to generalize the distribution to include all spin-1 observables, which is of course not very useful for a graphical illustration. In many cases, however, previous knowledge about the dynamics allows restricting the phase space to a certain subspace of observables where the quantum features of the state will be prominent. Even though the Wigner function is a quasiprobability distribution, it fulfills certain important aspects of a probability distribution. Mainly it is normalized, i.e. $\int dS_x dQ_{yz} W(S_x, Q_{yz}) = 1$ and the marginals of the distribution give the correct probability distribution for the respective observables, e.g. $p(S_x) = \int dQ_{yz} W(S_x, Q_{yz})$. The last point is a unique feature of the Wigner function which sets it apart from other quantum mechanical quasiprobability distributions [42]. This means, given a quantum state $\hat{\rho}$ one can use the Wigner formalism to predict the measurement statistics of an ideal projective measurement for example of S_x .

What makes the Wigner function a quasiprobability distribution is the fact that it can also have negative values. This is because we used a quantum density matrix to calculate the characteristic function, so the inverse Fourier transform does, in general, not yield a classical probability distribution. It turns out that the negativities of the Wigner function can be associated with highly correlated, nonclassical states [43], for example the cat state [37], which is a maximally entangled state. Since we cannot measure the full Wigner function directly but only its marginals these negativities do not introduce inconsistencies between measurements and this representation.

The probability distribution we calculated before for the coherent polar state is also a Wigner distribution and belongs to the important class of Gaussian states. These are states that have Gaussian shaped Wigner functions. They are very close to classical states in the sense that the Wigner function is a true probability distribution and the quantum correlations are not that strong to introduce negativities.

In an experiment one usually wants to turn the argument around, i.e. from a given measurement statistics one wants to find out the underlying quantum state or equivalently its Wigner distribution. For this one has to employ quantum state tomography, which means to measure the probability distribution in different measurement bases, i.e. to measure the different marginals. Out of the marginals of the distribution one can then attempt to reconstruct the original Wigner function via various algorithms [44].

2.4.3. The Husimi distribution

The Wigner function is not the only way to represent a quantum state but there exist a whole range of quasiprobability distributions which provide an equivalent representation. Another one commonly used is the so-called Husimi Q function [45]. One way to define this distribution is via coherent states as they form an overcomplete basis of the Hilbert space. The Husimi function for the phase space, spanned by \hat{S}_x and \hat{Q}_{yz} , is given by [46]

$$Q(S_x, Q_{yz}) = c \sum_{\alpha} \langle S_x, Q_{yz} | \hat{\rho} | S_x, Q_{yz} \rangle_{\alpha}, \quad (2.29)$$

where $|S_x, Q_{yz}\rangle_{\alpha}$ is a coherent state with expectation values $\langle \hat{S}_x \rangle_Q = S_x$ and $\langle \hat{Q}_{yz} \rangle_Q = Q_{yz}$. Since the mean value of the two operators does in general not uniquely identify a coherent state in a spin-1 system, we label the different states with α . The prefactor c is chosen such that the distribution is normalized, i.e. $\int dS_x dQ_{yz} Q(S_x, Q_{yz}) = 1$. This distribution is often easier to calculate than the Wigner function and provides a more intuitive representation since it is always positive, which can be verified by inserting the definition of a general density matrix into Eq. (2.29)

$$\begin{aligned} Q(S_x, Q_{yz}) &= c \sum_{\alpha} \langle S_x, Q_{yz} | \sum_i P_i |\psi_i\rangle \langle \psi_i| |S_x, Q_{yz} \rangle_{\alpha} \\ &= c \sum_{\alpha, i} P_i |\langle S_x, Q_{yz} | \psi_i \rangle|^2. \end{aligned} \quad (2.30)$$

Even though the Husimi function is normalized and non-negative it is still a quasiprobability distribution because, in contrast to the Wigner function, its marginals do not provide the correct measurement statistics for a corresponding projective measurement. Comparing the marginals of both distributions it turns out the one from the Husimi distribution have a larger width. In fact, one can show that the Husimi function is the Wigner distribution convoluted with a Gaussian filter that has the width of a coherent state [46], i.e.

$$Q(S_x, Q_{yz}) \propto \int dS'_x dQ'_{yz} W(S'_x, Q'_{yz}) e^{-\frac{1}{2N} [S_x + Q_{yz} - (S'_x + Q'_{yz})]^2}. \quad (2.31)$$

This smoothing is responsible for removing the negativities of the Wigner function but it also broadens the whole distribution. For a comparison between the Husimi and the

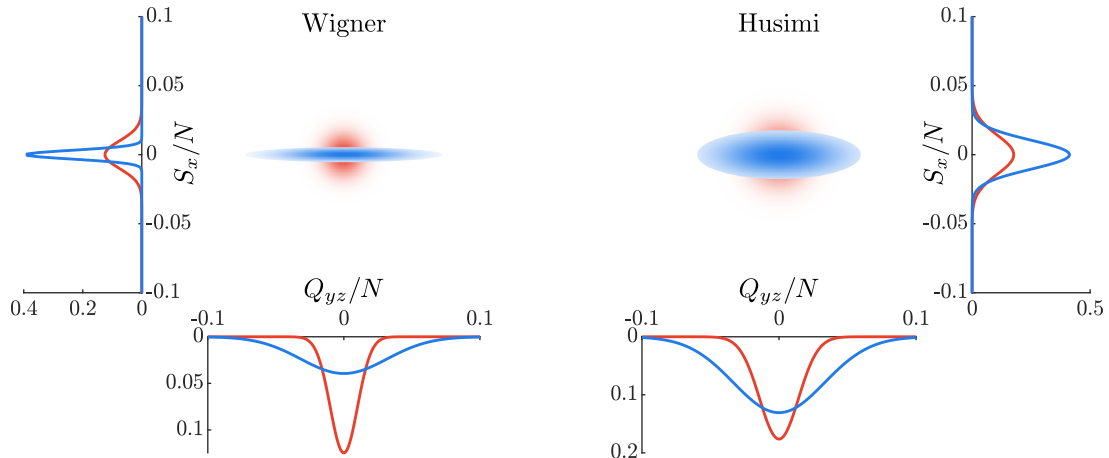


Figure 2.6.: **Wigner and Husimi function:** Comparison between the Wigner (left) and the Husimi (right) representation for the same coherent (red) and squeezed state (blue). For more examples see [37]

Wigner distribution for a coherent and a squeezed state, i.e. a Gaussian state with reduced fluctuations along one observable, see Fig. 2.6. Since this filtering is reversible, the Husimi function is equivalent to the Wigner function and provides a complete representation of the quantum state.

Even though the Husimi distribution does not yield the correct marginals associated with a projective measurement as described above, we will later (Sec. 8.1) see that it is indeed connected to a more general type of measurement, where it provides the correct measurement statistics.

2.5. Quantum correlations

Entanglement has already been recognized by Schrödinger as a central concept of quantum mechanics which sets it apart from classical theories [47, 48]. Besides the philosophical implications that have been discussed since its discovery [49], entanglement is nowadays considered a key resource for future quantum enhanced technologies [50]. For the discussion of quantum correlations we choose here the historic approach by starting with steering, a term coined by Schrödinger as a response to the famous Einstein-Podolsky-Rosen (EPR) paradox [49], which first placed entanglement into the focus of interest.

2.5.1. EPR-Steering

Even though the EPR paradox has already been widely discussed in literature, we will outline here the basic argument and its implications as it provides an insightful introduction to entanglement and its distinguishing features. Let us consider two systems, A and B, as well as two non-commuting observables \hat{Q}_X and \hat{P}_X ($X \in \{A, B\}$) with $[\hat{Q}_X, \hat{P}_X] \neq 0$. These observables could either be position and momentum as in the original argument or conjugate spin observables as described before. Because of the uncertainty relation it is then impossible in a single subsystem, e.g. A, to measure both observables with arbitrary

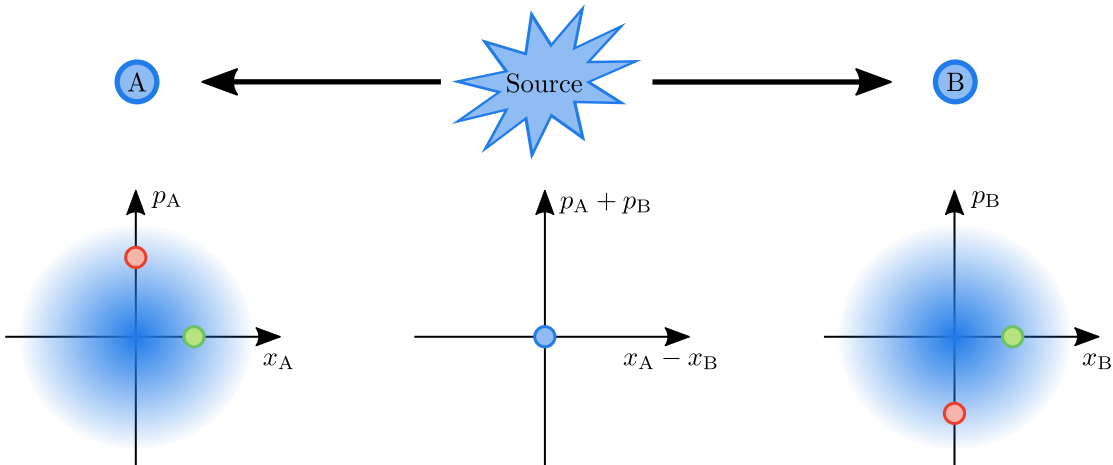


Figure 2.7.: **The EPR paradox:** A source emits two highly entangled particles. Measuring the position and momentum of each particle alone gives the distribution illustrated by the shaded area (left and right) which is consistent with the Heisenberg uncertainty relation. However, each result of a position measurement in system A is perfectly correlated with the result in system B, while the results for the momentum measurements are perfectly anticorrelated. Using the information in system B to infer the results in system A gives in the perfect case a point-like distribution (middle) which surpasses the Heisenberg bound of the single system.

precision. Or, in other words, there is no way of simultaneously knowing precisely the value of \hat{Q}_A and \hat{P}_A , because, as Feynman put it, “nature herself does not even know” [51].

At the same time, quantum mechanics allows for correlations such that if we choose to measure the observable \hat{Q}_B in system B and obtain the result Q_B , we find that it is perfectly correlated with the one in A, i.e. $Q_A = Q_B$. The knowledge gained in system B, therefore, allows us to predict the measurement result of Q_A in A with certainty. Analogously, if we decide to measure on the next identically prepared system the observable \hat{P}_B , we find that the results are perfectly anticorrelated, i.e. $P_A = -P_B$ as sketched in Fig. 2.7. Quantum mechanically this is possible, because the operators $\hat{Q}_A - \hat{Q}_B$ and $\hat{P}_A + \hat{P}_B$ actually commute, i.e. $[\hat{Q}_A - \hat{Q}_B, \hat{P}_A + \hat{P}_B] = 0$.

In principle the two systems can be infinitely far apart. From a classical point of view, one would then assume that a measurement in B does not influence A (locality). Thus, it should be possible to attribute simultaneously a precise value for both observables in system A without disturbing this system (realism), which is in conflict with the uncertainty relation. Thus, EPR correctly concluded that the completeness of quantum mechanics is at odds with the assumptions of local realism. In a response to this work, Schrödinger recognized that such a situation could only arise if the two systems at one point in time have interacted and in the process became entangled [47]. For such an entangled state a local description of A and B is not correct to understand what happens globally and a measurement on system B will therefore instantaneously affect the state in A, for which he coined the term steering.

It is important to note that even though quantum mechanics has this nonlocal property, this is not in contradiction to the theory of relativity, because the measurement choice, for example in B, cannot be used to send any information to A. Irrespective of the

measurement choice one will always find the same measurement statistics in A. Only by comparing the results, via classical communication, one can verify that the two systems must have been entangled. This is referred to as no-signaling [52]. After Bell showed, that it is indeed possible to experimentally test the assumptions of local realism [53], it is nowadays, after many Bell tests [54, 55, 56], well established that quantum mechanics is complete and we need to give up our idea of local realism.

2.5.2. Steering criterion

Experimentally, it is of course impossible to measure the perfect correlations envisioned in the EPR paradox. One can, however, extend the original argument to include the more realistic scenario of imperfect correlations [20]. As the local observables in each subsystems are non-commuting, their measurement statistics have to fulfill the local uncertainty relation. We get, for example, for the variance product in system A [36]

$$\Delta^2 Q_A \Delta^2 P_A \geq \frac{1}{4} |\langle [\hat{Q}_A, \hat{P}_A] \rangle_Q|^2 = c_A. \quad (2.32)$$

Suppose that system A and B always measure the same observable, then the information gained in B is used to get only an estimate for the measurement result in A, i.e.

$$Q_{A,\text{inf}} = g Q_B \quad P_{A,\text{inf}} = h P_B, \quad (2.33)$$

where in the simplest case the measurement results in B are just modified by prefactors g and h as described here. The precision of this estimate is quantified by the inference variance defined as $\Delta^2 Q_{A|B} = \Delta^2(Q_A - Q_{A,\text{inf}})$. If then the product of the two inference variances is smaller than the bound given by the local uncertainty, then one arrives at similar conclusions as in the original EPR argument. One therefore defines the steering inequality

$$S_{A|B} = \Delta^2 Q_{A|B} \Delta^2 P_{A|B} \geq c_A, \quad (2.34)$$

where a steering product $S_{A|B} < c_A$ verifies so-called EPR steering, which we label as A is steered by B. In this sense, EPR steering is a directional entanglement measure and there are indeed states which feature only one-way steering, where A is steered by B but not the other way around [57]. The quantum mechanical bound on the steering product is determined by the commutation relation of the inference operators

$$[\hat{Q}_A - g\hat{Q}_B, \hat{P}_A - h\hat{P}_B] = [\hat{Q}_A, \hat{P}_A] + gh [\hat{Q}_B, \hat{P}_B], \quad (2.35)$$

which is why one needs a combination of correlation in one basis (e.g. $g > 0$) and anticorrelation in the conjugate basis ($h < 0$) in order to violate the steering inequality. In principle, any post-processing of the measurement results obtained in B is allowed to get an optimal estimate of the measurement result in A, since such classical operations cannot introduce any entanglement. The post-processing just influences the quantum mechanical bound via the commutation relation of the inference operators.

2.5.3. Quantum information and LOCC

EPR steering correlations lie at the heart of many quantum information protocols. These protocols are usually discussed under the so-called LOCC paradigm standing for “local

operations and classical communication". That is, given the two systems A and B, often called Alice and Bob, share an entangled state, they are only allowed to use local operations and communicate via classical means. With these operations they cannot increase the overall entanglement but can try to use their entangled resource to accomplish a given task better than it would be possible if they only had classically correlated states.

In this context, EPR steering is also called a one-sided device independent protocol. In this scenario, Bob tries to convince Alice that they share an entangled quantum resource. After agreeing on the measurement protocol, only Alice has to ensure that the correct observables are measured. Bob sends her his estimates and only if he has measured the same observables, he is able to predict her results. If Bob just sends her random data, uses a wrong post processing or measures the wrong observables this can only increase the inference variance. Therefore, Alice does not care how the estimates have been obtained but as soon as her measurement results are predicted better than the local uncertainty relation, she knows that their states are entangled.

Based on this idea and the fact that the entanglement is lifted as soon as one part of the quantum resource is measured, one can envision different protocols for quantum cryptography based on EPR steering [18]. The idea behind these protocols is that Alice and Bob want to certify that no one intercepted their quantum channel. If someone measured the state in between, Bob would not be able to predict the measurement outcomes of Alice with the required accuracy. Thus, they can use steering to certify that their quantum channel has not been disturbed and then send each other keys via this secure channel to encode their messages. While one may be concerned about the efficiency of such a protocol, there are also other tasks for which EPR correlations are vital, such as quantum teleportation [58] and quantum information processing [17].

As a short remark, a Bell state provides even more possibilities and a Bell test is, in this context, referred to as a two-sided device independent protocol. This is because for EPR steering Alice has to assume that she measures two noncommuting observables which obey the quantum mechanical uncertainty relation. In a Bell test, an independent observer could evaluate the results which are sent to him by Alice and Bob and decide if they violate a Bell inequality statistical arguments without knowing the uncertainty relations of the corresponding operators. This comes however at a cost of a very fragile Bell state [20].

2.5.4. Entanglement

EPR steering, as it turns out, is already a strong form of entanglement in the sense that all steerable states are entangled but not all entangled states violate a steering inequality. In general, entangled states are defined as being the opposite to separable states. That means that the state of the total system $|\psi\rangle$, consisting of subsystems A and B, is entangled if it cannot be written in biseparable form, i.e. as a product state [59]

$$|\psi\rangle \neq |\psi_A\rangle \otimes |\psi_B\rangle, \quad (2.36)$$

or equivalently in terms of density matrices

$$\hat{\rho} \neq \sum_i P_i \hat{\rho}_{A,i} \otimes \hat{\rho}_{B,i}, \quad (2.37)$$

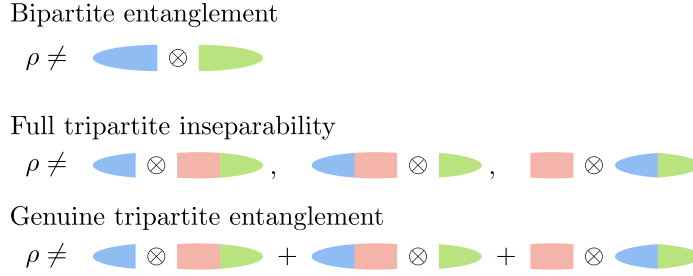


Figure 2.8.: Sketch for the different entanglement definitions: While for bipartite system only one notion of entanglement exists, the situation for multipartite systems is more involved and different notions of entanglement exist. In the context of this thesis, we will discuss the detection of genuine multipartite entanglement, where the definition of the tripartite case is sketched in the last panel. In contrast, the definition of full tripartite inseparability is depicted in the middle.

with $\sum_i P_i = 1$. It has also been sometimes defined in positive terms, that a state is entangled if it is a resource for a nonclassical task [60]. Both definitions are, in practice, not very useful and even theoretically it is often hard to determine whether a given state can be written as a product state, let alone to predict whether it is a useful resource. Thus, there is an ongoing theoretical effort to find criteria that are sufficient to verify entanglement, but which provide in general not a necessary condition [61, 60].

While many quantum information protocols rely on EPR steering, entanglement itself is already a useful resource for certain tasks. Fig. 2.6 introduced already a so-called squeezed state which features a reduction of fluctuations in one observable at the cost of increased fluctuations in the conjugate observable. The reduced fluctuations of these states can be used for quantum enhanced precision measurements [62, 63, 9], e.g. to probe external magnetic fields with a precision beyond classical limits [64]. Pictorially speaking, this is possible because the field is not probed with a collection of independent atoms, but with an ensemble of correlated, i.e. entangled, atoms which increases the sensitivity on the parameters of the external field [10, 11].

Multipartite systems

We can also extend the concept of entanglement from the bipartite scenario to multipartite situations. While for pure states many definitions are equivalent, there are in general different notions of entanglement for mixed states [65]. In close analogy to above, we can define bipartite entanglement by sorting the subsystems of an m -partite system into two sets X_α and its conjugate \bar{X}_α , where α labels the specific bipartition. If one can show that the state is entangled across all bipartitions, that is for each partition α , we cannot write the state in biseparable form

$$\hat{\rho} \neq \sum_k \eta_{\alpha,k} \hat{\rho}_{X_\alpha,k} \otimes \hat{\rho}_{\bar{X}_\alpha,k} \quad \forall \alpha, \quad (2.38)$$

then the state is called “full m -partite inseparable” [66, 67]. If, in addition, it cannot be written as a superposition of biseparable states

$$\hat{\rho} \neq \sum_{\alpha} P_{\alpha} \sum_k \eta_{\alpha,k} \hat{\rho}_{X_{\alpha},k} \otimes \hat{\rho}_{\bar{X}_{\alpha},k}, \quad (2.39)$$

the state is genuine m -partite entangled [68]. For a graphical representation of these definitions see Fig. 2.8. Genuine multipartite entangled states play an important role for spatially distributed quantum protocols such as quantum communication networks [69, 70] and measurement based quantum computation [71, 72] via so-called graph states [73].

3. Experimental system and control

After presenting the basic theoretical aspects of this thesis, we will now focus on the experimental system, a spinor Bose-Einstein condensate of ^{87}Rb . We will shortly summarize the condensation process and provide details about the control of the spin states and the measurement procedure. A main focus for the design of the experimental setup has been a high stability, such that the experiment is able to run unattended for days in order to acquire a high statistics which compensates the comparatively long repetition interval of about 37 s. A sketch of the relevant experimental components can be found in Fig. 3.1.

3.1. Bose-Einstein condensation and trapping configurations

Here, a short overview of the condensation sequence is provided, where further details can be found in earlier publications [74, 75, 76, 77, 78, 79]. Each experimental realization starts with a 3D magneto-optical trap (MOT) that is loaded from a 2D MOT in about 7 s; the actual loading time of the MOT is shorter, however, some time is added to keep the length of each experimental sequence roughly fixed to 37 s for stability. After a short sequence of sub-Doppler cooling in an optical molasses, the atoms are loaded in a magnetic trap with a time orbiting potential (TOP trap) [80]. The magnetic trap is designed such that the low-field seeking ($F, m_F = (1, -1)$) state is trapped, while any residual $F = 2$ atoms are pushed out by shortly switching on the MOT beams. We initiate evaporative cooling by lowering the strength of the TOP trap such that atoms with a high kinetic energy are expelled. In this way, we produce after ≈ 25 s an atomic sample of about 10^6 atoms near the critical temperature for condensation. The final trap is a crossed optical dipole trap consisting of two far red-detuned focused laser beams (referred to as waveguide and XDT) emitted from a single 1030 nm Yb:Yag source (Innolight Corona). For a reliable transfer of the atoms the crossing point of the two beams is below the position of the magnetic trap. By lowering the strength of the magnetic trap the atoms are descending due to gravity and get caught in the dipole trap. In the end, another evaporative cooling stage is implemented by lowering the power of the crossed dipole beams to reach condensation. Depending on this last condensation ramp we can tune the final atom number between $\approx 1,000$ and $\approx 100,000$ atoms in the condensate. After condensation, the typical temperature of the atomic cloud is about 20 nK, compared to a critical temperature of ≈ 150 nK for 10.000 atoms in the crossed dipole trap. After condensation, the atoms are loaded into the final trap geometry. Depending on the requirements of the experiment, we choose in the context of this work between two different settings.

One trap geometry is a crossed-dipole trap where the energy spacing of the external degrees of freedom is large enough such that they are largely frozen but where we can still individually address specific spatial modes via the interactions between the atoms. For this trap geometry we ramp the power of both beams back up after evaporation.

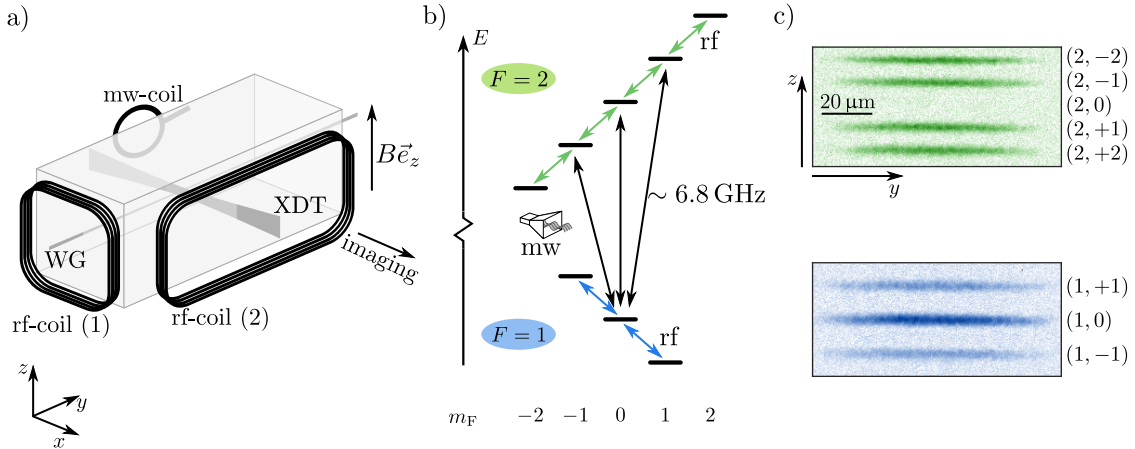


Figure 3.1.: **Experimental components:** a) Sketch of the experimental setup. The BEC is prepared inside a glass cell where the atoms are trapped within a crossed optical dipole trap. This trap consists of two far red-detuned laser beams referred to as waveguide (WG) and XDT. In the vertical z -direction we apply a homogeneous magnetic field along which we define the quantization axis. To manipulate the spin states of the atoms we employ microwave (mw) and radiofrequency (rf) fields. For detection, high intensity absorption imaging is used with an optical resolution of $\approx 1 \mu\text{m}$. b) Level scheme of ^{87}Rb in the electronic groundstate including the first-order Zeeman shift. To couple the two hyperfine manifolds we use mw fields at a frequency of $\approx 6.8 \text{ GHz}$. The magnetic substates are coupled via rf fields. c) Typical absorption images of the condensate in the crossed-dipole trap after expansion for the two hyperfine manifolds; the state $(2, 0)$ is not populated here.

This results in trapping frequencies of $(\omega_{||}, \omega_{\perp}) \approx 2\pi \times (50, 286) \text{ Hz}$, where we can adjust the final value by the power of the beams. The second trap geometry is a quasi one-dimensional trapping potential where the BEC has a spatial extension in longitudinal direction on the order of $400 \mu\text{m}$. For this, we adiabatically lower the XDT to load the BEC into the elongated dipole trap provided by the waveguide with trapping frequencies $(\omega_{||}, \omega_{\perp}) \approx 2\pi \times (2, 250) \text{ Hz}$. For the measurement of the trap frequencies see Appendix A.1.

3.2. Magnetic field shifts

During the experiments, we apply a homogeneous magnetic bias field B in z -direction along which we define our quantization axis. This field shifts the energy of the magnetic substates in both hyperfine manifolds due to the Zeeman effect. We take into account the first- and second-order shift given by

$$E_Z/h = g_{1,F} m_F B + g_{2,F} (4 - m_F^2) B^2 \quad (3.1)$$

with the Planck constant h . The first- and second-order g-factors are

$$\begin{aligned} g_{1,F} &\approx \begin{cases} -700 \text{ kHz/G} & \text{for } F = 1 \\ 702 \text{ kHz/G} & \text{for } F = 2 \end{cases} \\ g_{2,F} &\approx \begin{cases} -72 \text{ Hz/G}^2 & \text{for } F = 1 \\ 72 \text{ Hz/G}^2 & \text{for } F = 2 \end{cases} \end{aligned} \quad (3.2)$$

While the absolute value of the g-factors is nearly the same in both manifolds, their sign is different, which will become important for the addressability of the two manifolds. An explicit calculation of these parameters can be found in [79]. For the experiments reported here, we usually apply a magnetic field between 0.8 and 2 G which is actively stabilized using a fluxgate sensor mounted close to the glass cell. This leads to a shot-to-shot stability of about 50 μG (see Appendix A.2). For an overview of the energy levels of the $F = 1$ and $F = 2$ manifold including the first-order Zeeman shift see Fig. 3.1b).

Using the spin operators defined before, the Hamiltonian for the magnetic field shifts in the $F = 1$ manifold is given by

$$\hat{\mathcal{H}}_B = h p_B \hat{S}_z - h \frac{q_B}{2} \hat{Q}_0 \quad (3.3)$$

with $p_B = g_{1,1}B$ and $q_B = -g_{2,1}B^2$. Thus, the first-order Zeeman shift leads to a dynamical evolution of the Larmor phase (Larmor precession), while the second-order Zeeman shift causes a dynamical evolution of the spinor phase.

3.3. Imaging and post-processing

The populations in the different magnetic substates are measured with high intensity absorption imaging [81, 82], which, in addition, is selective on the $F = 1$ and $F = 2$ hyperfine state. To spatially separate the different magnetic substates, we apply a magnetic field gradient (Stern-Gerlach pulse) along the z -direction while switching off the dipole traps. We first image the atoms in the $F = 2$ manifold by employing light that is resonant with an excited electronic state (D_2 light). Each imaging pulse has typically a duration of 15 μs during which about 300 photons are scattered by each atom. Thus, the atoms are subsequently blown out of focus by the imaging light. To record the atoms in the atoms in the $F = 1$ manifold light resonant with the $F = 1$ manifold is added for the following image. To reduce noise contributions from the imaging, we can also leave out the first pulse and image both manifolds in one image. Afterwards we take two reference images without any atoms which are used to reconstruct the atomic densities. Example images are shown in Fig. 3.1c). For detection, we use the fast kinetics mode of the CCD camera (Princeton Instruments PIXIS 1024BR) which allows us to take four consecutive images with a separation of ≈ 1.2 ms. At the end of the imaging sequence a small part of the chip is not illuminated by any imaging light and is used to estimate the background counts of the camera.

For the evaluation region shown in Fig. 3.1c) the precision of the measurement corresponds to $\approx \pm 35$ atoms in each magnetic substate due to photon shot noise contributions from the absorption and the reference image. The imaging system has a magnification factor of 31 such that each pixel on the camera corresponds to 0.42 μm in the object plane of the atoms. For the imaging sequence we position the objective as close as possible

to the glass cell to achieve a high numerical aperture of $NA = 0.45$ which results in an optical resolution of $\approx 1 \mu\text{m}$. This sequence realizes a projective measurement as described before, where the measurement of the particles in the different magnetic substates corresponds to a measurement along the S_z -direction of the spin sphere.

To reduce the noise on the atomic densities caused by optical fringes, we employ a fringe removal algorithm as detailed in [83]. For that we set up a library of typically 700 reference images and construct an optimal reference image via linear combination. This optimal reference image is optimized on an empty region of the absorption image, i.e. a region where no atoms are detected. Because of the averaging over many reference images, the photon shot noise on the optimal reference image is largely reduced such that its contribution becomes negligible. Thus, the overall photon shot noise is reduced by a factor of $\sqrt{2}$, which increases the measurement precision to about ± 25 atoms in each magnetic substate.

Expansion in waveguide

In the crossed dipole trap the condensate typically has a spatial extension of 2 to 3 μm in transversal direction and 7 to 10 μm in longitudinal direction which corresponds to the Thomas-Fermi radius. For atom numbers between 10.000 and 40.000, which we typically load into this trap geometry, this results in a very high optical density which would require very high intensities of the imaging light ($> 100 I_{\text{sat}}$, where I_{sat} is the saturation intensity). Such high intensities largely increase the imaging noise. Thus, in order to get a reasonable optical density of 1 at intensities of $\approx 20 I_{\text{sat}}$, we switch off the XDT prior to the imaging. We subsequently let the condensate expand in the remaining waveguide potential for up to 10 ms, after which the condensate has reached a spatial extension of typically 60 to 100 μm . In addition to lowering the optical density, the expansion eases the detection of spatial structures in longitudinal direction that may have evolved during the dynamics. As the maximal expansion time of 10 ms is very short compared to the $\pi/2$ time of the longitudinal trap frequency which would be on the order of 100 ms, this expansion does not give us any momentum information of the condensate [84] but corresponds to a self-similar expansion of the atomic cloud [85].

3.4. Rf spin rotations

To induce spin rotations in the two hyperfine manifolds we use magnetic radiofrequency (rf) fields, where we can choose between two rf coils to apply the signal as shown in Fig. 3.1a). We generate the rf signal with an arbitrary function generator (Agilent 33522A) which is afterwards amplified (for a technical noise analysis of the rf signal see Appendix A.4). The rf coil generates a linearly oscillating magnetic field $\vec{B}_{\text{rf}}(t) = B_{\text{rf}} \cos(\omega_{\text{rf}} t + \phi_{\text{rf}}) \vec{e}_y$ perpendicular to the offset field, e.g. along the y -direction. Here, ω_{rf} and ϕ_{rf} denote the frequency and phase of the rf field, respectively. In the $F = 1$ manifold the interaction with the atoms is described by the time-dependent Hamiltonian

$$\hat{\mathcal{H}}_{\text{rf}}(t) = 2\hbar\Omega_{\text{rf},0} \cos(\omega_{\text{rf}} t + \phi_{\text{rf}}) \hat{S}_y, \quad (3.4)$$

with the reduced Planck constant $\hbar = h/2\pi$ and the resonant Rabi frequency given by $\Omega_{\text{rf},0} = |g_{1,1}|B_{\text{rf}}/2$.

To remove the time dependence we transform the system into the rotating frame of the rf-pulse with the same orientation as the Larmor precession as determined by $\text{sgn}(g_{1,1})$. If the rf-pulse is resonant, i.e. $\omega_{\text{rf}} = 2\pi \cdot p_B$, this yields

$$\begin{aligned}\hat{\mathcal{H}}_{\text{rf}}^{\text{rot}} &= e^{-i\omega_{\text{rf}}t\hat{S}_z} \hat{\mathcal{H}}_{\text{rf}} e^{i\omega_{\text{rf}}t\hat{S}_z} \\ &= 2\hbar \Omega_{\text{rf},0} \cos(\omega_{\text{rf}}t + \phi_{\text{rf}}) [\cos(\omega_{\text{rf}}t)\hat{S}_y - \sin(\omega_{\text{rf}}t)\hat{S}_x] \\ &= \hbar \Omega_{\text{rf},0} [\cos(\phi_{\text{rf}})\hat{S}_y - \sin(\phi_{\text{rf}})\hat{S}_x].\end{aligned}\quad (3.5)$$

Thus, a resonant rf pulse induces spin rotations (Rabi oscillations) with a rotation frequency given by the resonant Rabi frequency $\Omega_{\text{rf},0}$. The rotation axis is determined by the phase of the rf field. For the last line we have used the rotating wave approximation and neglected terms with frequency $2\omega_{\text{rf}}$. This is well justified as long as the Rabi frequency is much lower than the rf frequency, i.e. $\Omega_{\text{rf},0} \ll \omega_{\text{rf}}$ [86]. Intuitively, this approximation assumes that the rotation axis changes its orientation very fast compared to the rotation of the state around this axis and therefore the effect on the state is averaged out.

If the rf frequency does not match the resonance frequency $\omega_0 = p_B/\hbar$, the state will, in the rotating frame, still precess around the S_z -axis. This is described by $-\hbar\delta\hat{S}_z$ with the detuning $\delta = \omega_0 - \omega_{\text{rf}}$. Thus, the evolution of the internal state is governed by the Hamiltonian

$$\hat{\mathcal{H}}_{\text{B}}^{\text{rot}} = \hbar \Omega_{\text{rf},0} [\cos(\phi_{\text{rf}})\hat{S}_y - \sin(\phi_{\text{rf}})\hat{S}_x] - \hbar\delta\hat{S}_z.\quad (3.6)$$

Therefore, for an off-resonant rf pulse the effective axis of rotation is tilted out of the S_{\perp} -plane.

Strictly speaking, the rotation axis for the rf pulse is defined by the phase difference between the Larmor phase and the rf phase. Since after condensation all atoms are in the state $(1, -1)$ the Larmor phase is initially undefined. We, thus, define the first rf pulse such that it induces a rotation around the S_y axis of the spin sphere. The first rf pulse then provides the phase reference for all subsequent spin rotations. The same argument holds when we prepare the polar state as the initial state.

We can apply the same treatment to the $F = 2$ manifold, by changing the operators to the corresponding spin-2 operators and taking into account the different sign of the g-factor. Because the absolute value of the g-factors in both manifolds are similar, an rf field tuned into resonance with the $F = 1$ manifold will also induce off-resonant spin rotation in $F = 2$. This will be discussed in more detail in 6.2.1.

Long rf rotations and the second-order Zeeman shift

So far we have neglected the effect of the second-order Zeeman shift for the spin rotations. For the typical experimental parameters the rf Rabi frequency is on the order of $\Omega_{\text{rf},0} \approx 2\pi \cdot 7 \text{ kHz}$ while the second-order Zeeman shift is on the order of $2\pi \cdot 100 \text{ Hz}$. Therefore, this shift will only become relevant after several Rabi cycles. To observe this effect we induce spin rotations starting in the state $(1, -1)$ and record the z -projection of the spin, i.e. the atom number imbalance $N^-/N = (N_{1,+1} - N_{1,-1})/N$ normalized to the total atom number N . Without the second-order Zeeman shift we would expect Rabi oscillations i.e.

$$\frac{N^-(t_{\text{rf}})}{N} = -\cos(\Omega_{\text{rf},0} \cdot t_{\text{rf}}),\quad (3.7)$$

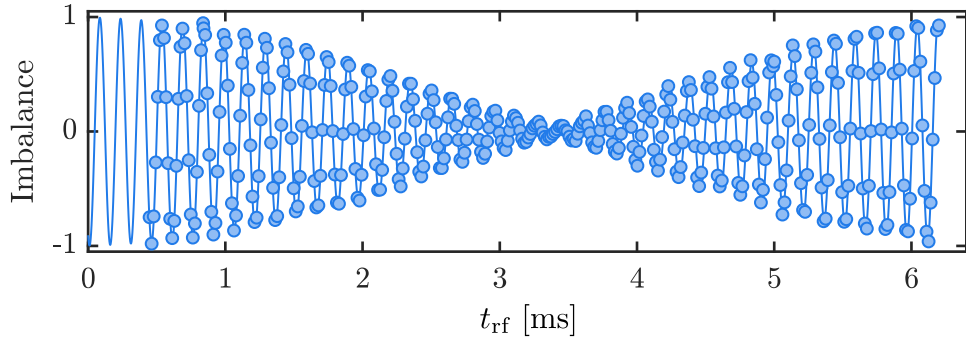


Figure 3.2.: **Rabi oscillations in $F = 1$:** Experimentally, we observe a modulation of the imbalance N^-/N for long rf pulse durations (t_{rf}). From a fit (blue line) we extract a fast frequency of $\Omega_{\text{rf},0} = 2\pi \cdot 6.6 \text{ kHz}$, corresponding to the Rabi frequency, and a modulation frequency of $\omega_Q = 2\pi \cdot 71 \text{ Hz}$ which is connected to the second-order Zeeman shift.

where t_{rf} is the duration of the rf pulse. Experimentally, however, we find a modulated Rabi oscillation as shown in Fig. 3.2. A fit to the data yields a resonant Rabi frequency of $\Omega_{\text{rf},0} = 2\pi \cdot 6.6 \text{ kHz}$ and a modulation frequency of $\omega_Q/2\pi = 71 \text{ Hz}$.

As argued before, the second-order Zeeman shift can be described in the Hamiltonian by the operator \hat{Q}_0 . Since a rotation around Q_0 reduces the transversal spin length, we expect that this modulates the contrast of the Rabi oscillation, which is equivalent to a modulation of the total spin length. For this experiment we have set the external magnetic field to 1.44 G which results in an second-order Zeeman shift of $q_B = 150 \text{ Hz}$. This differs by a about factor of two from the observed modulation frequency. However, as explained in 2.1.5, the reduction of the spin length depends on the mean value of S_z . For $|S_z| \approx 0$ the spin length is dynamically modulated according to $\propto \cos(2\pi q_B \cdot t)$, but for $|S_z| \approx 1$ the effect of the second-order Zeeman shift is equivalent to an additional rotation of the spin around S_z while the spin length stays constant. Since the S_z projection of the state constantly changes during the Rabi evolution, we would intuitively expect the modulation to be slower than the second-order Zeeman shift. Simulating the Rabi oscillations with the experimental parameters confirms that the modulation frequency is indeed a factor of two lower than the second-order Zeeman shift.

3.5. Microwave control

To drive transitions between the two hyperfine manifolds we use microwave (mw) fields. Coupling two magnetic substates corresponds to a two-level system which is described by spin-1/2 operators. For the theoretical description we define the operators in second quantization

$$\hat{C}_x^{m_1, m_2} = \frac{1}{2} \hat{a}_{1, m_1}^\dagger \hat{a}_{2, m_2} + \text{h.c.} \quad \hat{C}_y^{m_1, m_2} = \frac{1}{2} i \hat{a}_{1, m_1}^\dagger \hat{a}_{2, m_2} + \text{h.c.} \quad (3.8)$$

where $\hat{a}_{F, m_F}^{(\dagger)}$ is the annihilation (creation) operator in the state (F, m_F) where m_F is the magnetic substate in the respective hyperfine manifold. Because of the selection rules for dipole transitions only couplings with $\Delta m_F = m_1 - m_2 = \{0, \pm 1\}$ are allowed. Since the

linear Zeeman shift is nearly the same in both manifolds but with an opposite sign, the resonance frequencies for couplings with $\Delta m_F = \pm 1$ are typically separated by ≈ 1 kHz while also the Rabi frequency is on the order of a few kHz. Therefore, if we set the mw frequency to resonantly couple for example the states $(1, -1) \leftrightarrow (2, 0)$ we simultaneously couple off-resonantly the states $(1, 0) \leftrightarrow (2, -1)$. The only exception are transitions to the states $(2, \pm 2)$ and transitions with $\Delta m_F = 0$.

We use two different commercial mw generators (HP 8673D and HP 83620A). The first mw generator is always set to a fixed frequency of ≈ 6.8 GHz which we feed into an I/Q mixer. Into the other input port we feed an rf signal generated by a direct digital synthesizer (DDS). Changing the rf frequency allows us to tune the frequency at the output of the mixer in about 50 μ s. Additionally, by controlling the phase of the rf source we can tune the phase of the mw output signal. Due to the fast switching times we mainly use this mw source for state preparation.

The second mw generator is directly connected via an amplifier to the mw coil without I/Q mixer. The advantage of this generator is that we use its internal control circuit to actively stabilize the mw power directly before the mw coil. For that we inserted a directional coupler after the mw amplifier to feed part of the signal back into the internal control loop. We mainly use this generator when we need a highly stable mw power, for example, to induce spin dynamics, which will be discussed in detail in the following chapter.

Preparation of a coherent polar state

As the coherent polar state, where all atoms occupy the state $(1, 0)$, is the starting point for many experiments presented here, we explicitly describe here the preparation sequence that is used in the experiment. After the condensation all atoms occupy the state $(1, -1)$. We then employ two successive mw π -pulses coupling the states $(1, -1) \leftrightarrow (2, 0)$ and $(2, 0) \leftrightarrow (1, 0)$ to transfer the population into the state $(1, 0)$. Afterwards we apply a strong magnetic field gradient along the z -direction to remove any residual atoms in the states $(1, \pm 1)$ from the trap. After the Stern-Gerlach pulse we wait for 100 ms to let the magnetic field stabilize before proceeding with the experimental sequence. For the polar state the states $(1, \pm 1)$ are not populated, this means that the Larmor phase is also undefined and the first rf- rotation serves as a phase reference.

3.6. Magnetic field control sequence

Even though the shot-to-shot fluctuations of the magnetic field is on the order of only 50 μ G, the value can drift over time. This is mainly due to temperature drifts in the electronics. To compensate for these drifts we perform approximately every hour a Ramsey-type control sequence. For this we employ a mw $\pi/2$ -pulse to generate an equal superposition of the states $(1, -1)$ and $(2, 0)$. We deliberately detune this pulse by $\delta_R = 2\pi \cdot 400$ Hz from resonance. As this detuning is small compared to the Rabi frequency of $2\pi \cdot 3.3$ kHz, the effect on the population transfer is negligible. It will, however, lead to a dynamically evolving phase shift between the state and mw pulse, which depends on the Ramsey time t_R . In the spin-1/2 sphere, this pictorially means that the state which is initially perpendicular to the rotation axis will rotate around the equator with the frequency given by the detuning. Depending on the angle between the state and the rotation axis, a second

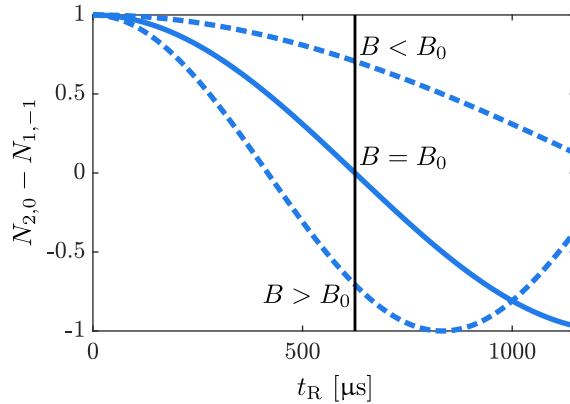


Figure 3.3.: Magnetic field control measurement: To stabilize the magnetic field we employ a Ramsey type sequence between the states $(1, -1)$ and $(2, 0)$ which we deliberately detune from resonance by 400 Hz. Measuring the imbalance $(N_{2,0} - N_{1,-1})/N$ after a Ramsey time of $t_R = 625 \mu\text{s}$ yields the shift of the magnetic field from the set value B_0 .

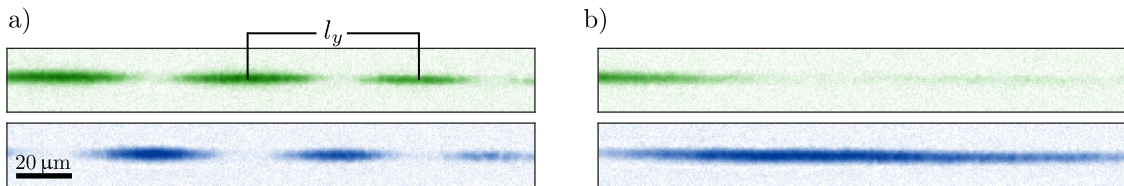


Figure 3.4.: Compensation of the magnetic field gradient: a) Atomic signal in $F = 2$ (upper) and $F = 1$ (lower) without gradient compensation. b) Atomic signal after compensation.

$\pi/2$ rotation will lead to different population imbalances, i.e.

$$(N_{2,0} - N_{1,-1})/N = \cos(\delta_R \cdot t_R) \quad (3.9)$$

as shown in Fig. 3.3). In our case, after a Ramsey time of $t_R = 625 \mu\text{s}$ the state will be aligned with the rotation axis. Therefore, the final spin rotation will not change the population imbalance of 0.

Experimentally, we use exactly this signal after a Ramsey time of $625 \mu\text{s}$ to stabilize our magnetic field. If the magnetic field shifts to a lower value, it effectively decreases the detuning and we will find a positive imbalance. Equivalently, if the magnetic field has shifted to higher values, it will effectively increase the detuning which leads to a negative imbalance in the final signal. With this method we can extract the sign as well as the strength of the field drift. Experimentally, we average over 5 consecutive measurements and feed the extracted measured magnetic field drift forward to the setpoint of the magnetic field stabilization. In this way, we can correct drifts on the order of $\pm 600 \mu\text{G}$ before the sign of the drift cannot be determined unambiguously anymore. For details on the magnetic field stabilization see [79].

Magnetic field gradient

The magnetic bias field is not perfectly homogeneous over the spatial extension of the WG trap but features a small linear gradient, i.e. $\partial B_z / \partial y \neq 0$. The major part of this gradient is compensated by positioning permanent refrigerator magnets around the glass cell. To eliminate the residual gradient we employ the following sequence. We prepare an elongated atomic cloud in the waveguide configuration and use a mw $\pi/2$ -pulse to create an equal superposition of the states $(1, -1)$ and $(2, -2)$. The differential magnetic moment between these states corresponds to about $3 \cdot |g_{1,1}|$ which renders this configuration very sensitive to magnetic field changes. We again employ a Ramsey-type measurement as before with an interrogation time of $t_R = 100$ ms. In this measurement, however, we are not interested in the total phase shift, which exceeds the stability of our magnetic field, but in the relative phase difference in space. The effect of the magnetic field gradient is that at each point along the waveguide direction the spin precesses with a slightly different frequency compared to the mw field. After the second readout pulse one finds a spatially modulated imbalance between the two states given by

$$\frac{n_{2,-2}(y) - n_{1,-1}(y)}{n(y)} = \cos(2\pi \frac{y}{l_y} + \phi) \quad (3.10)$$

where n_{F,m_F} are the spatially resolved atom numbers in the state (F, m_F) and ϕ is an arbitrary offset phase; the signal for an uncompensated magnetic field gradient is shown in Fig. 3.4a). Out of the spatial length scale l_y the magnetic field gradient is calculated to be

$$\left| \frac{\partial B_z}{\partial y} \right| \approx \frac{1}{3|g_{1,1}|t_R l_y}. \quad (3.11)$$

By applying a constant current through the rf-coil (1) we compensate the magnetic field gradient as shown in Fig. 3.4b) up to a few nG/ μ m. Because the magnetic field that is generated by the rf-coil in y -direction is much smaller than the applied offset field in z -direction, the overall direction and value of the bias field remains approximately unchanged. This method is mainly limited by the interaction of the atoms which also gives a spatial detuning in the harmonic potential due to density dependent interaction shifts. However, the compensation we achieve is sufficient such that we detect no significant effect of a residual magnetic field gradient in the experiments described in the following.

4. Interactions and spin-mixing

Experimentally, we use the process of spin-mixing to generate nonclassical states. Starting in the state $(1, 0)$, this mechanism coherently produces highly entangled particle pairs in the states $(1, \pm 1)$, which, in the following, we refer to as side modes. This process is analogous to spontaneous parametric down-conversion in quantum optics [87], where it is used to generate highly entangled photon pairs [88, 89] employed in quantum information protocols such as quantum teleportation [90] and Bell tests [55].

Here, we will review how spin-mixing arises in a spinor BEC from the contact interactions between the atoms. We restrict the discussion to the $F = 1$ manifold; more details and the extension to $F = 2$ can be found in [26, 91]. For the spin-mixing experiments detailed here, the atoms are prepared in the crossed dipole trap to increase the interaction strength via a higher atomic density. While the spatial degree of freedom in this trapping configuration is largely frozen out, we can still use spin-mixing to excite distinct spatial modes of an effective external potential which will be introduced in the following. To include the spatial degree of freedom in our theoretical description we define the operator

$$\hat{\Psi}_m^{(\dagger)}(\mathbf{r}) = \psi_m(\mathbf{r}) \hat{a}_m^{(\dagger)} \quad (4.1)$$

which annihilates (generates) a particle in the magnetic substate m with the spatial wavefunction $\psi_m(\mathbf{r})$. For the beginning of the discussion, we consider a single mode approximation meaning that all magnetic substates occupy the same condensate wavefunction $\psi_c(\mathbf{r})$ which can be found as the minimum of the Gross-Pitaevski equation [92].

4.1. Interaction Hamiltonian

Due to the diluteness of the BEC it is sufficient to take only binary collisions into account since three or more-body collisions are highly unlikely. We also neglect the effect of long range dipole-dipole interactions and start by considering contact interactions typically modeled by a δ pseudopotential [93]. The collisions are assumed to be spherically symmetric such that the total angular momentum is conserved \mathcal{L} . For ultracold, identical bosons, only head-on collisions with a total angular momentum of $\mathcal{L} = 0$ (s-wave regime) are allowed, as the energy is too low to overcome the centrifugal barrier for higher angular momenta in the center of mass frame. The two identical spin-1 particles involved in the collision form a total spin, which due to bosonic exchange symmetry can for $\mathcal{L} = 0$ only take even values of $\mathcal{F} = \{0, 2\}$. This gives two collisional channels where each is characterized by an individual s-wave scattering length. The interaction Hamiltonian in units of Hz is then given as [26, 91]

$$\hat{\mathcal{H}}_{\text{Int}}/h = \frac{1}{2} \frac{2\hbar}{M} (a_0 \hat{P}_0 + a_2 \hat{P}_2), \quad (4.2)$$

where M is the atomic mass and $\hat{P}_{\mathcal{F}} = \sum_{M=-\mathcal{F}}^{\mathcal{F}} |\mathcal{F}, M\rangle \langle \mathcal{F}, M|$ is the projector on the state with total spin \mathcal{F} . The scattering lengths for the two channels are [94]

$$\begin{aligned} a_0 &= 101.8 \pm 0.2 \text{ } a_B \\ a_2 &= 100.4 \pm 0.1 \text{ } a_B \end{aligned} \quad (4.3)$$

with the Bohr radius $a_B = 5.3 \cdot 10^{-11}$ m.

Using the completeness relation and some spin algebra, i.e.

$$\begin{aligned} (i) \quad \mathbb{1}_a \otimes \mathbb{1}_b &= \hat{P}_0 + \hat{P}_2 \\ (ii) \quad \hat{\vec{S}}_a \cdot \hat{\vec{S}}_b &= \frac{1}{2} \sum_{\mathcal{F}} \left[(\hat{\vec{S}}_a + \hat{\vec{S}}_b)^2 - \hat{\vec{S}}_a^2 - \hat{\vec{S}}_b^2 \right] \hat{P}_{\mathcal{F}} \\ &= \frac{1}{2} \sum_{\mathcal{F}} [\mathcal{F}(\mathcal{F}+1) - 2F(F+1)] \hat{P}_{\mathcal{F}} \\ &= -2\hat{P}_0 + \hat{P}_2, \end{aligned} \quad (4.4)$$

where a and b label the two interacting particles. Solving these two relations for \hat{P}_0 and \hat{P}_2 and inserting the expression in Eq. (4.2) yields in second-quantization the interaction Hamiltonian

$$\hat{\mathcal{H}}_{\text{Int}}/h = \frac{\tilde{c}_0}{2} : \hat{N}^2 : + \frac{\tilde{c}_1}{2} : \hat{\vec{S}} \cdot \hat{\vec{S}} : . \quad (4.5)$$

Here, $: :$ denotes normal ordering, i.e. that all annihilation operators are placed to the right of the creation operators. The spin independent and spin dependent coupling constants, \tilde{c}_0 and \tilde{c}_1 , are given via

$$\begin{aligned} c_0 &= \frac{2\hbar}{M} \frac{a_0 + 2a_2}{3} \\ c_1 &= \frac{2\hbar}{M} \frac{a_2 - a_0}{3}, \end{aligned} \quad (4.6)$$

with $\tilde{c}_j = \chi c_j$, where $\chi = \int d\mathbf{r} \psi_0^2 \psi_{+1}^* \psi_{-1}^*$ quantifies the mode overlap. In the single mode approximation where all states occupy the same spatial mode, this is $\chi = \int d\mathbf{r} |\psi_C(\mathbf{r})|^4$.

For the $F = 1$ manifold of ^{87}Rb the coupling constant c_1 is negative. This means that the energy functional Eq. (4.5) is minimized if the spin of all atoms is aligned. Therefore, the interaction in this manifold is called ferromagnetic.

4.2. Spin-mixing

While the spin independent part of the Hamiltonian leads to some overall energy shift which is essential to find the spatial ground state of the condensate, the spin dependent part causes internal dynamics between the magnetic substates. To see this one inserts the definition of the spin operators in second quantization and expands the spin-dependent

Hamiltonian in terms of the ladder operators

$$\begin{aligned}
 \hat{\mathcal{H}}_{\text{Spin}}/\hbar &= \frac{\tilde{c}_1}{2} :(\hat{S}_x \hat{S}_x + \hat{S}_y \hat{S}_y + \hat{S}_z \hat{S}_z): \\
 &= \tilde{c}_1 \hat{N} \\
 &\quad + \tilde{c}_1 (\hat{N}_0 - \frac{1}{2})(\hat{N}_{+1} + \hat{N}_{-1}) \\
 &\quad + \frac{\tilde{c}_1}{2} :(\hat{N}_{+1} - \hat{N}_{-1})^2: \\
 &\quad + \tilde{c}_1 (\hat{a}_0^\dagger \hat{a}_0^\dagger \hat{a}_{+1} \hat{a}_{-1} + \hat{a}_{+1}^\dagger \hat{a}_{-1}^\dagger \hat{a}_0 \hat{a}_0).
 \end{aligned} \tag{4.7}$$

The first term gives some overall energy shift and can be removed as a total energy offset. The second term gives a relative energy shift between the state $(1, 0)$ and the side modes $(1, \pm 1)$. The second line is a shift caused by a finite magnetization of the state which is usually not relevant for the experiments discussed in the following. The last term is the so-called spin-mixing Hamiltonian. It coherently transforms two atoms in the state $(1, 0)$ into atom pairs in the states $(1, \pm 1)$ and vice versa [95].

To describe the initial dynamics one often employs a so-called undepleted pump approximation which is valid as long as the state $(1, 0)$ is highly populated and consequently $N \approx N_0 \gg N^+$, where $N^+ = N_{+1} + N_{-1}$ is total population in the side modes $(1, \pm 1)$. Within this limit the operator $\hat{a}_0^{(\dagger)} \approx \sqrt{N} e^{(-)i\phi_0}$ is approximated by a complex number. If the states $(1, \pm 1)$ are initially unoccupied, the time evolution can then be calculated analytically and one finds on resonance

$$|\psi\rangle(t) = \frac{1}{\cosh(\kappa t)} \sum_{N^+} \left[-ie^{-2i\phi_0} \tanh(\kappa t) \right]^{N^+} \left| \frac{N^+}{2}, N - N^+, \frac{N^+}{2} \right\rangle \tag{4.8}$$

with the coupling strength $\kappa = 2\pi \cdot N \tilde{c}_1$. Here, we expanded the state in the Fock basis as introduced in Sec. 2.2. Since spin-mixing conserves the total magnetization, the dimension of the accessible Hilbert is largely reduced and each basis state can be identified by the side mode population $N^+ = \{0, 2, \dots, N\}$. The mean population of the side modes evolves exponentially as

$$\langle \hat{N}^+ \rangle_Q = 2 \sinh^2(\kappa t) \stackrel{\kappa t \gg 1}{\approx} \frac{1}{2} e^{2\kappa t} - 1. \tag{4.9}$$

The spin-mixing dynamics generate a highly-entangled two-mode squeezed vacuum state [96, 24, 12, 9], which has already been shown to provide a useful resource for quantum enhanced interferometry [97, 98].

Dependence on atom number

The coupling constant $\kappa = 2\pi \cdot N \tilde{c}_1$ suggests that the coupling strength depends linearly on the total atom number. However, one also has to consider the mode overlap χ . Assuming the Thomas-Fermi approximation, i.e. that the interaction energy dominates the kinetic energy, the density of the condensate is given by [92]

$$\begin{aligned}
 n_{\text{TF}}(r, y) &= \frac{1}{c_0} [\mu_{\text{TF}} - V_{\text{ext}}(r, y)] \\
 &= \frac{1}{c_1} [\mu_{\text{TF}} - \frac{M}{2}(\omega_\perp^2 r^2 + \omega_\parallel^2 y^2)]
 \end{aligned} \tag{4.10}$$

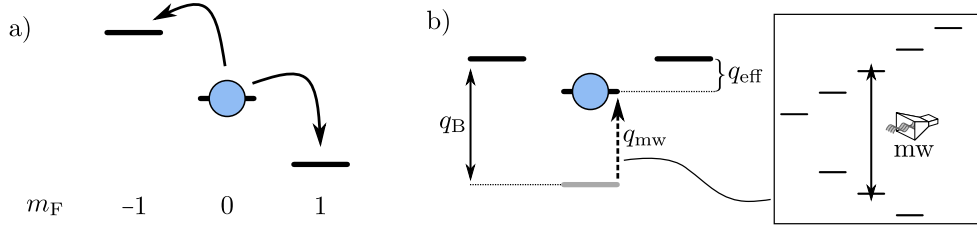


Figure 4.1.: **Experimental energy scales:** a) As illustrated here, the first-order Zeeman shift is not the relevant energy scale for the spin-mixing process, since the energy required for generating a particle in the state $(1, -1)$ is gained by generating one in the state $(1, +1)$. b) One therefore needs to consider the second-order Zeeman shift (q_B) which detunes the spin-mixing process from resonance. Using off-resonant mw coupling between the states $(1, 0) \leftrightarrow (2, 0)$ we can tune this energy splitting which gives us control over the spin dynamics.

where μ_{TF} is the chemical potential. For $\mu_{\text{TF}} < V_{\text{ext}}(r, y)$, the density vanishes, which means that, within this approximation, the condensate fills the external potential up to the chemical potential which is given by

$$\mu_{\text{TF}} = \frac{\hbar\omega_{\text{ho}}}{2} \left(\frac{15N}{a_{\text{ho}}} \frac{a_0 + 2a_2}{3} \right)^{2/5} \quad (4.11)$$

with $\omega_{\text{ho}} = \sqrt[3]{\omega_{\perp}^2 \cdot \omega_{\parallel}}$ and the corresponding harmonic oscillator length $a_{\text{ho}} = \sqrt{\hbar/M\omega_{\text{ho}}}$. In the single-mode approximation we can then calculate the mode overlap via

$$\chi = \int d\mathbf{r} |\psi_c(\mathbf{r})|^4 = 2\pi \int r dr dy |n_{\text{TF}}(r, y)/N|^2. \quad (4.12)$$

The limits of this integration are given by the Thomas-Fermi radii which are found by setting

$$\frac{M}{2}(\omega_{\perp}^2 r^2 + \omega_{\parallel}^2 y^2) \stackrel{!}{=} \mu_{\text{TF}}. \quad (4.13)$$

With this, we find for the mode overlap

$$\chi \propto N^{-3/5} \quad (4.14)$$

and thus, we get for the atom number dependence on the interaction strength

$$\kappa \propto N\chi \propto N^{2/5}. \quad (4.15)$$

4.3. Experimental control

The spin-mixing process conserves the magnetization of the state and therefore the energy under the first-order Zeeman shift stays constant (see Fig. 4.1a)). Mathematically, this means that the energy contribution of the first-order Zeeman shift can be removed from the dynamics using Lagrange multipliers [99]. The relevant detuning for this process

is given by the second-order Zeeman which introduces an energy offset between the atoms in the state $(1, 0)$ and $(1, \pm 1)$. Depending on the bias field, this detuning typically corresponds to values between $q_B = 50$ and 150 Hz while the coupling strength of the spin-mixing process is on the order of 2 Hz. Therefore, the spin-mixing process is far off-resonant.

To control this process we employ so-called mw dressing to shift the energy of the state $(1, 0)$ with respect to $(1, \pm 1)$ [100]. For this we off-resonantly couple the states $(1, 0) \leftrightarrow (2, 0)$, which causes an energy shift of the state $(1, 0)$ due to the ac-Stark shift. The resonant Rabi frequency is typically on the order of $\Omega_{\text{mw}} \approx 2\pi \cdot 9.5$ kHz while the detuning is about $\delta_{\text{mw}} \approx 2\pi \cdot 150$ kHz. This means that the probability to transfer atoms to the state $(2, 0)$ during mw dressing is $\eta = \Omega_{\text{mw}}^2 / (\Omega_{\text{mw}}^2 + \delta_{\text{mw}}^2) < 0.5\%$.

With this dressing the effective detuning of the spin-mixing process is

$$q_{\text{eff}} = q_B + q_{\text{mw}} \quad \text{with } q_{\text{mw}} = \frac{1}{2\pi} \frac{\Omega_{\text{mw}}^2}{4\delta_{\text{mw}}}. \quad (4.16)$$

Thus, we can control the spin-mixing dynamics by changing the detuning of the mw field. Since the coupling strength of the spin-mixing is on the order of a few Hz, this requires that the effective detuning q_{eff} has to be precisely controlled via the mw dressing. This requires a high stability of the Rabi frequency, i.e. of the mw power. Consequently, we use we use the power-stabilized mw generator to induce the mw dressing. With this generator the relative shot-to-shot fluctuations on the mw power are less than 0.3%.

For a magnetic field of ≈ 1 G the first-order Zeeman effect leads to an energy splitting between the magnetic substates of ≈ 700 kHz such that the Stark shift due to off-resonant coupling to other magnetic substates is usually neglected, even though it also contributes a few Hz to the effective detuning. Experimentally, we use spectroscopy measurements to determine the precise value of the mw detuning at which the spin-mixing process is in resonance.

4.4. Mean-field dynamics on the spin-nematic sphere

The spin-nematic sphere introduced above offers a convenient way to visualize the spin dynamics [24]. To see this we take a closer look at the Hamiltonian describing the internal dynamics. As argued before, the effective energy offset q_{eff} between the states $(1, 0)$ and $(1, \pm 1)$ is described by the operator \hat{Q}_0 . Thus, neglecting the first-order Zeeman shift the Hamiltonian is given by

$$\hat{H}/\hbar = -\frac{q_{\text{eff}}}{2}\hat{Q}_0 + \frac{\tilde{c}_1}{2} : \left(\hat{S}_x^2 + \hat{S}_y^2 + \hat{S}_z^2 \right) :. \quad (4.17)$$

We restrict the discussion to the surface of the spin-nematic sphere spanned by the operators $\{\hat{Q}_{yz}, \hat{S}_x, \hat{Q}_0\}$ but the treatment is analogous in all spin-nematic subspaces as the spin-mixing process is independent of the Larmor phase. For now, we neglect the quantum fluctuations and just concentrate on the mean-field dynamics. The effect of this Hamiltonian is illustrated in Fig. 4.2. The first term describes a rotation around the Q_0 axis. The term \hat{S}_x^2 is a shearing and can be thought of as a rotation around the S_x -axis which depends on the value of S_x and therefore changes sign as soon as the state crosses the $S_x = 0$ line. For a state on the surface of this spin-nematic sphere the mean magnetization vanishes, i.e. $S_z = 0$, and additionally $S_y = 0$. Therefore, the effect

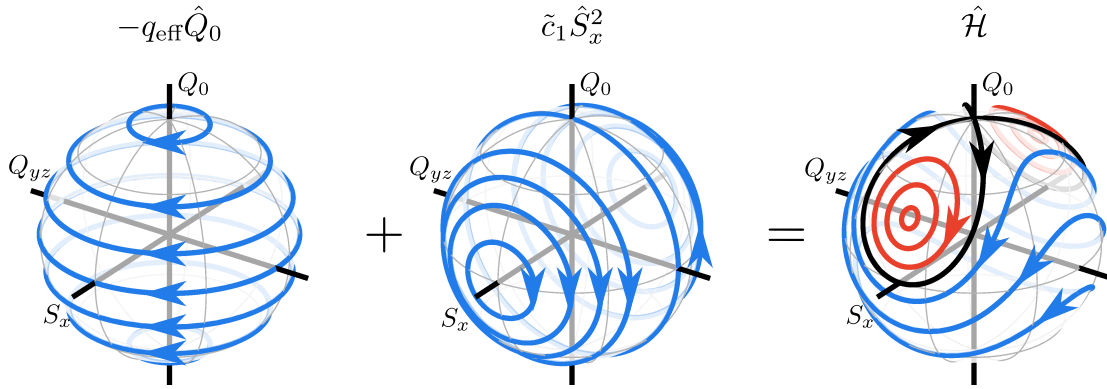


Figure 4.2.: Mean-field trajectories on the spin-nematic sphere: The two different contribution to the total Hamiltonian lead to a rotation (left) and a shearing (middle) on the spin-nematic sphere. On the right the combined trajectories for $q_{\text{eff}} = -N\tilde{c}_1$ are shown. The black line is usually referred to as separatrix which separates the self-trapping region (red lines) from the running phase mode (blue lines).

of the other two shearing terms can be neglected. Because spin-mixing conserves the magnetization and the Larmor phase, it is ensured that the state stays on the surface of the sphere during the dynamics.

The mean-field energy on this spin-nematic subspace is given by

$$E_{\text{MF}} = -h \frac{q_{\text{eff}}}{2} Q_0 + h \frac{\tilde{c}_1}{2} S_x^2. \quad (4.18)$$

For $q_{\text{eff}} \gg \tilde{c}_1$ the first term dominates and we find stable points at the poles of the sphere, corresponding to polar and transverse polar states. We now study the stability of the polar state under a change of the parameter q_{eff} . For that we calculate the slope and curvature of the energy in the direction of S_x . Because the phase space is spherical the value of Q_0 is not an independent parameter but is connected to S_x via $Q_0 = \sqrt{N^2 - S_x^2 - Q_{yz}^2}$ for the northern hemisphere. With this we find for the slope and curvature at the pole

$$\begin{aligned} \left. \frac{\partial E_{\text{MF}}}{\partial S_x} \right|_{S_x=Q_{yz}=0} &= 0 \\ \left. \frac{\partial^2 E_{\text{MF}}}{\partial S_x^2} \right|_{S_x=Q_{yz}=0} &= h\left(\frac{q_{\text{eff}}}{N} + 2\tilde{c}_1\right). \end{aligned} \quad (4.19)$$

Without mw dressing q_{eff} is positive and much larger than $2N\tilde{c}_1$. Therefore, the curvature is positive and the polar state minimizes the mean-field energy Eq. (4.18). In the $F = 1$ manifold $\tilde{c}_1 < 0$ and, thus, the curvature changes its sign at $q_{\text{cr}} = -2N\tilde{c}_1$. Consequently, for $0 \leq q_{\text{eff}} < q_{\text{cr}}$ the polar state becomes unstable and the spin-mixing process starts to macroscopically populate the states $(1, \pm 1)$. This corresponds to a so-called Pitchfork bifurcation and two new stable points arise which are found by setting

$$\left. \frac{\partial E_{\text{MF}}}{\partial S_x} \right|_{Q_{yz}=0} \stackrel{!}{=} 0 \quad \Rightarrow \quad S_{x,1} = 0, \quad S_{x,2/3} = \pm \frac{1}{2\tilde{c}_1} \sqrt{4N^2\tilde{c}_1^2 - q_{\text{eff}}^2}. \quad (4.20)$$

This situation is illustrated in Fig. 4.2. In this regime, there are two different types of trajectories, running phase (blue) and closed oscillations (red), which are separated by a so-called separatrix (black line). For $q_{\text{eff}} < 0$, the two stable points are located on the southern hemisphere of the spin-nematic phase-space. In this situation, the transverse polar state becomes unstable while the polar state is again stable.

4.5. Truncated Wigner simulation

The classical trajectories introduced before can be used to study the quantum evolution of a given initial state via a so-called truncated Wigner simulation [101]. The idea is to sample the initial Wigner distribution propagate each point via these classical trajectories. This method is naturally restricted to initial states with positive Wigner functions such as coherent states. The trajectories then deform the initial distribution analogously to a Fokker-Planck equation in classical statistics. It turns out that especially for the short times, where the distribution is still Gaussian, this method captures very well the quantum evolution [102, 103]. However, as we follow the classical trajectories the final result will at one point not be able to fully capture the quantum dynamics. We know that spin-mixing produces highly entangled non-classical two-mode squeezed states and that the Wigner function of such non-classical states can become negative. This, however, is not captured in the simulation and the probability distribution always stays positive as the different trajectories do not interfere as in contrast to a full quantum calculation. This is because higher order terms for the evolution have been truncated. However, also in this regime the simulation provides some intuition about the dynamics of the quantum state.

Numerically, truncated Wigner simulations are typically much easier to implement than a full quantum calculation. To calculate the dynamics of a coherent polar state one samples the Wigner distribution of the state via

$$\psi_S = \sqrt{N} \begin{pmatrix} \zeta_{+1} \\ \zeta_0 \\ \zeta_{-1} \end{pmatrix} = \begin{pmatrix} X_1 \\ \sqrt{N} \\ X_2 \end{pmatrix}, \quad (4.21)$$

where X_i ($i = \{1, 2\}$) are complex random numbers with mean $\langle X_i \rangle = 0$ and variance $\Delta^2 X_i = 1/2$. These fluctuation are sometimes referred to as the quantum one-half which initiate the spin-mixing dynamics. As a consistency check, we can use these states to calculate the variance of the spin $S_x = \psi_S^\dagger \hat{S}_x \psi_S$, which yields $\Delta^2 S_x = N$ as expected for a coherent polar state. To get the classical equation of motion for each of the three components we use the quantum mechanical time evolution of the mode operators, i.e. $d\hat{a}_m^{(\dagger)}/dt = i[\hat{\mathcal{H}}, \hat{a}_m^{(\dagger)}]/\hbar$ and insert the classical approximation

$$\begin{aligned} \hat{a}_{+1}^{(\dagger)} &\rightarrow \sqrt{N} \zeta_{+1}^{(*)} \\ \hat{a}_0^{(\dagger)} &\rightarrow \sqrt{N} \zeta_0^{(*)} \\ \hat{a}_{-1}^{(\dagger)} &\rightarrow \sqrt{N} \zeta_{-1}^{(*)}, \end{aligned} \quad (4.22)$$

where ζ_m is a complex number with $|\zeta_m|^2 = N_m/N$. For these numbers one then gets the following classical equations of motion

$$\begin{aligned}\frac{d\zeta_{+1}}{dt} &= -i2\pi N \tilde{c}_1 [(|\zeta_{+1}|^2 + |\zeta_0|^2 - |\zeta_{-1}|^2)\zeta_{+1} + \zeta_0^2 \zeta_{-1}^*] \\ \frac{d\zeta_0}{dt} &= i2\pi q_{\text{eff}} \zeta_0 - i2\pi N \tilde{c}_1 [(|\zeta_{+1}|^2 + |\zeta_{-1}|^2)\zeta_0 + 2\zeta_{+1} \zeta_{-1} \zeta_0^*] \\ \frac{d\zeta_{-1}}{dt} &= -i2\pi N \tilde{c}_1 [(-|\zeta_{+1}|^2 + |\zeta_0|^2 + |\zeta_{-1}|^2)\zeta_{-1} + \zeta_0^2 \zeta_{+1}^*].\end{aligned}\quad (4.23)$$

This set of coupled differential equations can be solved numerically. The results for $q = -N\tilde{c}_1 = 2 \text{ Hz}$ and $N = 100$ are shown in Fig. 4.3.

4.5.1. Short-time dynamics and spin-nematic squeezing

Starting from the coherent polar state the initial distribution spreads along one axis of the separatrix while the fluctuations are reduced on the orthogonal axis. This results in a so-called spin-nematic squeezed state [24], which has still a Gaussian distribution along each axis. Such squeezed states are already a useful resource for quantum enhanced metrology [9] and feature entanglement between the individual particles [10].

4.5.2. Long time dynamics and non-Gaussian states

For longer evolution times ($t = 180 \text{ ms}$) the distribution becomes non-Gaussian as the state wraps around the spin-nematic sphere. As the state enters this depleted pump regime some points also leave the surface of the $\{\hat{Q}_{yz}, \hat{S}_x, \hat{Q}_0\}$ sphere and deviate from the classical trajectory. This is because the Larmor phase is initially undefined, since the polar state has no population in the states $(1, \pm 1)$. The spin-mixing process then assigns a random Larmor phase to the state as soon as these modes are populated. Note that in the truncated Wigner simulation the random Larmor phase is produced by the sampling of the initial state.

Thus, in each realization we plotted just one projection of the transversal spin $S_\perp(\phi_L)$ on the spin-nematic sphere and the same holds for the transversal quadrupole moment $Q_\perp(\phi_L)$. In the simulation, we can remove the effect of the Larmor phase by directly evaluating the transversal spin length and the transversal quadrupole moment. With this we find that the state indeed follows the classical trajectory as indicated by the separatrix [104] (see Fig. 4.3).

Even though the marginal distributions of this non-Gaussian state are larger than the one of the squeezed and even of the initial coherent state, these states still provide metrological gain as they still feature strong entanglement in a particle basis as quantified by the quantum Fisher information [105]. The Wigner distribution of this non-Gaussian is expected to show some negativities due to interference effects. This can however not be captured by our simulation method which clearly shows the limitations of this scheme. Yet, it still provides an intuitive picture of the spin-mixing dynamics.

4.6. Effective potential

So far we have treated the spin-mixing process under the assumption that all magnetic substates have the same spatial wavefunction. Thus, we have so far neglected the spatial

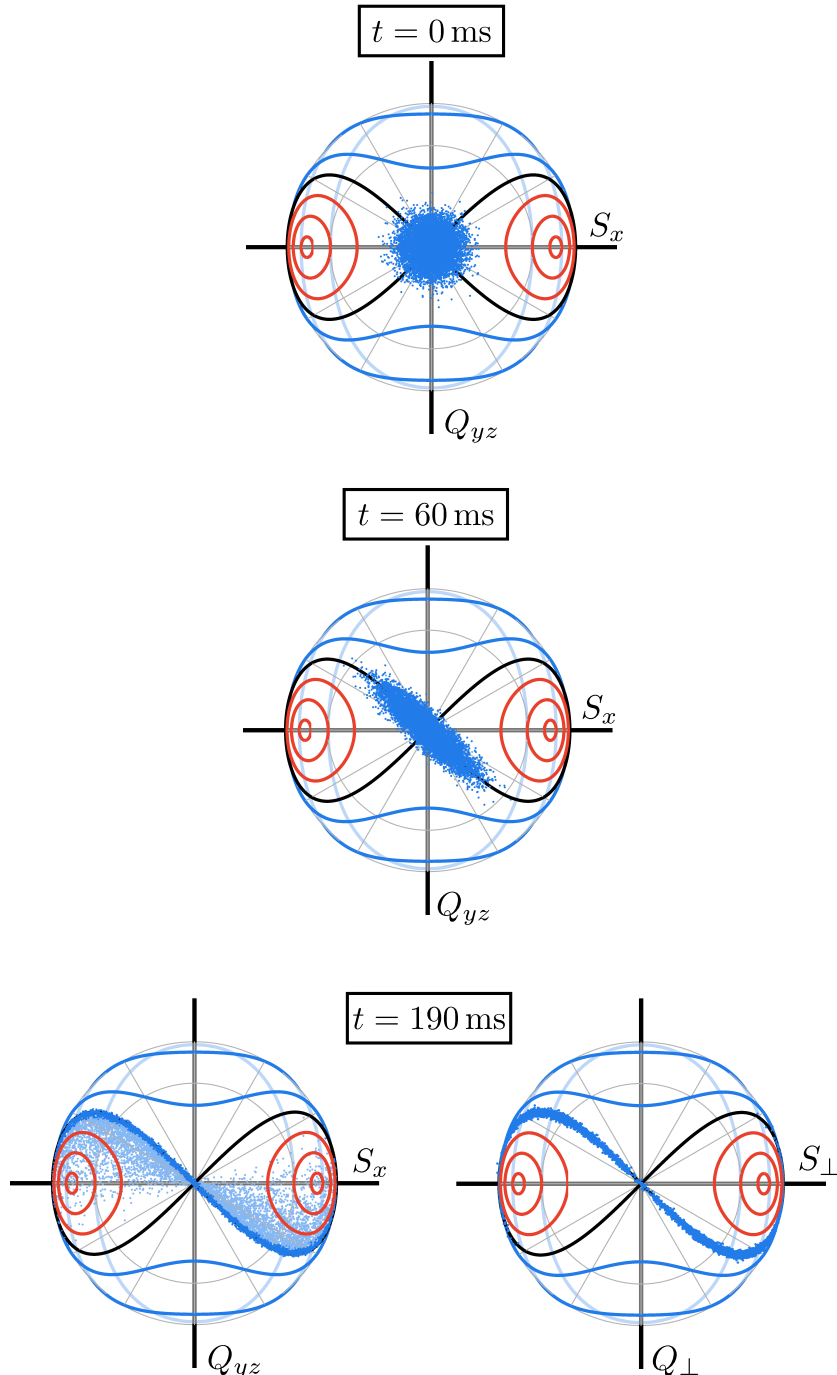


Figure 4.3.: Truncated Wigner simulation: In the simulation we employ $N = 100$ atoms and set the parameters $q_{\text{eff}} = -2N\tilde{c}_1 = 2 \text{ Hz}$. On the upper plot the sampled distribution of the initial coherent state is shown, where we employ 10,000 samples. For short evolution times ($t = 60 \text{ ms}$) the initial fluctuations are redistributed among two orthogonal directions forming a squeezed state. For longer times ($t = 180 \text{ ms}$) the state becomes non-Gaussian and is no longer fully represented on the surface of the spin-nematic sphere. The reason for this is that starting from the polar state the Larmor phase is initially undefined. The spin-mixing process then assigns a random phase to the state as soon as the modes are populated while we only extract one projection of the resulting transversal spin. By evaluating the transversal spin S_\perp and quadrupole moment Q_\perp we remove the effect of the Larmor phase and each initial point follows the classical trajectory.

degree of freedom. In the crossed dipole trap, however, it is also possible to populate excited spatial modes using spin-mixing. One would naively expect that the energy spacing of these modes is given by the external trapping potential, i.e. $\Delta E/\hbar = \omega_{\parallel} \approx 50$ Hz. However, because of the interaction between the atoms, the excitation will happen on top of the condensate mode. This results in a much lower energy spacing [106, 107].

Few-particle excitations on top of a large condensate

Taking into account the spatial component of the operators, yields for the single particle Hamiltonian in second quantization

$$\hat{\mathcal{H}}_0 = \int d\mathbf{r} \sum_{m_F} \hat{\Psi}_{m_F}^\dagger \left(-\frac{\hbar^2 \nabla^2}{2M} + V_{\text{ext}}(\mathbf{r}) - h q_{\text{eff}} m_F^2 \right) \hat{\Psi}_{m_F}, \quad (4.24)$$

where V_{ext} is the external trapping potential. As argued before, only the second-order Zeeman shift is included here. Analogously, we obtain for the interaction Hamiltonian (Eq. (4.5))

$$\hat{\mathcal{H}}_{\text{Int}} = c_0 :[\hat{\Psi}^\dagger(\mathbf{r}) \hat{\Psi}(\mathbf{r})]^2: + c_1 : \hat{\Psi}^\dagger(\mathbf{r}) \hat{\mathcal{S}} \hat{\Psi}(\mathbf{r}) \hat{\Psi}^\dagger(\mathbf{r}) \hat{\mathcal{S}} \hat{\Psi}(\mathbf{r}):, \quad (4.25)$$

where $\hat{\mathcal{S}}_i$ are the single-particle spin-operators. To derive the effective potential for excitations in the state $(1, \pm 1)$ one considers the fluctuation around a highly populated polar state [108]. One can then use a Bogoliubov ansatz for the spinor field operators

$$\hat{\Psi}(\mathbf{r}) = \begin{pmatrix} \hat{\Psi}_{+1} \\ \hat{\Psi}_0 \\ \hat{\Psi}_{-1} \end{pmatrix} \approx \begin{pmatrix} 0 \\ \sqrt{n_0(\mathbf{r})} \\ 0 \end{pmatrix} + \begin{pmatrix} \delta \hat{\Psi}_{+1} \\ \delta \hat{\Psi}_0 \\ \delta \hat{\Psi}_{-1} \end{pmatrix}. \quad (4.26)$$

Inserting this Bogoliubov approximation and keeping terms only up to second order in the fluctuations $\delta \hat{\psi}_{m_F}^{(\dagger)}$ yields for the complete Hamiltonian

$$\begin{aligned} \hat{\mathcal{H}} &= \hat{\mathcal{H}}_0 + \hat{\mathcal{H}}_{\text{Int}} \\ &\approx \int d\mathbf{r} \sum_{m_F} \delta \hat{\Psi}_{m_F}^\dagger(\mathbf{r}) \left(-\frac{\hbar^2 \nabla^2}{2M} + V_{\text{eff}}(\mathbf{r}) - q_{\text{eff}} m_F \right) \delta \hat{\Psi}_{m_F}(\mathbf{r}) \\ &\quad + n_0(\mathbf{r}) c_1 \left(\delta \hat{\Psi}_{+1}^\dagger(\mathbf{r}) \delta \hat{\Psi}_{-1}^\dagger(\mathbf{r}) + \delta \hat{\Psi}_{+1}(\mathbf{r}) \delta \hat{\Psi}_{-1}(\mathbf{r}) \right). \end{aligned} \quad (4.27)$$

The last term describes again spin-mixing and the effective external potential is given by

$$V_{\text{eff}}(\mathbf{r}) = V_{\text{ext}}(\mathbf{r}) + (c_0 + c_1) n_0(\mathbf{r}). \quad (4.28)$$

Inserting the density profile in the Thomas-Fermi approximation (see Eq. (4.10)) yields

$$V_{\text{eff}}(\mathbf{r}) = \begin{cases} \frac{c_1}{c_0} \mu - \frac{c_1}{c_0} V_{\text{ext}}(\mathbf{r}) & \text{for } |\mathbf{r}| \leq r_{\text{TF}} \\ V_{\text{ext}}(\mathbf{r}) & \text{else} \end{cases} \quad (4.29)$$

where r_{TF} is the Thomas-Fermi radius. To derive this effective potential we shifted the overall energy by the chemical potential μ . Inserting the expression for the external

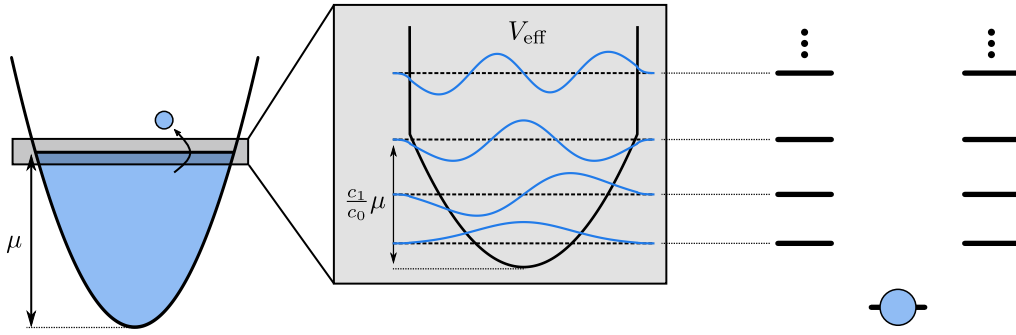


Figure 4.4.: Effective potential for spin-mixing: In the Thomas-Fermi regime, any single-particle excitation will be on top of an external potential that is filled up by the condensate. The gray box shows a example of the resulting effective potential and the energy eigenstates calculated for 40,000 atoms. The interactions lead to a harmonic + box like potential which provides additional resonances for the spin-mixing process with a energy splitting on the order of a few Hz.

potential yields explicitly in the longitudinal direction

$$V_{\text{eff},\parallel}(x) = \begin{cases} \frac{c_1}{c_0}\mu + \frac{1}{2}M\left(\sqrt{\frac{c_1}{c_0}}\omega_{\parallel}\right)^2 x^2 & \text{for } |x| \leq r_{\text{TF},\parallel} \\ \frac{1}{2}\omega_{\parallel}^2 x^2 & \text{for } |x| > r_{\text{TF},\parallel}, \end{cases} \quad (4.30)$$

where the Thomas-Fermi radius is given by $r_{\text{TF},\parallel} = \sqrt{2\mu/M\omega_{\parallel}^2}$. For 40,000 atoms and a longitudinal trapping frequency of $\omega_{\parallel} = 2\pi \cdot 50$ Hz, we calculate a value of $r_{\text{TF},\parallel} \approx 11 \mu\text{m}$.

An intuitive picture for the effective potential is shown in Fig. 4.4. The atoms in the condensate fill the external trapping up to the chemical potential. Any small excitation happens on top of this “sea of atoms”. Therefore, the particles experience, in first approximation, a box potential that is slightly modified due to the spin-dependent interaction. The modified potential inside the Thomas-Fermi radius is still harmonic with an effective trap frequency of $\omega_{\text{eff}} = \sqrt{c_1/c_0} \omega_{\parallel} \approx 2\pi \cdot 3.5$ Hz. For our experimental parameters, the chemical potential is calculated to be $\mu \approx h \cdot 2.2$ kHz which results in a depth of the harmonic potential given by $c_1/c_0 \mu \approx h \cdot 10$ Hz. Thus, only the two energetically lowest spatial modes are still in a harmonic potential while higher excitations approximately experience a box-like potential.

Using mw dressing we can tune the effective detuning q_{eff} such that the spin-mixing process is in resonance with these excited spatial modes of the effective potential. The coupling to these spatial modes is modified by the mode overlap

$$\chi_k = \int d\mathbf{r} \psi_c^2(\mathbf{r}) \psi_k^2(\mathbf{r}), \quad (4.31)$$

where ψ_c is the wavefunction of the condensate given by the Thomas-Fermi approximation and ψ_k is the wavefunction of the states $(1, \pm 1)$ in the k^{th} excited mode of the effective potential.

It is interesting to note that the possibility to excite these spatial modes is a special property of the spin-mixing process and is a consequence of the fact that it is a two-

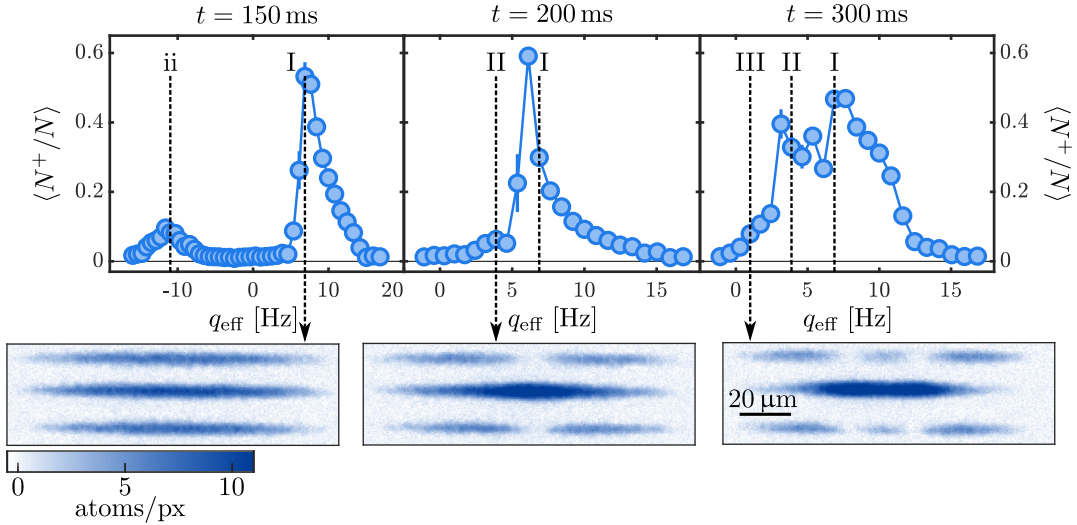


Figure 4.5.: Spectroscopy of the spin-mixing resonance for different evolution times: In the upper plots, the mean value of the normalized side mode populations $\langle N^+ / N \rangle = \langle (N_{+1} + N_{-1}) / N \rangle$ is plotted as a function of the effective detuning q_{eff} . We observe the excitation of three different spatial modes in the longitudinal trapping potential (I – III), where the corresponding atomic densities are shown below. Additionally, we find a resonance corresponding to an excited spatial mode in the transversal potential as shown in the left plot at $q_{\text{eff}} \approx -11$ Hz (ii).

particle process. In contrast, rf-rotations as a single-particle process cannot excite these modes as the Franck-Condon factor, i.e. the wavefunction overlap of two different spatial modes vanishes $\int dx \psi_i^*(x) \psi_j(x) = \delta_{ij}$ while in contrast χ_k does not vanish. To address these modes with rf-rotation would require state dependent potentials [109].

4.7. Spectroscopy of spatial modes

To explore this effective potential we experimentally start with $N = 40,000$ atoms in the state $(1, 0)$, with the magnetic field set to 0.884 G. Using mw dressing we tune the effective detuning q_{eff} and measure after some evolution time the mean population $\langle N^+ \rangle = \langle N_{+1} + N_{-1} \rangle$ of the side modes normalized to the total atom number (see Fig. 4.5). After 100 ms of evolution we observe two distinct resonances with an energy difference of $\approx h \cdot 18$ Hz. Via the measured density profile we identify the resonance at $q_{\text{eff}} \approx 7$ Hz (I) with the ground state mode (referred to as ground mode) of the longitudinal effective potential. The second resonance is located around $q_{\text{eff}} \approx -11$ Hz (ii) which we identify with the first excited mode of the effective transversal potential.

After longer evolution times the resonance peak near the ground mode gets broader and we observe the population of spatially excited modes in the longitudinal trapping potential (II, III) which are expected to have an energy spacing of ≈ 3 Hz. Since this is on the same order as the spin-mixing strength these resonance peaks overlap. Due to the smaller mode overlap of the higher excited modes with the condensate mode one expects a smaller spin-mixing strength which is consistent with the observation that these modes are only visible after longer evolution times.

Spectroscopy shift

The interaction strength in this experimental setting is about $|N\tilde{c}_1| \approx 5$ Hz. From a mean-field description one would expect that the resonance of the ground mode would be in the range of $q_{\text{eff}} = 0$ Hz – 10 Hz. Experimentally, however, we find that the resonance starts already at $q_{\text{eff}} = 14$ Hz and therefore the spectroscopy signal is shifted by about 4 Hz with respect to the theoretical value even when we consider all possible energy shifts due off-resonant mw coupling between the different magnetic substates.

One contribution to this shift is presented in the following. The start of the resonance at $q_{\text{eff}} = 10$ Hz is defined via the homogeneous theory, where we did not take into account the effective potential. Since the ground mode is still in the harmonic part of this potential, the energy shift with respect to the chemical potential is given by

$$\frac{c_1 \mu}{c_0 h} + \sqrt{\frac{c_1}{c_0} \frac{\omega_{\parallel}}{2\pi}} \approx -7.8 \text{ Hz} \quad (4.32)$$

where we set, in the experiment, the longitudinal trap frequency to $\omega_{\parallel} = 2\pi \cdot 38$ Hz. This has to be compared to the mean-field shift from the homogeneous theory, which is already included in the definition of the critical value of $q_c = 10$ Hz. In the undepleted pump approximation, this shift amounts to $N\tilde{c}_1 = -5$ Hz (see 2nd term in Eq. (4.7)). Thus, we expect an additional shift by the effective potential of -2.8 Hz which accounts for the major part of the shift we observe in the spectroscopy. The residual part might be attributed to uncertainties in the measured dressing Rabi frequency. In the following, we just consider the shift from the off-resonant coupling of $(1, 0) \leftrightarrow (2, 0)$ to calculate q_{eff} , since the exact value is not essential for the experiments as we will always use a spectroscopy to calibrate the value of q_{eff} according to the specific spatial mode we want to address.

4.8. Time evolution of spatial modes

We now take a closer look at the time dynamics of the different spatial modes, which are shown in Fig. 4.6. Again, we initially prepare 40,000 atoms in the state $(1, 0)$ and tune the spin-mixing process into resonance in the regime of the three energetically lowest spatial modes. For the ground mode we find, after an initial exponential rise, coherent oscillations of the side mode population. This is expected from a single-mode approximation.

For the two excited modes this is not the case anymore. One reason is that the derivation of the effective potential becomes questionable as the side modes are highly occupied. Additionally, in the mean-field picture one expects according to Eq. (4.23) that the energy of the state $(1, 0)$ is reduced as the states $(1, \pm 1)$ are populated. This means that even if one tunes spin-mixing into resonance with an excited spatial mode, the energy shift due to the population of the side modes can tune it into resonance with lower spatial modes if the energy spacing is not large enough. The original spatial mode is then off-resonant and one would not expect to observe coherent dynamics. In this regime, we also examined the spatial profiles of the states $(1, \pm 1)$ which do not exhibit a single spatial mode as shown in Fig. 4.5 but appear like a mixture of multiple modes. This indicates that the dynamics can no longer be described via a single-mode approximation.

To evaluate the coupling to the different spatial modes more quantitatively we analyze the time evolution of $\langle N^+ \rangle$. Within the undepleted pump approximation, i.e. $N_0 \gg N^+$

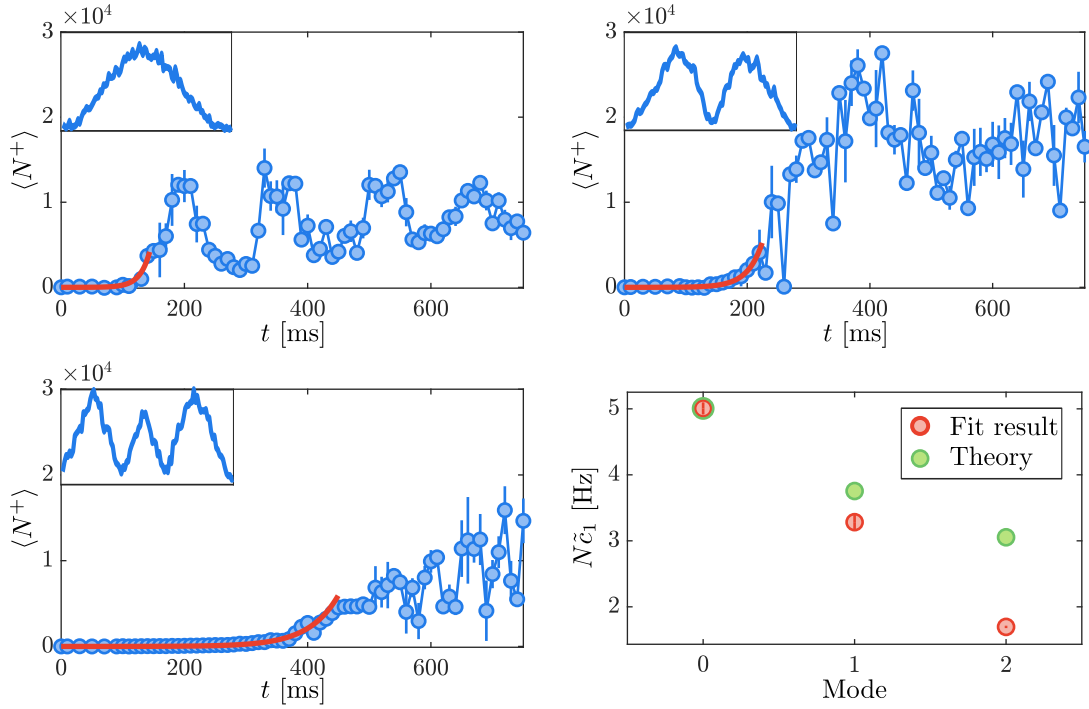


Figure 4.6.: Time evolution of the first three spatial modes: We initially prepare 40,000 atoms in the state $(1, 0)$ and tune spin-mixing into resonance with the spatial modes of the effective potential. In this setting we extract the mean population in the side modes as a function of the evolution time. The insets depict the corresponding profiles obtained in a single experimental realization of the short time dynamics. While the ground mode exhibits coherent dynamics, the higher modes are dominated by multimode dynamics. Fitting the initial rise of the mean atom number (red line) we extract the coupling strength of each mode. Comparison with the theoretical prediction by considering the mode overlap χ_k shows that the measured interaction strengths are significantly lower than expected. The theoretical values have been normalized to the experimentally extracted coupling strength of the ground mode. Thus, the two values are per definition identical for the ground mode.

the time dependence of the side mode population is given by

$$\langle N^+ \rangle = 2 \sinh^2(\kappa_k t) \quad \text{with } \kappa_k = 2\pi \cdot N \chi_k c_1. \quad (4.33)$$

The effective coupling strength to the excited states is connected to the wavefunction overlap χ_k of the condensate mode ψ_c and the wavefunctions of the side modes $\psi_{\pm 1,k}$. To experimentally extract the coupling strength we fit the short-time dynamics for each spatial mode, i.e. in a region where $\langle N^+ \rangle < 4,000$. We then compare the measured values with the ones expected from a numerical calculation. For this we determine the eigenfunctions of the effective potential and calculate the overlap χ_k with the wavefunction of the condensate in the Thomas-Fermi approximation. To fix the energy scale, we normalize the theoretical values to the experimentally extracted coupling strength of the ground mode. For the spatially excited modes, we expect a reduction of the overlap χ_k , which is also observed experimentally. However, the experimental values for the excited modes are significantly lower than the theoretical ones as shown in Fig. 4.6.

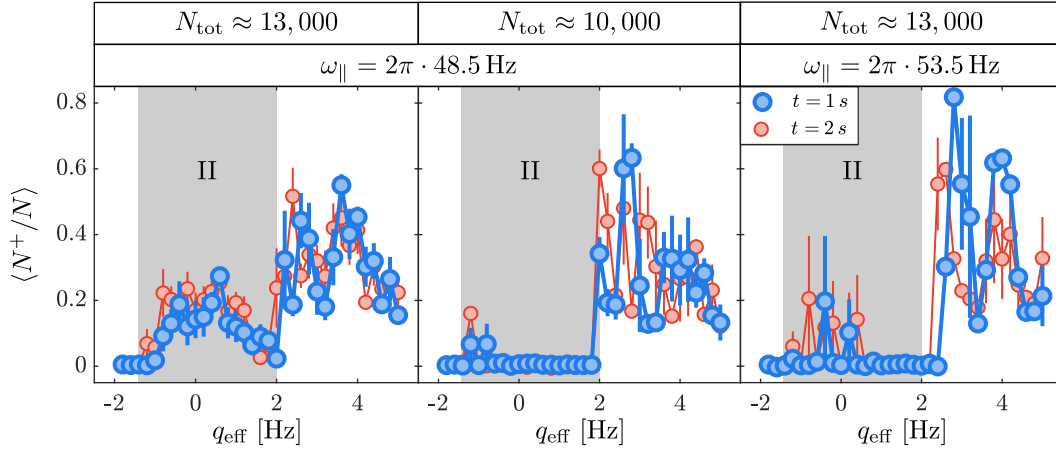


Figure 4.7.: Spectroscopy for different atom numbers and external trapping frequencies: Spectroscopy signal for the ground and first excited (II) mode after 1 s (blue) and 2 s (red) of evolution time. Reducing the atom number below some critical value (middle) as well as increasing the longitudinal confinement (right) dramatically reduces the signal of the excited mode which is then only sporadically populated even after 2 s of evolution time.

One reason for this deviation might be that Eq. (4.33) is only true for $q_{\text{eff},k} = -N\chi_k c_1$, where $q_{\text{eff},k}$ quantifies the energy difference from the state $(1, 0)$ to the k^{th} excited mode of the states $(1, \pm 1)$. Otherwise the coupling κ_k is modified according to [26]

$$\kappa_k = \sqrt{q_{\text{eff},k}(q_{\text{eff},k} + 2N\chi_k c_1)}, \quad (4.34)$$

which is maximal for $q_{\text{eff},k} = -N\chi_k c_1$. For the measurement, we varied q_{eff} with a stepsize of ≈ 1.5 Hz. Thus, we might have missed in the measurement the optimal value of $q_{\text{eff},k}$ by 0.75 Hz. However, the resulting modification of the coupling strength can also not account for the measured deviations.

Another possibility is that, due to the large overlap of the resonances, the dynamics of the respective mode at $q_{\text{eff},k} = -N\chi_k c_1$ is dominated by the dynamics in the energetically lower mode. Experimentally, we used the spatial profiles extracted from the short time dynamics to identify the resonant mode. However, this only works in a regime where the dynamics of this spatial mode dominate. Depending on the resonance overlap this regime might not include $q_{\text{eff},k} = -N\chi_k c_1$. For a large overlap we might even detect a higher spatial mode only at the edge of its resonance region and would therefore extract a lower coupling strength.

4.9. Single mode addressing

From an experimental point of view it is desirable to control the overlap of the ground and first excited mode such that one can switch between single- and multi-mode dynamics. Experimentally, this overlap can either be tuned by changing the energy spacing or the interaction strength.

In the regime where the energy of the lowest spatial modes is dominated by the harmonic part of the effective potential, i.e. for high atom numbers with $c_1/c_0 \cdot \mu >$

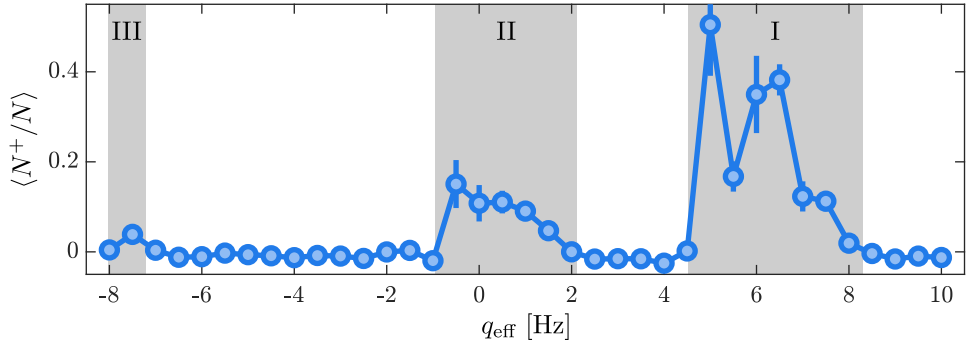


Figure 4.8.: Spectroscopy with reduced heating: By lowering the power of the waveguide we recover the first excited spatial mode for an atom number of 11,000 and $\omega_{\parallel} = 2\pi \cdot 53.5$ Hz. Here, the resonances are clearly separated and can be individually addressed.

$3/2\hbar\sqrt{c_1/c_0}\omega_{\parallel}$, the mode spacing is directly changed by tuning the longitudinal trapping frequency. Thus, increasing the longitudinal trapping frequency within this regime will reduce the mode overlap. For low particle numbers, the mode spacing is dominated by the box-like part of the effective potential where the energy spacing is controlled by the width of the box $\Delta E \sim 1/d_{\text{box}}^2$. The width is given by two times the Thomas-Fermi radius

$$d_{\text{box}} = 2r_{\text{TF},\parallel} = 2\sqrt{\frac{2\mu}{M\omega_{\parallel}^2}} \propto \frac{N^{1/5}}{\omega_{\parallel}^{4/5}} \quad \Rightarrow \quad \Delta E \propto \frac{\omega_{\parallel}^{8/5}}{N^{2/5}}. \quad (4.35)$$

Therefore, in both regimes increasing the longitudinal trapping frequency will enhance the mode spacing. Alternatively, one can reduce the total atom number. This also increases the mode spacing in the box-potential as shown in Eq. (4.35). At the same time, a lower atom number reduces the spin-mixing strength (see Eq. (4.15)) which further decreases the overlap of the two resonances.

The left plot of Fig. 4.7 shows a spectroscopy signal for $\approx 13,000$ atoms where the resonance of the two modes share a very small overlap. However, reducing the atom number further largely switches off spin-mixing into the excited mode. From other experiments we have indications that the heating in our system leads to decoherence of a state with a transversal spin length [110]. It could be that for low atom numbers the decoherence rate gets larger than the spin-mixing strength such that populating this mode is inhibited [111]. Analogously, the increase of the longitudinal confinement above some critical value drastically reduces spin-mixing into the excited mode. As before, this could be explained by decoherence, since a higher power of the XDT is accompanied by an increase of the heating rate. Thus, if the XDT is too strong the decoherence might become larger than the spin-mixing strength.

Alternatively, we can change the transversal confinement by lowering the power of the WG beam. This lowers the chemical potential which moves the excitations in the box-potential further apart. On top of that we can tune the power to the edge of the evaporation ramp. In this setting, not only the heating is reduced but the condensate is constantly cooled which leads to a much longer coherence time. We even find no significant enhancement of the atom loss [110]. This setting corresponds to a transversal trapping frequency of $\omega_{\perp} = 2\pi \cdot 170$ Hz and we recover the resonances of the lowest three

spatial modes even for low atom numbers of 11,000 atoms and a longitudinal confinement of $\omega_{\parallel} = 2\pi \cdot 53.5$ Hz. There, the resonance peaks are well separated and can be individually addressed (see Fig. 4.8).

4.10. Variance analysis

For detecting spin-mixing we have so far only used the population of the side modes after a given evolution time. For short times, this means detecting very small atom numbers which is experimentally challenging. In the following we use that spin-mixing also changes the second moment of the probability distribution of an initial polar state in the S_x - Q_{yz} plane as shown in Fig. 4.3. For this we define the observable

$$\begin{aligned}\hat{F}(\phi_S) &= \cos(\phi_S - \phi_{S,0}) \hat{S}_x + \sin(\phi_S - \phi_{S,0}) \hat{Q}_{yz} \\ &= \frac{1}{\sqrt{2}} \left[e^{-i(\phi_S - \phi_{S,0})} \hat{a}_0^\dagger (\hat{a}_{+1} + \hat{a}_{-1}) + \text{h.c.} \right],\end{aligned}\quad (4.36)$$

where we introduced the offset spinor phase $\phi_{S,0}$, such that $\phi_S = 0$ corresponds to the phase value with minimal fluctuations. Using the analytic solution for the time evolution in the undepleted pump approximation (Eq. (4.8)) we get for the variance of $\hat{F}(\phi_S)$ at $q_{\text{eff}} = -N\tilde{c}_1$

$$\Delta^2 F(\phi_S) = \langle \hat{F}^2(\phi_S) \rangle_Q = \langle N \rangle [\cosh(2\kappa t) - \sinh(2\kappa t) \cos(2\phi_S)], \quad (4.37)$$

where we used $\langle \hat{F}(\phi_S) \rangle_Q = 0$. For $t = 0$ we recover the fluctuations of the coherent polar state of N . After some evolution time the fluctuations of the initial state are redistributed which results in a spin-nematic squeezed state. For the spinor phases $\phi_{S,\min} = 0$ and $\phi_{S,\max} = \pi/2$ we find the reduced and enhanced fluctuations of

$$\begin{aligned}\Delta^2 F(0)/\langle N \rangle &= e^{-2\kappa t} \\ \Delta^2 F(\pi/2)/\langle N \rangle &= e^{2\kappa t}\end{aligned}\quad (4.38)$$

compared to a coherent polar state. By combining this result with Eq. (4.9) one can directly connect the maximal fluctuations with the mean populations of the side modes

$$\Delta^2 F(\pi/2)/\langle N \rangle \approx 2\langle \hat{N}^+ \rangle_Q \quad \text{for } e^{2\kappa t} \gg 1. \quad (4.39)$$

Thus, even small mean populations in the side mode lead to a large increase of the maximal fluctuations, for example 10 atoms increase the coherent state fluctuations by a factor of 20 making this a very sensitive probing scheme. This is also true for other values of q_{eff} with $0 \leq q_{\text{eff}} \leq -2N\tilde{c}_1$. However, for different values of $q_{\text{eff}} \neq -N\tilde{c}_1$ we would find a different orientation of the squeezing ellipse in the S_x - Q_{yz} plane as well as a modified time dependence.

4.11. Spatially resolved fluctuation spectroscopy

To measure these fluctuations experimentally we apply an rf $\pi/2$ spin rotation which maps the relevant observable onto the population difference of the side-modes, i.e. $\hat{F}(\phi_S) \rightarrow N^- = N_{+1} - N_{-1}$. For the spectroscopy we do not actively tune the measured spinor phase

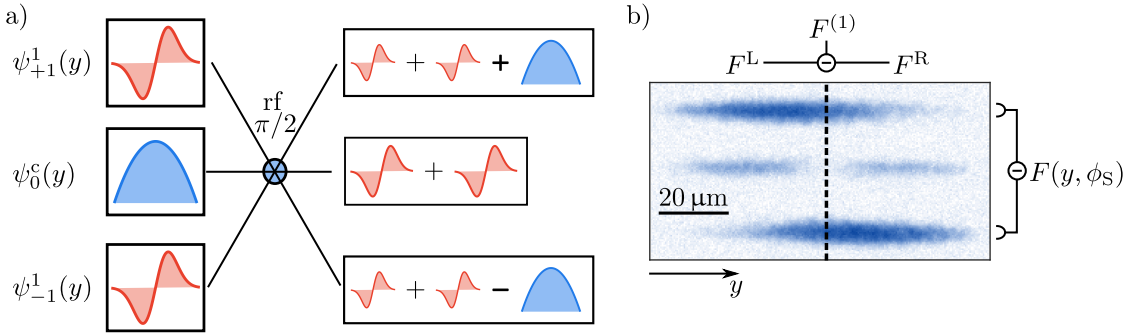


Figure 4.9.: Spin readout for spatially excited modes: An rf $\pi/2$ -pulse is equivalent to a three-port beamsplitter in optics. If the spin-mixing process has been tuned into resonance with the first excited spatial mode, its antisymmetric mode will interfere with the symmetric mode of the condensate at the output of this beamsplitter. As a result the measured spin observable will also feature a spatial antisymmetry. For the first excited mode we take the resulting symmetry into account as follows: We split the absorption signal into two halves and evaluate the atom number difference in each half, which corresponds to the local spin observable $F^{\text{L/R}}$ in the left (L) and right (R) half. Subtracting these two values from each other yields the spin observable for the first excited mode $F^{(1)}(\phi_S) = F^{\text{L}} - F^{\text{R}}$.

but evaluate the fluctuations at an arbitrary but fixed spinor phase ϕ_S . As the orientation of the state will anyway change as we tune q_{eff} we should be able to find a spectroscopy signal in the variance. Additionally, as the state gets non-Gaussian for longer evolution times we will definitely see an increased variance there.

Since the rf pulse transfers the population from the state $(1, 0)$ to the side mode, the states $(1, \pm 1)$ will be highly populated after the rotation. Experimentally, this eases the detection of the population in $(1, \pm 1)$ and with that the extraction of the fluctuations in N^- . Such a measurement scheme is analogous to homodyne detection routinely used in continuous-variable quantum optics [96]. There it enables the measurement of optical field quadratures [112], which correspond to the spin measurement in our case, as well as the measurement of small photon numbers without photon counting [113, 114].

To evaluate the contributions from the population of the ground mode, we analyze the fluctuations of the atom number difference N^- between the total population of the states $(1, \pm 1)$. For spatially excited modes, however, we have to take into account the symmetry of their respective wavefunction. As an example we take the first excited mode the wavefunction of which has an antisymmetry between the left and right half as shown in Fig. 4.9a). Similar to a three-port beamsplitter the rf pulse employed for the readout will not change the spatial mode of each input state, but it will mix in the output states $(1, \pm 1)'$ the antisymmetric wavefunction of the side modes with the symmetric wavefunction of the condensate. This leads to an interference of the two wavefunctions depending on the phase between the condensate and the side modes. This interference leads to an asymmetry between the left and right half in the states $(1, \pm 1)'$. Because the sign of the condensate contribution is reversed between the two output states, the interference in the state $(1, +1)'$ will be opposite to the one in $(1, -1)'$. Consequently, if

we detect in the left half of $(1, +1)'$ a significantly higher atom number we expect to find in $(1, -1)'$ a higher atom number in the right half which is shown in Fig. 4.9b).

Thus, evaluating the atom number difference $n^{-,L/R} = n_{+1}^{L/R} - n_{-1}^{L/R}$ in the left (L) and right (R) half of the absorption image, we find that $n^{-,L} \approx -n^{-,R}$. If we analyzed, as before, $N^- = n^{-,L} + n^{-,R}$, we would expect to find no signal for the first excite mode. Instead one has to take the antisymmetry into account by evaluating $N^{-,(1)} = n^{-,L} - n^{-,R}$. In the same way, this analysis suppresses the signal from the symmetric ground mode. For higher modes we would have to divide the signal further to take into account the respective symmetry of the mode. In the following, we denote by $N^{-,(k)}$ the optimal analysis of the k^{th} mode.

To put this argument into theoretical terms, one considers the local observables $\hat{F}(\phi_S, y)$ with $\hat{F}(\phi_S) = \int dx \hat{F}(\phi_S, x)$. For example, the local spin operator $\hat{S}_x(y)$ is given by

$$\begin{aligned}\hat{S}_x(y) &= \frac{1}{\sqrt{2}} \hat{\psi}_0^\dagger(y) (\hat{\psi}_{+1}(y) + \hat{\psi}_{-1}(y)) + \text{h.c.} \\ &\approx \frac{1}{\sqrt{2}} e^{-i\phi_0} \hat{a}_{0,c}^\dagger \left(\sum_k \psi_c^*(y) \psi_k(y) \hat{a}_{+1,k} + \sum_k \psi_c^*(y) \psi_k(y) \hat{a}_{-1,k} \right) + \text{h.c.},\end{aligned}\quad (4.40)$$

where $\hat{a}_{\pm 1,k}$ is the annihilation operator for a particle in the state $(1, \pm 1)$ in the k^{th} spatial mode and $\psi_k(x)$ the corresponding wavefunction. Here, we assume that the particles in the state $(1, 0)$ always occupy the condensate wavefunction. This means that the global observable $\hat{S}_x = \int dx \hat{S}_x(x)$ just contains contributions from the ground mode since $\int dx \psi_c^*(x) \psi_k(x) \approx \delta_{0,k}$. And consequently the dynamics of the ground mode determines the corresponding fluctuations $\Delta^2 S_x$.

Analogously, the contributions of the first excited mode is described by the operator

$$\hat{F}^{(1)} = \int_{-\infty}^{y_{\text{Mid}}} dy \hat{F}(y) - \int_{y_{\text{Mid}}}^{\infty} dy \hat{F}(y). \quad (4.41)$$

Similarly, we define the operator $\hat{F}^{(k)}$ that contains the contribution from the k^{th} excited mode. This entails splitting the integral at each zero-crossing of the spatial wavefunction and reversing the sign after each zero-crossing. This is analogous to a Fourier analysis, but with the modes of the effective potential as basis functions.

Measuring the fluctuations therefore does not only allow us to measure the spin-mixing process for small occupation numbers but additionally to filter out the different mode contributions. This is especially advantageous when the resonances overlap. To demonstrate this, we prepare again a larger of 40,000 atoms such that the different spatial modes have a significant overlap and tune q_{eff} . The results are shown in Fig. 4.10. In the experiment we normalize the fluctuations to the mean atom number $\langle N^+ \rangle$ in the side mode, i.e. we compare the fluctuations to the shot-noise limit of a coherent polar state with mean atom number $\langle N^+ \rangle$.

Already after 50 ms of evolution time we find a contribution from the three lowest spatial modes to the spectroscopy corresponding to a mean population of about 40 atoms in the ground mode and less than 2 atoms in the second excited mode. We also see that the three modes have a large overlap but with our variance analysis we are able to resolve the different contributions.

After 140 ms of evolution time we also measure a signal from the second excited mode at $q_{\text{eff}} = 16$ Hz where this mode is expected to be off-resonant. This might indicate to

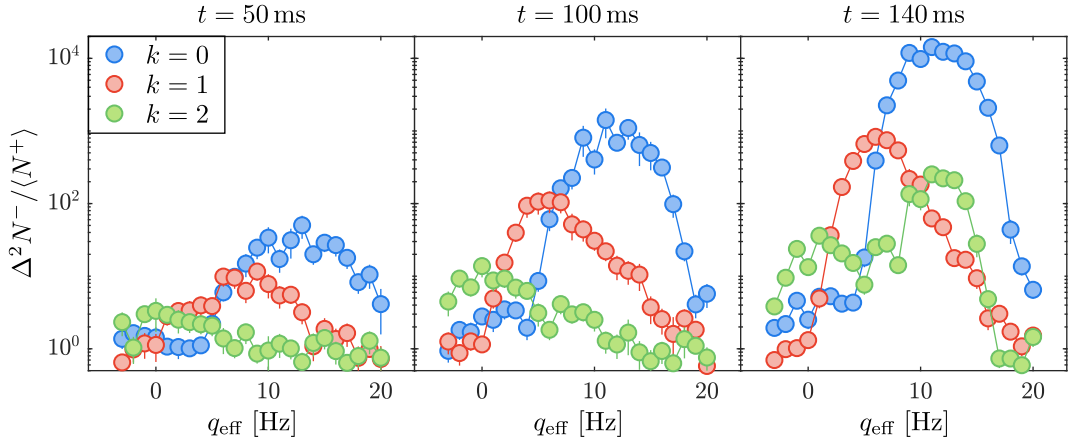


Figure 4.10.: Fluctuation spectroscopy: We analyze the fluctuations of $N^{-,(k)}$ for the three energetically lowest spatial modes and normalize them to the mean atom number $\langle N^+ \rangle$ in the side modes. The results are plotted here in semilogarithmic scale. After 140 ms of evolution time we find already indications of multimode dynamics. These manifest via the growth of the second excited mode in a region $q_{\text{eff}} \approx 16$ Hz where this mode should be off-resonant. To determine the error on the variance we use a jackknife resampling method [115].

the onset of more complex multimode dynamics in which the approximations we used before are no longer valid. For example, the spatial wavefunction of the state $(1, 0)$ might contain some contributions from spatially excited modes.

4.12. Tomography of spatial modes

For the spectroscopy we analyzed the fluctuations of $N^{-,(k)}$ at a fixed spinor phase ϕ_S . But in the experiment this phase can also be tuned. For this, we switch off the mw dressing after a chosen evolution time which causes this phase to dynamically evolve as

$$\phi_S(t) = \phi_{S,0} + 2\pi \cdot \frac{q_k}{2} t, \quad (4.42)$$

which corresponds to a rotation on the spin-nematic sphere around Q_0 . Here, q_k is the energy difference between the state $(1, 0)$ and the state $(1, \pm 1)$ in the k^{th} mode. This energy difference contains the second-order Zeeman shift $q_B = 56$ Hz (at a magnetic field of $B = 0.884$ G) and additional shifts which can be calculated from the effective potential. With this method we measure different projections of the squeezed state which corresponds to a tomographic analysis of the state. With Eq. (4.42) the time dependence of the fluctuations can also be used to determine the energy of the different spatial modes with respect to the state $(1, 0)$ as shown in Fig. 4.11a).

For this measurement, we prepare 40,000 atoms in the state $(1, 0)$ and set the longitudinal trapping frequency to $\omega_{\parallel} = 2\pi \cdot 65$ Hz. To populate the three energetically lowest modes we tune q_{eff} to $-1, 4$ and 11 Hz and let the system evolve for 160, 120 and 70 ms, respectively. These values of q_{eff} correspond to the maxima found in the spectroscopy as shown in Fig. 4.10. We subsequently switch off the mw dressing which causes the

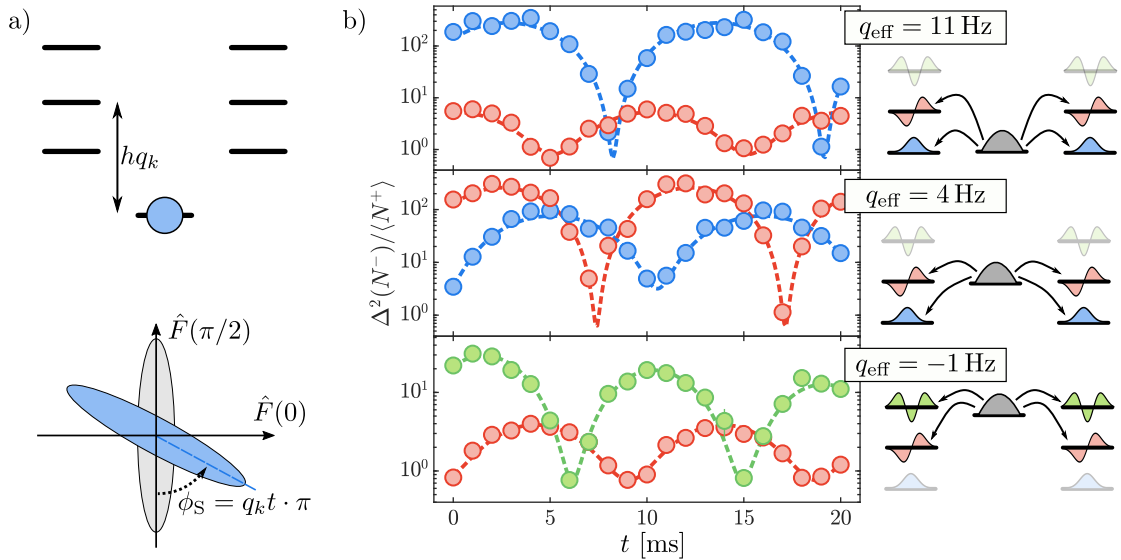


Figure 4.11.: Tomography of fluctuations: a) The energy difference between the condensate mode and the k^{th} spatial mode hq_k is given by the second-order Zeeman shift and the mode spacing in the effective potential. This energy difference determines the time evolution of the spinor phase and with that the orientation of the fluctuations ellipse as shown in the lower plot. b) Variance signal as a function of the phase evolution time for the three spatial modes (color coding as in Fig. 4.10). We tune q_{eff} to (11, 4, -1) Hz (upper, middle and lower graph) with evolution times of 70, 120 and 160 ms, respectively. To extract the frequency each signal is fitted with a sine function (dashed lines). For the second excited mode we find an additional decay of the amplitude which we include in the fit as an exponential decay. For the corresponding lifetime we extract a value of $\tau = 20$ ms.

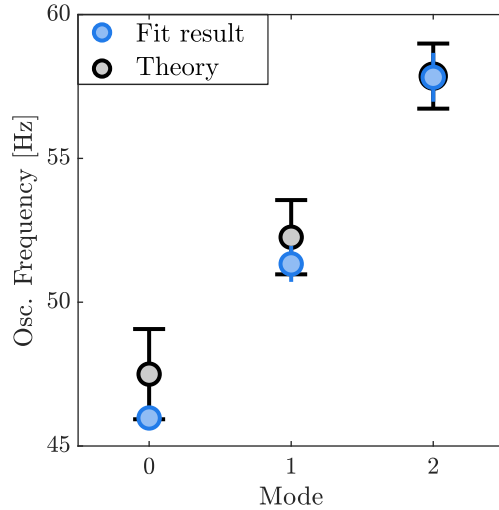


Figure 4.12.: **Extracted oscillation frequencies:** We plot the extracted oscillation frequencies of a fit to the fluctuation signal as shown in Fig. 4.11 for the lowest three spatial modes of the effective potential (blue points). We compare these with the theoretical values for the energy eigenstates of the effective potential according to Eq. (4.30). We find good agreement between the experimental and theoretical values. The error on the theory prediction originates from the uncertainty on c_1 as given in [94].

spinor phase to dynamically evolve before applying the rf-rotation for the readout. As explained above we exploit the symmetry of the spatial modes to filter out the desired mode. For each setting of q_{eff} we find that at least two spatial modes are populated as shown in Fig. 4.11b). The signal of each spatial mode is fitted with a sinusoidal curve as expected from Eq. (4.37) to extract the frequency, i.e. the energy of each mode. For the second excited mode we find an additional exponential decay with a lifetime of ≈ 20 ms.

We then compare the experimental result to a numerical calculation of the energy eigenstates in the effective potential given by Eq. (4.30) (see Fig. 4.12). The error in the theory calculation comes from the uncertainties on the scattering lengths taken from [94] in Eq. (4.3) which amounts to a relative uncertainty on the spin dependent interaction strength of $\Delta c_1/c_1 \approx 16\%$. Interestingly, the experimental values feature a lower uncertainty than the theoretical prediction. Theoretical and experimental values agree within this error confirming that the effective potential provides a good description of the experimental setting.

5. Spatially distributed entanglement and EPR steering

The generation of entanglement between spatially distinct regions is a major challenge in neutral ultracold systems as the interactions are mostly short ranged. This has restricted their use so far in quantum informational protocols which require entanglement between individually addressable systems. While we have concentrated in the preceding chapter on the characterization of the spin-mixing process in the effective potential, we will now use this knowledge to generate a spin-nematic squeezed state in a single spatial mode. Due to the indistinguishability of the atoms the resulting quantum correlations are shared between all particles of the condensate. We demonstrate that these correlations can be distributed between distinct spatial modes by expanding the atomic cloud. To reveal entanglement we use the EPR steering criterion which additionally certifies that the generated entangled state is useful for quantum informational tasks. Based on the steering criterion we develop an entanglement witness with which we verify at least genuine 5-partite entanglement. The main results presented in this chapter have been summarized in [116].

5.1. Surpassing the standard quantum limit

As first shown in [24] spin-mixing leads to spin-nematic squeezing, i.e. the fluctuations are redistributed such that the variance $\Delta^2 F(0) < \langle N \rangle$. Experimentally, this means that we have to measure the population difference N^- with a high precision such that we are able to detect fluctuations below the shot-noise limit. Therefore, the experimental system has to be carefully adjusted and calibrated to achieve the required sensitivity.

5.1.1. Shot noise limited detection

One major contribution to this precision is the technical stability of the rf and mw field which we use for state manipulation. For example, we have to make sure that the power of the rf field, which induces the $\pi/2$ spin rotation prior to the imaging, is stable. If the power fluctuates, then in each realization the rotation would be slightly different. This would add noise to our detection and would therefore limit our ability to measure an absolute reduction of the fluctuations below the classical limit. In the experiment, the power of the rf and mw fields have already a very high stability (see Appendix A.4 and A.5 for an analysis of the rf and mw stability). However, as these technical fluctuations affect each atom individually the resulting variance scales with $\propto N^2$. Thus, we restrict in the following the atom number to $\approx 11,000$ atoms compared to 40,000 atoms used in the previous experiments to reduce the effect of residual technical fluctuations. Together with the chosen trapping frequencies $(\omega_{||}, \omega_{\perp}) = 2\pi \cdot (51, 286)$ Hz, this lower atom number has the additional advantage that the spin dynamics will be restricted to a single spatial mode, i.e. the ground mode of the effective potential as shown in Fig. 4.7.

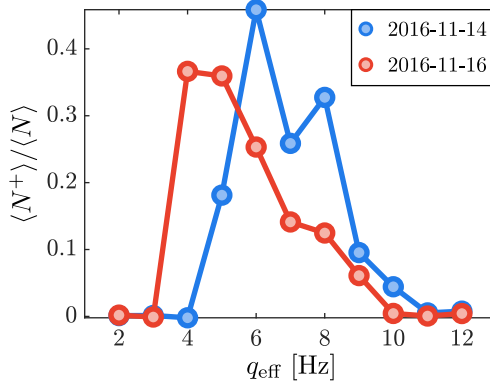


Figure 5.1.: **Spectroscopy signal for a typical control measurement:** In order to detect drifts of the mw power, we do a spectroscopy measurement every three hours. The plot here shows an example of a shift in the spectroscopy by 1 Hz after two days of measurements. We use this information to exclude the corresponding data in the post-analysis.

Furthermore, we have to ensure that the photon counts on the camera are converted into the correct atom number. The calibration of the imaging can be checked by measuring the fluctuations of a coherent spin state (CSS) and showing that these equal the expected shot-noise [82]. Thus, for a correct imaging calibration, we expect to find for the coherent polar state $\Delta^2 N_{\text{CSS}}^- = \langle N \rangle$. Suppose we did not extract the correct atom number and instead the measured value $N_{k,M} = \alpha N_{k,R}$ with $k \in \{-1, 0, +1\}$ differed from the real value $N_{k,R}$ by some factor α , then measuring the fluctuations of a coherent polar state would give

$$\begin{aligned} \Delta^2 N_{\text{CSS},M}^- &= \Delta^2(N_{+1,M} - N_{-1,M}) = \alpha^2 \Delta^2(N_{+1,R} - N_{-1,R}) = \alpha^2 \langle N_R \rangle \\ &= \alpha \langle N_M \rangle. \end{aligned} \quad (5.1)$$

Thus, if the measured atom number were smaller than the real one ($\alpha < 1$), one would measure reduced fluctuations even for a classical state. This highlights the importance of a correct imaging calibration. For details on this calibration see Appendix A.3.1.

5.1.2. Spectroscopy control sequence

We also have to take care that the value of q_{eff} is stable over many experimental realization. A variation of this parameter would slightly change the orientation of the squeezed state. The measured fluctuations would, thus, be averaged over these orientations which increases the fluctuations at the minimum.

In the experiments presented here, we set the magnetic field to $B = 1.44$ G which leads to a second-order Zeeman shift of $q_B = 149$ Hz. For the mw dressing we employ a resonant Rabi frequency of $\Omega_{\text{mw}} = 2\pi \cdot 9.46$ kHz. Using Eq. (4.16) we can connect the fluctuations of the mw power to the variations of q_{eff} . It turns out that for $q_{\text{eff}} \approx 0$ already a change of the Rabi frequency by $2\pi \cdot 30$ Hz leads to a change in q_{eff} by 1 Hz. This corresponds to a relative stability of the mw power on the order of 0.6%. We thus use the externally stabilized mw described before to reduce the shot-to-shot fluctuations of the mw power as much as possible.

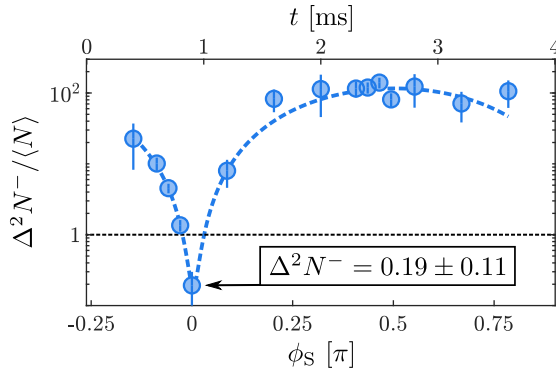


Figure 5.2.: **Spin-nematic squeezing:** The measured fluctuations of N^- are plotted after 150 ms of spin-mixing evolution time. The dashed blue line is a sinusoidal fit to the data and the black dashed line depicts the classical limit of a coherent polar state. Tuning the spinor phase via dynamical evolution, we find a minimal value of the fluctuations of $\Delta^2 N^- = 0.19 \pm 0.11$. This means that at this point the fluctuations are squeezed by -7.2 dB. The errorbars depict the 1 standard deviation (s.d.) interval as extracted via jackknife resampling.

However, there are still small drifts possible, for example, due to temperature changes in the electronics. To detect this, we take a spectroscopy measurement of the spin-mixing resonance every three hours and check for shifts of the spectroscopy signal. We can then either compensate these drifts in the experiment or, alternatively, use these measurements for a post-selection of the data. In the data analysis, we discard experimental realizations as soon as we detect a shift in the spectroscopy signal by 1 Hz.

For the spectroscopy measurement, we use an evolution time of 2 s. The left edge of the spectroscopy signal features a steep slope, since the polar state suddenly turns from highly unstable into a stable point with no transfer to the side modes. Using this point as a reference we detect changes in q_{eff} of ≈ 1 Hz (see Fig. 5.1). For the measurements presented here, the spectroscopy signal was typically stable over the course of about three to four days.

5.1.3. Spin-nematic squeezing

For measuring spin-nematic squeezing, we take special care to remove any residual population in the states $(1, \pm 1)$ after transferring the atoms to the state $(1, 0)$, since already a single atom increases the measured fluctuations after a $\pi/2$ spin rotation. Therefore, in addition to the Stern-Gerlach pulse, we apply two mw π -pulses coupling the states $(1, \pm 1) \leftrightarrow (2, \pm 1)$ directly before switching on the mw dressing. This removes any atoms which are retrapped after the Stern-Gerlach or which are produced via off-resonant spin-mixing during the waiting time of 100 ms after the Stern-Gerlach pulse.

After preparation of the polar state we use mw dressing to initiate spin-mixing resonant with the ground mode and let the state evolve for 150 ms. Afterwards, we adjust the spinor phase via dynamical evolution under the second-order Zeeman shift. In the end, we switch off the XDT to let the atomic cloud expand for 7 ms in the remaining waveguide potential after which we use an rf $\pi/2$ pulse to map the observable $\hat{F}(\phi_S)$ onto the population difference $N^-(\phi_S)$. We first employ a fast scan with low statistic to determine the phase

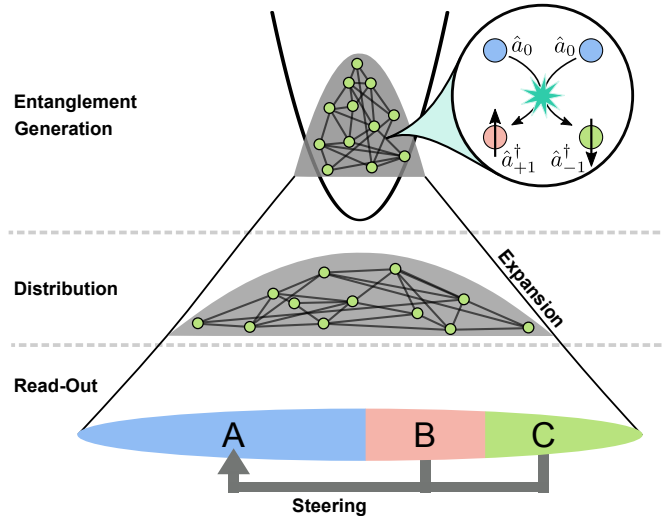


Figure 5.3.: **Distribution of entanglement in space:** Using spin-mixing in a tightly confining potential we generate entanglement that is shared among all identical atoms of the condensate. Subsequent expansion of the atomic cloud distributes this entanglement in space. The spatial resolution of the readout allows us to define distinguishable subsystems on the atomic signal. Using EPR steering we can then test for entanglement between these spatial regions.

evolution time corresponding to $\phi_S = 0$, i.e. measuring minimal fluctuations. After this we sample four points around the minimum and maximum with very high statistics.

With this we find minimal fluctuations of $\Delta^2 N^-/\langle N \rangle = 0.19 \pm 0.11$ well below the classical limit of 1 (Fig. 5.2). Here, we additionally subtracted the photon shot noise contribution which is calculated via Gaussian error propagation of the measured photon numbers and amounts to 0.14. Even without subtraction we measure reduced fluctuations of $\Delta^2 N^-/\langle N \rangle = 0.33 \pm 0.11$. The measured spin-nematic squeezing directly demonstrates entanglement between the spins of the atoms [10, 117, 11]. Since the particles in the condensate are indistinguishable this means that these correlations are shared between all particles in the condensate [4, 5].

5.2. Steering between spatially distinct regions of the atomic cloud

We now take a different point of view on the expansion of the atomic cloud. In the preceding chapter we used this method mainly to lower the optical density and to increase the resolution in order to ease the detection of the different spatial modes. However, from a quantum informational point of view, we use the tight confinement of the initial trap to generate entanglement between the atoms via short range contact interaction. By switching off the crossed dipole beam the generated entanglement is distributed in space via the expansion of the BEC. This enables the generation of entanglement between spatially distinct regions using just contact interactions. After the expansion the high optical resolution of our imaging allows us to partition the atomic signal into distinct regions (see Fig. 5.3).

In order to verify entanglement between distinct regions of the expanded atomic cloud we use EPR steering. For this, the system needs to fulfill two requirements: one needs

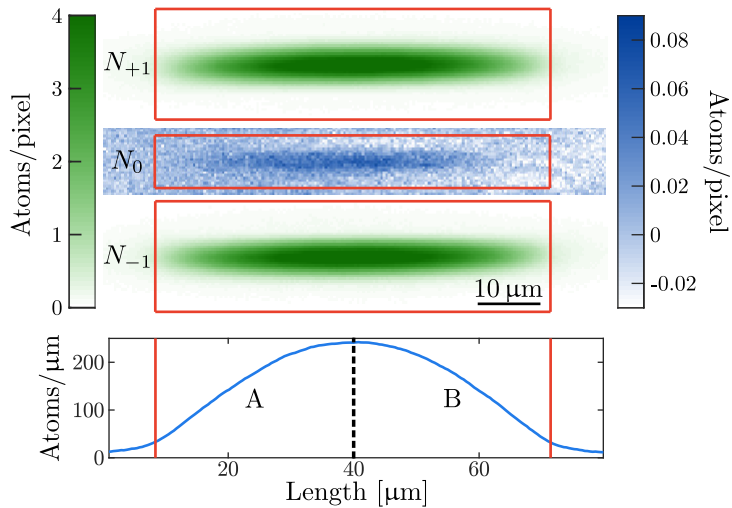


Figure 5.4.: Mean absorption image and analysis regions: Here, the average absorption signal over 1247 realizations after 150 ms of evolution time is shown. The red lines depict the evaluation regions. We use two different color scales, since after the $\pi/2$ rotation the population in $(1, 0)$ is much smaller than the one in the states $(1, \pm 1)$. The mean population in $(1, 0)$ amounts to $\langle N_0 \rangle \approx 25$ atoms which provides a direct measurement of the term $\hat{V}_x - \hat{N}^+$ in the commutation relation (5.2). Compared to the total atom number of 11,000 atoms, the resulting correction for the uncertainty relation is less than 1% and thus negligible. The lower plot shows the density profile integrated in vertical direction over all densities. The dashed line indicates the bipartitioning of the signal to define the subsystems A and B.

to be able to define two distinct subsystems, A and B, and one needs to measure two non-commuting observables in each of the two subsystems. In the case of spin-mixing we choose the two observables $\hat{F}(0)$ and $\hat{F}(\pi/2)$. These two operators have the same commutation relation as \hat{S}_x and \hat{Q}_{yz} (see Eq. (2.17), i.e.

$$[\hat{F}(0), \hat{F}(\pi/2)] = i(2\hat{Q}_0 + \hat{V}_x - \hat{N}^+). \quad (5.2)$$

Experimentally, the rf $\pi/2$ pulse maps the observable $\hat{F}(\phi_S)$ onto the population difference $N^-(\phi_S)$. The commutation relation (5.2) is then translated into an uncertainty relation for the population difference [36]

$$\frac{\Delta^2 N^-(0)}{\langle N \rangle} \frac{\Delta^2 N^-(\pi/2)}{\langle N \rangle} \geq 1, \quad (5.3)$$

which is valid in each subsystem with the corresponding local atom number $N_{A/B}$. For Eq. (5.3) we have used the undepleted pump approximation, specifically that

$$\langle (2\hat{Q}_0 + \hat{V}_x - \hat{N}^+) \rangle_Q \approx 2\langle N \rangle. \quad (5.4)$$

As an additional feature of the readout sequence we can check this approximation with the recorded data since the rf pulse maps the observable $\hat{V}_x - \hat{N}^+$ onto the population $2N_0$. Even for the longest evolution time of 150 ms which is employed in the experiment we find $\langle 2N_0 \rangle < 100$ compared to a total atom number of 11,000. The correction for the uncertainty relation is therefore less than 1% which confirms that the undepleted pump approximation is well justified.

5.2.1. Steering inequality

Following the steering argument [20] we choose to use the measurement results obtained in system B to estimate an inferred value $N_{A,\text{inf}}^-(\phi_S)$ for the corresponding measurement result in system A. The precision of this estimation is quantified by the inference variance

$$\Delta^2 N_{A|B}^-(\phi_S) = \Delta^2 \left(N_A^-(\phi_S) - N_{A,\text{inf}}^-(\phi_S) \right). \quad (5.5)$$

Steering is verified if this inference allows predicting the measurement results in A more precisely than expected from the local uncertainty relation, i.e. if the steering product

$$S_{A|B} = \frac{\Delta^2 N_{A|B}^-(0)}{N_A} \frac{\Delta^2 N_{A|B}^-(\pi/2)}{\langle N_A \rangle} < 1. \quad (5.6)$$

It is important to note that one can use any post-processing of the data obtained in subsystem B as this classical processing cannot a posteriori introduce entanglement. The steering criterion has the advantage that it does not require any a priori knowledge about the measured state and, thus, provides an entanglement criterion that can be adapted to a wide range of experimental systems.

5.2.2. EPR Steering between spatially distinct atomic clouds

Experimentally, we define the two subsystems by dividing the absorption signal into two halves, where we label the left and right half as subsystem A and B, respectively.

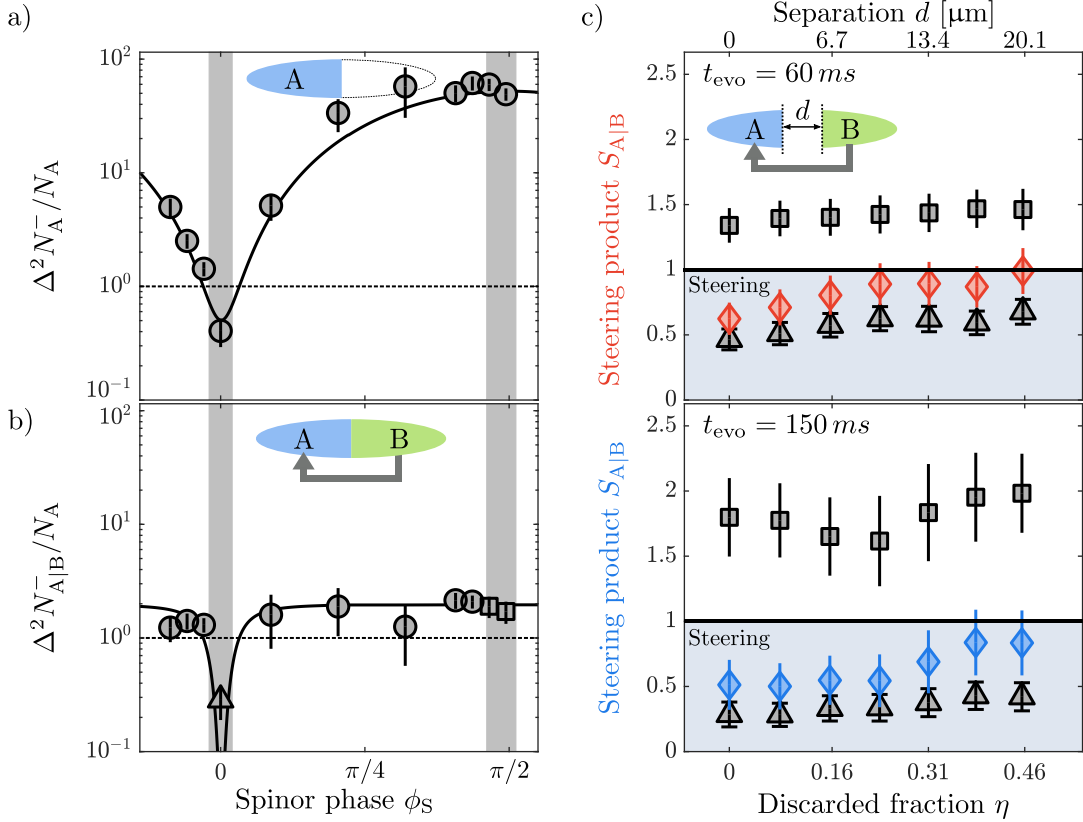


Figure 5.5.: Einstein-Podolsky-Rosen steering: a) Analyzing the variance $\Delta^2 N_A^-$ after 150 ms of evolution time in a single subsystem A yields reduced and enhanced fluctuations compared to a coherent spin state (dashed line) consistent with the uncertainty relation. The black line is a theory prediction. b) Using the measurement results in subsystem B to estimate the corresponding results in A leads to the inference variance $\Delta^2 N_{A|B}^-$, where the maximal fluctuations are largely reduced. c) Evaluating the steering product for 60 ms (red diamonds) and 150 ms (blue diamonds) of evolution time reveals steering between the two halves of the atomic cloud. The square and the triangles indicate the value of maximal and minimal fluctuations. The steering persists even when introducing an artificial barrier between the atoms by neglecting a fraction of atoms η in the middle of the evaluation region which highlights the non-local character of the generated entanglement. The errorbars depict the 1 s.d. interval.

For the definition of the evaluation regions on the absorption image see Fig. 5.4. If we neglect the information in part B and just analyze the populations difference $N^-(\phi_S)$ in the left half (see Fig. 5.5a)), we find after 150 ms of evolution time reduced fluctuations at $\phi_S = 0$ compared to a classical coherent polar state. Likewise we find at $\phi_S = \pi/2$ largely enhanced fluctuations such that the uncertainty product $\Delta^2 N_A^-(0) \Delta^2 N_A^-(\pi/2) / \langle N_A \rangle^2 = 0.41 \cdot 49$ is well above the uncertainty limit.

In a next step, we use the information gained in system B to estimate the measurement results in system A. Since any post-processing in system B is allowed without changing the steering criterion, we further subdivide B into 5 parts. From the resulting values $N_{B,k}^-(\phi_S)$ we estimate the results in system A via the linear combination $N_{A,\text{inf}}^- = \sum_{k=1}^5 g_k(\phi_S) N_{B,k}^-(\phi_S)$. The real numbers $g_k(\phi_S)$ are chosen to minimize the inference variance $\Delta^2 N_{A|B}^-(\phi_S)$ (5.5). The measured inference variance is shown in Fig. 5.5b). While the inference reduces the fluctuation for all measured spinor phases the strongest reduction happens for the maximal fluctuations at $\phi_S = \pi/2$ by a factor of 20.

We then use the inference variances at $\phi_S = 0, \pi/2$ to calculate the steering product as defined in Eq. (5.6). Experimentally, we find $S_{A|B} = 0.62 \pm 0.12$ and $S_{A|B} = 0.51 \pm 0.19$ after 60 ms and 150 ms of evolution time, respectively. For both experimental settings we detect $S_{A|B} < 1$ which confirms EPR steering between the left and right half of the atomic cloud. To increase the statistics we included measurements in a 0.04π interval around $\phi_S = \pi/2$. Within this range the uncertainty relations and therefore the steering criterion change by less than 2%.

To highlight the spatial separation of the entanglement we introduce a barrier by symmetrically discarding a fraction of atoms η in a region in the middle of subsystem A and B. The results are shown in Fig. 5.5c). We verify steering up to a discarded fraction of $\approx 1/3$ which corresponds to a spatial separation of $\approx 13.5 \mu\text{m}$ between subsystem A and B. This demonstrates that entanglement between indistinguishable particles can indeed be turned into quantum informational useful entanglement within the LOCC paradigm.

5.2.3. Monogamy of steering

For discarding more than a third of the atoms, we find that the steering criterion is no longer satisfied. This result is consistent with monogamy of steering [118]. If we consider the discarded region as subsystem C the monogamy relation is formulated as

$$S_{A|B} \cdot S_{A|C} \geq 1. \quad (5.7)$$

This means that if for example subsystem A is steered by B, i.e. $S_{A|B} < 1$, it cannot simultaneously be steered by C. Theoretically, discarding atoms is equivalent to tracing out the corresponding part of the density matrix ρ_{ACB} . If we assume that the entanglement is evenly shared among all atoms, this implies that the reduced density matrix ρ_{AB} will be closer to a mixed state the more atoms we discard. After discarding more than a third of the atoms, region C contains more atoms than each of the other two regions individually. Therefore the density matrix ρ_{AC} should feature stronger correlations than ρ_{AB} . Thus, one expects to find that A is steered by the region C and, consequently, one should not find steering between A and B, which is consistent with our experimental result. Intuitively one could also argue that every region contains some information about the measurement results in A. However, by discarding more than a third of the atoms the discarded part

actually contains more information than B. Thus, assuming monogamy of steering A should be steered by the discarded system C and not anymore by B.

5.2.4. Beamsplitter picture

If we assume that the atoms do not interact during their expansion in the waveguide potential, we can also think of the partitioning of the absorption signal in terms of beam-splitting operations. Such a treatment has also been used in optics to describe partitions of an expanding light field [119, 67]. We will demonstrate in the following that this description is consistent with our experimental findings. In this respect, the experiment can be viewed as direct implementation of the theoretical proposal discussed in [16] to distribute entanglement between identical particles among distinguishable modes via beamsplitter operations.

After splitting the absorption image into two halves there is a 50% probability in each magnetic substate to find a particle in system A or B. In this respect, we treat the initial condensate modes \hat{a}_k with $k \in \{-1, 0, 1\}$ as one input of a balanced beamsplitter where the second input port $\hat{a}_{\text{aux},k}$ is initially empty. These input operators are then connected to the output ports A and B via

$$\begin{pmatrix} \hat{a}_{A,k} \\ \hat{a}_{B,k} \end{pmatrix} = \frac{1}{\sqrt{2}} \begin{pmatrix} 1 & 1 \\ 1 & -1 \end{pmatrix} \begin{pmatrix} \hat{a}_k \\ \hat{a}_{\text{aux},k} \end{pmatrix}. \quad (5.8)$$

With this we can connect the relevant observables in subsystem A and B to the single mode operators of the initial condensate, i.e.

$$\begin{aligned} \hat{F}_A(\phi_S) &= \frac{1}{\sqrt{2}} \left[e^{-i(\phi_S - \phi_{S,0})} \hat{a}_{A,0}^\dagger (\hat{a}_{A,+1} + \hat{a}_{A,-1}) + \text{h.c.} \right] \\ &= \frac{1}{2\sqrt{2}} \left[e^{-i(\phi_S - \phi_{S,0})} (\hat{a}_0^\dagger + \hat{a}_{\text{aux},0}^\dagger) (\hat{a}_{+1} + \hat{a}_{\text{aux},+1} + \hat{a}_{-1} + \hat{a}_{\text{aux},-1}) + \text{h.c.} \right], \end{aligned} \quad (5.9)$$

and analogously for $\hat{F}_B(\phi_S)$. Using the undepleted pump approximation and the fact that the second input port is initially empty we can calculate the fluctuations of these observables in the respective subsystem (see supplementary information in [116])

$$\frac{\Delta^2 F_A(\phi_S)}{\langle N/2 \rangle} = \frac{1}{2} [1 + \cosh(2\kappa t) - \sinh(2\kappa t) \cos(\phi_S)]. \quad (5.10)$$

This shows that even for infinite squeezing the minimal fluctuations, that can be measured in one half, are bounded by 1/2. For an infinitely squeezed one would find globally that atom numbers in $(1, \pm 1)$ are always perfectly correlated, i.e. $N_{+1} = N_{-1} = N/2$, and, thus, $\Delta^2 N^- = 0$. However, the beamsplitter introduces binomial fluctuations in each subsystem. Using a binomial distribution with probability $p_A = 0.5$ to detect a particle in system A we can calculate the residual fluctuations in A for an infinitely squeezed state via

$$\begin{aligned} \Delta^2 N_A^- &= \Delta^2 N_{A,+1} + \Delta^2 N_{A,-1} \\ &= p_A(1 - p_A) \frac{\langle N \rangle}{2} + p_A(1 - p_A) \frac{\langle N \rangle}{2} = \frac{1}{2} \frac{\langle N \rangle}{2} \end{aligned} \quad (5.11)$$

Within the undepleted pump approximation we analogously calculate the correlations between the two halves

$$\frac{\langle \hat{F}_A(\phi_S) \hat{F}_B(\phi_S) \rangle_Q}{\langle N/2 \rangle} = \frac{1}{2} [-1 + \cosh(2\kappa t) - \sinh(2\kappa t) \cos(\phi_S)]. \quad (5.12)$$

Thus, for the inference operator $\hat{F}_{A|B}(0) = \hat{F}(0)_A + \hat{F}(0)_B$ at the minimum one finds

$$\begin{aligned} \frac{\Delta^2(F_{A|B}(0))}{\langle N \rangle} &= (\Delta^2 F_A(0) + \Delta^2 F_B(0) + 2\langle \hat{F}_A(0) \hat{F}_B(0) \rangle_Q) / \langle N \rangle \\ &\approx e^{-2\kappa t}, \end{aligned} \quad (5.13)$$

where we used for the last equality that $\kappa t \gg 1$. These fluctuations are identical to the squeezing found in Eq. (4.38). This is not surprising as such an evaluation corresponds to measuring the whole cloud without partitioning the signal.

Analogously, we find for the inference operator $\hat{F}_{A|B}(\pi/2) = \hat{F}_A(\pi/2) - \hat{F}_B(\pi/2)$ at the maximum

$$\frac{\Delta^2(F_{A|B}(\pi/2))}{\langle N \rangle} = 1. \quad (5.14)$$

This means that the fluctuations at the maximum are reduced to the shot-noise limit. This confirms the argument we used previously to distinguish the different spatial modes in the fluctuation signal (see Sec. 4.11), i.e. the antisymmetric analysis cancels the contribution from the symmetric ground mode. For the steering criterion one then has to calculate the product

$$S_{A|B} = \frac{\Delta^2(F_{A|B}(0))}{\langle 2N \rangle} \cdot \frac{\Delta^2(F_{A|B}(\pi/2))}{\langle 2N \rangle} = 4e^{-2\kappa t}. \quad (5.15)$$

Thus, within this beamsplitter description it is indeed possible to verify steering as soon as the overall squeezing $\exp(-2\kappa t) < 0.25$.

To incorporate different splitting ratios between the two subsystems we can change the coupling matrix to the one of an imbalanced beamsplitter. This changes, for example, the operators in A to $\hat{a}_{A,k} = (\sqrt{\eta_A} \hat{a}_k + \sqrt{1-\eta_A} \hat{a}_{\text{aux},k})$ with the atomic fraction $\eta_A = N_A/N$ in A. The scenario can also be extended to the case where we discard a fraction of the atoms. For this one defines three output ports A, B and C. Consequently, one needs two initially empty input ports. For more details see supplementary information in [116].

5.2.5. Steering and entanglement in different experimental settings

In parallel to our results there have been two other experiments which achieved entanglement between spatially separated modes. In [120] they used ≈ 500 Rb atoms in a two-component BEC on an atom chip. After generating a spin squeezed state and expanding the atomic cloud they similarly observe steering between spatially distinct parts of the cloud. As their expanded cloud is more radially symmetric they can also partition the absorption signal along the second spatial direction and with that observe steering between a variety of post-selected patterns.

In [111] they employ, similar to our experiment, a spinor BEC of ^{87}Rb with around 20,000 particles. There, spin-mixing is tuned into resonance with the first excited state of the effective potential which is subsequently populated by a relatively large number

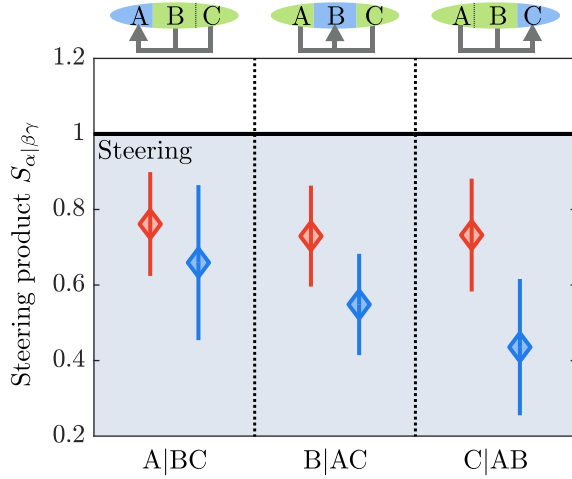


Figure 5.6.: Threeway EPR steering: We divide the absorption signal into three parts of equal lengths ($\approx 20 \mu\text{m}$), labeled A, B and C. By combining the measurement results in two subsystems we infer the corresponding results in the remaining one and determine the steering product, which is denoted by the red and blue diamonds for 60 and 150 ms of evolution time, respectively. For both evolution times, we find a violation of the steering inequality for all three combinations. This confirms threeway steering. The errorbars correspond to the 1 s.d. interval.

of 5,000 particles. In this setting, they verify entanglement between the two halves of the atomic cloud. This confirms that the scheme presented here for generating entanglement between spatially distinct regions is not limited to our special choice of parameters. Instead it has been demonstrated to work in different atom number regimes and for different interactions, i.e. in a spin-1 and a pseudo-spin 1/2 system.

5.2.6. Threeway EPR steering

As argued above, we expect the correlations to be evenly distributed over the whole atomic cloud. Therefore, we divide the absorption signal into three parts of equal length ($\approx 20 \mu\text{m}$), labeled A, B and C. Analogously to the bipartite case, we calculate the inference variance $\Delta^2 N_{A|BC}^-$ for all permutations of ABC. As shown in Fig. 5.6 we find that each part of the atomic cloud is steered by the remaining parts which demonstrates threeway steering [67]. Fundamentally, the detection of symmetric EPR steering puts some additional constraints on local hidden variable models [20]. But as steering still includes the assumption of the uncertainty relation, it cannot rule out all local hidden variable models. Threeway steering also has applications in quantum information protocols where it is discussed in the context of quantum secret sharing schemes. The idea is that two parties would have to work together to correctly predict the measurement results of the third party [121] which can then be used to establish a secure communication channel between the three parties. Since the size of a BEC is not well suited for this kind of quantum communication, we use threeway steering here as a measure to characterize the generated entanglement structure.

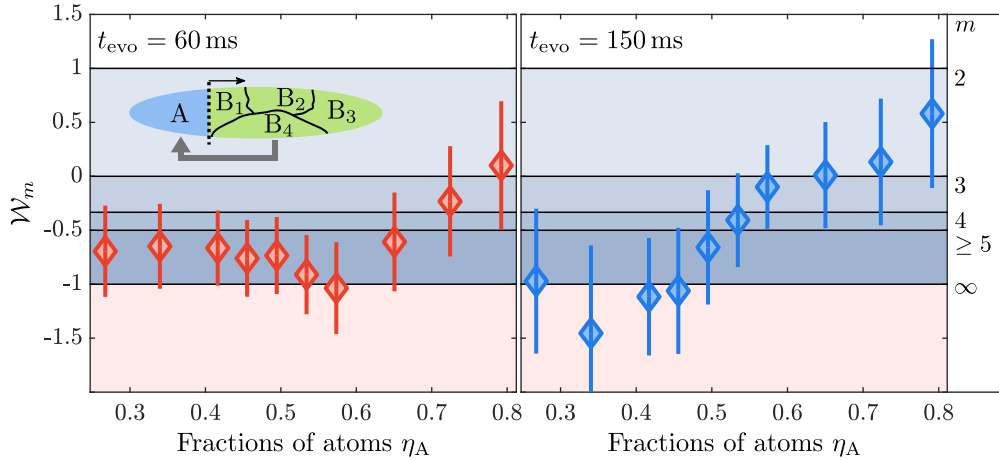


Figure 5.7.: Genuine 5-partite entanglement: In the bipartite steering scenario, the steering product can be used to construct a witness \mathcal{W}_m for genuine multipartite entanglement. For this we divide the signal again into two parts A and B, where the partition is quantified by the fraction of atoms $\eta_A = N_A/N$ in A. The blue shadings indicate the regions where genuine m -partite entanglement is witnessed with the corresponding m given on the right. The entangled subsystems are given by A and $m-1$ further subdivisions of B with equal atom number (see inset for an example). The region marked by the red shading is quantum mechanically inaccessible as it is below the uncertainty limit of the inference operators used for the steering product. Using this witness we reveal up to genuine 5-partite entanglement for both evolution times. The errorbars depict the 1 s.d. interval.

We restrict the analysis to three-way steering since more partitions of the absorption signal would lead to smaller evaluation regions. If the length scales become too small one has to take into account classical correlations that are induced by the absorption imaging which distributes the atomic signal over multiple pixels on the camera. This will be discussed in detail later. We quantified these classical correlations by analyzing the partitions of a coherent polar state and found that for partition lengths above $20 \mu\text{m}$ these correlations are negligible.

5.3. Detection of genuine 5-partite entanglement

EPR steering gives a stronger constraint on the quantum state than entanglement in the sense that not all entangled states feature steering. This enables the construction of a witness \mathcal{W}_m for genuine m -partite entanglement based on the bipartite steering product $S_{A|B}$. For this we divide the absorption signal again into two parts A and B, where the partition is quantified by the fraction of atom $\eta_A = N_A/N$ in A. In this case, we use the inference $N_{A,\text{inf}}^-(\phi_S) = g(\phi_S)N_B^-(\phi_S)$ without further subdivisions of B different to before. Again, the factors $g(\phi_S)$ are chosen to minimize the corresponding inference variance. Based on this inference, we generalize the derivation in [67] (for details see [116]) to construct the following witness for genuine m -partite entanglement

$$\mathcal{W}_m = \frac{\eta_A}{1-\eta_A} \frac{(1-\sqrt{S_{A|B}})}{g(0)g(\pi/2)} < \frac{3-m}{m-1}. \quad (5.16)$$

Fulfilling Eq. (5.16) means that the state must be at least genuinely m -partite entangled, where the entangled subsystems are defined by A and $m - 1$ subdivisions of B with equal atom numbers. This witness is valid as long as $g(0) \cdot g(\pi/2) < 0$. This translates to measuring correlations between the two systems in one operator basis and anticorrelations in the conjugate basis which is anyway a precondition to detect steering as explained in 2.5.2.

For $m = 3$ one recovers the usual steering inequality showing that there is a close connection between steering and higher partite entanglement in continuous-variable systems. For $m = 2$ we find another bound for bipartite entanglement. In the limit of $m \rightarrow \infty$ the right hand side of Eq. (5.16) becomes -1 . This value corresponds to the limit on the steering product $S_{A|B}$ determined by the uncertainty relation

$$[\hat{F}_{A,\text{inf}}(0), \hat{F}_{A,\text{inf}}(\pi/2)] = [\hat{F}_A(0) + g(0)\hat{F}_B(0), \hat{F}_A(\pi/2) + g(\pi/2)\hat{F}_B(\pi/2)] \quad (5.17)$$

of the inference operators. Thus, a value below -1 is excluded by quantum mechanics.

As explained before, we experimentally divide the absorption signal again into two subsystems and vary the splitting between the two system which we characterize by the inferred fraction $\eta_A = \langle N_A/N \rangle$. By inferring the results in A by B, we find up to genuine 5-partite entanglement for both spin-mixing evolution times as shown in Fig. 5.7. This means explicitly that, if we would subdivide B into four further subsystem with equal atom numbers, one would find that the whole system is genuinely 5-partite entangled. The subdivisions of B are defined in a particle basis. But as shown in this chapter, this can be converted into entanglement between individually addressable modes. Thus, this witness further characterizes the entanglement structure and the potential usefulness of the generated state for quantum information protocols.

5.4. Experimental imperfections

To identify possible improvements in the experimental setup we compare the squeezing results with a theoretical prediction that has been calculated via a truncated Wigner simulation (see Fig. 5.8 and for a full quantum calculation see supplementary information in [116]). By adjusting the simulation to the extracted maximal variance $\Delta^2 N^-(\pi/2)/\langle N \rangle$ we obtain the spin-mixing parameters $N\tilde{c}_1 = -2.5$ Hz and $q_{\text{eff}} = 2.4$ Hz. According to the simulation we should measure after 150 ms of evolution time a much higher spin-nematic squeezing of ≈ -20 dB compared to the experimental value of ≈ -7.2 dB.

In the simulation, we can model these deviations by introducing shot-to-shot fluctuations on the resonant Rabi frequency of 6 Hz. This corresponds to relative power fluctuations of 0.1% and translates to a fluctuation of q_{eff} by 0.2 Hz. This leads to a varying orientation of the squeezed state which effectively results in a larger variance at the minimum. Another effect which reduces the observed squeezing is the finite stepsize for scanning the spinor phase. Experimentally, we employed a phase-stepping of 0.03π . If one assumes that we missed the minimum by half a stepsize which is the largest possible deviation, this leads to the same squeezing as observed in the experiment.

As the squeezing measurement becomes for longer evolution times more sensitive on the correct setting of the spinor phase, these two contribution mainly affect the experimental result after 150 ms of evolution time. In the end the measured fluctuations are probably caused by a combination of both effects, i.e. the q-fluctuations might in reality

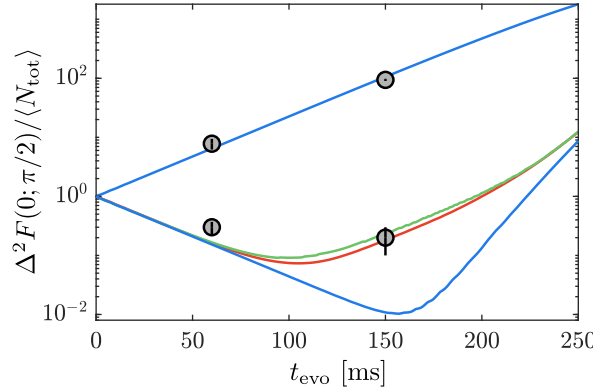


Figure 5.8.: **Comparison theory vs. experiment:** We compare the theoretical expectation (blue lines) for $\Delta^2 F(0)$ and $\Delta^2 F(\pi/2)$ obtained via a truncated-Wigner simulation with the experimental data (gray points). The parameters of the simulation have been adjusted to match the measured maximal variances. We find significant deviations from the ideal theory prediction for the data point obtained after 150 ms of evolution time. We can model these fluctuations either by including power fluctuations on the mw dressing (red curve) or by assuming that we experimentally missed the optimal spinor phase setting by half of the chosen stepsize (green line). The rise of $\Delta^2 F(0)$ after 150 ms of evolution time indicates the departure from the undepleted pump approximation.

be lower and the remaining excess fluctuations stem from the finite stepsize used in the experiment to scan the spinor phase.

5.5. Classical correlations induced by imaging

In the steering evaluation we restricted the length of the partitions to a value above 20 μm . For smaller regions, classical correlations caused by the absorption imaging might become relevant. To quantify these correlations we analyze the fluctuations of a coherent spin state (CSS). For this we prepare all atoms in the state $(1, 0)$ and apply an rf $\pi/2$ -rotation without any spin-mixing evolution.

After partitioning the resulting absorption signal into regions of equal length we evaluate their fluctuations $\Delta^2 N_{i,\text{CSS}}^-$. Theoretically, for each subsystem i the fluctuations should be equal to the corresponding mean atom number $\langle N_i \rangle$. For small partition lengths, however, we find a reduction of the fluctuations below the classical limit as shown in Fig. 5.9a). The reason for this is that during the imaging process the absorption signal of each atom is spread out over multiple pixels. This leads to classical correlations between the pixels over a certain length scale as visualized in Fig. 5.9b).

We find that the reduction of fluctuations is well described by a function of the form

$$\zeta(x) = \sqrt{\frac{bx^2}{1 + bx^2}}, \quad (5.18)$$

where x is the length of the partition. At $|x|_{1/2} = 1/\sqrt{3b}$ one finds a reduction of $\Delta^2 N_{i,\text{CSS}}^- / \langle N_i \rangle = 0.5$. From the fit we extract a value of $|x|_{1/2} = 2.0 \pm 0.1 \mu\text{m}$. To connect

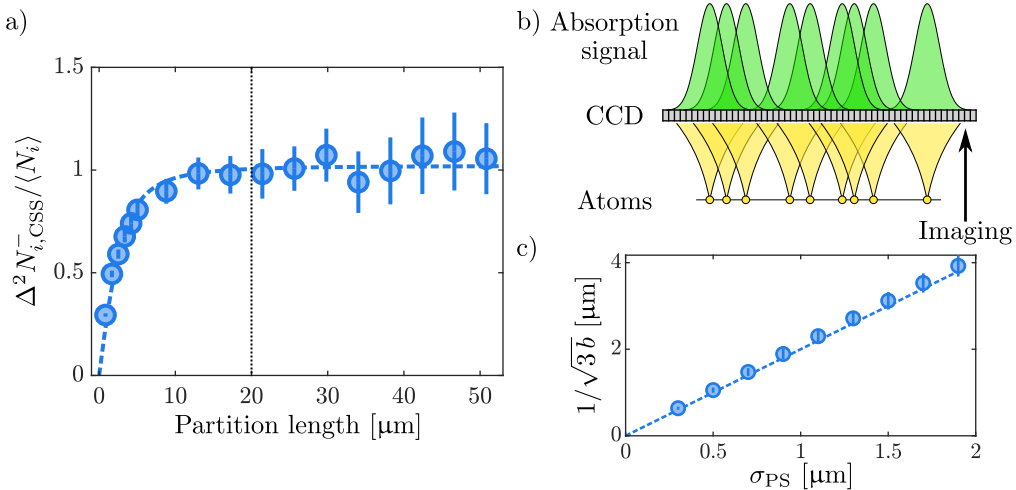


Figure 5.9.: Classical correlations after absorption imaging: a) We prepare a coherent spin state by initializing all 11,000 atoms in the state $(1, 0)$. After an rf $\pi/2$ -rotation we partition the absorption signal into regions of equal length and analyze their fluctuations which are normalized to their classical expectation. For small length scales we find a reduction of the fluctuations which we fit according to Eq. (5.18) (blue dashed line). For length scales above $20 \mu\text{m}$ we find these correlations to be negligible. The errorbars depict the 1 s.d. interval. However, it should be noted that the shown data points are not statistically independent. b) During imaging the absorption signal of each atom is spread over multiple pixels due to the finite width of the point spread function. This leads to correlations between neighboring pixels as indicated on the right side. c) By employing a Mont-Carlo simulation we connect the fitted value of b with the width of the point spread function σ_{PS} of the imaging. We approximately find $1/\sqrt{3b} \approx 2\sigma_{\text{PS}}$. With this we extract a width of $\sigma_{\text{PS}} = 1 \mu\text{m}$.

this value to the width σ_{PS} of the imaging point spread function we employ Monte-Carlo simulations of the imaging process where we tune the value of σ_{PS} . From this simulation we extract the relation $\sigma_{\text{PS}} \approx |x|_{1/2}/2$ (see Fig. 5.9c)). Thus, we obtain for our experimental setting a value of $\sigma_{\text{PS}} \approx 1 \mu\text{m}$.

One contribution to this point spread function is the optical resolution which in our case amounts to $\sigma_{\text{opt}} \approx 0.55 \mu\text{m}$ [82]. An additional contribution comes from the photon recoil of the imaging light. While scattering the photons each atom performs a random walk which leads to a spread of its signal beyond the optical resolution. An upper limit to this effect is given by [122] $\sigma_{\text{sc}} = v_{\text{rec}} \sqrt{\Gamma_{\text{sc}}} \tau^{3/2} / 3$. Here, $\Gamma_{\text{sc}} = 2\pi \cdot 6 \text{ MHz}/2$ is the scattering rate for high saturation and $v_{\text{rec}} = 6 \text{ mm/s}$ is the recoil velocity. For our imaging duration $\tau = 15 \mu\text{s}$ we find $\sigma_{\text{sc}} \approx 0.5 \mu\text{m}$. These two effects together would amount to a point spread function with width $\sigma_{\text{PS}} = \sqrt{\sigma_{\text{sc}}^2 + \sigma_{\text{opt}}^2} = 0.74$ suggesting that these are the main contributions to the classical correlations.

In the steering analysis we restricted the partition lengths to $> 20 \mu\text{m}$ which is well in the saturation regime of $\zeta(x)$.

5.6. Undefined Larmor phase

In the treatment above we neglected the Larmor phase and assumed that our readout works always at a fixed $\phi_L = 0$ such that we measure in each shot $F(\phi_S)$. Experimentally, however, this phase is uncontrolled. This is because for the initial polar state ϕ_L is undefined and we provide no phase reference via an rf-pulse. Thus, as soon as spin-mixing populates the states $(1, \pm 1)$ this phase is randomly chosen. On the other hand, even if we would accidentally provide some phase reference in the beginning ϕ_L would be randomized after a few ms due to magnetic field fluctuations.

To account for the Larmor phase we define the operator

$$\hat{F}_\perp(\phi_S, \phi_L) = \cos(\phi_S - \phi_{S,0})\hat{S}_\perp(\phi_L) + \sin(\phi_S - \phi_{S,0})\hat{Q}_\perp(\phi_L), \quad (5.19)$$

where the operators $\hat{S}_\perp(\phi_L)$ and $\hat{Q}_\perp(\phi_L)$ are defined as in Eq. (2.15). The problem is that for this operator the commutator as in (5.2) is now

$$[\hat{F}_\perp(0, \phi_{L,1}), \hat{F}_\perp(\pi/2, \phi_{L,2})] = 2i\hat{N} \cdot \cos(\phi_{L,1} - \phi_{L,2}), \quad (5.20)$$

where we neglected here the correction part. This means that for $\phi_{L,1} - \phi_{L,2} = \pi/2$ the commutator and therefore the steering bound vanishes. However, in the following, we will show that the steering bound given above is still valid, if we assume that the Larmor phase is indeed random in every realization.

For that we define the uncertainty bound $b = \Delta^2 F_\perp(0, \phi_L) \Delta^2 F_\perp(\pi/2, \phi_L)$ which is the same for each value of ϕ_L . We then assume that in each experimental realization we randomly sample ϕ_L from a discrete set containing n_L values. The uncertainty product is then given by

$$\begin{aligned} \frac{1}{n_L} \sum_i \Delta^2 F_\perp(0, \phi_{L,i}) \frac{1}{n_L} \sum_j \Delta^2 F_\perp(\pi/2, \phi_{L,j}) &\geq \frac{1}{n_L^2} \sum_i \Delta^2 F_\perp(0, \phi_{L,i}) \sum_j \frac{b}{\Delta^2 F_\perp(0, \phi_{L,j})} \\ &= \frac{b}{n_L^2} \sum_{i,j} \eta_{ij} \\ &= \frac{b}{n_L^2} \left[n_L + \sum_{i < j} \left(\eta_{i,j} + \frac{1}{\eta_{i,j}} \right) \right] \\ &\geq \frac{b}{n_L^2} \left[n_L + 2 \frac{n_L(n_L - 1)}{2} \right] \\ &= b, \end{aligned} \quad (5.21)$$

where we have defined $\eta_{i,j} = \Delta^2 F_\perp(0, \phi_{L,i}) / \Delta^2 F_\perp(0, \phi_{L,j})$ and used that $\eta_{i,j} + 1/\eta_{i,j} \geq 2$ for $\eta_{i,j} > 0$. This derivation can also be extended to the continuous case by exchanging the summation with an integral.

Theoretically one could also argue that starting with a polar state the fluctuations are symmetric with respect to the Larmor phase. Since the spin-mixing process is independent of the Larmor phase this symmetry will not change during the evolution and it does not matter which Larmor phase is read out, since it will always be bounded by the uncertainty product (5.3). This argument, however, makes assumptions about the state that has been produced which is always difficult to prove in reality. Experimentally, there

could be some unidentified process which breaks the symmetry of the state with respect to the Larmor phase. But since the randomization of the Larmor phase is ensured by the magnetic field fluctuations, this experimental imperfection is turned into a feature that ensures the validity of the steering argument.

6. Simultaneous readout of conjugate observables

For the measurement results in the preceding chapters we have used projective measurements as outlined in the theory part 2.3. By measuring the atomic populations in the different magnetic substates of the $F = 1$ hyperfine manifold, we projected the spin-1 state onto an eigenbasis of its Hilbert space. With this method the detection is limited to extract information only about commuting observables of the spin-1 state and in order to access noncommuting observables we have to prepare the same state again and apply a unitary prior to the measurement, e.g. tuning the spinor phase ϕ_S as to measure the noncommuting observables $\hat{F}(\phi_S)$.

There exist, however, also more general notions of a quantum measurements which are often discussed in the context of so-called positive operator valued measures (POVMs) [34]. It turns out that with these types of measurement it is possible to extract information about multiple noncommuting spin-1 observables in a single experimental realization. In the following, we will give a short overview over the theory of POVMs and show how they can be experimentally implemented. This provides a powerful method to analyze quantum states and we demonstrate that it can even be used to extract quantum correlations. The main results presented in this chapter have been summarized in [123].

As a short note: since in the following chapters, the magnetic substates of the $F = 2$ manifold will also play a central role, we adjust the previously used notation and include a label of the hyperfine manifold when referring to a specific substate. This means we change the subscripts, for example, of the creation operators $\hat{a}_{m_F} \rightarrow \hat{a}_{F,m_F}$.

6.1. Positive operator valued measures

In the theory part we introduced projective measurements as standard measurement techniques to extract information out of a given quantum state. Mathematically, the main difference to a measurement basis of projectors is that POVM elements (\hat{E}_i) do not have to be orthogonal, this means for the corresponding single particle operators $\hat{E}_i \hat{E}_j \neq 0$ (for $i \neq j$). As a direct consequence a POVM can have more elements than the dimension of the Hilbert space. As an example for the spin-1 case, one can define the following POVM elements which will be useful to illustrate the connection to an experimental implementation

$$\begin{aligned}\hat{E}_0 &= \frac{1}{6}\hat{N} + \frac{1}{4}\hat{S}_x + \frac{1}{8}\hat{V}_x - \frac{1}{16}\hat{Q}_{zz}, & \hat{E}_1 &= \frac{1}{6}\hat{N} - \frac{1}{4}\hat{V}_x + \frac{1}{8}\hat{Q}_{zz}, \\ \hat{E}_2 &= \frac{1}{6}\hat{N} - \frac{1}{4}\hat{S}_x + \frac{1}{8}\hat{V}_x - \frac{1}{16}\hat{Q}_{zz} \\ \hat{E}_3 &= \frac{1}{6}\hat{N} + \frac{1}{4}\hat{S}_z + \frac{1}{8}\hat{Q}_{zz}, & \hat{E}_4 &= \frac{1}{6}\hat{N} - \frac{1}{4}\hat{Q}_{zz}, \\ \hat{E}_5 &= \frac{1}{6}\hat{N} - \frac{1}{4}\hat{S}_z + \frac{1}{8}\hat{Q}_{zz}.\end{aligned}\tag{6.1}$$

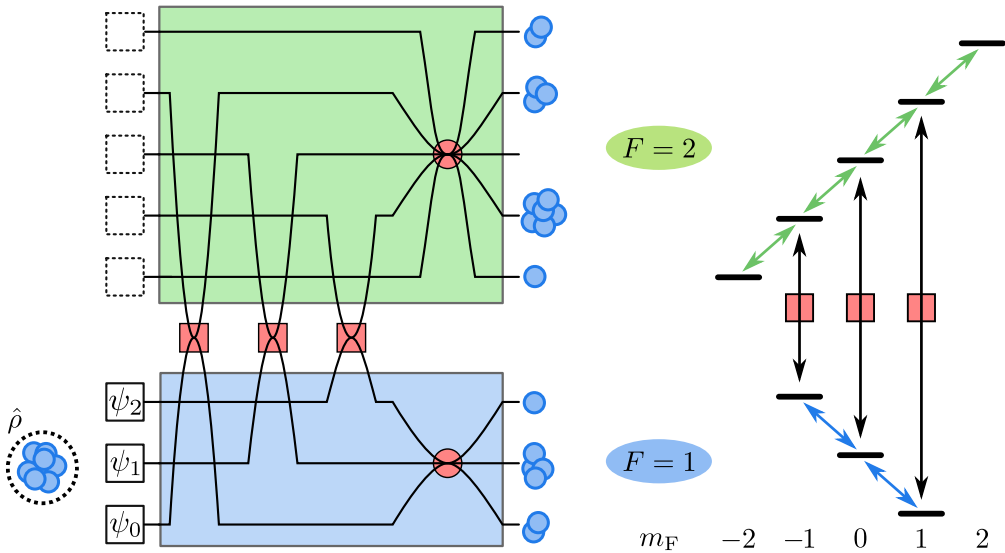


Figure 6.1.: **POVM measurement scheme:** Coupling the state in $F = 1$ to initially empty auxiliary modes one effectively increases the dimension of the Hilbert space for the readout. Performing independent manipulations in both Hilbert spaces together with a projective measurement on an ensemble of particles yields a distribution of particles over all modes involved in this measurement scheme. In analogy to a standard projective measurement, as introduced in Fig. 2.4, the populations in these modes contain information about the observables of the quantum state. Since this measurement schemes involve more modes, we gain access to additional observables which can even be non-commuting. This constitutes a generalized measurement which is often described in the framework of positive operator valued measures (POVMs). Experimentally, we implement this scheme by coupling the state in the $F = 1$ hyperfine manifold via mw fields to the initially empty magnetic substates in $F = 2$. Together with independent spin rotations in both hyperfine manifolds we have full control over the readout basis which enables the simultaneous extraction of multiple spin-1 observables.

One can immediately verify the completeness relation $\sum_i \hat{E}_i = \hat{N}$. Additionally, the last three elements are not orthogonal with respect to the rest of the POVM elements. By comparing the last three elements with Eq. (2.22) one finds that these correspond to a projective measurement in the \hat{S}_z basis (with an additional factor of 1/2). The first three elements correspond to a measurement in the \hat{S}_x basis, i.e. a projective measurement after a $\pi/2$ spin rotation. Therefore, within this POVM formalism it is possible to extract information about two non-commuting observables, as in this example about the spin in x - and in z -direction, which is different from conventional projective measurements.

6.1.1. Naimark's extension

It has been shown that POVMs can be implemented by performing a projective measurement in a higher dimensional manifold. This is known as Naimark's extension [124] and is schematically shown in Fig. 6.1. By coupling the state to initially unoccupied modes one effectively increases the dimension of the Hilbert space for the readout. Performing unitary transformations in the original and auxiliary Hilbert space allows setting the desired POVM. In the end, one uses a projective measurement in this enlarged space to extract the information. Since the population of each basis state in this enlarged Hilbert space contains some information about the quantum state, one would intuitively expect that such a scheme could enlarge the information that one can extract from a single projective measurement. In the single-particle case, such readout techniques have for example been used for quantum state discrimination [125].

Experimentally, the extension of the Hilbert space corresponds to coupling the spin-1 state to the initially unoccupied magnetic substates of the $F = 2$ hyperfine manifold. For example, the POVM (6.1) is implemented by first using 3 mw $\pi/2$ -pulses coupling the states $(1, k) \leftrightarrow (2, k)$ with $k \in \{0, \pm 1\}$. This transfers in the mean half of the population to the $F = 2$ manifold. These populations contain the information about the z -component of the spin. Applying a $\pi/2$ spin rotation in the $F = 1$ manifold selectively changes the readout basis there to the \hat{S}_x basis. Thus, after a projective measurement of the populations in both manifolds one can identify $\langle \hat{E}_i \rangle_Q$ for $i \in \{0, 1, 2\}$ with the mean populations of the magnetic substates in the $F = 1$ manifold and, analogously, $\langle \hat{E}_i \rangle_Q$ for $i \in \{3, 4, 5\}$ with the mean population of the substates in the $F = 2$ manifold. This enables the simultaneous readout of the two spin directions. One may wonder, how such a measurement scheme can be consistent with the uncertainty relation. It turns out that the coupling to the initially unoccupied modes will introduce additional fluctuations which will lead to a less precise readout of the two observables. We will discuss this in more detail later.

6.1.2. Informationally complete measurements

For completeness, we briefly introduce two special types of POVMs which are used in the quantum information literature. As mentioned in 2.3, a general quantum state in d dimensions is described by $d^2 - 1$ operators and a standard projective measurement within this Hilbert space yields information about $d - 1$ commuting observables. Similarly, a POVM consisting of n elements provides information about $n - 1$ operators as one information is contained in the sum of all POVMs which yields the total atom number or equivalently the normalization of the state. Therefore, to probe all relevant operators of a general single-particle state with a single measurement setting, one needs a POVM with at least d^2 elements. If the POVM contains information about all $d^2 - 1$ operators it

is called informationally complete [126, 127]. If the state is pure, then only $2d$ elements are needed for informational completeness [35].

Thus, after measuring an ensemble of independent particles with this kind of POVM, one can estimate all parameters of the quantum state. In general, the precision of this estimation is not only given by the number of particles but also depends on the observable one attempts to estimate. Take as an example the implementation of the simultaneous readout of S_x and S_z discussed before. If one uses a different coupling to the $F = 2$ manifold, e.g. transferring a quarter of the population to $F = 2$, then the precision on the spin in x -direction will be better than on the one in z -direction.

That is why there exist a special type of informationally complete POVMs, the so-called symmetric informationally complete (SIC) POVMs [128]. These have exactly the minimal number of d^2 elements and the corresponding POVMs E_i have the same inner Hilbert-Schmidt product [129]

$$\text{tr} [\hat{E}_i \hat{E}_j] = \frac{1}{d+1}. \quad (6.2)$$

This means that the basis states $|\phi_i\rangle$ of the measurement operators, with $\hat{E}_i = |\phi_i\rangle\langle\phi_i|$, all have the same overlap

$$|\langle\phi_i|\phi_j\rangle|^2 = \frac{1}{d+1}. \quad (6.3)$$

This ensures that all observables are measured with the same precision. For a spin-1/2 system this graphically means that the measurement bases are along equiangular lines in the spin sphere.

6.2. Experimental implementation

As shown before, POVMs can be implemented by a readout in some higher dimensional manifold. Experimentally, we use the initially unoccupied magnetic substates of the $F = 2$ manifold as auxiliary modes to extend the dimension of the Hilbert space for the readout. Since our imaging is capable to selectively address each manifold, we can read out all populations in a single experimental realization and thereby increase the accessible information. Even without hyperfine selective imaging we would still be able to gain additional information by populating the magnetic substate $(2, \pm 2)$ where the different magnetic moment would lead to a selective imaging after Stern-Gerlach separation.

As a short note: Inserting the numbers for a spin-1 system with dimension $d = 3$, we would need 9 POVM elements for an informationally complete measurement of the single-particle state. Together with the magnetic substates in $F = 2$ we have in total only 8 levels for the readout. Therefore we cannot directly implement an informationally complete measurement by just using unitary transformation in the two hyperfine manifolds. To get simultaneous information about all spin-1 operators, one could, for example, couple a small fraction of the atoms from one magnetic substate in the $F = 1$ manifold to $F = 2$ and measure these atoms with a separate imaging pulse. Afterwards one uses all 8 magnetic substates to implement the remaining POVM elements. With the right unitaries one could then get an informationally complete measurement basis.

In order to experimentally implement arbitrary POVMs we need to have complete control over the measurement basis in both manifolds. It has been shown that this is achieved by mw coupling between the hyperfine manifolds and additionally the ability

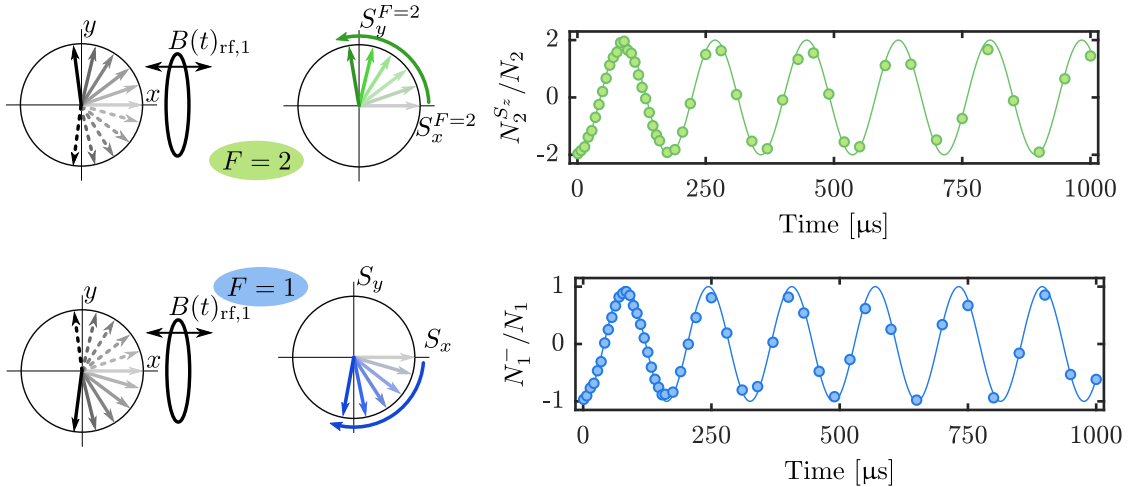


Figure 6.2.: Rabi oscillations with a single rf coil: A single rf coil generates a linearly oscillating field that can be decomposed into two counterrotating fields as indicated by the dashed and solid arrows. Since the sign of the g-factor is different in $F = 1$ and $F = 2$, the Larmor precession has a different orientation in each manifold. By using a single rf-coil for spin rotations the spin in each manifold couples to the component of the magnetic field that has the same orientation of rotation (solid arrow). Therefore after preparing an initial state within a 50/50 superposition of the state $(1, -1)$ and $(2, -2)$ one observes Rabi oscillations in both manifolds. For $F = 2$ we evaluated the atom number difference $N_2^{S_z} = 2N_{2,+2} + N_{2,+1} - N_{2,-1} - 2N_{2,-2}$, which corresponds to the z -projection in an spin-2 system.

to perform selective spin rotations within each manifold [130]. As an example, take the POVM elements in Eq. (6.1). For an implementation, we would need to perform a spin rotation in $F = 1$ without coupling the substates in $F = 2$.

6.2.1. Hyperfine selective spin rotations

In Sec: 3.4 we have already discussed that a single rf-coil can be used to induce spin rotations in both hyperfine manifolds. Because the absolute value of the first-order g-factors are nearly the same for both manifolds ($|g_{1,1}| \approx |g_{1,2}|$), the resonance frequency will at a typical magnetic field of 1 G only differ by about 2 kHz which is on the same order as our typical Rabi frequencies. Therefore, even if we tune the frequency of the rf-field into resonance with the $F = 1$ hyperfine manifold we will simultaneously off-resonantly couple the magnetic substates in the $F = 2$ manifold as shown in Fig. 6.2.

The g-factors of the two manifolds, however, have different sign. Thus, the Larmor precession has a different orientation in each manifold. But with a single rf-coil we can not exploit this difference because the linearly oscillating field, that is generated by the coil, can be decomposed into two counter-rotating magnetic fields. In each manifold the state couples then to the rotating field that corotates with the Larmor precession.

To exploit the different signs of the g-factors we combine the fields of two rf-coils to generate a rotation magnetic field. For that, we matched the individual Rabi frequencies, such that the oscillating magnetic fields have the same amplitude at the position of the atoms. We then tune the phase difference of the two oscillating fields to generate

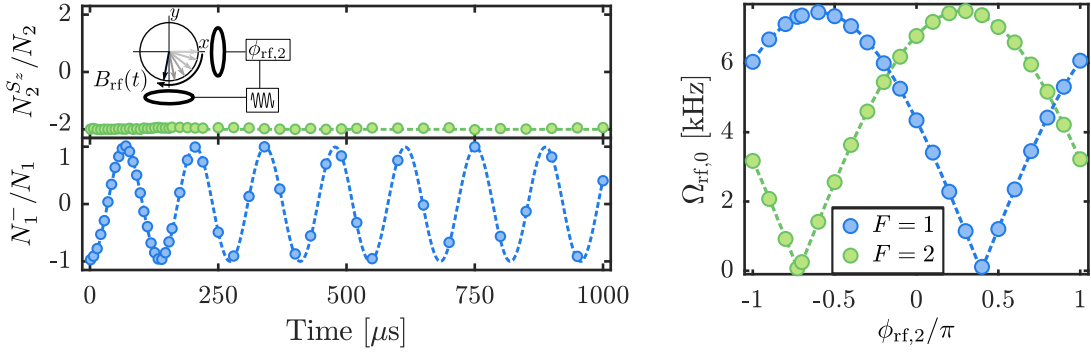


Figure 6.3.: **Selective spin rotations:** Using two rf coils one can generate a rotating magnetic field which selectively couples, for example, the magnetic substates of the $F = 1$ manifold as shown in the left plot. Experimentally we tune the phase difference $\Phi^- = (\phi_{\text{rf},1} - \phi_{\text{rf},2})/2$ by adjusting the phase of the second rf-coil $\phi_{\text{rf},2}$. We extract the Rabi frequency in both manifolds for different values of $\phi_{\text{rf},2}$ (right plot) and fit the resulting data according to Eq. (6.8) (dashed line). We find a nearly complete suppression of the coupling in $F = 1$ for $\phi_{\text{rf},2} = 0.40\pi$ and in $F = 2$ for $\phi_{\text{rf},2} = -0.72\pi$

a rotating field which will only couple the respective hyperfine manifold. If the two magnetic fields are in orthogonal direction they are described by the Hamiltonian

$$\hat{\mathcal{H}}_{\text{rf}}(t) = 2\hbar\Omega_{\text{rf},0} [\cos(|\omega_0|t + \phi_{\text{rf},1})\hat{S}_x + \cos(|\omega_0|t + \phi_{\text{rf},2})\hat{S}_y]. \quad (6.4)$$

Again, we write here just spin-1 operators, but the treatment is completely equivalent when exchanging these operators with the corresponding ones in $F = 2$. Analogously to Eq. (3.5) we transform into the rotating frame with the same orientation as the Larmor precession which yields

$$\begin{aligned} \hat{\mathcal{H}}_{\text{rf}}^{\text{rot}} = & 2\hbar\Omega_{\text{rf},0} \cos\left(\Phi^- \pm \frac{\pi}{4}\right) \\ & \left[\cos\left(\Phi^+ \mp \frac{\pi}{4}\right) \hat{S}_x \mp \sin\left(\Phi^+ \mp \frac{\pi}{4}\right) \hat{S}_y \right] \end{aligned} \quad (6.5)$$

for $\text{sgn}(g_{1,F}) = \pm 1$. Here, we defined the sum and difference phase of the two rf fields as $\Phi^+ = (\phi_{\text{rf},1} + \phi_{\text{rf},2})/2$ and $\Phi^- = (\phi_{\text{rf},1} - \phi_{\text{rf},2})/2$, respectively. Thus, the resonant Rabi frequency is modified when using two orthogonal coils and depends on the phase difference Φ^-

$$\Omega_2(\Phi^-) = 2\Omega_{\text{rf},0} \left| \cos\left(\Phi^- \pm \frac{\pi}{4}\right) \right| \quad (6.6)$$

Setting the phase difference to $\Phi_1^- = \pi/4$ and $\Phi_2^- = -\pi/4$ one selectively addresses the $F = 1$ and $F = 2$ manifold, respectively (see Fig. 6.3). This corresponds to left and right-handed rotating magnetic fields.

In addition, the two linearly oscillating magnetic fields do not have to be orthogonal to switch off the coupling in one manifold. Suppose the second rf coil produces a field along the direction $\cos(\theta)y + \sin(\theta)x$ instead of the y -direction, where θ denotes the deviation

angle. In this case, one obtains for the Hamiltonian

$$\hat{\mathcal{H}}_{\text{rf}}^{\text{rot}} = 2\hbar \Omega_{\text{rf},0} \cos\left(\Phi^- \mp \frac{\theta}{2} \pm \frac{\pi}{4}\right) \left[\cos\left(\Phi^+ \pm \frac{\theta}{2} \mp \frac{\pi}{4}\right) \hat{S}_x \mp \sin\left(\Phi^+ \pm \frac{\theta}{2} \mp \frac{\pi}{4}\right) \hat{S}_y \right]. \quad (6.7)$$

Thus for non-orthogonal fields the resonant Rabi frequency is given by

$$\Omega_2(\Phi^-, \theta) = 2\Omega_{\text{rf},0} \left| \cos\left(\Phi^- \mp \frac{\theta}{2} \pm \frac{\pi}{4}\right) \right| \quad (6.8)$$

Therefore, even for nonorthogonal fields it is possible to selectively address a single hyperfine manifold. For example, to selectively couple the $F = 1$ manifold one sets $\Phi_1^- = \pi/4 + \theta/2$. However, compared to the situation, where both rf fields are orthogonal, the Rabi frequency in $F = 1$ is reduced by a factor $\cos(\theta) \leq 1$.

One can think of this in the following way: A linearly oscillating field can always be decomposed into two counterrotating fields. Thus, even for non-orthogonal linear fields, one can find a setting of their relative phase, such that one orientation of the rotating fields is out of phase by 180° and is therefore canceled. For orthogonal fields, this corresponds to the setting where the other orientation is in phase such that the two corotating fields add up. But for non-orthogonal fields, they are not perfectly in phase and, thus, the Rabi frequency is reduced.

On the experimental side, this means that the exact alignment of the two rf-coils is not critical to induce hyperfine selective spin rotations. In our experiment we also find that the two linear magnetic fields are not perfectly orthogonal but deviate by an angle of $\theta = 10^\circ$. This is bigger than the geometric misalignment of the two coils and stems from field inhomogeneities.

6.2.2. Phase imprints

To control the measurement basis we additionally use mw pulses to imprint arbitrary phases on the magnetic substates. For this we exploit that, using the I/Q mixer, we can control the phase of the mw pulses by tuning the phase of the two rf-fields that are mixed with the mw field. For example, to change the phase of the state $(1, 0)$, we employ two mw π -pulses coupling the states $(1, 0) \leftrightarrow (2, 0)$ with a relative phase difference of ϕ_{mw} . Such a sequence does not change the population of the state but will imprint the relative phase ϕ_{mw} on the state $(1, 0)$ and will thereby advance the spinor phase by $\phi'_S = \phi_S + \phi_{\text{mw}}$.

Since the mapping of the transversal spin direction for the readout is already determined by the phase of the rf pulse we do not need to control the Larmor phase of the state with this method. Thus, we use this phase imprint here only to tune the spinor phase. This technique is an alternative to the dynamical phase imprint via the second-order Zeeman shift and has the advantage that it is much faster than the dynamical imprint, which helps to reduce technical fluctuations on the final readout.

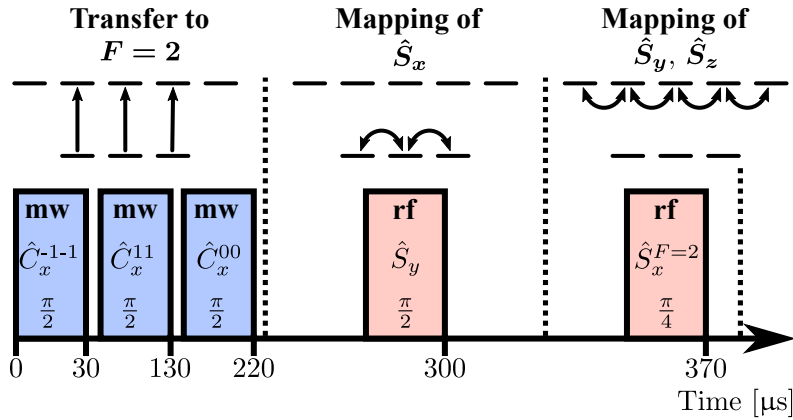


Figure 6.4.: **Readout sequence for the simultaneous readout of all three spin directions:** The upper row depicts the coupling between the two hyperfine manifolds while the lower boxes contain the rotation operators together with the employed rotation angle. In our experiment the whole sequence takes about 370 μs .

6.3. Simultaneous readout of all spin directions

A simultaneous readout of multiple observables is especially advantageous in situations where one parameter, for example the Larmor phase, cannot be experimentally controlled. This can either be fundamental for example in the case of spontaneous symmetry breaking or due to some experimental imperfection. In these cases it is not possible to prepare exactly the same state in each realization to analyze correlations between the different spin-1 observables.

In general, one can think of many alternative sequences to set a specific readout basis, which enables the simultaneous extraction of the desired observables. In the following, we will present two different techniques to read out all three spin-directions in a single experimental realization. With this, each realization can be plotted as a point on a spin sphere providing an illustrative representation of the generated state.

The first readout sequence is sketched in Fig. 6.4. We first use three mw $\pi/2$ -pulses coupling the states $(1, k) \leftrightarrow (2, k)$ with $k \in \{0, \pm 1\}$. This splits the state between the $F = 1$ and $F = 2$ manifold. A selective $\pi/2$ spin rotation in $F = 1$ around the S_y axis maps the spin observable \hat{S}_x onto the population difference of $(1, \pm 1)$. We then use a $\pi/4$ spin-rotation around the S_x axis in $F = 2$ to map the observables \hat{S}_y as well as \hat{S}_z onto the populations in $F = 2$. This is possible because the rotation in the $F = 2$ manifold couples more magnetic substates. This provides access to additional spin-1 observables.

The total unitary operator that describes this readout sequence is given by

$$\hat{U} = e^{-i\frac{\pi}{4}\hat{C}_x^{F=2}} \cdot e^{i\frac{\pi}{2}\hat{S}_y} \cdot e^{-i\frac{\pi}{2}\hat{C}_y^{00}} \cdot e^{-i\frac{\pi}{2}\hat{C}_y^{+1+1}} \cdot e^{-i\frac{\pi}{2}\hat{C}_y^{-1-1}}. \quad (6.9)$$

Expressing the final projective measurement in the $F = 1$ and $F = 2$ manifolds in terms of the original spin-1 operators yields the following POVM elements:

$$\begin{aligned}
 \hat{N}'_{1,-1} &= \frac{1}{6}\hat{N} - \frac{1}{4}\hat{\mathcal{S}}_x + \frac{1}{8}\hat{V}_x - \frac{1}{16}\hat{Q}_{zz} + \hat{f}_0 \\
 \hat{N}'_{1,0} &= \frac{1}{6}\hat{N} - \frac{1}{4}\hat{V}_x + \frac{1}{8}\hat{Q}_{zz} + \hat{f}_1 \\
 \hat{N}'_{1,+1} &= \frac{1}{6}\hat{N} + \frac{1}{4}\hat{\mathcal{S}}_x + \frac{1}{8}\hat{V}_x - \frac{1}{16}\hat{Q}_{zz} + \hat{f}_2 \\
 \hline
 \hat{N}'_{2,+2} &= \frac{5}{64}\hat{N} + \frac{1}{16}\sqrt{\frac{3}{2}}\hat{\mathcal{S}}_y + \frac{1}{8\sqrt{2}}\hat{\mathcal{S}}_z + \frac{\sqrt{3}}{32}\hat{Q}_{yz} - \frac{1}{32}\hat{V}_x + \frac{3}{128}\hat{Q}_{zz} + \hat{f}_3 \\
 \hat{N}'_{2,+1} &= \frac{5}{48}\hat{N} + \frac{1}{8}\sqrt{\frac{3}{2}}\hat{\mathcal{S}}_y - \frac{1}{16}\hat{V}_x - \frac{1}{16}\hat{Q}_{zz} + \hat{f}_4 \\
 \hat{N}'_{2,0} &= \frac{13}{96}\hat{N} - \frac{\sqrt{3}}{16}\hat{Q}_{yz} + \frac{3}{16}\hat{V}_x + \frac{5}{64}\hat{Q}_{zz} + \hat{f}_5 \\
 \hat{N}'_{2,-1} &= \frac{5}{48}\hat{N} - \frac{1}{8}\sqrt{\frac{3}{2}}\hat{\mathcal{S}}_y - \frac{1}{16}\hat{V}_x - \frac{1}{16}\hat{Q}_{zz} + \hat{f}_6 \\
 \hat{N}'_{2,-2} &= \frac{5}{64}\hat{N} - \frac{1}{16}\sqrt{\frac{3}{2}}\hat{\mathcal{S}}_y - \frac{1}{8\sqrt{2}}\hat{\mathcal{S}}_z + \frac{\sqrt{3}}{32}\hat{Q}_{yz} - \frac{1}{32}\hat{V}_x + \frac{3}{128}\hat{Q}_{zz} + \hat{f}_7,
 \end{aligned} \tag{6.10}$$

where $\hat{N}'_{F,m_F} = U^\dagger \hat{N}_{F,m_F} U$. The relevant spin observables, which we aim to extract, are highlighted in red. Here, \hat{f}_i summarize all operators that contain $\hat{a}_{2,j}$ ($\hat{a}_{2,j}^\dagger$) in linear and second order. Thus the operators \hat{f}_i contain the contributions from the initially unoccupied $F = 2$ manifold. The observables of interest are obtained via a linear combination of the different \hat{N}_{F,m_F} . For example, \hat{S}_x is extracted via $2(\hat{N}_{1,+1} - \hat{N}_{1,-1}) = \hat{S}_x + 2(\hat{f}_2 - \hat{f}_0)$.

Strictly speaking, the measurement operators in Eq. (6.10) form no POVM because they contain the additional operators \hat{f}_j and are orthogonal. This is not surprising since these measurement operators correspond after all to a projective measurement in a higher dimensional Hilbert space. Because the magnetic substates in $F = 2$ are initially unoccupied the mean $\langle \hat{f}_i \rangle_Q$ vanishes and thus the expectation values of these measurement operators corresponds to the one of the respective POVM. Thus, we can estimate the mean of S_x by evaluating the measured population difference $2(N_{1,+1} - N_{1,-1})$. In this sense, one calls the readout sequence presented here an implementation of POVM but in a strict sense there exists nor direct experimental implementation of a POVM. This part is often neglected in the discussion of POVMs, since they are mostly described in the context of single-particle states, where one is just interested in the mean of the observables. However, the terms \hat{f}_j will become important later when analyzing higher moments of the spin observables for the analysis of many-body states.

6.3.1. Spin wave

To demonstrate the capabilities of this scheme to spatially resolve a complex spin structure we prepare a spin wave in a spatially extended BEC. After evaporation we load the BEC of $\approx 40,000$ atoms into the elongated waveguide potential with trapping frequencies $(\omega_\parallel, \omega_\perp) = 2\pi \cdot (2.3, 170)$ Hz. In this trapping configuration the atomic cloud has a spatial extension on the order of ~ 300 μm . Initially, all atoms occupy the state $(1, -1)$.

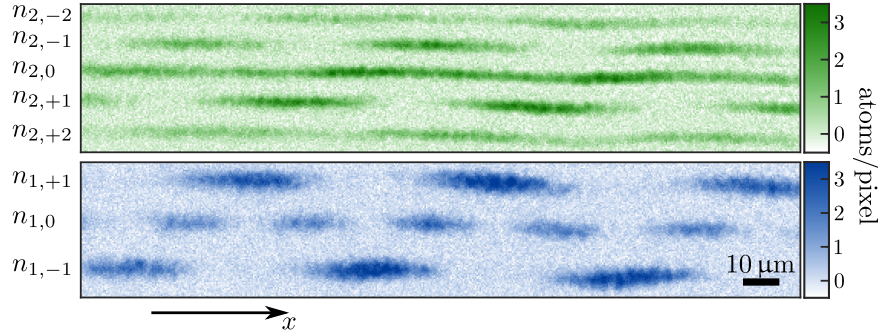


Figure 6.5.: Absorption image of the atomic densities measured in the two hyperfine manifolds: From the measured densities in the $F = 1$ manifold (blue) we extract the spin observable S_x . The other two spin directions are encoded in the densities of the $F = 2$ manifold.

An rf $\pi/2$ rotation around S_y then rotates the initial spin in z -direction into a spatially homogeneous spin with $S_x(y)/n(y) = -1$. We subsequently apply a constant current through rf coil (1) to generate a magnetic field gradient along the longitudinal direction of the cloud with $\partial B_z / \partial y \approx 0.2 \mu\text{G}/\mu\text{m}$. This leads to a spatially varying evolution of the Larmor phase. We employ this gradient for about 100 ms and with that generate a spin wave with the spin vector rotating in the S_\perp plane of the spin sphere. In a last step we use another rf pulse to tilt the spin wave out of the S_\perp plane by an angle of $\pi/4$. With this sequence we generate a spin wave involving all three spin directions. This spin wave corresponds to a classical coherent state such that the mean spin values are sufficient to fully describe the state and additional noise contributions due to the coupling to empty modes can be neglected.

After this preparation we employ the readout sequence detailed above to extract all three spin directions in a single experimental realization. The resulting absorption image after Stern-Gerlach separation is shown in Fig. 6.5. The local value of the three spin directions is then extracted from the measured atom numbers via

$$\begin{aligned} n_1^{S_x}(y) &= n_{1,+1}(y) - n_{1,-1}(y) \\ n_2^{S_y}(y) &= \frac{4}{\sqrt{6}} (n_{2,+1}(y) - n_{2,-1}(y)) \\ n_2^{S_z}(y) &= \sqrt{2} [2n_{2,+2}(y) - n_{2,+1}(y) \\ &\quad + n_{2,-1}(y) - 2n_{2,-2}(y)], \end{aligned} \tag{6.11}$$

where $n_{F,m}(y)$ is the local atom number in the evaluation interval of $\delta y \approx 5 \mu\text{m}$ in the state (F, m_F) . On the left hand side we introduced the notation $n_F^{S_i}$ where the subscript reminds us, in which hyperfine manifold the linear combination is read out and the superscript S_i encodes the spin direction that is contained in this combination of atom numbers. We use this notation to keep in mind that we are “only” evaluating combinations of the measured atom numbers which comprises information about the specific spin direction of the state. By normalizing these linear combination to the local atom number in the respective manifold we can estimate $\langle n_F^{S_i}(y)/n_F(y) \rangle = \langle \hat{S}_i(y)/\hat{n}(y) \rangle_Q$. Note that the combinations $n_F^{S_i}$ correspond to the local operators $\hat{S}_i/2$. But, since we normalize them to the atom numbers in the respective manifold with $n_F = n/2$, the factor of 2 cancels. This normalization has

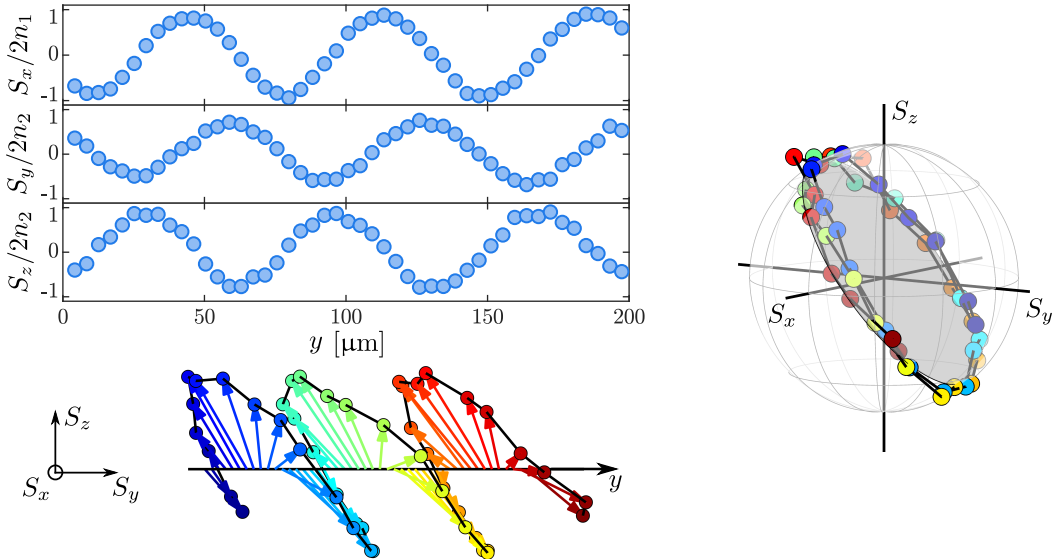


Figure 6.6.: Spin wave evaluation: From the measured densities as shown in Fig. 6.5 we estimate the value of the three spin directions according to Eq. (6.11). We find for all three spin directions an oscillatory behavior as expected for the prepared spin wave. Plotting the spin values as a three dimensional vector for each evaluation interval y we recover the generated spin wave. Alternatively, we can plot these vectors inside a spin sphere, where we neglect the spatial coordinate. From this plot we can directly infer the orientation of the spin wave as indicated by the gray plane.

the advantage that it also gives the correct result for different splitting ratios between the two manifolds.

Here, we use in each evaluation region about 700 particles to estimate the mean of the corresponding observable. The result is shown in Fig. 6.6. From this measurement we are able to reconstruct the three dimensional spin vector in each evaluation interval and the result is consistent with the initially generated spin wave.

6.3.2. Readout with conventional projective measurements

We have shown that using our new readout technique it is possible to extract all three spin directions and with that resolve the structure of the prepared spin wave. The question is whether we could have achieved the same result by using three measurements employing a standard projective measurement sequence. By setting in each realization a different readout basis one could also extract all three spin observables. However, since the preparation of the spin wave takes about 100 ms after the first rf pulse, the Larmor phase is completely randomized after this time due to magnetic field fluctuations. That means that the spatial pattern as observed in Fig. 6.5 would be randomly shifted in each realization. Therefore, it is impossible to extract the correlations between the observables with the standard readout technique, even though the state we analyze is merely a single-particle state. As seen before, 100 ms is about the minimal time scale for spin-mixing dynamics. Thus, our readout makes it possible to analyze correlations between orthogonal spin directions that arise during such interactions even after long evolution times which has been studied in [22, 131].

6.3.3. Calibration of the readout

In order to read out the observable S_x in $F = 1$ and S_y in $F = 2$ the relative phases of the mw and rf pulses have to be controlled. As explained before, the rf phase determines which transversal spin projection in the S_\perp -plane is read out. To be a bit more precise it is the difference between the Larmor phase of the state in the respective hyperfine manifold $\phi_L^{F=1,2}$ and the corresponding rf phase $\phi_{\text{rf}}^{F=1,2}$, which determines the observable $S_\perp(\phi_L^F - \phi_{\text{rf}}^F)$. In principle the first rf pulse for the preparation of the spin wave sets the phase reference for the subsequent rf pulses. However, this initial phase is randomized due to magnetic field fluctuations. We therefore define for the first readout pulse $\phi_L^{F=1} - \phi_{\text{rf}}^{F=1} = 0$ and per definition we get

$$n_1^{S_x}(y) = n_{1,+1}(y) - n_{1,-1}(y). \quad (6.12)$$

The spin direction that is read out in $F = 2$ consequently depends on the phase difference $\Delta\phi_L = \phi_L^{F=1} - \phi_L^{F=2}$ of the states as well as the phase difference of the two rf pulses $\Delta\phi_{\text{rf}} = \phi_{\text{rf}}^{F=1} - \phi_{\text{rf}}^{F=2}$.

The Larmor phase difference between the states in $F = 1$ and $F = 2$ evolves dynamically with the first-order Zeeman effect $\Delta\phi_L(t_L) = (g_{1,1} - g_{1,2})B/h \cdot t_L \approx 2g_{1,1}B/h \cdot t_L$, where t_L denotes the time between the mw pulses and the final rf readout pulse in $F = 2$. Additionally, we can experimentally imprint a phase difference by changing the relative phases of the mw pulses that couple the two hyperfine manifolds. As usual, the first mw pulse acts as a phase reference for all subsequent pulses. In our case, the first mw pulse couples the states $(1, -1) \leftrightarrow (2, -1)$. By changing the relative phase $\phi_{L,\text{mw}}$ between this pulse and the one coupling the state $(1, 1) \leftrightarrow (2, 1)$ this phase is imprinted as an additional phase difference between the two states, i.e. $\Delta\phi_L = \phi_{L,\text{mw}}$.

Experimentally the time $t_L \approx 200 \mu\text{s}$ is fixed by the length of the mw pulses. At this time scale the effect of magnetic field fluctuations are negligible. We then could control the observable that is read out in $F = 2$ either by tuning the phase difference of the mw pulses $\phi_{L,\text{mw}}$ or alternatively of the rf pulses $\Delta\phi_{\text{rf}}$. In our case, we use the rf phase $\phi_{\text{rf}}^{F=2}$ of the second rf pulse as a control parameter.

While the rf-phase determines the spin direction that is read out in the S_\perp plane, the final readout also depends on the spinor phase $\phi_S^{F=2}$. As explained before a change of the spinor phase by $\pi/2$ would alter the readout from S_\perp to Q_\perp . Similar to the Larmor phase we can control this by tuning the relative phase between the pulses coupling $(1, \pm 1) \leftrightarrow (2, \pm 1)$ and $(1, 0) \leftrightarrow (2, 0)$, i.e. $\Delta\phi_S^{F=2} = \phi_{\text{mw}}^{00} - (\phi_{\text{mw}}^{11} + \phi_{\text{mw}}^{-1-1})/2$ which is analogous to the definition of the spinor phase. Experimentally, we keep the phases ϕ_{mw}^{11} and ϕ_{mw}^{-1-1} fixed and control the spinor phase via the phase ϕ_{mw}^{00} .

To ensure that we read out the correct observables in the experiment we use a calibration measurement to determine the two phases ϕ_{mw}^{00} and $\phi_{\text{rf}}^{F=2}$ such that we extract the observable S_y from the measured densities in $F = 2$. This is done via two measurement involving two types of spin waves. For the first measurement, we prepare a spin wave in the S_\perp -plane as described before omitting the last tilting pulse. For the second measurement we prepare a spin wave in plane parallel to the S_\perp -plane with a finite value of $S_z/N = 0.9$. This is done by using a shorter rf pulse at the beginning of the spin-wave preparation.

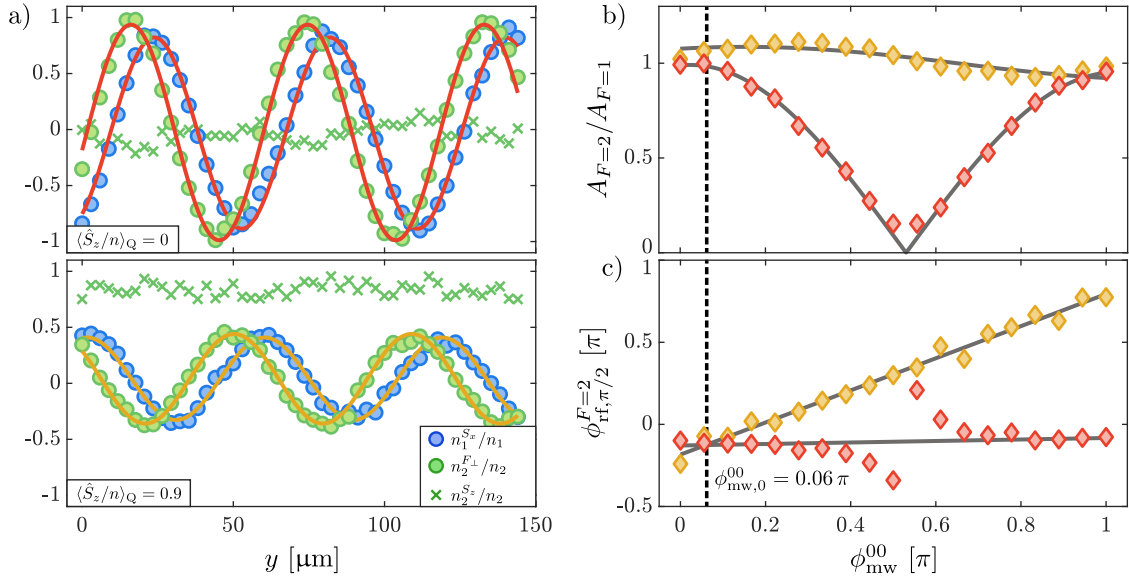


Figure 6.7.: Calibration of spin readout: a) For the calibration we prepare two spin waves with constant $\langle n_2^{S_z} / n_2 \rangle = 0$ (upper panel) and $\langle n_2^{S_z} / n_2 \rangle = 0.9$ (lower panel). We fit the signal extracted from a single absorption image in $F = 1$ (blue symbols) and $F = 2$ (green symbols) with a sine to extract their relative spatial phases and amplitudes A_F . b) We plot the extracted of the amplitude ratios as a function of ϕ_{mw}^{00} . For the spin wave with $\langle n_2^{S_z} / n_2 \rangle = 0$ we can extract $\phi_{mw,0}^{00}$ from the point where the amplitude ratio is 1. c) Repeating the measurement for fixed ϕ_{mw}^{00} and varying $\phi_{rf}^{F=2}$ we extract the value $\phi_{rf,\pi/2}^{F=2}$ at which the two signals have a relative spatial phase shift of $\pi/2$. While for the spin wave, with $\langle S_z \rangle = 0$, this value is constant, for the second spin wave, it depends linearly on ϕ_{mw}^{00} . Applying a linear fit to both results (gray solid lines) yields the value of $\phi_{mw,0}^{00} = 0.06\pi$ at the crossing point. This provides a stronger constraint on this parameter than the method used in b).

In each measurement, we employ the readout sequence detailed above and record the population differences

$$\begin{aligned} n_1^{S_x}(y) &= n_{1,+1}(y) - n_{1,-1}(y) \\ n_2^{F_\perp}(y) &= \frac{4}{\sqrt{6}} (n_{2,+1}(y) - n_{2,-1}(y)) \\ n_2^{S_z}(y) &= \sqrt{2} [2n_{2,+2}(y) - n_{2,+1}(y) \\ &\quad + n_{2,-1}(y) - 2n_{2,-2}(y)]. \end{aligned} \tag{6.13}$$

The goal of the calibration is that $n_2^{F_\perp}$ contains information about the spin observable S_y , i.e. that we tune ϕ_{mw}^{00} and $\phi_{\text{rf},2}$ such that $F_\perp(\phi_{\text{mw}}^{00}, \phi_{\text{rf}}^{F=2}) = S_y$, where F_\perp is defined as in Eq. (5.19).

We start the discussion with the spin wave prepared in the S_\perp -plane. After the preparation we systematically tune the two phases ϕ_{mw}^{00} and $\phi_{\text{rf}}^{F=2}$. For an exemplary plot of the experimental signal see upper panel of Fig. 6.7a). As expected for the preparation sequence we measure for S_z a constant value with $\langle n_2^{S_z} / n_2 \rangle \approx 0$. $n_1^{S_x}(y)$ as well as $n_2^{F_\perp}(y)$ are oscillating as a function of the position y . Both signals are fitted with a sine function to extract their amplitudes $A_{F=1/2}$ and relative phases. Varying the rf phase $\phi_{\text{rf}}^{F=2}$ shifts the spatial phase between the two signals. From this we extract the rf phase $\phi_{\text{rf},\pi/2}^{F=2}$ at which the two signals have a spatial phase difference of $\pi/2$. If the spinor phase were correctly adjusted, this would correspond to measuring two orthogonal spin directions in $F = 1$ and $F = 2$ and we could identify $F_\perp = S_y$.

However, as explained before, changing the phase of the mw pulse ϕ_{mw}^{00} will change the spinor phase $\phi_S^{F=2}$ of the state in $F = 2$. This will change the readout in this manifold from a spin observable \hat{S}_\perp to a quadrupole operator in the \hat{Q}_\perp plane. Since for the prepared spin wave the mean of these quadrupole operators is zero, a change of the mw phase will influence the amplitude of the signal in $F = 2$ according to $A_{F=2} = |\cos(\phi_{\text{mw}}^{00} - \phi_{\text{mw},0}^{00})|$. This is shown in Fig. 6.7b). Thus, by scanning the phase of the mw and recording the amplitude, we can extract the phase $\phi_{\text{mw},0}^{00}$ at which the amplitude is 1 and we therefore measure a spin operator in $F = 2$. In our case, we find a value of $\phi_{\text{mw},0}^{00} = 0.06\pi$.

As a consistency check we analyze the second spin wave where we find $\langle n_2^{S_z} / n_2 \rangle = 0.9$ as expected from the preparation sequence (see lower panel of Fig. 6.7). Again we find an oscillating signal for $n_1^{S_x}(y)$ and $n_2^{F_\perp}(y)$ but with a lower amplitude corresponding to a finite value of S_z . Again, we fit both signals to extract the amplitude and relative phase of both oscillations. By scanning the phase of the rf pulse we extract $\phi_{\text{rf},\pi/2}^{F=2}$ for each setting of the mw phase. For this spin wave, however, the mean of the quadrupole operators is not zero but $\langle \hat{S}_\perp(\phi_L) \rangle_Q \approx \langle \hat{Q}_\perp(\phi_L + \pi/2) \rangle_Q$ (see Theory 2.1.5). Therefore, scanning the phase of the mw pulse will not change the amplitude as before (see Fig. 6.7b)) but the phase $\phi_{\text{rf},\pi/2}^{F=2}$. In this setting, the phase $\phi_{\text{rf},\pi/2}^{F=2}$ depends linearly on ϕ_{mw}^{00} as shown in Fig. 6.7c). From this signal we extract $\phi_{\text{mw},0}^{00}$ from the point at which $\phi_{\text{rf},\pi/2}^{F=2}$ has the same value as in the measurement of the other spin wave. Because of the linear dependence this puts a tighter constraint on $\phi_{\text{mw},0}^{00}$ and we consistently find a value $\phi_{\text{mw},0}^{00} = 0.06\pi$.

Using these two kind of spin waves for calibration has an additional advantage. If one just uses a single spin wave with $\langle S_z \rangle = 0$ care has to be taken that it has full spin length, i.e. $\langle \hat{S}_{\perp,\max} \rangle_Q = 1$. Since the evolution under the magnetic field gradient takes about 100 ms, the spinor phase will also dynamically evolve. Thus, one has to adjust the timings such that the final state has a transversal spin length of 1. If, however, the spin

length is reduced, i.e. $A_{F=1} < 1$, then the condition $A_{F=1} = A_{F=2}$ is ambiguous and one needs the second kind of spin wave to find the correct setting of the mw phase.

6.3.4. Technical error contributions to this readout

In the following, we will go into more detail discussing the effect of technical fluctuations on this specific readout scheme. Within the calibration measurement we find two main contributions that influence the readout: the length of the rf-pulse, or more precisely its deviation from a $\pi/4$ pulse, and residual couplings of the selective $F = 1$ rf pulses to the $F = 2$ manifold. For the calibration measurement these contributions do not influence the extraction of the correct phase settings, but it is important to understand their effect if one wants to use this readout sequence for precision measurements. We will discuss the effect of these misalignments for the spin wave with finite $\langle \hat{S}_z/n \rangle_Q \approx 0.9$.

From the preparation sequence we would expect to find a spatially constant value of $\langle n_2^{S_z}/n_2 \rangle = 0.88$ irrespective of the mw and rf phase. Experimentally, however, we observe that this value is not constant but instead depends on the rf phase $\phi_{\text{rf}}^{F=2}$ as shown in Fig. 6.8a) for two examples of the rf phase. Similarly, we expect for the prepared spin wave that the spatial variation of $n_2^{F_\perp}/n_2$ is centered around 0. Thus, averaging this signal over the spatial extension of the condensate and over many experimental realization we should obtain a mean value of $\langle n_2^{F_\perp}/n_2 \rangle = 0$. Experimentally, we find that the center of this spatial oscillation also shifts as we vary $\phi_{\text{rf}}^{F=2}$ (see Fig. 6.8a)). Thus, the average $\langle n_2^{F_\perp}/n_2 \rangle$ also depends on the phase of the second rf pulse. Both effects do not depend on the phase of the mw pulse.

To analyze this further we extract the mean of $\langle n_2^{S_z}/n_2 \rangle$ and $\langle n_2^{F_\perp}/n_2 \rangle$ as a function of $\phi_{\text{rf}}^{F=2}$ which is plotted in Fig. 6.8b). Both signals resemble an oscillatory behavior as a function of $\phi_{\text{rf}}^{F=2}$ where we sampled half of the period. Thus, we fit both curves with a sine function to extract the offset and the amplitude of this oscillation. Using a numerical simulation we find that the offset and amplitude have two different origins which will be presented in the following.

As a source for the offset we identify a wrong pulse time for the final rf pulse. For the $\pi/4$ -rotation we use a pulse with a time of $t_{\text{rf}} = 17.25 \mu\text{s}$ which corresponds to an assumed resonant Rabi frequency of $\Omega_{\text{rf},0} = 2\pi \cdot 7.25 \text{ kHz}$. However, we theoretically find that the measured offset depends linearly on the true Rabi frequency and our experimental results are consistent with a Rabi frequency of $\Omega_{\text{rf}} = 2\pi \cdot 7.51 \text{ kHz}$ (see Fig. 6.8c)). Thus, the assumed Rabi frequency or more precisely the pulse time is wrong by about 4% leading to a shift of the measured $\langle n_2^{S_z}/n_2 \rangle_{\text{rf}}$ and $\langle n_2^{F_\perp}/n_2 \rangle_{\text{rf}}$ by 0.07 compared to the true value. Because of this linear dependence the readout of S_z and F_\perp is very sensitive on the correct setting of the pulse length .

As a reason for the oscillatory behavior we identify a small residual coupling in $F = 2$ of the first rf-pulse which should be selective to the $F = 1$ manifold. Via a numerical simulation, as shown in Fig. 6.8c) we find that the experimental results are consistent with a suppression of the Rabi coupling in $F = 2$ by a factor of $\gamma \approx 0.036$ corresponding to a residual Rabi frequency of $\gamma\Omega_{\text{rf}} = 2\pi \cdot 270 \text{ Hz}$. Since the rf frequency has been set to resonance with $F = 1$, the Rabi is additionally detuned by $2\pi \cdot 1.77 \text{ kHz}$. Because of this, the population transfer in $F = 2$ for a pulse time of $34.5 \mu\text{s}$ is negligible and amounts to less than 0.3%. With the final rf-pulse, however, this small population gets mixed with a macroscopic population of the other magnetic substates leading to interference which results in a measurable signal. That is the reason why this signal depends on the phase

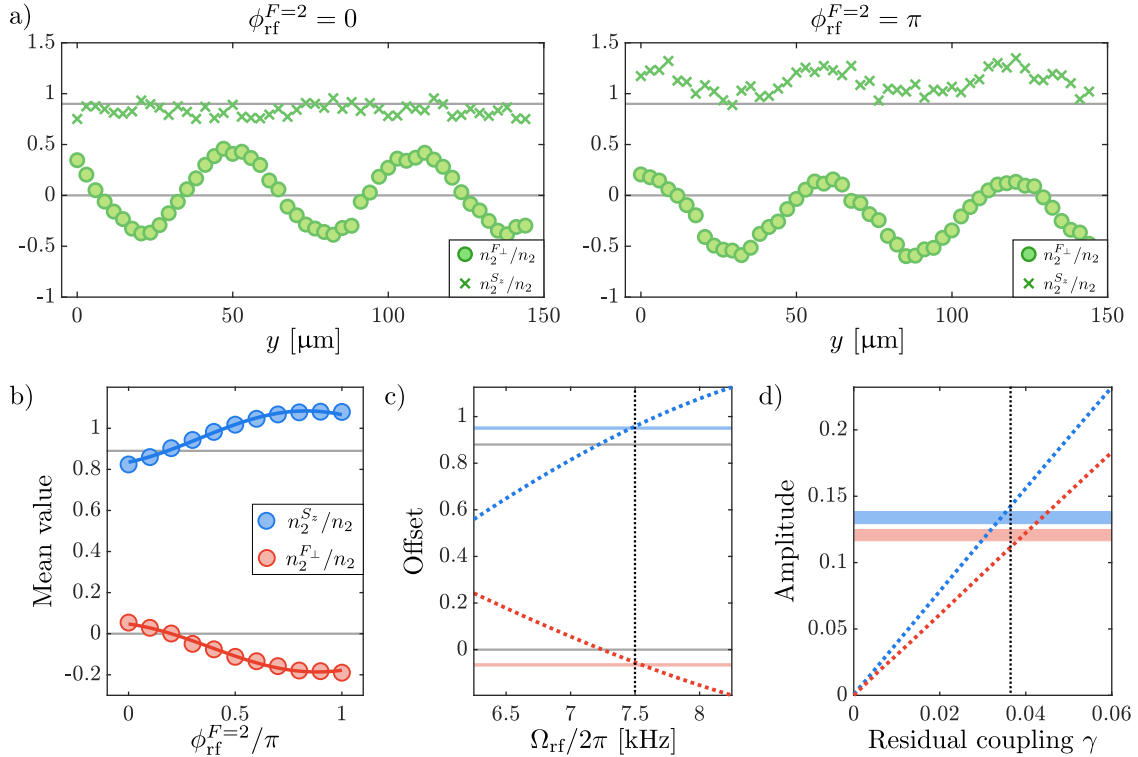


Figure 6.8.: Effects of residual coupling and wrong pulse times: a) For the spin wave with finite $\langle \hat{S}_z/n \rangle_Q \approx 0.9$ we find that the measured value of $\langle n_2^{S_z}/n_2 \rangle$ depends on the phase of the second rf pulse, which is shown here for the two phase settings $\phi_{\text{rf}}^{F=2} = 0$ (left) and $\phi_{\text{rf}}^{F=2} = \pi$ (right). Additionally the center of the spatial oscillation of $n_2^{F_{\perp}}/n_2$ shifts as we vary $\phi_{\text{rf}}^{F=2}$. Experimentally, we find no dependence on the phase of the mw pulse. The gray lines indicate the mean values that are expected from the preparation sequence. b) To analyze this effect we extract the mean of $\langle n_2^{S_z}/n_2 \rangle$ (blue points) and $\langle n_2^{F_{\perp}}/n_2 \rangle$ (red points) as a function of $\phi_{\text{rf}}^{F=2}$. The two values have been averaged over the spatial extension of the condensate as well as over many experimental realizations. We find for both signals an oscillatory behavior and fit both curves with a sine function (solid lines) to extract the offset and amplitude of this oscillation. The gray lines correspond again to the expectation of the preparation sequence. c) As the reason for the offset we identify a wrong calibration of the final rf pulse. For the $\pi/4$ spin rotation we have used a pulse duration of $t_{\text{rf}} = 34.5 \mu\text{s}$ assuming a resonant Rabi frequency of $\Omega_{\text{rf},0} = 2\pi \cdot 7.25 \text{ kHz}$. Using a numerical simulation, we study the offset of the two signals as a function of the Rabi frequency assuming a fixed pulse time of $t_{\text{rf}} = 34.5 \mu\text{s}$ (blue and red dashed lines). Comparing the simulation with the values extracted from the fit in b) (light blue and red lines), we find that the experimental values are consistent with a true Rabi frequency of about $\approx 7.5 \text{ kHz}$ as indicated by the dashed line. Thus, the time of the employed rf pulse is wrong by about 4%. d) For the amplitude of the signal in b) we identify a residual coupling γ of the first rf pulse in $F = 1$ to the $F = 2$ manifold. The results of the simulations are again shown as dashed lines while the extracted values from b) are shown as solid lines, where the width indicates the 1 standard deviation interval of the fit. Comparing the prediction with the experimental data we find a suppression of the Rabi frequency in the $F = 2$ manifold by a factor of $\gamma \approx 0.036$ corresponding to a residual Rabi frequency of $\gamma \Omega_{\text{rf}} = 2\pi \cdot 270 \text{ Hz}$.

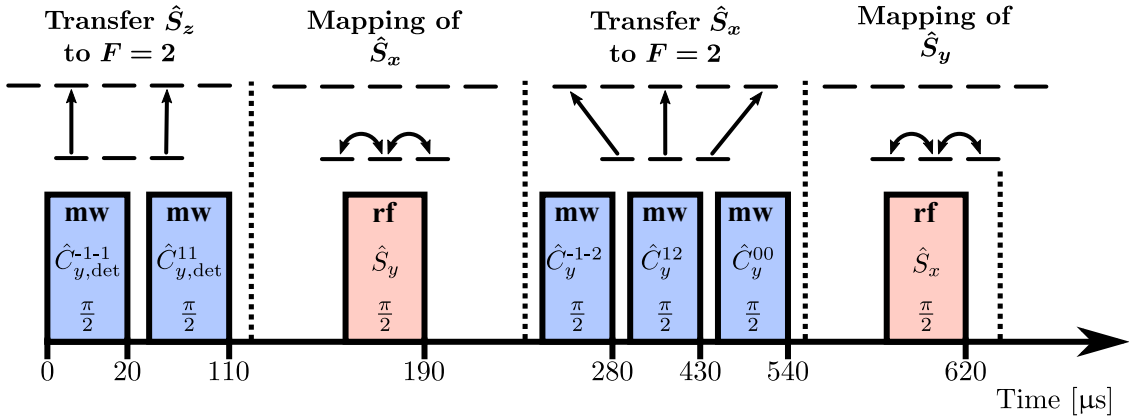


Figure 6.9.: Alternative sequence for the simultaneous readout of all three spin directions.

of the second rf-pulse since this alters the interference from constructive to destructive. Since the transferred population is so small, a residual coupling in $F = 1$ during the final rf pulse in $F = 2$ is negligible.

6.4. Alternative readout sequence

As explained before, employing an rf pulse in $F = 2$ for the readout, requires controlling the phase of the rf- as well as the mw-pulses. This is a big advantage in cases where one wants to read out the observable in $F = 2$ at different spinor phases, because one just needs to change the phase of the respective coupling pulse. This is typically much faster than other phase imprint methods and therefore shortens the whole readout sequence which is beneficial in terms of technical fluctuations. But in certain situations controlling the phases of all the pulses can also be a source of technical noise and as we have seen such a readout is also sensitive to misalignments of the rf pulse. Thus, we present here a different readout sequence to extract all spin directions, where we restrict the rf-rotations to the $F = 1$ manifold making the phase control of the mw-pulses obsolete.

This readout sequence is sketched in Fig. 6.9. We first use two mw $\pi/2$ pulses coupling the states $(1, \pm 1) \leftrightarrow (2, \pm 1)$ which have been detuned from resonance by the Rabi frequency. A $\pi/2$ rotation then transfers a quarter of the population in the corresponding magnetic substates to the $F = 2$ manifold. With this we encode the information about the observable \hat{S}_z into these states. Next, we employ a $\pi/2$ spin-rotation in $F = 1$ around S_y to map the spin \hat{S}_x onto the population difference of $(1, \pm 1)$. We subsequently transfer half of the population to the $F = 2$ manifold using three mw pulses coupling the states $(1, 0) \leftrightarrow (2, 0)$ and $(1, \pm 1) \leftrightarrow (1, \pm 2)$, which additionally stores this spin information in $F = 2$. A final $\pi/2$ -spin rotation in $F = 1$ around S_x maps the third spin observable \hat{S}_y onto the population difference there. By adjusting the length of the mw pulses one can adjust how many atoms are used for the estimation of the respective spin observables.

With this sequence we extract all three spin observables via

$$\begin{aligned} n_2^{S_x}(y) &= -\frac{4}{\sqrt{3}}[n_{2,+2}(y) - n_{2,-2}(y)] \\ n_1^{S_y}(y) &= \frac{4}{\sqrt{3}}[n_{1,+1}(y) - n_{1,-1}(y)] \\ n_2^{S_z}(y) &= 4[n_{2,+1}(y) - n_{2,-1}(y)]. \end{aligned} \quad (6.14)$$

In this sequence we have to normalize the measured atom numbers to the total local atom number $n(y) = n_1(y) + n_2(y)$ in order to estimate the corresponding mean spin. In Appendix B.1 we provide the evaluation for an arbitrary splitting ratio of the first two mw pulses.

6.4.1. Spin wave with spinor evolution

We use this readout to analyze a different kind of spin wave, which will provide an instructive illustration of the spin dynamics under a spinor phase evolution as described in Sec. 2.1.5. For that, we prepare a spin wave in the $S_x - S_z$ -plane. We use the same preparation sequence as before but the final rf pulse tilts the spin wave by $\pi/2$ out of the S_\perp -plane. After the preparation we use two mw π -pulses with a relative phase of ϕ_{mw}^{00} coupling the states $(1, 0) \leftrightarrow (2, 0)$. As explained before this imprints a spinor phase of $\phi_S = \phi_{\text{mw}}^{00}$ onto the state. For the prepared spin wave, the value S_z/n varies in an interval from -1 to 1 . Thus, we can experimentally extract the spinor phase evolution of spin states with different z -projections, which is shown in Fig. 6.10.

For a spin state with $S_z/n = 0$ a spinor phase evolution changes the spin length in the S_\perp -plane. In contrast, for $S_z/n > 0.9$ a change of the spinor phase keeps the spin length fixed but changes its orientation similar to a change of the Larmor phase by ϕ_S . This means for the prepared spin wave that the mean spin length will shrink near the equator of the spin sphere and will additionally twist with a higher z -projection. After changing the spinor phase by $\pi/2$, the phase resembles an eight on the spin sphere. An additional evolution of the spinor then unfolds the eight again and we retrieve the initially prepared spin wave.

For the spinor phase of $\phi_S = 180^\circ$ our readout does not detect $S_{\perp,\max}/n = 1$ as one would expect for the prepared state. This could again be due to some residual coupling of the $F = 2$ manifold. Since after the first rf-pulse, we mix a possible small population in the states $(2, \pm 2)$ with the high populations of the states $(1, \pm 1)$ inducing interference. This could then influence the readout of the S_\perp observables.

6.5. Detection of quantum correlations

So far we have used our new readout technique to analyze single-particle states. Even though the states had a spatial structure, they were described by coherent states without entanglement between the particles. Therefore, it was sufficient to analyze the mean of the extracted observables where the additional Poissonian noise due to coupling to initially empty states can be neglected. We will now extend this readout scheme to many-particle states and show that despite the additional noise contribution this readout is capable to detect quantum correlations in such states.

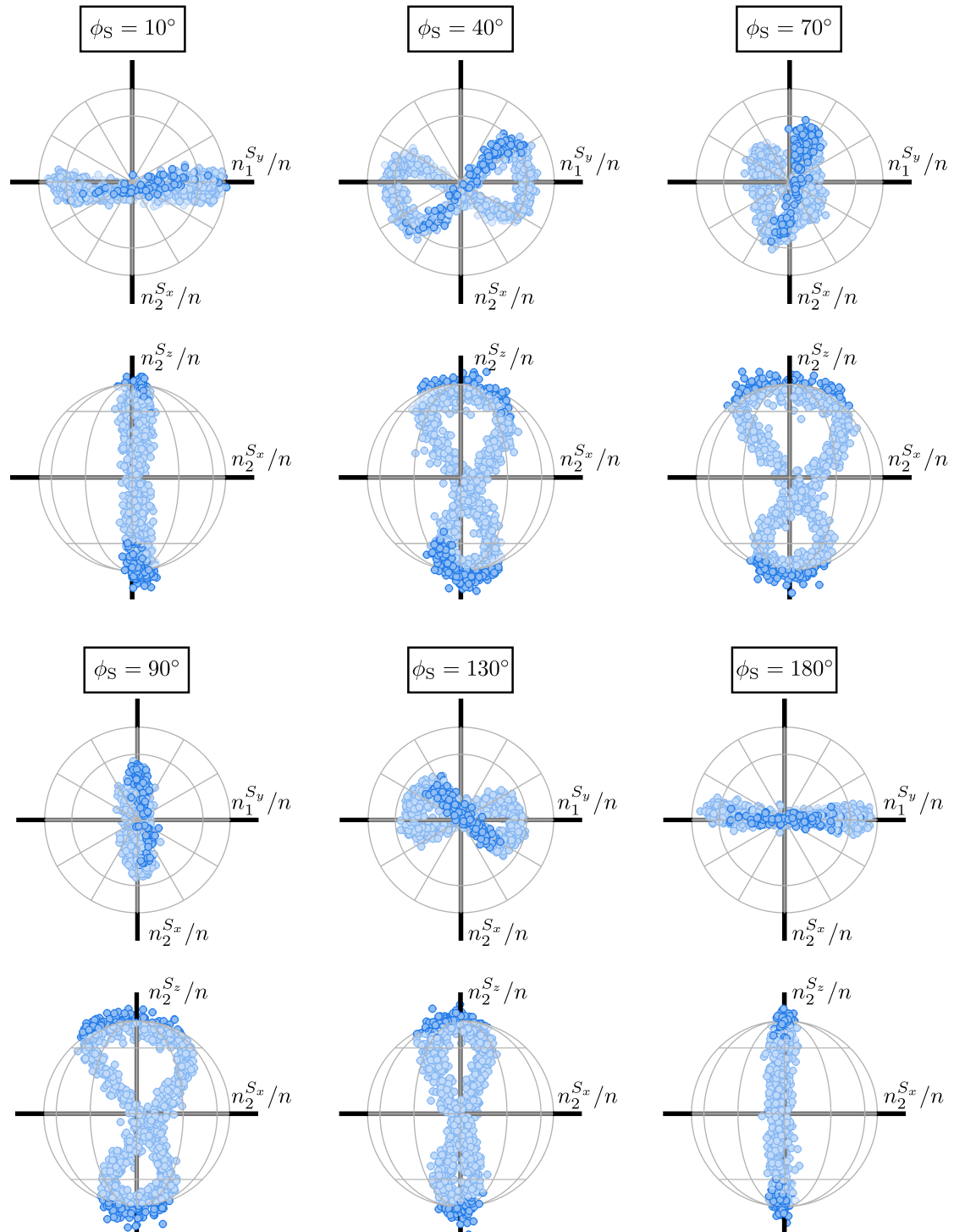


Figure 6.10.: Spinor phase evolution of a spin wave: We plot the values of the three spin observables extracted from the spatially resolved evaluation of 10 experimental realizations. For this we bin the spatial profiles into evaluation regions with a length of $\approx 2 \mu\text{m}$. With this we resolve the structure in spin space due to a change of the spinor phase.

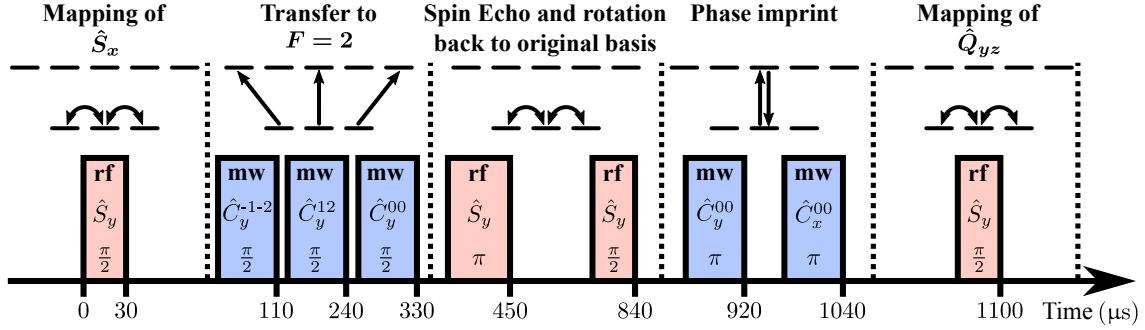


Figure 6.11.: Pulse sequence for the simultaneous readout of S_x and Q_{yz} .

For generating a quantum correlated state we initialize around 20,000 atoms in the state $(1, 0)$ and use spin-mixing to generate a spin-nematic squeezed state. As explained before the initial dynamics are well described in a phase space spanned by the observables \hat{S}_x and \hat{Q}_{yz} . For the steering measurement we had to use tomography by scanning the spinor phase to measure spin-nematic squeezing, i.e. the minimum fluctuations of the observable $\hat{F}(\phi_S) = \cos(\phi_S)\hat{S}_x + \sin(\phi_S)\hat{Q}_{yz}$. The idea here is to use the simultaneous readout to extract S_x and Q_{yz} from a single experimental realization. With this we could analyze $\hat{F}(\phi_S)$ for all possible values of ϕ_S without the need for tomography. However, since we are interested in higher moments of the probability distribution, the coupling to the initially empty modes will now become relevant and introduce additional fluctuations.

To simultaneously readout these two observables we use the following readout sequence as sketched in Fig. 6.11. With an rf $\pi/2$ spin-rotation around the S_y -direction we map the observable \hat{S}_x onto the population difference of the states $(1, \pm 1)$. We then use three mw $\pi/2$ -pulses coupling the states $(1, 0) \leftrightarrow (2, 0)$ and $(1, \pm 1) \leftrightarrow (2, \pm 2)$ to transfer half of the population to the $F = 2$ manifold. Thus, the information about \hat{S}_x is encoded into the $F = 2$ manifold. In order to extract \hat{Q}_{yz} we first rotate the state back using an additional rf $\pi/2$ spin-rotation around the y -axis in $F = 1$. At this stage a spin echo sequence is used to cancel the effect of magnetic field fluctuations. We then imprint a phase of $\pi/2$ on the state $(1, 0)$ by applying two resonant mw π -pulses coupling the states $(1, 0) \leftrightarrow (2, 0)$ with a relative phase of $\pi/2$. An additional rf $\pi/2$ -rotation then maps the observable \hat{Q}_{yz} onto the population difference of $(1, \pm 1)$.

To extract the information about the observables \hat{S}_x and \hat{Q}_{yz} we evaluate the atom number differences

$$\begin{aligned} n_1^-(y) &= n_{1,+1}(y) - n_{1,-1}(y) \\ n_2^-(y) &= n_{2,+2}(y) - n_{2,-2}(y) \end{aligned} \quad (6.15)$$

from which we obtain the correspondence $\langle n_1^-(y)/n_1(y) \rangle = \langle \hat{Q}_{yz}(y) \rangle_Q$ and $\langle n_2^-(y)/n_2(y) \rangle = \langle \hat{S}_x(y) \rangle_Q$. After Stern-Gerlach splitting all relevant densities for extracting n_1^- and n_2^- are spatially non-overlapping since the magnetic moments of $(2, \pm 2)$ are twice as large as the ones of $(1, \pm 1)$. Thus, we extract all populations from a single exposure without the need for hyperfine selective absorption imaging which has the additional benefit of reduced imaging noise (see Fig. 6.12a)).

Using mw dressing we tune spin-mixing into resonance with the first excited mode of the effective potential. As explained before, in order to extract the relevant observable of this antisymmetric mode we divide the absorption image into two halves (L/R) and

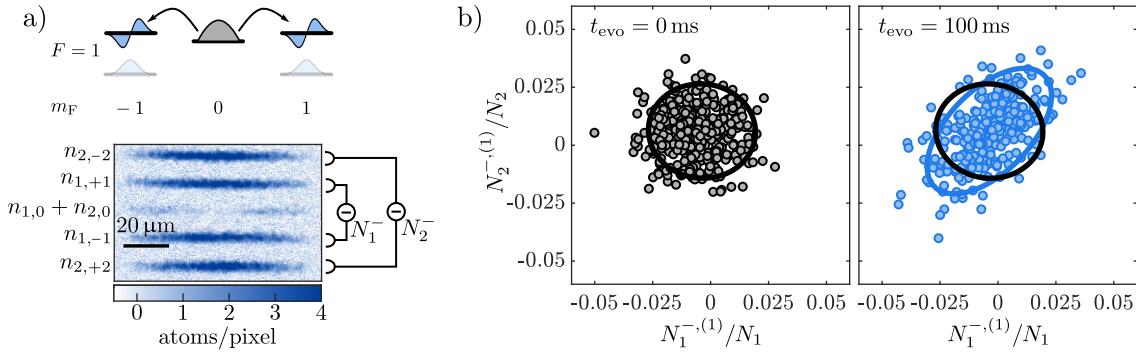


Figure 6.12.: **Experimental evaluation:** a) We tune the spin-mixing process into resonance with the first excited spatial mode. Because of the different magnetic moments we can detect the relevant atomic densities with a single absorption image. b) Plotting the individual experimental results for the measured pairs $\{N_1^{-,(1)}/N_1, N_2^{-,(1)}/N_2\}$ reveals for the initial state a symmetric distribution (left). After 100 ms of spin-mixing evolution (right) we find a redistribution of the initial fluctuations. The blue and black lines depict the 2 s.d. intervals of the two distributions.

extract in each half the corresponding atom number difference. With that the signal of the first excited mode is extracted via

$$\begin{aligned} N_1^{-,(1)} &= n_1^{-,\text{L}} - n_1^{-,\text{R}} \\ N_2^{-,(1)} &= n_2^{-,\text{L}} - n_2^{-,\text{R}}. \end{aligned} \quad (6.16)$$

This means, from every experimental realization we get a pair of measurement values $\{N_1^{-,(1)}/N_1, N_2^{-,(1)}/N_2\}$ which contains information about the correlations between the two observables $\{\hat{Q}_{yz}, \hat{S}_x\}$. By simply plotting the values extracted from around 300 experimental realizations we find without spin-mixing a symmetric distribution as shown in Fig. 6.12b). This is expected for the initial coherent state. After 100 ms of evolution time we find that the fluctuations have been redistributed and the measured distribution shows an elliptical shape. For the short axis we find that the fluctuations are reduced compared to the initial state, which indicates the generation of a spin-nematic squeezed state.

6.5.1. Surpassing the shot-noise limit

The distribution we measured allows us to evaluate the variance of $\Delta^2 F^{(1)}(\varphi)$ for every value of the projection angle φ without the need to experimentally scan the spinor phase ϕ_S . To show that the fluctuations are indeed squeezed it is not enough to compare them to the initial state since there might be some additional technical fluctuations which, for example, could have increased the width of the initial distribution. Thus, to be more quantitative we have to compare the fluctuations of the generated state with the shot-noise limit of a coherent polar state. Similar as before, for each of the two atom number differences, $N_1^{-,(1)}$ and $N_2^{-,(1)}$, the shot-noise limit can be calculated assuming a multinomial distribution of the atoms. This limit is given by the total atom numbers N_1 and N_2 in the respective manifold as the population of the states $(1, 0)$ and $(2, 0)$ after 100 ms is

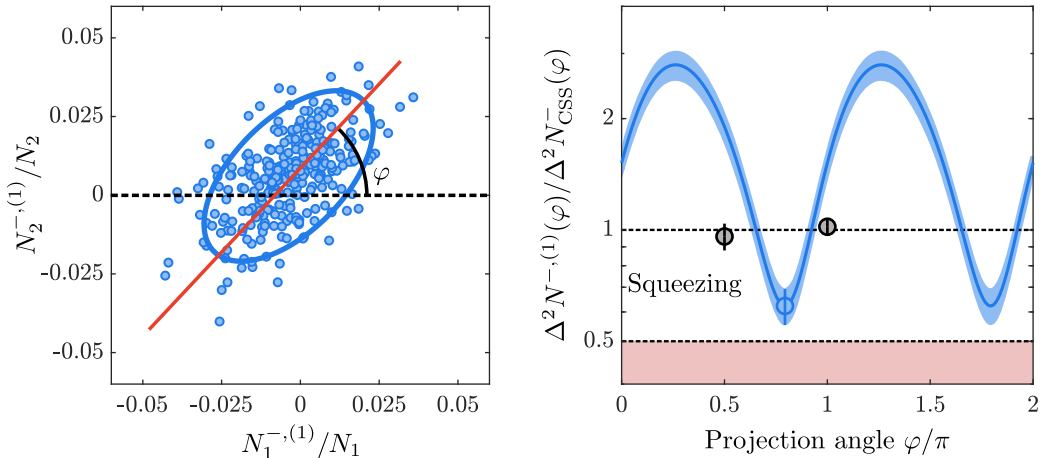


Figure 6.13.: **Spin-nematic squeezing:** To verify squeezing of the two dimensional distribution we evaluate the variance for different projection angles φ and normalize it to the respective shot-noise limit (blue curve on the right). The blue shading represents the 1 s.d. band. We find minimal fluctuations of 0.62 ± 0.07 below the standard quantum limit (black dashed line) demonstrating spin-nematic squeezing. The red shading indicates the fundamental limit of 0.5 for this readout scheme. The gray points correspond to independent imaging calibration measurements in the $F = 1$ and $F = 2$ manifold using a coherent polar state.

still negligible. To quantify the fluctuations along the different projection angles φ of the measured distribution we evaluate the variance $\Delta^2 N^{-,(1)}(\varphi)$ of

$$N^{-,(1)}(\varphi) = \cos(\varphi)N_2^{-,(1)} + \sin(\varphi)N_1^{-,(1)}, \quad (6.17)$$

which contains information about the observable $\hat{F}^{(1)}(\phi_S)/2$ as defined in Eq. (4.36). To make the definitions consistent the spinor phase is then connected to the projection angle via an offset phase, i.e. $\varphi = \phi_S + \phi_{S,0}$. Since for a coherent polar state the measured fluctuations in $F = 1$ and $F = 2$ are uncorrelated we get for the corresponding classical limit

$$\Delta^2 N_{\text{CSS}}^-(\varphi) = \cos^2(\varphi)N_2 + \sin^2(\varphi)N_1. \quad (6.18)$$

For perfect $\pi/2$ mw pulses, with $N_1 = N_2 = N/2$ this expression would be independent of the angle φ . However, in our case we observe a slight imbalance of the atom numbers consistent with 0.53π pulses. As shown in Fig. 6.13, after 100 ms of evolution time we infer minimal fluctuations of 0.62 ± 0.07 clearly below the standard quantum limit, certifying squeezing. For this value we subtracted independently characterized noise contributions from the imaging (see Appendix A.3.2). Without subtraction we find a value 0.81 ± 0.07 which is still below the classical limit. We experimentally checked the classical limit by analyzing in a separate measurement the fluctuations of a coherent polar state in $F = 1$ and $F = 2$. The measured values are shown as gray points in Fig. 6.13.

The squeezing by nearly a factor of 2 (-3 dB) is close to the fundamental limit that can be detected with this readout technique. We have already encountered this limit for the steering measurement when evaluating just one half of the atomic cloud. The argument in this case is the same. One can think of the mw pulses as beamsplitters where one input port, corresponding to the $F = 2$ manifold, is initially empty. Thus, we get for the average

$\langle N^{-,(1)}(\varphi) \rangle = \langle \hat{F}^{(1)}(\phi_S)/2 \rangle_Q$. Assuming perfect $\pi/2$ mw pulses, corresponding to 50/50 beamsplitters, the measured fluctuations of $N^{-,(1)}(\varphi)$ are connected to the fluctuations of the observable $\hat{F}^{(1)}(\phi_S)$ via

$$\zeta(\phi) = \frac{\Delta^2 N^{-,(1)}(\varphi)}{\Delta^2 N_{\text{CSS}}^-(\varphi)} = \frac{1}{2} \frac{\Delta^2 F^{(1)}(\phi_S)}{\langle N \rangle} + \frac{1}{2}. \quad (6.19)$$

For details on the derivations of this formula see supplementary information in [123]. Thus, even for vanishing fluctuations of the input state, the measurable suppression with this readout is bounded by 0.5. From the measurement we infer minimal and maximal fluctuations of $\zeta(\varphi_{\min}) = 0.62 \pm 0.07$ and $\zeta(\varphi_{\max}) = 2.80 \pm 0.25$. Using Eq. (6.19) we compute the corresponding uncertainty product for the observable $\hat{F}^{(1)}(0, \pi/2)$ and obtain

$$\frac{\Delta^2 F^{(1)}(0)}{\langle N \rangle} \cdot \frac{\Delta^2 F^{(1)}(\pi/2)}{\langle N \rangle} = 0.24 \cdot 4.6 = 1.1 \pm 0.6, \quad (6.20)$$

which is consistent with a minimal uncertainty state. As explained before the detection of spin-nematic squeezing already certifies that the atoms of the condensate are entangled. This means that our readout has the capability to detect quantum correlations. Moreover, compared to the steering measurement it does not suffer from a finite step size for sampling the spinor phase, since we can, with a single measurement setting, measure all possible projection angles.

6.6. Applicability to other systems

It is important to note that this readout scheme is not limited to the system presented here but can be applied to other systems that feature initially unpopulated states to which one can couple for the readout. All the techniques used for this readout (projective measurement and rf and mw manipulation) are readily available in many experimental setups making an implementation of this readout feasible.

An interesting aspect would be the implementation of an informationally complete measurement similar to [132]. This could, for example, be realized in a pseudo-spin-1/2 system consisting of the states $(1, +1)$ and $(2, -1)$ which has been extensively studied in our experimental setup [75, 76, 77, 78, 79]. There, only a total of 4 states are needed to implement an informationally complete measurement. In this case, informational completeness refers to the single-particle basis. However, we have just shown that such a measurement still contains information about the original quantum correlations in a many-body state which we will also discuss in more detail later. For details on a informationally complete readout sequence in a pseudo-spin-1/2 system see Appendix B.3.

7. Entanglement detection using a simultaneous readout

By demonstrating squeezing we directly know that the spins in the condensate must be entangled in a particle basis. Applying the same logic as for the steering measurement this means that, after the expansion, spatially distinct regions of the condensate are entangled. For the steering measurement we needed to experimentally scan the spinor phase and acquire for each setting enough statistics in order to reveal the correlations and anticorrelations in the two conjugate observables. With the new readout technique presented before we would not need to scan this phase but could just acquire the required statistics in a single measurement setting and then check in the post-analysis all possible correlations between the different measurement directions.

The entangled states we prepare here have a relatively simple entanglement structure in the sense that the spatial correlations and anticorrelations are in the same operator basis, i.e. that the results $F_A(0)$ ($F_A(\pi/2)$) in system A are (anti-)correlated with the results $F_B(0)$ ($F_B(\pi/2)$) in system B. This means that we can resolve these correlations by setting the measurement basis globally. However, one could also think of more complex states where for example the measurement result $F_A(0)$ in system A is correlated with the measurement result of $F_B(\pi/2)$ in system B. Then, using standard projective measurements one would need to set the measurement basis locally. Moreover, if one has no a priori knowledge about the correlated measurement directions one has to try different combinations of basis settings which becomes experimentally infeasible as one includes more and more spatial modes. Here, our readout offers the advantage that one could check all possible correlations with a single measurement setting, which would provide an extremely useful tool for state characterization in multimode settings.

7.1. Entanglement measures based on uncertainty relations

But can this readout technique actually verify entanglement between spatially distinct regions? In Ch. 5 we showed that EPR steering provides a rather general method to verify entanglement based on the measurement of two noncommuting observables. From a fundamental point of view, however, it is impossible to use a simultaneous measurement of two conjugate observables to violate a steering inequality. Because a violation of this inequality means that we are able to guess the measurement results of two noncommuting observables in one system better than predicted by the local uncertainty relation. Quantum mechanically, this is possible as long as we measure only one of these observables in one experimental realization, because we could think of the measurement as influencing the global state. However in a simultaneous measurement this would mean, that both observables are simultaneously better determined than allowed by the uncertainty relation.

Using the results from the squeezing measurement we can also plug in the numbers to convince ourselves that it is indeed not possible to violate the steering inequality even for an optimal setting of the squeezing measurement described in Sec. 6.5. Let us therefore label the two halves of the cloud as A and B to connect the notation to the steering measurement. We assume perfect $\pi/2$ pulses for the transfer to the $F = 2$ manifold such that $N_1 = N_2 = N/2$. Then we know that for an infinitely squeezed state we could measure a squeezing of $\Delta^2 N^{-,(1)}(\varphi_{\min})/\langle N/2 \rangle = \Delta^2(N_A^-(\varphi_{\min}) - N_B^-(\varphi_{\min}))/\langle N/2 \rangle = 0.5$. Since we only populated the first excited mode, we expect for the ground mode to measure classical fluctuation, i.e. $\Delta^2 N^-(\varphi_{\max})/\langle N/2 \rangle = \Delta^2(N_A^-(\varphi_{\max}) + N_B^-(\varphi_{\max}))/\langle N/2 \rangle = 1$. Thus, we get for the steering product

$$S_{A|B} = \frac{\Delta^2 N_{A|B}^-(\varphi_{\min})}{\langle N/2 \rangle} \cdot \frac{\Delta^2 N_{A|B}^-(\varphi_{\max})}{\langle N/2 \rangle} = 0.5 \cdot 1 = 0.5. \quad (7.1)$$

We now have to compare this value to the uncertainty relation of the corresponding operators in system A. As explained before the measured quantity $N_A^-(\varphi)$ contains information about the observable $\hat{F}_A(\phi_S)/2$. With this we would get for the uncertainty relation with $N_A = N/2$

$$\frac{\Delta^2(F_A(0)/2)}{\langle N/2 \rangle} \cdot \frac{\Delta^2(F_A(\pi/2)/2)}{\langle N/2 \rangle} \geq \frac{1}{16} < S_{A|B}. \quad (7.2)$$

Thus, even in the optimal case we would not violate the steering criterion as expected from the argument given before.

7.1.1. Duan entanglement criterion

We recall that steering is already a strong form of entanglement and there might be other witnesses for entanglement where the bound is easier to reach with this readout. One of these witnesses that are based on the measurement of two noncommuting observables is the Duan criterion [133]. Given two conjugate observables with $\Delta^2 F_X(0)\Delta^2 F_X(\pi/2) \geq c_X$ ($X \in \{A, B\}$), we can rewrite the uncertainty relation in terms of the sum of the variances by using that $(x^2 + y^2)/2 \geq xy$, i.e.

$$\Delta^2 F_X(0) + \Delta^2 F_X(\pi/2) \geq 2\sqrt{c_X}. \quad (7.3)$$

Similar to steering we now use subsystem B to predict the measurement outcomes in A by using an inference of the form

$$\begin{aligned} \hat{F}_{A|B}(0) &= |a|\hat{F}_A(0) + \frac{1}{a}\hat{F}_B(0) \\ \hat{F}_{A|B}(\pi/2) &= |a|\hat{F}_A(\pi/2) - \frac{1}{a}\hat{F}_B(\pi/2) \end{aligned} \quad (7.4)$$

with some real number a . It can then be shown that for a separable state the sum of the inferred variances is bounded by

$$D = \Delta^2(F_{A|B}(0)/2) + \Delta^2(F_{A|B}(\pi/2)/2) \geq \frac{1}{2}(a^2\sqrt{c_A} + \frac{1}{a^2}\sqrt{c_B}). \quad (7.5)$$

The idea behind the Duan criterion is that for two separable systems, A and B, the inference will not reduce the measurement uncertainty but will increase it according to the uncertainty relation in each individual subsystem. Only if the two systems are entangled can this inference submerge the bound for separable states. In contrast, for steering the bound is given by the uncertainty relation in one subsystem alone and one has to show that the inference reduces the uncertainty below even this bound. Consequently, showing $D < a^2 \sqrt{c_A}/2$ certifies that A is steered by B [20].

For Gaussian states such as spin squeezed states, the Duan criterion is actually a necessary and sufficient condition for entanglement. Thus, using this criterion we should be able to certify entanglement for the spin-nematic squeezed state. Assuming that we divide the atomic signal into two halves containing equal atom numbers such that $\sqrt{c_A} = \sqrt{c_B} = \langle N/2 \rangle$ we find for $a = 1$ that $D/\langle N/2 \rangle \geq 1$. Using the numbers from the squeezing measurement as before we find

$$\frac{D}{\langle N/2 \rangle} = \frac{\Delta^2 N_{A|B}^-(\phi_{\min})}{\langle N/2 \rangle} + \frac{\Delta^2 N_{A|B}^-(\phi_{\max})}{\langle N/2 \rangle} = 0.5 + 1 > 1. \quad (7.6)$$

Therefore, with this measurement scheme we can also not violate this bound of the Duan criterion.

7.1.2. Arthurs-Kelly uncertainty relation

The reason that we cannot submerge the bound of the Duan criterion is that we have used the uncertainty relation of the observables $\hat{F}(\phi_S)/2$ as if we would have measured them in a standard projective measurement. But in such a measurement we can in principle measure each of the conjugate observables with arbitrary precision. In a simultaneous readout, this is of course not possible since it would violate the uncertainty relation, so we are only allowed to perform a fuzzy measurement as soon as we attempt to simultaneously measure two conjugate observables. This increased variance is also the reason why the measurable squeezing is bounded by 0.5. Therefore we need to derive an uncertainty relation for the measurement operators $\hat{N}^-(\phi)$ itself. In general, these operators can be modeled as

$$\begin{aligned} \hat{N}^-(0) &= \frac{1}{2}\hat{F}(0) + \hat{A} \\ \hat{N}^-(\pi/2) &= \frac{1}{2}\hat{F}(\pi/2) + \hat{B} \end{aligned} \quad (7.7)$$

where we set $\varphi = \phi_S$. The additional operators \hat{A} and \hat{B} with $\langle \hat{A} \rangle_Q = \langle \hat{B} \rangle_Q = 0$ ensure that the measurement operators commute since we could measure the atom number differences in principle with arbitrary precision. In our case, these two operators correspond to the contributions from the initially empty $F = 2$ manifold. Using that $[\hat{N}_{F=1}^-, \hat{N}_{F=2}^-] \stackrel{!}{=} 0$ we obtain for the commutation relation of \hat{A} and \hat{B}

$$[\hat{A}, \hat{B}] = -\frac{1}{4}[\hat{F}(0), \hat{F}(\pi/2)] - \frac{1}{2}[\hat{A}, \hat{F}(\pi/2)] - \frac{1}{2}[\hat{F}(0), \hat{B}]. \quad (7.8)$$

These two operators introduce additional noise and therefore enable the simultaneous measurement of the two noncommuting operators by making it less precise. In general,

it can be shown [37]

$$\begin{aligned}\Delta^2 N^-(0) \Delta^2 N^-(\pi/2) &= \frac{1}{16} \Delta^2 F(0) \Delta^2 F(\pi/2) + \langle \hat{A}^2 \rangle_Q \langle \hat{B}^2 \rangle_Q + \frac{1}{4} \Delta^2 F(\pi/2) \langle \hat{A}^2 \rangle_Q + \frac{1}{4} \Delta^2 F(0) \langle \hat{B}^2 \rangle_Q \\ &\geq \left(\frac{1}{4} \Delta F(0) \Delta F(\pi/2) + \sqrt{\langle \hat{A}^2 \rangle_Q \langle \hat{B}^2 \rangle_Q} \right)^2.\end{aligned}\quad (7.9)$$

For the last line, we used that

$$\frac{1}{4} \Delta^2 F(\pi/2) \langle \hat{A}^2 \rangle_Q + \frac{1}{4} \Delta^2 F(0) \langle \hat{B}^2 \rangle_Q \geq \frac{1}{2} \Delta F(0) \Delta F(\pi/2) \sqrt{\langle \hat{A}^2 \rangle_Q \langle \hat{B}^2 \rangle_Q}, \quad (7.10)$$

i.e. that the arithmetic mean is bounded from below by the geometric mean. We estimate the second term in Eq. (7.9) via the commutation relation (7.8)

$$\begin{aligned}\langle \hat{A}^2 \rangle_Q \langle \hat{B}^2 \rangle_Q &\geq \frac{1}{4} \left| \langle [\hat{A}, \hat{B}] \rangle_Q \right|^2 \\ &= \frac{1}{4} \left| -\frac{1}{4} \langle [\hat{F}(0), \hat{F}(\pi/2)] \rangle_Q - \frac{1}{2} \langle [\hat{A}, \hat{F}(\pi/2)] \rangle_Q - \frac{1}{2} \langle [\hat{F}(0), \hat{B}] \rangle_Q \right|^2.\end{aligned}\quad (7.11)$$

Since the operators \hat{A} and \hat{B} which describe the initially unoccupied modes are not correlated with the spin observables \hat{F} , the last two terms vanish and we obtain

$$\langle \hat{A}^2 \rangle_Q \langle \hat{B}^2 \rangle_Q \geq \frac{1}{4} \left| \left\langle -\frac{1}{4} [\hat{S}_x, \hat{Q}_{yz}] \right\rangle_Q \right|^2 = \frac{1}{4} \left(\frac{\langle N \rangle}{2} \right)^2. \quad (7.12)$$

Inserting this result into Eq. (7.9), we arrive at the uncertainty relation of the two measurement operators

$$\frac{\Delta^2 N^-(0)}{\langle N/2 \rangle} \frac{\Delta^2 N^-(\pi/2)}{\langle N/2 \rangle} \geq 1 = 4 \cdot \frac{\Delta^2(F(0)/2)}{\langle N/2 \rangle} \frac{\Delta^2(F(\pi/2)/2)}{\langle N/2 \rangle}. \quad (7.13)$$

This is the Arthurs-Kelly uncertainty relation [134] for the simultaneous readout of two noncommuting observables. Thus, the factor of four is the price one has to pay to simultaneously get information about two noncommuting observables.

With this uncertainty relation we can derive an entanglement criterion in analogy to the Duan-criterion. The main argument in the derivation of the Duan-criterion was that, for a separable state, the sum of the inference variances are bounded from below by the variances of the corresponding local observables [133]. This argument can equivalently be applied to the Arthurs-Kelly uncertainty relation and we obtain a modified Duan-criterion for the simultaneous readout of two conjugate observables

$$\begin{aligned}D &= \Delta^2 \left(N_{A|B}^-(0) \right) + \Delta^2 \left(N_{A|B}^-(\pi/2) \right) \geq a^2 \sqrt{c_A} + \frac{1}{a^2} \sqrt{c_B} \\ &\stackrel{a=1}{=} 2 \cdot \langle N/2 \rangle.\end{aligned}\quad (7.14)$$

Here the bound on the right hand side is increased by a factor of two. Inserting the numbers for spin-nematic squeezed state we find that an optimal measurement could indeed reveal entanglement between the two subsystems.

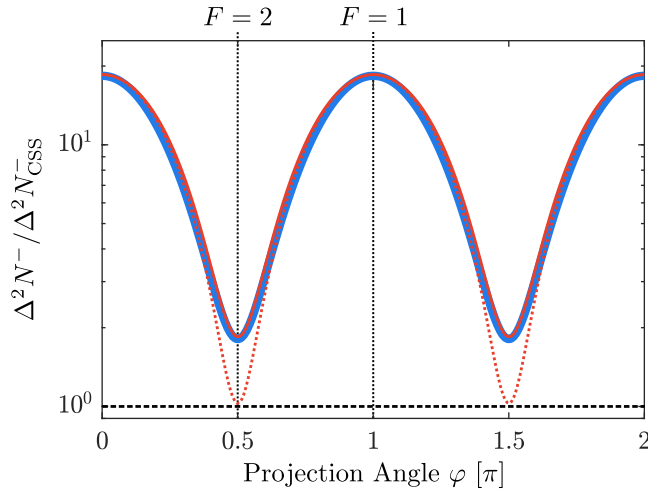


Figure 7.1.: Noise analysis of the readout sequence: We evaluate the variance of the population differences without relative analysis. This corresponds to the analysis of the ground mode. We evaluate the different projection angles in the same way as in Fig. 6.13 (blue curve). Since we find the same signal for all evolution times we average over these realizations to increase the statistics. We find that the fluctuations are determined by the excess noise in the $F = 1$ and $F = 2$ manifold corresponding to projection angles $\varphi = 0, \pi$ and $\varphi = \pi/2, 3\pi/2$, respectively. We simulate the effect of magnetic field fluctuations with (red line) and without (red dotted line) additional noise on the mw pulses. Relative shot-to-shot fluctuations on the Rabi frequency of $\sigma_{\text{mw}} = 0.8\%$ together with magnetic field fluctuations of $\sigma_B = 6.5 \mu\text{G}$ reproduce the experimental signal.

7.1.3. Technical fluctuations

In principle, we could now apply this criterion directly to the experiment discussed in Sec. 6.5 where we have found $\Delta^2 N^{-1}(\varphi_{\min})/\Delta^2 N_{\text{CSS}}^-(\varphi_{\min}) \approx \Delta^2 N_{\text{inf}}^-(0)/\langle N/2 \rangle = 0.62$. Since we tuned the spin-mixing process selectively into resonance with the first excited mode, we would expect to find shot-noise when evaluating the population differences without the relative analysis, i.e. $\Delta^2 N^-(\varphi)/\Delta^2 N_{\text{CSS}}^-(\varphi) = 1 \forall \varphi$. Therefore, using the modified Duan criterion we should in principle be able to directly verify entanglement between the different halves of the atomic cloud. In the experiment, however, we find that the variance $\Delta^2 N^-(\varphi)$ is not independent of the projection angle and especially we find at $\varphi_{\min} + \pi/2$ increased fluctuations corresponding to about 5 times the shot-noise limit.

Analyzing the variance as a function of the projection angle we find for all evolution times the same signal as shown in Fig. 7.1, even for the initial state. We obtain maximal fluctuation at $\varphi = 0$ corresponding to the measurement in the $F = 1$ manifold with $\Delta^2 N_1^-/\langle N_1 \rangle = 18$. Even the minimal measured fluctuations at $\varphi = \pi/2$ are a factor of 2 higher than the shot-noise limit. These correspond to the measurement in the $F = 2$ manifold. Since these noise contributions stay the same irrespective of the evolution time we suspect technical noise as the cause for the enhanced fluctuations. This also fits to the observation that the noise in the $F = 1$ manifold is even higher as more readout pulses are involved for the mapping in $F = 1$. The analysis of the first excited mode cancels these

contributions since they are homogeneous over the atomic cloud. That is the reason why we can detect squeezing despite technical fluctuations.

Let us now examine the reason for these fluctuations more thoroughly. In the $F = 2$ manifold, the noise can either be caused by fluctuations of the rf pulse for the spin rotation or by fluctuations of the mw pulses for the population transfer. The initial polar state is very resilient to power fluctuations of the rf pulse since any rotation angle yields an equal probability to measure a particle in one of the states $(2, \pm 2)$. We, thus, identify power fluctuations on the mw pulses as the main contribution for the increased noise. We find that the experimentally observed signal is consistent with relative shot-to-shot fluctuations of the mw Rabi frequency of $\sigma_{\text{mw}} = \Delta\Omega_{\text{mw}}/\Omega_{\text{mw}} = 0.8\%$. This is consistent with the value we find from an independent characterization of the mw pulses (see Appendix A.5).

Using a simulation of the readout sequence we identify magnetic field fluctuations as the main reason for the enhanced noise in $F = 1$, even though the magnetic field is already stabilized to a very high degree. But it turns out that our readout sequence is also extremely sensitive to these fluctuations. This is because after the first rf $\pi/2$ rotation for the mapping of \hat{S}_x we need another $\pi/2$ rotation with the same phase to turn the state back in order to imprint the spinor phase in the next step. If the two phases are not the same then we would change the orientation of the state on the spin-nematic sphere. We theoretically check how a fluctuating phase between these two pulses would affect the final readout. Neglecting the spin echo pulse and the mw pulses, the unitary transformation for the readout including these phase fluctuations $\delta\phi$ is given by

$$\hat{U} = e^{-i\frac{\pi}{2}\hat{S}_y} \underbrace{e^{-i\frac{\pi}{2}\hat{Q}_0/2}}_{\text{Phase imprint}} e^{-i\frac{\pi}{2}(\cos(\delta\phi)\hat{S}_y + \sin(\delta\phi)\hat{S}_x)} e^{-i\frac{\pi}{2}\hat{S}_y}. \quad (7.15)$$

Evaluating $N_1^{-(0)} = N_{1,+1} - N_{1,-1}$ corresponds to a measurement of the spin observable \hat{S}_z . Thus, to understand the effect of such phase fluctuations we calculate

$$\langle \hat{U}^\dagger \hat{S}_z \hat{U} \rangle_{\text{Exp}} = \cos(2\delta\phi) Q_{yz} + \sin(2\delta\phi) Q_0 \approx Q_{yz} + 2\delta\phi \cdot N_{1,0}. \quad (7.16)$$

Thus, if the phases of the rf pulses do not match we mix into the readout of Q_{yz} contributions from the observable Q_0 , which corresponds to the number of atoms in the state $(1, 0)$. Since within the undepleted pump approximation $N_{1,0} \approx N_1$, the fluctuations of the population difference are increased by

$$\begin{aligned} \Delta^2 N_1^- / \langle N_1 \rangle &= \Delta^2 Q_{yz} / \langle N_1 \rangle + 4 \langle N_{1,0} \rangle^2 \Delta^2(\delta\phi) / \langle N_1 \rangle \\ &\approx 1 + 4 \langle N_1 \rangle \Delta^2(\delta\phi). \end{aligned} \quad (7.17)$$

In the measurement we measure in $F = 1$ a particle number of $\langle N_1 \rangle \approx 10,000$ atoms. With this the excess fluctuations of ≈ 18 can be explained by a fluctuating phase with variance $\Delta^2(\delta\phi) = 4.3 \cdot 10^{-4}$. For the timings of the readout sequence this value corresponds to magnetic field fluctuations with a standard deviation of $\sigma_B = 6.5 \mu\text{G}$. For the readout we already employ a spin-echo sequence to reduce the effect of shot-to-shot fluctuations of the magnetic field which would be on the order of $50 \mu\text{G}$. But even the tiny residual fluctuations are enough to increase the noise of the readout by a sizable amount.

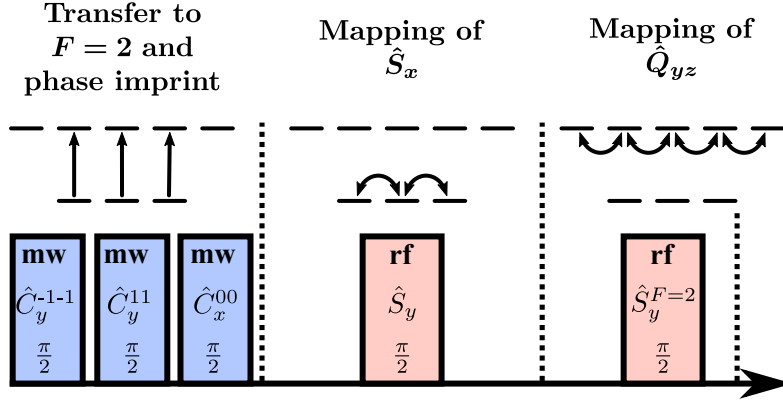


Figure 7.2.: Alternative readout sequence for the simultaneous extraction of \hat{S}_x and \hat{Q}_{yz} .

7.1.4. Stability of the mw transfers

Here, we shortly discuss how to improve the stability of the mw transfers which cause the enhanced fluctuations in the $F = 2$ manifold. In terms of stability $\pi/2$ pulses are not optimal for transferring half of the population because at this point the cosine that parameterizes the transfer has the highest slope. Therefore, the transferred fraction will be very sensitive on the mw power.

To minimize the effect of power fluctuations, it is better to use π pulses as there the transferred fraction is very insensitive on small fluctuations of the Rabi frequency Ω_{mw} . One can then adjust the transferred fraction with the detuning δ_{mw} of the pulse via

$$\eta_\pi = \frac{n_{2,j}}{n_{1,k}} = \frac{\Omega_{\text{mw}}^2}{\Omega_{\text{mw}}^2 + \delta_{\text{mw}}^2}. \quad (7.18)$$

For example, transferring half of the atoms would correspond to setting the detuning $\delta = \Omega$.

However, in situations where the relative phase of the states in the $F = 2$ manifold is important resonant $\pi/2$ pulses are preferable for the state transfer. This is important for readout sequences that involve another spin rotation in $F = 2$ after the transfer.

7.1.5. Alternative readout sequence for \hat{S}_x and \hat{Q}_{yz}

Even if we can mitigate the technical noise contributions in the $F = 2$ manifold, the large fluctuations in the $F = 1$ manifold would still make the detection of entanglement impossible. Thus, we either have to further improve the stability of our magnetic field which is already at a very high level or alternatively switch to a different readout sequence which is less sensitive to these kind of fluctuations. The sensitivity of the previous sequence is due to the backrotation of the state. Thus, we could mitigate the effect of magnetic field fluctuations by applying a spin rotation in the $F = 2$ manifold and imprint the spinor phase during the mw splitting as shown in Sec. 6.3.3 for the calibration of the spin wave readout.

Specifically, we could first use three mw $\pi/2$ pulses to transfer half of the population to the states $(2, 0)$ and $(2, \pm 1)$. There, we tune the phase of the mw pulses such that the pulse coupling the states $(1, 0) \leftrightarrow (2, 0)$ has a $\pi/2$ phase shift compared to the other two

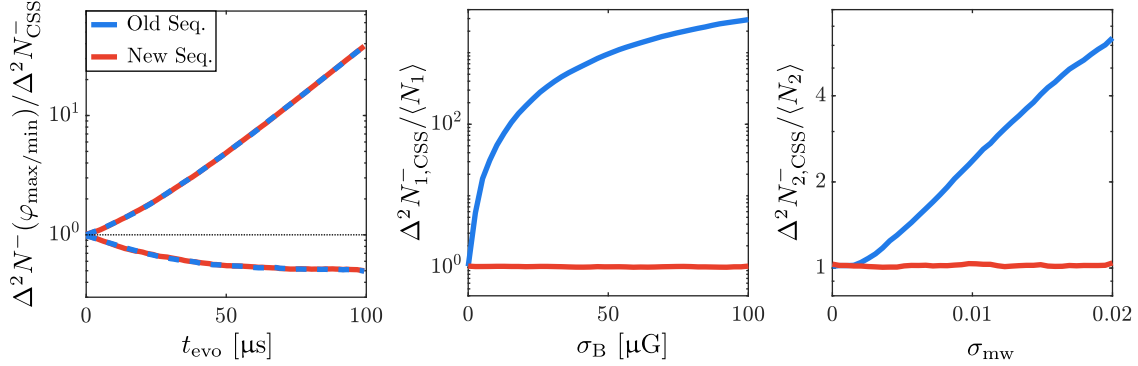


Figure 7.3.: Comparison between old and new readout sequence for the simultaneous extraction of S_x and Q_{yz} : In the left plot the detectable minimal and maximal fluctuations after a given spin-mixing evolution time are shown, which are the same for both readout techniques. Comparing, however, the influence of magnetic field fluctuations σ_B on the measurement in $F = 1$ (middle) and relative fluctuations of the mw Rabi frequency σ_{mw} for the measurement in $F = 2$ (right), we see that the new readout sequence proposed here is less sensitive to these effects.

pulses. This imprints a spinor phase of $\pi/2$ onto the state $(2, 0)$. We then use an rf $\pi/2$ rotation in $F = 1$ around S_y to map the spin observable \hat{S}_x onto the population difference of $(1, \pm 1)$. A second $\pi/2$ rotation in $F = 2$ with the same relative phase, i.e. around $S_y^{F=2}$ then maps the observable \hat{Q}_{yz} onto the population difference of $(2, \pm 2)$ (see Fig. 7.2).

We use a truncated Wigner simulation to check that this sequence is still capable of detecting squeezing as shown in Fig 7.3. Indeed, the simulation shows no difference in the squeezing signal between the two readout sequences. Additionally, we check the sensitivity on the different noise contributions mentioned before and find that this sequence is rather insensitive to magnetic field fluctuations as well as power fluctuations of the mw pulses. The latter is due to the additional rotation in $F = 2$ after the splitting, which averages over possible imbalances caused by the mw transfer. This readout is, thus, a promising candidate for the detection of entanglement between different spatial regions. Additionally, the $\pi/2$ rotation in $F = 2$ maps the observable \hat{Q}_0 onto the population of the state $(2, 0)$. Thus, with this sequence we could completely represent the state on the spin-nematic sphere.

To use this readout one has of course to do a calibration measurement to determine once the relative phases of the readout pulses. As we have seen for the readout of the spin wave, such a sequence is also sensitive to residual couplings between the two hyperfine manifolds. But with a careful alignment of the setup one should be able to suppress the technical fluctuations sufficiently to detect quantum correlations.

7.2. Alternative entanglement detection schemes

So far we have just discussed entanglement witnesses based on the measurement of two conjugate observables. Since most witnesses are only a sufficient but not a necessary condition for entanglement, they might not be optimal in all cases. For example the Duan criterion is not violated for all non-Gaussian entangled states. Therefore, we will here outline a possible alternative route to detect entanglement via the measurement in two mutually unbiased bases [135].

7.2.1. Simultaneous measurement in two mutually unbiased bases

Given a Hilbert space of dimension d with two orthonormal basis sets $\{|\alpha_i\rangle\}$ and $\{|\beta_i\rangle\}$, then these bases are called mutually unbiased if

$$|\langle \alpha_i | \beta_j \rangle|^2 = \frac{1}{d} \quad \forall i, j \in \{1, \dots, d\}. \quad (7.19)$$

The idea behind such bases is that the measurement in one basis yields no information about the measurement result in the other basis given two consecutive measurement on the sample [136]. For example, Suppose one has measured a particle in the first basis after which the it is in the state $|\alpha_i\rangle$, then for a subsequent measurement in the second basis one has an equal probability of $1/d$ to measure the particle in one of the states $\{|\beta_i\rangle\}$, i.e. one has no prior knowledge about the measurement outcome in the second basis.

It has been shown theoretically [135, 137] as well as experimentally [138] that measurements in two mutually unbiased bases are sufficient to detect entanglement as well as quantifying its dimensionality [139]. From an intuitive point of view, this makes sense, because each measurement basis reveals information about the state that has not been contained in the other measurement basis. Therefore, a clever choice of the two measurement bases might result in very powerful entanglement criteria. The definition of mutually unbiased bases is also in close analogy to the definition of symmetric informationally complete POVMs (6.3), where the underlying idea is somewhat similar.

In our case, we do not have access to the individual particles of the condensate. Thus, we use for the definition of a mutually unbiased basis the single-particle spin-1 basis. It is important to note that the concept of mutual unbiased bases is different from a measurement of conjugate observables. Take for example the measurement bases of the conjugate observables \hat{S}_z and \hat{S}_x . Suppose the first measurement is performed in the \hat{S}_z basis, where the basis states are the magnetic substates. There, one detects a particle in the state $(1, 1)$. To measure afterwards in the \hat{S}_x basis one has to implement a $\pi/2$ -spin rotation, after which the probabilities to find a particle in a specific substate are not equal, but there is a higher probability of 0.5 to measure it in the state $(1, 0)$ compared to 0.25 in each of the states $(1, \pm 1)$. Thus, the measurement bases of two conjugate observables are in general not mutually unbiased.

While there is a lot of theoretical work for constructing and determining the number of mutually unbiased bases, one particular useful transformation to obtain a mutually unbiased basis is the quantum Fourier transform. Given a d -dimensional orthonormal

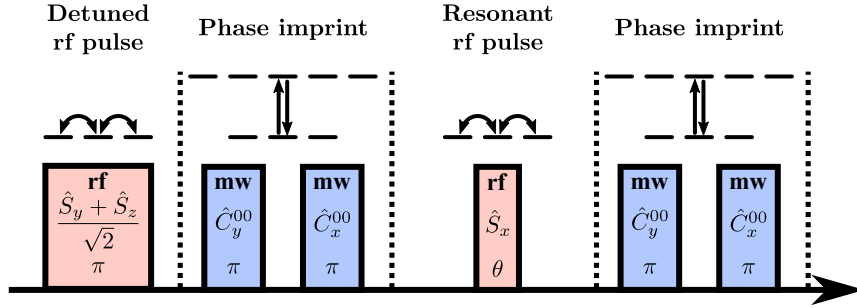


Figure 7.4.: Experimental sequence for the quantum Fourier transform.

basis $\{|0\rangle, \dots, |d-1\rangle\}$, the quantum Fourier transform of each state is defined as [34]

$$|j\rangle \longrightarrow \frac{1}{\sqrt{d}} \sum_{k=0}^{d-1} e^{i2\pi/d \cdot jk} |k\rangle \quad (7.20)$$

which is analogous to the discrete Fourier transform. For a spin-1 system the quantum Fourier transform in matrix notation is given by

$$\hat{\mathcal{FT}} = \frac{1}{\sqrt{3}} \begin{pmatrix} 1 & 1 & 1 \\ 1 & e^{i2/3\pi} & e^{-i2/3\pi} \\ 1 & e^{-i2/3\pi} & e^{i2/3\pi} \end{pmatrix}. \quad (7.21)$$

We see that independent of the initial state, the quantum Fourier transform leads to an equal population of all three states and additionally to an equiangular distribution of the phase in the complex plane.

7.2.2. Experimental implementation of the quantum Fourier transform

In a spin-1/2 system the quantum Fourier transform corresponds to the Hadamard gate which is routinely implemented for qubit quantum computation. Based on the implementation in qubit systems, there are different proposals how to implement the quantum Fourier transform in higher spin systems. It has been shown that it can always be implemented using Hadamard and controlled phase gates [140]. Alternatively, there exist proposal to employ spin-1/2 couplings in an extended manifold for the implementation of the Fourier transform in qutrit systems [141]. These sequences are, however, not very suitable for our system and would require multiple coupling pulses. We therefore propose here a different sequence which makes use of spin-1 rotations to efficiently implement the quantum Fourier transformation.

The sequence is sketched in Fig. 7.4. We first employ a π spin rotation around the axis $(S_z + S_y)/\sqrt{2}$, i.e by using an rf pulse that has a detuning equal to its Rabi frequency. Starting in the states $(1, \pm 1)$ this generates a state with spin length of 1 in the S_\perp -plane but with different phases than for a usual resonant $\pi/2$ rotation. The state $(1, 0)$ gets transformed into a transverse polar state. In a next step we imprint a spinor phase of $\pi/2$. While this transformation has no effect on the transverse polar state, it will remove the spin length of the other two states and generate a state in the Q_\perp -plane. For such quadrupole states any subsequent spin rotation will maintain an equal population of the

states $(1, \pm 1)$. A spin-rotation around S_x by an angle of $\theta = \arctan(-1/\sqrt{2})$ generates an equal population of all three magnetic substates irrespective of the initial state. In a last step, we imprint another spinor phase of $\pi/2$, which implements the correct relative phases. For an implementation of this sequence the last step is not relevant since we are anyway just interested in populations which are unchanged by the phase imprint.

To check that this sequence indeed provides an implementation of the quantum Fourier transform we calculate the corresponding unitary operator which is given by

$$\begin{aligned} \hat{U}_{\text{QFT}} &= e^{-i\pi/2\hat{Q}_0/2} \cdot e^{-i\theta\hat{S}_x} \cdot e^{-i\pi/2\hat{Q}_0/2} \cdot e^{-i\pi(\hat{S}_y + \hat{S}_x)/\sqrt{2}} \\ &= (\hat{a}_{1,+1}^\dagger, \hat{a}_{1,0}^\dagger, \hat{a}_{1,-1}^\dagger) \frac{1}{\sqrt{3}} \begin{pmatrix} e^{i2/3\pi} & 1 & e^{-i2/3\pi} \\ 1 & 1 & 1 \\ e^{-i2/3\pi} & 1 & e^{i2/3\pi} \end{pmatrix} \begin{pmatrix} \hat{a}_{1,+1} \\ \hat{a}_{1,0} \\ \hat{a}_{1,-1} \end{pmatrix} \end{aligned} \quad (7.22)$$

which is the quantum Fourier transform up to a global phase. If we want to combine this with our simultaneous readout, we could first set a measurement basis in $F = 1$, after which we transfer half of the population to the $F = 2$ manifold. Then we can use this sequence described above to set the mutually unbiased basis, which would yield a simultaneous readout in both bases.

Implementing these kind of measures will also require further theoretical work to adapt them to continuous-variable systems. So far these entanglement measures have been used for discrete systems where one counts certain measurement coincidences [138]. But for continuous-variables even with single particle resolution such a scheme is not feasible. One idea to translate the results from discrete to continuous systems is to bin the measurement results. However, one has to be careful since the binning can have an influence on the mutual unbiasedness as well as the entanglement witnesses [142, 143, 144]. The same difficulty applies to entropic entanglement criteria which have also been shown to outperform entanglement witnesses based on variance analysis [145].

8. State characterization using a simultaneous readout

In this chapter we will provide further insights into the connection between the measurement results from a simultaneous readout and the quantum state that is read out. We have seen in Fig. 6.12b) that simply plotting the data obtained from single realizations already captures the redistribution of fluctuations, which is typical for a squeezed state, and that we can relate the measured fluctuations back to the fluctuations of a corresponding projective measurement. It turns out that the results of the simultaneous readout indeed yield an experimentally accessible representation of the quantum state and as such provides an alternative to the standard tomographic strategies to reconstruct the Wigner distribution. In this regard, we will show that a simultaneous readout of two conjugate observables corresponds to a direct sampling of the corresponding Husimi distribution. Simultaneous readout techniques have also been studied in photonic systems and we will provide a short summary of the results obtained there, namely that a simultaneous readout is in many cases more efficient for extracting higher moments of a given quantum state compared to standard projective measurements. Finally, we will employ our readout technique to record the quantum dynamics on the spin-nematic phase space under spin-mixing evolution beyond the initial squeezing. This allows us to directly detect how the squeezed state transform into a non-Gaussian state and how the distribution refocuses after one cycle of spin-mixing. In the multimode setting, we also find indications of spin relaxation towards the minimum of the mean-field energy.

8.1. Connection between the simultaneous readout and the Husimi function

Let us here shortly summarize two main characteristics of the simultaneous readout when measuring a squeezed state. From Eq. (6.19) we know that the noise suppression that we can measure is bounded by 0.5. Additionally, the Arthurs-Kelly relation (Eq. (7.13)) states that for minimal uncertainty states the variance in each direction is twice as large as for the corresponding operators measured via a standard projective measurement. These two statements sound very familiar, as similar ones apply for comparing the Wigner and the Husimi distribution (see 2.4.3). For the Husimi function we also found that its marginals are not exactly the one of the Wigner distribution but their variances are broadened, e.g. for a coherent state by a factor of 2. Similarly, the width of the Husimi distribution for an infinitely squeezed state is bounded by 0.5.

This is not a coincidence as it turns out that a simultaneous measurement of two noncommuting observables with equal precision yields the Husimi function to the corresponding Wigner distribution [146, 147, 148]. This can be seen by calculating the quantum mechanical characteristic function for the two measurement operators introduce in

Eq. (7.7) normalized to the atom number in the respective manifold

$$\chi_Q(k_1, k_2) = \langle e^{i(k_1 \hat{N}_1^- / N_1 + k_2 \hat{N}_2^- / N_2)} \rangle_Q \quad (8.1)$$

Inserting the definition of the two operators and using the fact that each manifold contains half of the total atom number one gets

$$\begin{aligned} \chi_Q(k_1, k_2) &= \langle e^{\frac{i}{N}(k_1 \hat{S}_x + k_2 \hat{Q}_{yz} + 2k_1 \hat{A} + 2k_2 \hat{B})} \rangle_Q \\ &= \langle 1 + \frac{i}{N}(k_1 \hat{S}_x + k_2 \hat{Q}_{yz} + \hat{C}) \\ &\quad + \frac{(i)^2}{2N^2}(k_1 \hat{S}_x + k_2 \hat{Q}_{yz} + \hat{C})^2 \\ &\quad + \frac{(i)^3}{3!N^3}(k_1 \hat{S}_x + k_2 \hat{Q}_{yz} + \hat{C})^3 \dots \rangle_Q \end{aligned} \quad (8.2)$$

where we defined the operator $\hat{C} = 2k_1 \hat{A} + 2k_2 \hat{B}$, which summarizes the contributions from the initially empty modes in $F = 2$ with $\langle \hat{C} \rangle_Q = 0$. These empty modes and the spin-1 observables are uncorrelated such that

$$\langle (k_1 \hat{S}_x + k_2 \hat{Q}_{yz})^r \hat{C}^s \rangle_Q = \langle (k_1 \hat{S}_x + k_2 \hat{Q}_{yz})^r \rangle_Q \langle \hat{C}^s \rangle_Q. \quad (8.3)$$

Additionally, the fluctuations in the empty modes are Gaussian, i.e. [149]

$$\langle \hat{C}^s \rangle_Q = \begin{cases} 0 & \text{if } s \text{ is odd} \\ \langle \hat{C}^2 \rangle_Q^{s/2} (s-1)!! \frac{s!}{2^{s/2} (s/2)!} & \text{if } s \text{ is even,} \end{cases} \quad (8.4)$$

where $!!$ denotes the double factorial, which, in this case, is the product of all odd numbers from 1 to $s - 1$. It can also be expressed in terms of factorials via [150]

$$(s-1)!! = \frac{s!}{2^{s/2} (s/2)!} \quad (8.5)$$

Inserting this into the characteristic function yields

$$\begin{aligned} \chi_Q(k_1, k_2) &= \langle 1 + \frac{i}{N}(k_1 \hat{S}_x + k_2 \hat{Q}_{yz}) \\ &\quad - \frac{1}{2N^2}[(k_1 \hat{S}_x + k_2 \hat{Q}_{yz})^2 + \langle \hat{C}^2 \rangle_Q] \\ &\quad - \frac{i}{6N^3}[(k_1 \hat{S}_x + k_2 \hat{Q}_{yz})^3 + 3(k_1 \hat{S}_x + k_2 \hat{Q}_{yz}) \langle \hat{C}^2 \rangle_Q] \\ &\quad + \frac{1}{24N^4}[(k_1 \hat{S}_x + k_2 \hat{Q}_{yz})^4 + 6(k_1 \hat{S}_x + k_2 \hat{Q}_{yz})^2 \langle \hat{C}^2 \rangle_Q + 3\langle \hat{C}^2 \rangle_Q^2] + \dots \rangle_Q. \end{aligned} \quad (8.6)$$

Sorting the terms by powers of $\langle \hat{C}^2 \rangle_Q$ leads to

$$\begin{aligned}\chi_Q(k_1, k_2) &= \langle 1 & [1 + \frac{i}{N}(k_1 \hat{S}_x + k_2 \hat{Q}_{yz}) - \frac{1}{2N^2}(k_1 \hat{S}_x + k_2 \hat{Q}_{yz})^2 + \dots] \\ &- \frac{\langle \hat{C}^2 \rangle_Q}{2N^2} & [1 + \frac{i}{N}(k_1 \hat{S}_x + k_2 \hat{Q}_{yz}) - \frac{1}{2N^2}(k_1 \hat{S}_x + k_2 \hat{Q}_{yz})^2 + \dots] \\ &+ \frac{1}{2} \left(\frac{\langle \hat{C}^2 \rangle_Q}{2N^2} \right)^2 & [\dots] - \dots \rangle_Q \\ &= \langle e^{\frac{i}{N}(k_1 \hat{S}_x + k_2 \hat{Q}_{yz})} \rangle_Q \cdot e^{-\langle \hat{C}^2 \rangle_Q / (2N^2)}.\end{aligned}\tag{8.7}$$

Using Eq. (6.19) we know that the fluctuations in the initially empty modes are given by $\langle \hat{A}^2 \rangle_Q = \langle \hat{B}^2 \rangle_Q = N/4$. Thus, we have $\langle \hat{C}^2 \rangle_Q = N(k_1^2 + k_2^2)$ and we finally get for the characteristic function

$$\chi_Q(k_1, k_2) = \langle e^{\frac{i}{N}(k_1 \hat{S}_x + k_2 \hat{Q}_{yz})} \rangle_Q \cdot e^{-(k_1^2 + k_2^2)/(2N)}.\tag{8.8}$$

Therefore, we obtain the characteristic function of the Wigner distribution times a Gaussian filter with a width of $1/\sqrt{N}$, which is exactly the definition of the Husimi distribution. In this measurement we splitted the populations equally between the two manifolds. In general one can also use arbitrary splitting ratios which then lead to more general, so-called squeezed Husimi distributions, where the Gaussian filter is unisotropic [134, 148].

Since the Wigner and Husimi distributions are mostly discussed in quantum optics they are usually restricted to two observables. In our case, we are able to extend the simultaneous readout to more observables. For example the spin-mixing dynamics is not only restricted to a single spin-nematic sphere but we could also include the measurement of \hat{S}_y and \hat{Q}_{xz} . In analogy, this should add more noise to the measurement of each component but should still contain the full information of the quantum state. Therefore, experimentally we can measure more general types of Husimi distributions which are not restricted to two observables. In this sense, a Husimi distribution can be viewed a representation of a quantum state in terms of measurement statistics which are experimentally accessible via a simultaneous readout.

Thus, one can either use standard projective measurements to sample the marginals from the Wigner distribution and, after tomography, reconstruct the Wigner distribution. Or, alternatively, one can use a simultaneous measurement of multiple observables to directly sample the Husimi distribution, which contains also the complete information about the quantum state. The question now arises which one is better at determining a given quantum state. As the Husimi function is a filtered version of the Wigner function this filtering is in principle reversible. However, to get the correct quantum state one needs a high measurement precision, as many quantum correlated states can look largely like classical states in the Husimi distribution. Therefore it is important to measure the high frequency components of the distribution, i.e. one has to measure with a very high atom number resolution in order to identify the correct state [37]. However, also for a precise reconstruction of the Wigner distribution out of a tomographic measurement, one needs a high atom number resolution to capture the quantum features of certain states. For example, to measure a cat state with standard projective measurements single-particle resolution is required. While there exists no general answer which of the two readout techniques is more efficient, it has been shown that for many states the direct

sampling of the Husimi distribution is more efficient at extracting higher moments of the Wigner distribution. We will summarize these results in the following.

8.2. Efficient detection of quantum state properties

In quantum optics the standard projective measurement corresponds to a homodyne measurement, where the signal field is combined on a beamsplitter with a strong local oscillator field of the same frequency. The difference signal on the photodetectors then contains a quadrature component of the signal beam. By tuning the phase of the local oscillator one can then set the readout to the desired quadrature. This is the optical analog of a spin rotation followed by a projective measurement. For a simultaneous readout of both quadratures heterodyne detection is used, where the signal field is mixed with a local oscillator at a different frequency. The resulting beating signal then contains information about the two conjugate quadratures [151]. In more recent experiments, one also uses a splitting of the signal field analogous to our method combined with homodyne measurements to simultaneously extract the two quadratures [152]. But such schemes are sometimes still referred to as heterodyne measurements.

In this quantum optical framework, there have been theoretical [153] and experimental studies [154] to assess which of the two methods is better for extracting certain properties of Gaussian states. In a two dimensional phase space the covariance matrix of the Gaussian Wigner function is given by

$$G_W = \mu \begin{pmatrix} 1/\lambda & 0 \\ 0 & \lambda \end{pmatrix} \quad (8.9)$$

where the axis of the phase space have been chosen to coincide with the principal axes of this squeezed state and where the vacuum noise has been normalized to 1. Here, λ corresponds to the squeezing parameter and μ is a phase independent noise contribution with $\mu \geq 1$. In an ideal homodyne measurement one draws samples from the marginals of this distribution, where the projection axis is parameterized by the unit vector $\vec{n} = (\cos \varphi, \sin \varphi)^T$. Therefore a projective measurement samples a distribution with a marginal variance

$$\sigma_\varphi^2 = \vec{n}^T G_W \vec{n}. \quad (8.10)$$

For a simultaneous readout we sample the corresponding Husimi distribution where the covariance matrix of the Wigner distribution is enlarged by the vacuum noise

$$G_H = G_W + \mathbb{1}_2. \quad (8.11)$$

Since we directly sample from the two-dimensional distribution the variance along a certain projection is quantified by the conditional variance

$$\Sigma_\varphi^2 = (\vec{n}^T G_H^{-1} \vec{n})^{-1}. \quad (8.12)$$

This conditional variance takes into account that the simultaneous readout also extracts information about the correlations of the two observables. If the additional noise in the Husimi distribution was absent, the conditional variance would always be smaller than the marginal variance and would only coincide along the principal axes of the elliptical distribution. This can be directly translated into the statement that the simultaneous

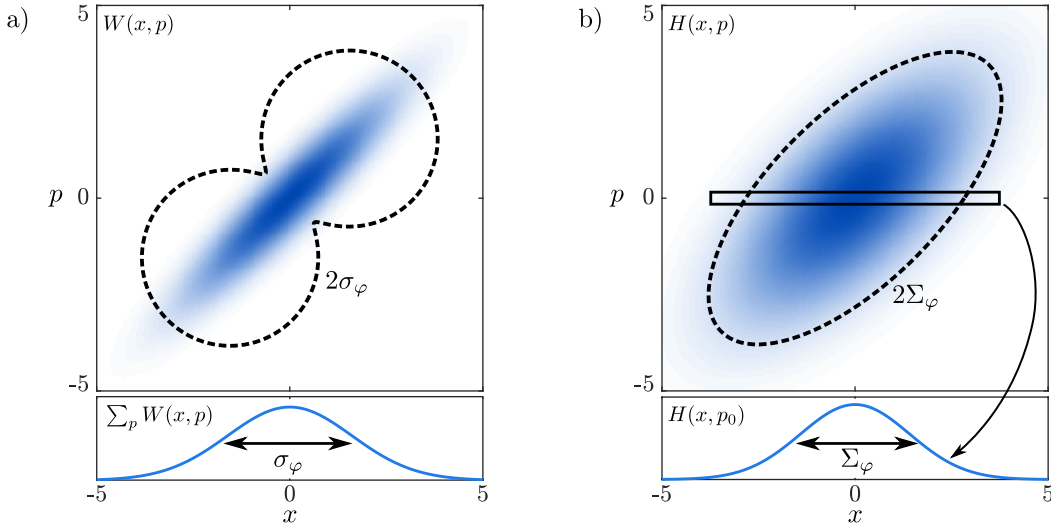


Figure 8.1.: **Uncertainties Wigner Vs. Husimi sampling:** a) The upper plot shows the Wigner distribution $W(x, p)$ of a pure squeezed state. In a projective measurement one tunes the projection angle φ and measures the corresponding marginal distribution $\sum_p W(x, p)$ (lower plot). The width of this distribution is characterized by the marginal standard deviation σ_φ . In this case, the accuracy of the state estimation is quantified by the average marginal variance over all projection angles. b) The upper plot depicts the corresponding Husimi distribution $H(x, p)$ of the same squeezed state. In a simultaneous readout one samples directly from the two-dimensional distribution, where the accuracy of the state estimation is quantified by the mean conditional variance Σ_φ^2 . The conditional variance corresponds to the width of the distribution for a fixed value of e.g. p_0 (lower plot).

readout would yield a more accurate estimator for the covariance matrix and with this for the quantum state [153].

However, including the additional noise of the Husimi distribution, it is not obvious, which method gives a more accurate estimate, i.e. whether the mean marginal variance of the Wigner is smaller than the mean conditional variance of the enlarged Husimi distribution (see Fig. 8.1). For a coherent state with $\mu = \lambda = 1$ we get $\Sigma_\varphi^2 = 2\sigma_\varphi^2$. Thus, for a coherent state it is better to sample the distribution with a projective measurement. In general, one can show that for all pure squeezed states ($\mu = 1$) the mean marginal variance of the Wigner distribution is smaller than the mean conditional variance of the Husimi distribution [153], which means that a projective measurement in this case is more efficient to extract the quantum state. However, this changes rapidly as soon as we add phase-independent noise to the state, i.e. $\mu > 1$. Then the simultaneous readout becomes more efficient than a projective measurement of the state. If we take as an example the spin-nematic squeezed state, fluctuations of q_{eff} would lead to $\mu > 1$ which would render a simultaneous readout more accurate to determine the covariance matrix of the state. Additionally, if one includes realistic detectors with efficiencies less than 1, then the simultaneous readout becomes also more efficient (except close to the coherent state), which has also been verified experimentally [154].

These results have also been generalized to first and second moment estimations for a wide range of states [155, 156]. There, it turns out that for the estimation of the first moment a simultaneous readout always outperforms a projective measurement scheme,

while their efficiency is only equal for minimal uncertainty states. For the estimation of the second-moment the analysis is more complex. But in most cases a simultaneous readout turns out to be advantageous for the estimation of the second-moment, even for non-Gaussian states such as Fock states.

8.3. Recording spin-mixing dynamics with a simultaneous readout

As our simultaneous readout gives us a direct access to the Husimi distribution without the need for state reconstruction, we can use it to follow directly the quantum dynamics of the spin-mixing process beyond the initial squeezing. We can then directly compare these results with the theoretical predictions given by the classical trajectories, which were a good description for the truncated Wigner simulation as shown in Sec. 4.5.

8.3.1. Single Mode dynamics

At first, we restrict the dynamics to a single spatial mode by tuning the process selectively into resonance with one mode of the effective potential. We use the same readout as for the squeezing measurement which maps the observable \hat{S}_x onto the population difference N_2^- in $F = 2$ and the observable \hat{Q}_{yz} onto the population difference in N_1^- in the $F = 1$ hyperfine manifold. In the upper part of Fig. 8.2 we show the long time dynamics of the ground mode. Starting from the distribution of the initial polar state (which is slightly distorted due to the technical fluctuations discussed before), the state follows the classical trajectories as indicated by the separatrix. After 400 ms the state becomes clearly non-Gaussian which we can resolve by just using around 150 experimental realizations, which is much less than required for quantum state tomography and state reconstruction. After 600 ms the state is spread over the spin-nematic sphere, which we also observed for the truncated Wigner simulation (see Fig. 4.3). We recall, that this spreading is caused by the randomization of the Larmor phase. Afterwards the state refocuses again and the cycle starts anew. This is a manifestation of the coherent nature of the spin-mixing process which has also been observed via coherent oscillations of the population in the state $(1, \pm 1)$ [157]. But here, we observe these coherent oscillations directly for the two-dimensional distribution.

We now tune the spin-mixing process into resonance with the first excited spatial mode of the effective potential to check whether this mode also follows the mean-field trajectories. For this mode we evaluate the relative atom number difference, i.e. $N_F^{-,1} = n_{F,L}^- - n_{F,R}^-$ in each manifold. The result is shown in the lower part of Fig. 8.2. Similarly to the dynamics in the ground mode we find that the state follows the classical trajectories. Since the mode overlap reduces the strength of the coupling the dynamics are a bit slower as the one in the ground mode. Additionally, we have to rescale the size of the phase space. This is because the spin-mixing process does not change the overall shape of the condensate, meaning that even after long evolution times we do not observe that the shape of the condensate transforms to the first excited spatial mode. This would also not be possible since the energy for such a process would be on a completely different level. This in turn means that even at $q_{\text{eff}} = 0$ the states $(1, \pm 1)$ cannot be populated by all atoms but just by a fraction which is determined by the mode overlap. Similarly the maximal transversal spin length will be restricted to this fraction. Thus, we rescale the

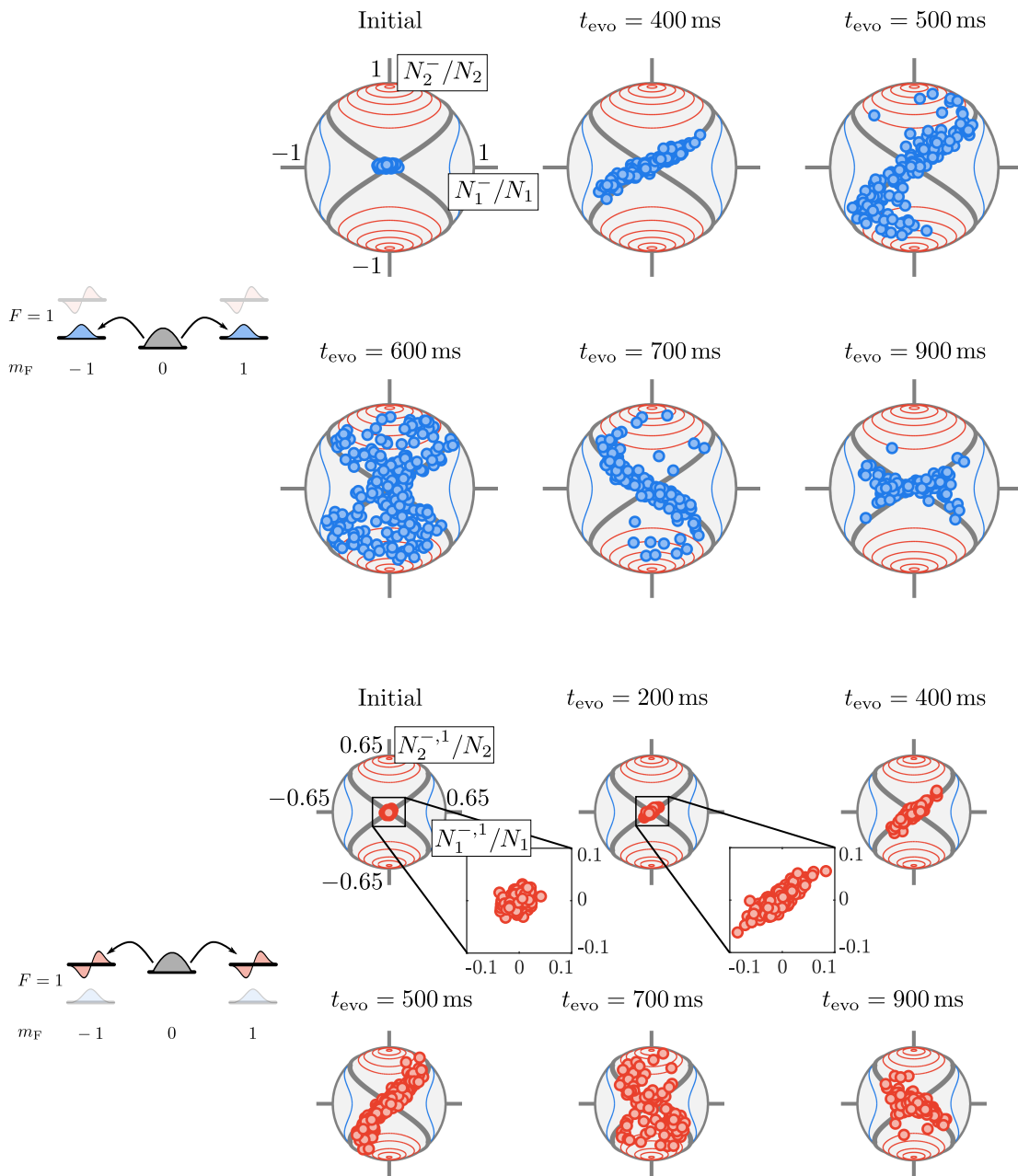


Figure 8.2.: Single mode dynamics of spin-mixing: For the upper part we tune the spin-mixing process selectively into resonance with the ground mode. We find that the initial state spreads along the classical trajectories of the phase space. Using our readout technique we directly (without state reconstruction) observe the emergence of a non-Gaussian state after 400 ms of evolution time and the refocusing of the state after 700 ms. For the lower part we tuned spin-mixing into resonance with the first excited spatial mode. We find that the dynamics in this mode also follow the classical trajectories given the phase space is scaled by the mode overlap between the condensate and the first excited mode, which we take from Fig. 4.6.

phase space by 0.65 which is the overlap we experimentally extracted in Fig. 4.6c). With this argument we find that the dynamics are well described by the classical trajectories and also feature coherent dynamics.

8.3.2. Corrections of phase imprint

For the dynamics shown in Fig. 8.2 we noticed that the phase imprint has not been correctly set to $\pi/2$ but was slightly off by about $\delta = 0.05\pi$. Therefore, the readout in $F = 1$ does not measure \hat{Q}_{yz} but

$$N_1^- = \frac{1}{2}[\cos(\delta)Q_{yz} + \sin(\delta)S_x]. \quad (8.13)$$

This leads to a distortion of the measured distribution such that the distribution that has spread over the spin-nematic phase space will not be symmetric if we divide the phase space along the $\hat{S}_x - \hat{Q}_0$ -plane. Similarly, the outgoing state will have a different angle to this plane on one side than on the other. But since we also have measured the value of S_x we can correct for that shift, which leads to the distributions shown here.

8.3.3. Beyond single mode dynamics

To examine the dynamics beyond the single mode approximation we tune the dynamics simultaneously into resonance with the two energetically lowest spatial modes of the effective potential and use our mode selective readout to observe the dynamics of each mode. This is shown in Fig. 8.3. For short evolution times of 250 ms we find that the ground mode follows the classical trajectories while the first excited mode clearly deviates from the single-mode trajectory which could be caused by the competition of the two modes. For longer evolution times the ground modes starts to deviate from the mean field trajectories and after 700 ms we see no coherent evolution anymore but the ground mode develops strong fluctuations along the S_x -direction. Even after an evolution time of 2 s the distribution remains qualitatively unchanged.

The large fluctuation along the S_x -direction indicates a relaxation of the state towards a finite transversal spin length which approximately corresponds to the minimum of the mean field energy. The large fluctuation would then come from a randomization of the Larmor phase since we only measure one spin direction. In experiments in the waveguide, we have already seen by simultaneously measuring \hat{S}_x and \hat{S}_y that the transversal spin length relaxes during the spin-mixing dynamics to some finite value [131]. There, however, the spin-mixing dynamics involve many spatial modes while in our case only two modes are initially in resonance. Still even in the XDT setting with the finite energy spacing of the spatial modes we find indications of a similar relaxation dynamics. To finally confirm this we would need to measure also in this setting both directions of the transversal spin. A truncated Wigner simulation with two competing modes in the states $(1, \pm 1)$ is not capable of reproducing the observed result. This points to some additional interactions between the modes which are not included in the simulation. This setting might be interesting for a study at the onset of multimode dynamics.

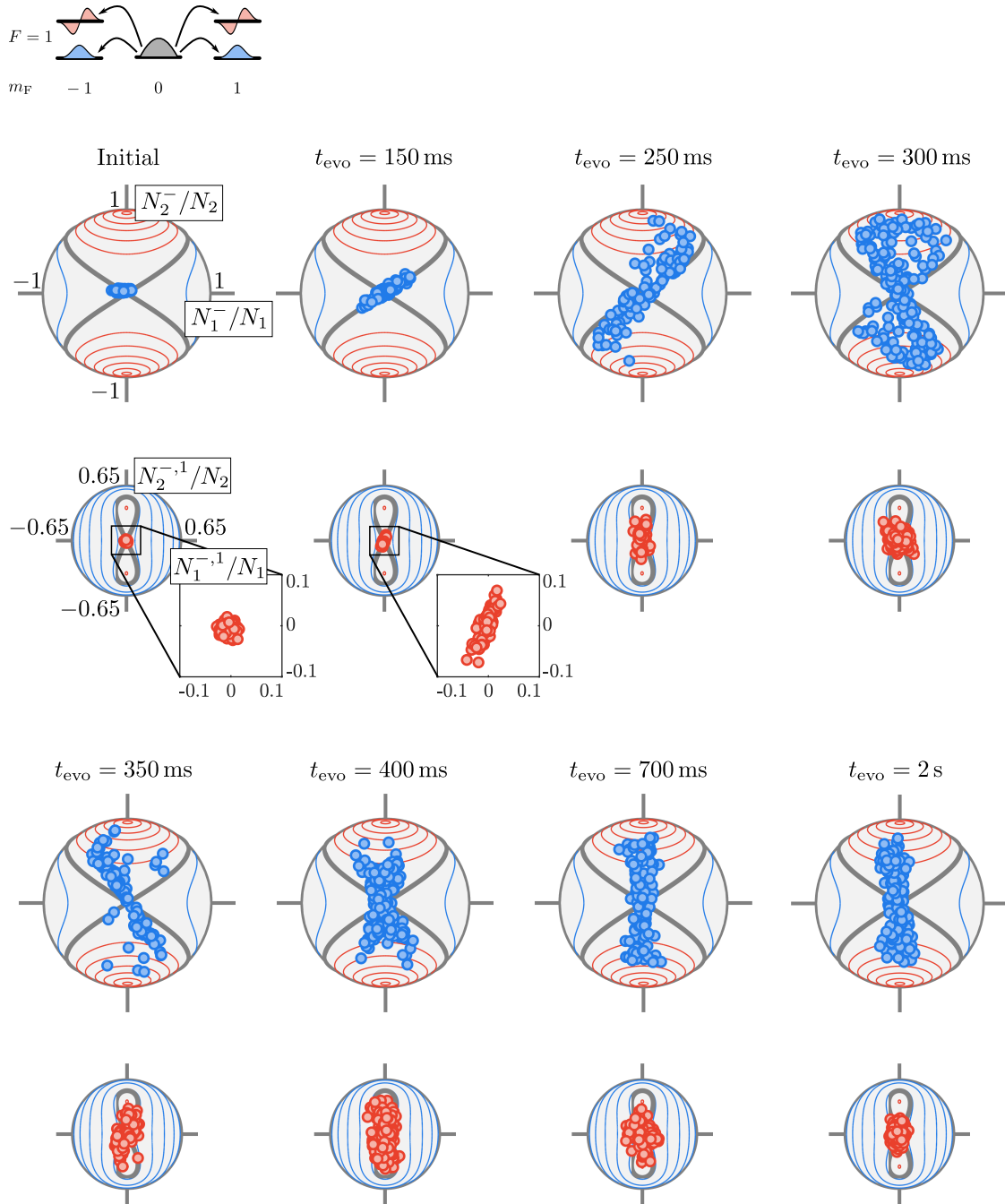


Figure 8.3.: Multimode dynamics of spin-mixing: We tune the spin-mixing process simultaneously into resonance with the ground and the first excited spatial mode. The short-time dynamics up to 150 ms are still consistent with the single-mode model. After 400 ms we observe no coherent dynamic and we measure large fluctuations in the ground mode along the S_x direction. This distribution persists up to 2 s of evolution time.

9. Outlook

In this thesis, we demonstrated that the local contact interactions in a BEC can be harnessed to generate entanglement between spatially separated regions. Starting with a spin-nematic squeezed state in a single spatial mode, we showed that these correlations are distributed in space by expanding the atomic cloud, which makes the entangled subsystems individually addressable. Demonstrating EPR steering between the different partitions of the atomic cloud certifies that the prepared state can be used as a resource in quantum information tasks. This extends the application of spin-squeezed states beyond metrological tasks and demonstrates that entanglement between identical particles provides indeed a useful resource for quantum information protocols.

Additionally, we have developed a new readout method which is based on coupling the spin state to the initially unoccupied states of the $F = 2$ manifolds. Together with selective spin rotations, this enables the readout of multiple spin-1 observables in a single projective measurement of this extended Hilbert space. While the coupling to the $F = 2$ manifold introduces additional binomial fluctuations, we could demonstrate that the readout is still capable of detecting quantum correlations. In principle, it is even possible to verify entanglement between spatially separated regions using a simultaneous readout scheme. In fact, the readout provides a complete description of the quantum state, since it corresponds to a direct sampling of the Husimi function. This offers an alternative to the commonly employed tomographic procedures to reconstruct the Wigner distribution. In the spatially extended system we have seen that this readout allows the extraction of spatial correlations between multiple spin observables. This is not only valuable for the detection of entanglement but also provides a new tool to study many-body dynamics far from equilibrium [22, 158]. Since the dynamics in these systems can be characterized in terms of correlation functions, our readout technique opens up the possibility to study correlations between orthogonal spin directions which turns out to be essential for the many-many dynamics induced by spin-mixing [159, 131].

In the following, we will again focus on the quantum informational implications of this work which provide the possibility of studying the generation of cluster states. In this context, we lay out a possible roadmap for using BECs for quantum information processing.

9.1. One-way quantum computation

So far, the implementation of quantum computation has been mainly concentrated around the circuit model. There, the basic idea is straightforward: just replace the classical bits by quantum mechanical two level system (qubits) and develop a universal set of elementary operations (quantum gates) to implement computational algorithms [34] (see Fig. 9.1a)). However, in contrast to classical bits, which can only have the values 0 and 1, qubits can also be in an arbitrary superposition of these two states, requiring a very high precision for the control of the qubit state. Moreover, a universal set of gates includes an entangling operation between an arbitrary pair of qubits. So far, the maximum number of qubits

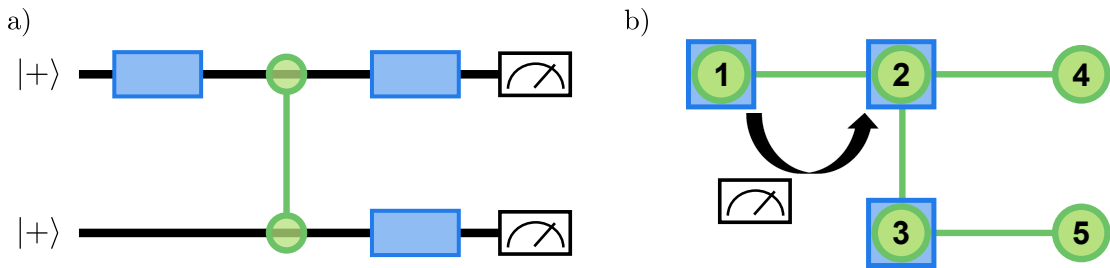


Figure 9.1.: Circuit vs. measurement based quantum computation: a) In a circuit based quantum computer one uses single qubits as input states. Using a complete set of one- (blue boxes) and entangling two-qubit (green lines) gates makes it possible to implement arbitrary unitary transformations which enable universal quantum computing. A final measurement in the computational basis yields the result of the quantum computation. b) In a measurement based quantum computer one initially prepares a highly entangled state, a so-called cluster state which is represented by a graph. This state is usually prepared via two-body interactions between the subsystems (1-5) as indicated by the green lines. The graph shown here realizes the same computation as the circuit shown in a). In this scheme, computation is performed by manipulations of single subsystems and subsequent readout which has then to be forwarded to set the unitary transformation in the following subsystem.

that are fully controlled are limited to 20 [160], which is far below the number required to surpass classical computers. Thus, the question is still unresolved whether the circuit model is scalable [161].

An alternative route is provided via the concept of one-way computation [21]. There, prior to the computation, a highly entangled cluster state is generated, which is represented by a two-dimensional graph as shown in Fig. 9.1b) and which is tailored to the specific algorithm one wants to implement [162]. Computation is then achieved by going in a specific order through the subsystems (represented by the nodes of the graph) and implementing a local unitary transformation in each subsystem followed by a local measurement. The unitary operation on subsequent systems is conditioned on the measurement results obtained in the previous ones. The main advantage of this scheme is that universal quantum computation can already be implemented with single qubit operations as the necessary entanglement structure is already contained in the initial cluster state (green lines in the graph). This expands the possibility of quantum computation to new systems where the preparation and control of large numbers of particles is well studied but where the online generation of entanglement is usually hard to achieve such as optical [72] and ultracold atomic systems [163, 164].

On top of that, one-way computation is not restricted to qubit systems but can also be extended to continuous-variable systems, where each node contains many-particles [165, 17, 166]. With this, one can exploit the advantages of continuous-variable systems such as unconditional entanglement generation. In optical systems, it has already been demonstrated that it is possible to implement basic computational operations [167, 168, 169] and to generate large cluster states with up to a million nodes [170, 171]. The weak interactions in photonic systems, however, limit the amount of entanglement that can be generated and with this the possible structure of the cluster state. Moreover, photons

cannot be stored which causes additional constraints on the implementation of quantum computing.

In this respect, atomic systems offer unique advantages as they feature stronger interactions than photonic systems and are routinely trapped with long coherence times. While indications of cluster state correlations have already been observed with a BEC trapped in an optical lattice potential [163], the systematic study of these states has so far been restricted to photonic systems. In the following, we will outline how the interatomic interactions could be exploited for the generation of cluster states.

9.2. Cluster state generation

In fact, a state that features EPR steering is equivalent to a two-node cluster state [119]. One-way computation is built on these correlations which cause that a measurement on given node steers the state of the subsequent nodes. By knowing the measurement result and therefore the state, one can then adjust the subsequent measurements to implement a specific algorithm on a given cluster state.

Before presenting two possible schemes for the generation of cluster states, we provide more details about the definition of a cluster state and its correlations. In general, a cluster state is represented by a graph which is determined by its edges (E) and vertices (V) [172]. The hallmark of such a graph state is that the measurement results at a given vertex in one observable, e.g. \hat{S}_x , are correlated with the measurement results in the conjugate basis \hat{Q}_{yz} of the connected vertices and similarly anticorrelated in the respective conjugate observables. Thus, strictly speaking, steering has different correlations, but for the bipartite state we can redefine the operator in one subsystem, e.g. B, such that $\hat{F}_B(\phi_S) \rightarrow \hat{F}_B(\phi_S + \pi/2)$.

In general, the vertices of the cluster state form a genuinely m -partite entangled state with correlations of the type [173, 174]

$$\Delta^2 \left[F_a(0) - \sum_{k \in \mathcal{N}(a)} F_k(\pi/2) \right] \rightarrow 0 \quad \forall a \in V \quad (9.1)$$

in the case of perfect correlations. Here, $\mathcal{N}(a)$ denotes all vertices connected to the given vertex a . Therefore, the detection of a cluster state usually requires the ability to set locally different measurement bases. Here, the simultaneous readout developed before provides a first check if such correlations are indeed present in an experimentally generated state.

9.2.1. Lattice potential

In our system we have the possibility to switch on a 1-dimensional lattice potential (for details see [78, 79]). This allows us to load the atoms, for example, from the waveguide potential into an array of wells, which we could treat as the nodes of a graph state (see Fig. 9.2). To generate the links between these nodes, it has been shown that it is sufficient to employ local squeezing together with beamsplitting operations between the neighboring wells [173]. In our case, this would mean to first use spin-mixing to generate a squeezed state in each lattice site and in a second step to lower the lattice potential to induce tunneling between neighboring sites, which realizes the beam-splitting operation. In this situation, however, some sort of local control would be needed as the squeezing ellipses of neighboring sites need to be oriented in orthogonal directions with respect

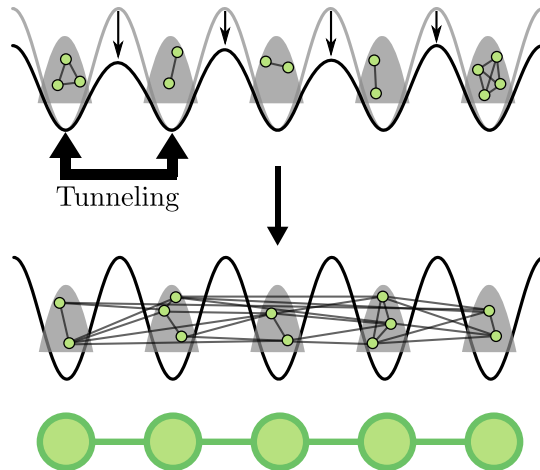


Figure 9.2.: Generation of cluster states in a lattice potential: To generate a linear cluster state we can load the BEC into 1D optical lattice. Using spin-mixing in each lattice we generate a locally entangled state. By lowering the trapping potential to enable tunneling, this entanglement spreads between the lattice sites which generates a linear cluster state.

to each other. Such schemes have already been demonstrated in optics for a first test of quantum gates [174, 167, 168, 169]. The experimental control over the spin-mixing interactions has the additional advantage that one can apply the squeezing operation again after the tunneling. This additional squeezing operation should yield a more entangled cluster state and therefore a better resource for quantum computation [173].

9.2.2. Multimode dynamics

It has been theoretically [175, 176] as well as experimentally [177] demonstrated that also multi-mode dynamics provide ways to generate computationally useful cluster state structures beyond linear graphs. In our setting, we can explore these possibilities by tuning spin-mixing into resonance with multiple spatial modes of the effective potential as shown in Fig. 9.3. After the expansion of the cloud we can then use the simultaneous readout technique to test for cluster state correlations between different spatial regions of the expanded condensate. As shown before, the mode overlap in the effective potential is experimentally well controlled. By tuning this parameter as well as q_{eff} we can experimentally test different settings for the reliable generation of cluster states. After the expansion we additionally have the possibility to retrap the atoms in the optical lattice potential for further manipulations of the generated state.

9.3. Local control

While the simultaneous readout provides a powerful tool for testing correlations between conjugate observables and finding the correlated measurement bases, a local probing and manipulation scheme is required to use a cluster-state for one-way computation. Experimentally, we have already implemented a setup to locally control the spin-states of the atoms using light-shifts from a detuned laser (see [178]). With these light shifts it is possible to induce local spin rotations as well as tuning an atomic sample locally in and

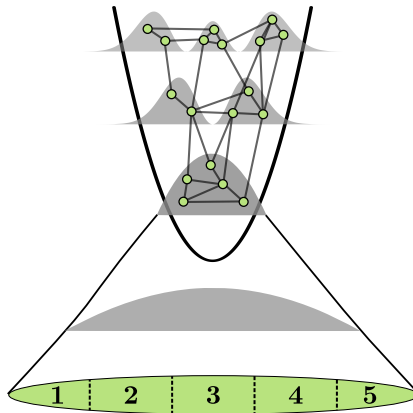


Figure 9.3.: Generation of cluster states via multimode dynamics: The generation of complex cluster states beyond linear chains usually requires multimode dynamics. In our setup this can be realized by tuning the spin-mixing into resonance with multiple external spatial modes. After expansion we can then check the resulting correlations using the simultaneous readout technique.

out of resonance for mw-coupling. This enables a local manipulation of the mw dressing and therefore provides a local control of the spin-mixing interactions as well as of the spinor phase evolution. This provides nearly all operations for a universal set of gates for one-way computation with Gaussian states [17]. However, for a complete set at least one non-Gaussian interaction is required, i.e. which is described by a Hamiltonian that is at least cubic in one operator. In quantum optics, this is usually achieved by using photon counting instead of homodyne detection. In an atomic system, one could instead use the interactions, for example, spin-mixing beyond the undepleted pump approximation which also introduces a non-Gaussian operation. Therefore, ultracold atomic systems offer new possibilities for the study of quantum computation given the interatomic interactions and the high level of control.

A. Technical parameters and imaging calibration

This chapter provides characterization measurements of experimental components, such as trapping frequencies and stability measurements of the magnetic field.

A.1. Trap frequencies

In this section the results of the trap frequency measurements are presented which we use as a characterization of the trap geometries. For further details on the dipole beams and the trapping potentials see [79]. The dipole traps in the experiment are generated by focused Gaussian laser beams. Thus, we can change the trapping frequencies by tuning the power of both beams, which we control via AOMs. The power in each beam is stabilized by diverting, directly after the optical fibers, a small fraction of the beam onto a photodiode (PD) which we use as the input signal of a control loop. We then tune the power of the beams by changing the set point of this control loop.

Longitudinal trap frequencies

To measure the trap frequency of the XDT, we employ the following sequence. The horizontal position of the XDT can be adjusted via a Piezo-controlled mirror. With this we slightly displace the position of the XDT before loading the atoms from the magnetic trap into the crossed dipole trap. After condensation we switch the position back to the original one and record the longitudinal displacement δy of the condensate. By displacing the condensate just by $\approx 2 \mu\text{m}$ we ensure to stay in the quadratic regime of the optical trap. The oscillation frequency yields then directly the trapping frequency. The upper plot in Fig. A.1 shows the measured signal. In order to save time for taking the data but still get a high precision on the frequency measurement, we sample a few oscillation periods at the beginning and then again after 500 ms.

We measure the trap frequencies for four different power settings on the photodiode. For a Gaussian beam the trap frequency should be proportional to the square root of the power which we use to fit the measured signal (see lower plot in Fig. A.1). From the fit we extract the relation

$$\omega_{\parallel} = 2\pi \cdot 22.9 \text{ Hz} \sqrt{\text{PD/V}} \quad (\text{A.1})$$

from which we read off the longitudinal trapping frequencies for a given PD power of the XDT.

Transversal trap frequencies

The transversal trap frequency is mainly determined by the power of the waveguide, whereas the power of the XDT has only a minor influence. Similar to before we measure

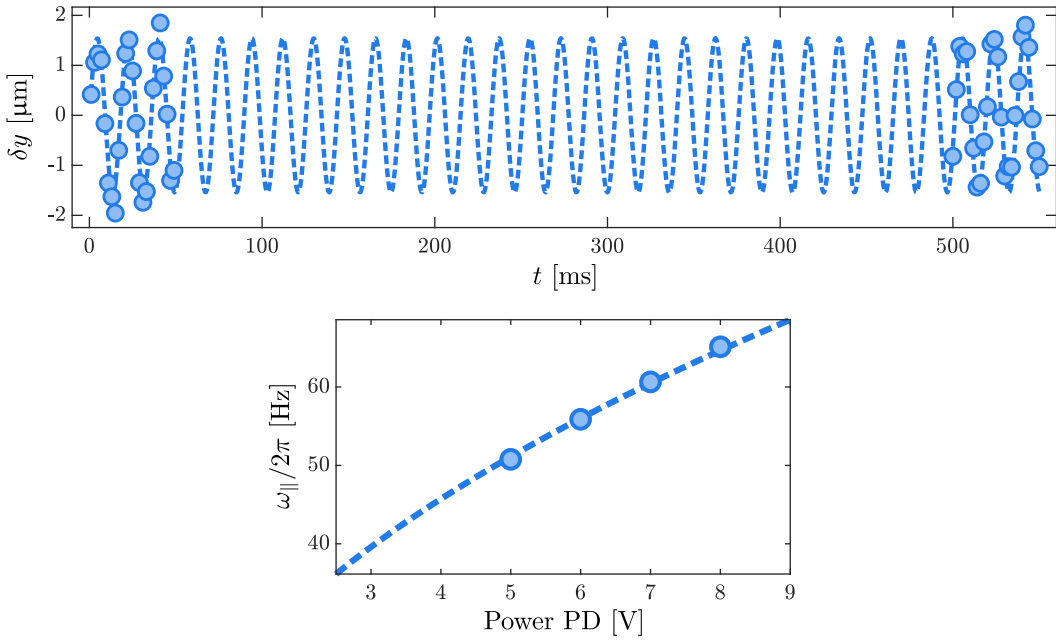


Figure A.1.: Measurement of the longitudinal trap frequencies: We use a Piezo-controlled mirror to switch the horizontal position of the XDT. Afterwards we measure the oscillations of the BEC position (δy) in longitudinal direction vs waiting time t . The upper plot shows an example of the measurement signal. The displacement of $\approx 2 \mu\text{m}$ is sufficiently small to stay in the harmonic part of the potential. In the measurement we just sample a few periods at the beginning and then again after 500 ms to increase the precision of the frequency measurement while reducing the amount of experimental realizations. The dashed line is a fit to the data to extract the trapping frequency. In the lower plot the extracted trapping frequencies for different beam powers as measured on the photodiode (PD) are shown. As the trap frequency is proportional to the square root of the power, we fit the data with the corresponding function. This curve (dashed line) provides a reference to read off the trapping frequencies at a given PD power.

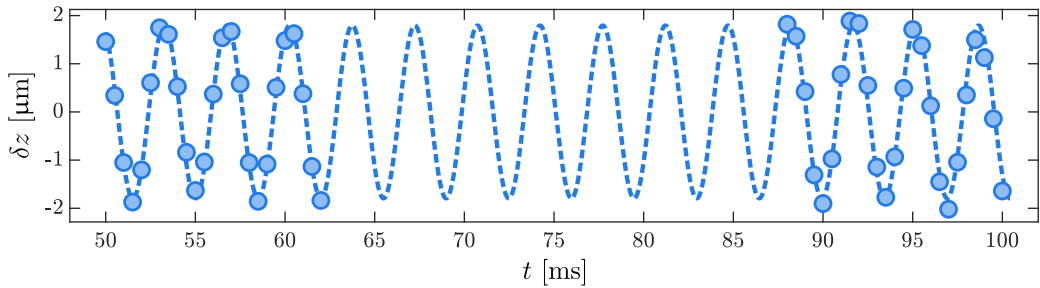


Figure A.2.: Measurement of transversal trap frequencies: After shortly switching off the waveguide, the atoms are recaptured and we record the oscillating vertical position δz of the BEC. The measurement shown here has been taken for a measured power of 4 V and from the fit (dashed line) we extract a transversal trap frequency of 286 Hz.

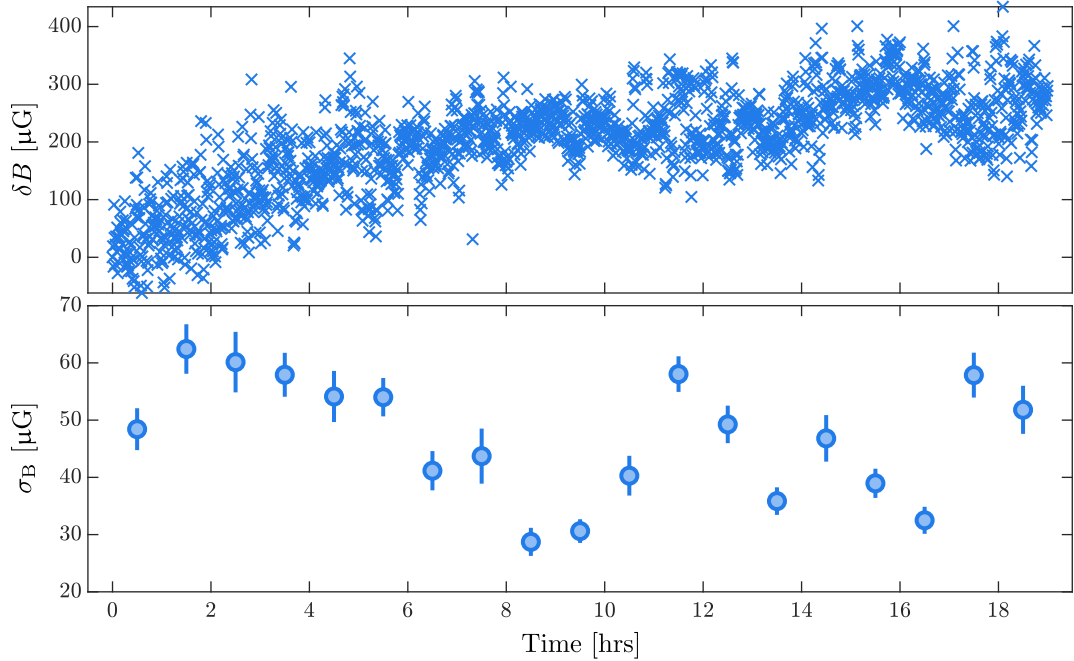


Figure A.3.: Long-time measurement of the magnetic field: Using a Ramsey-type sequence as described in the main text (Sec. 3.6) we measure the magnetic field over many hours to characterize its stability. Over the course of 19 hours the magnetic field drifted by about $300 \mu\text{G}$ (upper plot) which is mainly caused by temperature changes in the electronics. In a standard measurement protocol, we employ, in intervals of around one hour, a control measurement to compensate this drift. Evaluating the fluctuations of the magnetic field in a one-hour time window (lower plot) yields a value of around $\sigma_B \approx 50 \mu\text{G}$.

this frequency via oscillations of the BEC in the harmonic potential. After evaporation we shortly switch off the waveguide for $500 \mu\text{s}$ to let the atomic cloud fall under gravity for a short distance. Subsequently, we recapture the atoms and record the oscillation of its vertical position δz . An exemplary measurement for a power at the photodiode of 4 V is shown in Fig. A.2. We again limit the amplitude of the oscillation to a few μm to stay in the harmonic part of the potential. With such measurements we extract the following values for the transversal trap frequencies

PD [V]	$\omega_\perp/2\pi$ [Hz]
2	170
3	221
4	286

The error on the trap frequency measurements are typically on the order of a few Hz. For the lowest trap frequency of 170 Hz we additionally find a reduced heating of the atomic sample.

A.2. Stability of the magnetic field

To measure the stability of the magnetic field, we use a Ramsey-type sequence similar to the control sequence as described in Sec. 3.6. For this measurement we set the magnetic

field to 1.994 G. Starting from the state $(1, -1)$ we employ a $\pi/2$ mw pulse coupling this state to $(2, 0)$ where we detuned the mw from resonance by 357 Hz. After $\tau_R = 700 \mu\text{s}$ of phase evolution time we use another $\pi/2$ mw pulse coupling these two states and record in the end the population imbalance $N_{1,2}^-/N = (N_{2,0} - N_{1,-1})/N$. Neglecting the phase evolution during the first mw pulse (with a duration of $37 \mu\text{s}$) one would expect no imbalance in the case that the experimental magnetic field has no offset from the set value. Out of the imbalance we calculate the deviation of the real magnetic field via

$$\delta B = -\frac{\arcsin(N_{1,2}^-/N)}{2\pi\tau_R \cdot g_{1,1}} \quad (\text{A.2})$$

where $g_{1,1}$ is the g-factor of the $F = 1$ hyperfine manifold. We measured the magnetic field over the course of 19 hours which is shown in Fig. A.3. During this measurement the drift in the magnetic field is compensated. Otherwise the magnetic field could drift out of the sensitivity region of this measurement. But by keeping track of these changes we reconstruct together with the measured imbalances the magnetic field over the whole course of the measurement. During this measurement we find a drift of $\approx 300 \mu\text{G}$ of the magnetic field which is mainly caused by temperature changes.

In the experiment these drifts are usually compensated by employing a control measurement every hour. Thus, we are interested in the remaining fluctuations in between the control measurements. We therefore partition the measured signal in one-hour intervals and determine in each the magnetic fluctuations as shown in the lower plot of Fig. A.3. With this we find mean fluctuation of the magnetic field on the order of $\sigma_B \approx 50 \mu\text{G}$.

A.3. Imaging calibration

We use two different imaging calibrations for the experiments described in Ch. ?? and in Ch. 6, since, in between, we changed the optical path of the imaging light which can affect the imaging parameters. As explained in the main text, the imaging calibration is an essential part for measuring quantum correlations since a wrong calibration results in fluctuations, that are for example lower than the standard quantum limit even for a coherent spin state. Details of the imaging system and the derivation of the formulas can be found in [82, 78]. As explained in the main text, in each experimental realization we take multiple images where the first two are used to measure the absorption signal of the atoms in $F = 1$ and $F = 2$. Additionally, we take two images without atoms as a reference. Out of the measured photon numbers from the atomic signal I_{atom} and from the reference image I_{ref} , we extract the atom number in each pixel via

$$n_{\text{px}} = \left[\frac{1}{c_{\text{cl}}} \ln \left(\frac{I_{\text{atom}}}{I_{\text{ref}}} \right) + c_{\text{sat}} \frac{I_{\text{atom}} - I_{\text{ref}}}{\tau_L} \right] \cdot \frac{d_{\text{px}}^2}{\sigma_0}, \quad (\text{A.3})$$

where d_{px}^2 is the area of a pixel, σ_0 is the scattering cross section and τ_L is the duration of the imaging pulses. This formula is basically the Beer-Lambert law (first term) including saturation effects (second term). To experimentally calibrate the readout, we tune in the post-analysis the two parameters c_{cl} , which is connected to the imaging transition dipole moment, and c_{sat} , which is connected to the saturation intensity of the imaging transition. For the calibration of these two parameters we prepare a coherent spin state and exploit the fact that, for a correct calibration, the measured variance should be given by the shot

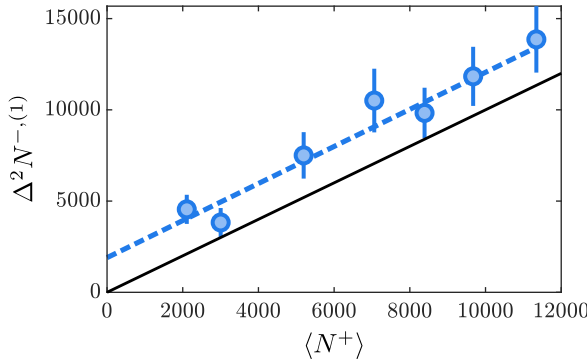


Figure A.4.: **Imaging calibration for the steering measurement:** After preparing a coherent state involving the states $(1, \pm 1)$ we evaluate the fluctuations of $N^{-,(1)}$ as a function of the mean atom number $\langle N^+ \rangle$. We find a slope of 1.0 ± 0.1 which is consistent with the value extracted from a measurement in the optical lattice.

noise limit. Since the measured variance also contains other noise contributions from the imaging, we vary the number of atoms which, for a correct calibration, should then give a linear dependence with slope 1. By going to higher atom numbers we can also determine the technical fluctuations of the coupling pulses involved in the calibration measurement as this would lead to a quadratic dependence.

Additionally, we systematically vary the imaging intensity. For lower intensities the saturation term in Eq. A.3 becomes negligible which we use to determine the parameter c_{cl} . For high imaging intensities the main contribution to the measured atom number comes from the saturation term which in turn is used to determine the value of c_{sat} . Experimentally, however, a higher imaging intensity also entails higher noise contributions from the imaging, such as optical fringes. The high noise can make a variance analysis difficult. Alternatively, we can also analyze the mean atom number. After having fixed the value of c_{cl} at low imaging intensities we adjust c_{sat} such that we measure for each imaging intensity the same mean atom number at a fixed atom number setting. This analysis is much more resilient to additional imaging noise contributions.

A.3.1. Imaging calibration for steering measurement

To calibrate the imaging parameters for the steering measurement, we prepared the condensate in an optical lattice potential. The lattice depth has been set to a very high value such that we get ≈ 35 independent BECs with atom numbers in the range from 100 to 700 atoms. This preparation has the advantage that we can acquire higher statistics for the same measurement time than by just generating a single condensate in each experimental realization. For preparing the coherent state we employed a mw $\pi/2$ pulse coupling the states $(1, -1) \leftrightarrow (2, 0)$ to split the population between the two states. A subsequent mw $\pi/2$ pulse transfers the population from $(2, 0)$ to the state $(1, +1)$. As in the steering measurement we then evaluate the fluctuations $\Delta^2 N^-$ of the atom number difference $N^- = N_{1,+1} - N_{1,-1}$ and compare it to the shot-noise limit given by the mean atom number $\langle N^+ \rangle = \langle N_{1,+1} + N_{1,-1} \rangle$. We tune the imaging parameters such that we measure for each imaging intensity $\Delta^2 N^- = 1 \cdot \langle N^+ \rangle + c$ with some finite offset c that contains contributions from photon shot-noise and additional imaging noise.

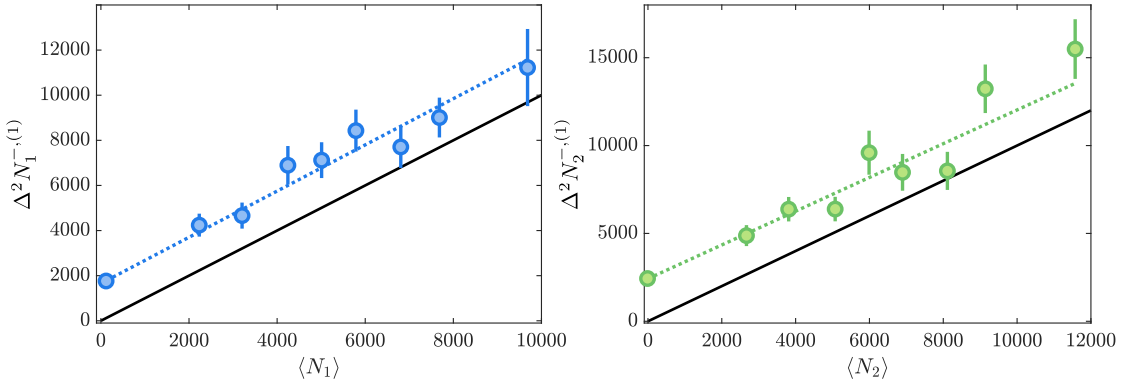


Figure A.5.: Results of the imaging calibration for the simultaneous readout: The left and right panels show the atom number fluctuations vs the total atom number measured in $F = 1$ and $F = 2$, respectively. The dashed lines are linear fits to the data while the black lines are the theoretical expectation for a coherent state without photon shot-noise contribution. This plot has been taken and adapted from [123]

As the trap geometry and the atom numbers are different for the actual steering measurement, we check the extracted imaging parameters by preparing a coherent state in the crossed dipole trap. Starting from the state $(1, -1)$ we use two mw pulses coupling the states $(1, -1) \leftrightarrow (2, 0)$ and $(2, 0) \leftrightarrow (1, 0)$. For the second pulse we use a fixed π pulse while we vary the length of the first pulse. Together with a magnetic field gradient (Stern-Gerlach pulse) which expels residual atoms in the magnetic substates $m_F \neq 0$ we adjust the total atom number N in the state $(1, 0)$. Subsequently, an rf $\pi/2$ -pulse is used to prepare an equal superposition of the states $(1, \pm 1)$. To suppress technical fluctuations we evaluate the fluctuations of $N^{-,(1)} = N^{-,L} - N^{-,R}$. In this measurement, we consistently find a slope of 1.0 ± 0.1 as shown in Fig. A.4.

A.3.2. Imaging calibration for simultaneous readout

This part has been taken from the supplemental material in [123] and adapted to the notation used in this thesis. To check the calibration of our imaging we prepare a coherent spin state with approximately equal mean atom numbers in the states $(1, \pm 1)$ and $(2, \pm 2)$. Starting from the state $(1, -1)$ we use two mw pulses coupling the states $(1, -1) \leftrightarrow (2, 0)$ and $(2, 0) \leftrightarrow (1, 0)$. For the second pulse we use a fixed π pulse while we vary the length of the first pulse. Together with a magnetic field gradient (Stern-Gerlach pulse) which expels residual atoms in the magnetic substates $m_F \neq 0$ we adjust the total atom number N in the state $(1, 0)$. Subsequently, an rf $\pi/2$ -pulse is used to prepare an equal superposition of the states $(1, \pm 1)$. These populations are then again split with two mw $\pi/2$ pulses coupling the states $(1, \pm 1) \leftrightarrow (2, \pm 2)$. This preparation leads to an equal probability of $1/4$ to find an atom in one of the four states.

Analogous to the squeezing measurement we divide the atomic signal into two halves and extract the atom number difference $N_F^{-,L/R} = n_{F,+F}^{L/R} - n_{F,-F}^{L/R}$ in each half and for each manifold $F = 1, 2$. To mitigate the technical noise contribution we subtract the value of the right half from the one of the left to obtain $N_F^{-,(1)} = N_F^{-,L} - N_F^{-,R}$. For each setting of the atom number we compute the variance $\Delta^2 N_F^{-,(1)}$ and plot it vs. the measured mean atom

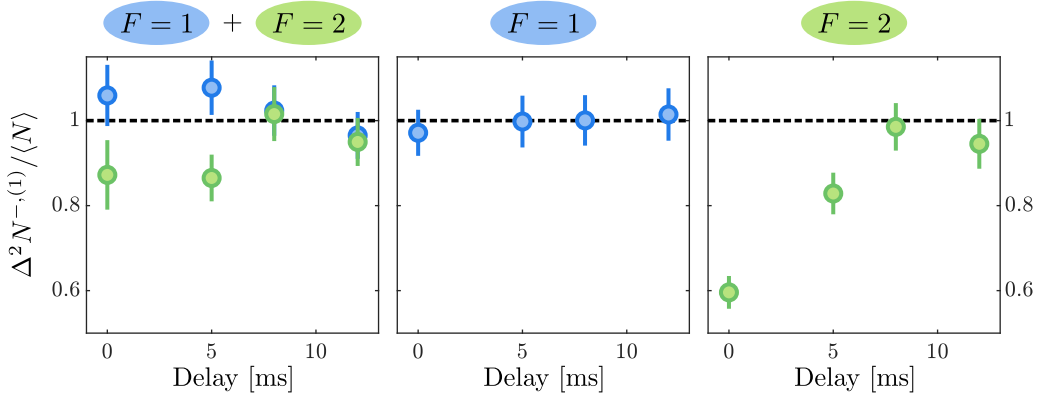


Figure A.6.: Buildup of correlations between the two halves during expansion: We varied the timing of the readout pulses with respect to the switching of the XDT for expansion. Here, 0 ms delay corresponds to applying the readout pulses 2 ms before switching off the XDT to expand the atomic cloud. As we employ an expansion time of 10 ms, a delay of the readout pulses by 12 ms corresponds to applying the pulses directly after the expansion and shortly before the imaging. In the case where only the $F = 2$ manifold is populated, we find a strong dependence on the timing of the pulses. In the case where both manifolds are populated we find a small dependence for the $F = 2$ manifold. For this measurement we employed a higher atom number of ≈ 17.000 atoms. Thus, we expect that for the squeezing measurement at lower atom number the effect has already saturated, which is consistent with the calibration measurement.

number $\langle N_F \rangle$ in the respective manifold as shown in Fig. A.5. For a coherent state one expects to find multinomial fluctuations of the populations implying $\Delta^2 N_F^{-,(1)} = \langle N_F \rangle$.

From a fit to the data we extract a slope of 1.02 ± 0.05 for $F = 1$ and a slope of 0.96 ± 0.08 for $F = 2$ which is consistent with coherent state fluctuations. For the offset we find $1,710 \pm 80$ for $F = 1$ and $2,090 \pm 170$ for $F = 2$. These values include the photon shot noise contribution of $1,150$ for $F = 1$ and $1,490$ for $F = 2$ which we compute via Gaussian error propagation from the number of detected photons.

A.3.3. Buildup of correlations during expansion

In the squeezing experiments we limit the atom number in each manifold to about 12.000 atoms in each manifold. The reason for this is, that we find for higher atom numbers reduced fluctuations in the $F = 2$ manifold even for a coherent state. Similarly, if we attempt an imaging calibration with a coherent state that just involves the states $(2, \pm 2)$, we find values inconsistent with a calibration involving both manifolds. In contrast to the steering measurement 5.2, where we employed the readout pulses after the expansion, in the squeezing measurement 6.5 we applied all pulses 2 ms before switching off the XDT to expand the atomic cloud. Thus, we suspect that for higher atom numbers correlations between the two halves of the atomic cloud are built up during expansion due to interactions.

To check this, we prepare a coherent polar state and vary the delay time of the readout pulse, i.e. a $\pi/2$ spin rotation, with respect to the switching of the XDT for expansion (see

Fig. A.6). The minimal delay time of 0 ms corresponds to applying the readout pulses 2 ms before switching off the XDT to expand the atomic cloud. As we employ an expansion time of 10 ms, the maximal delay time of 12 ms corresponds to applying the readout pulses directly after the expansion and shortly before the imaging. We compare three different scenarios. In the first one, we use, after the rf pulse, two mw $\pi/2$ pulses coupling the states $(1, \pm 1) \leftrightarrow (2, \pm 2)$ to transfer half of the population to the $F = 2$ manifold. In the second one, we do not apply any mw coupling such that only the states $(1, \pm 1)$ are populated and for the last configuration we use two mw π pulses to transfer the whole population to the states $(2, \pm 2)$. The mw pulses are always employed directly after the rf pulse. We tuned the total atom number such that for all three settings the mean atom number in each manifold is ≈ 17.000 atoms.

For the evaluation we use the same method as for the squeezing measurement and evaluate the variance of $\Delta^2 N_F^{-(1)} / \langle N_F \rangle$ in the respective manifold (see Fig. A.6) and subtract the photon shot noise contribution. In the case, where just the $F = 1$ manifold is populated we find no dependence of the measured fluctuations on the timing of the rf pulse. If both manifolds are populated we find in $F = 2$ a small dependence on the timing. If just the states $(2, \pm 2)$ are populated, then the measured fluctuations strongly depend on the timing of the readout pulses. This indicates that there are some interactions during the expansion that lead to a correlation of the atom number difference n_2^- between the left and right half of the atomic cloud. This interaction seems to be modified as soon as atoms in the other manifold are present.

To analyze these correlations further, we systematically increase the evaluation region starting symmetrically around the middle of the atomic cloud. For each region of size d we extract the fluctuations of $N_F^{-(1)}(d)$ and normalize them to the corresponding mean atom number in this region $\langle N_F(d) \rangle$. The results are shown in Fig. A.7. For all three cases, we find longer correlation lengths when the readout pulses are applied directly before the expansion. Consequently, when the pulses are applied near the end of the expansion, the correlation length is reduced in both manifolds and we find that the normalized fluctuations saturate as soon as the evaluation region exceeds a spatial extension of 40 μm . This is consistent with the classical correlation induced by the imaging that we extracted before, since an evaluation region of size $d = 40 \mu\text{m}$ corresponds to the situation where the two subsystems A and B each have a size of 20 μm , which is the limit we used for the steering measurement.

In the case that only the states $(2, \pm 2)$ are populated we find a large correlation length, which explains why the imaging calibration just involving the $F = 2$ manifold yielded an inconsistent result. For such a calibration we have to take care to apply the readout pulses after the expansion. In the case where both manifolds are populated, the correlation length in the $F = 2$ manifold is also enlarged but still much smaller than in the previous case.

Since interaction effects depend on the density and thus on the total atom number, we expect, that for lower atom numbers the effect is already saturated when analyzing the whole cloud. Otherwise, we would have seen this effect in the imaging calibration. Thus, the result of the squeezing measurement is unaffected by this measurement, but one should be careful when evaluating smaller regions of the atomic cloud.

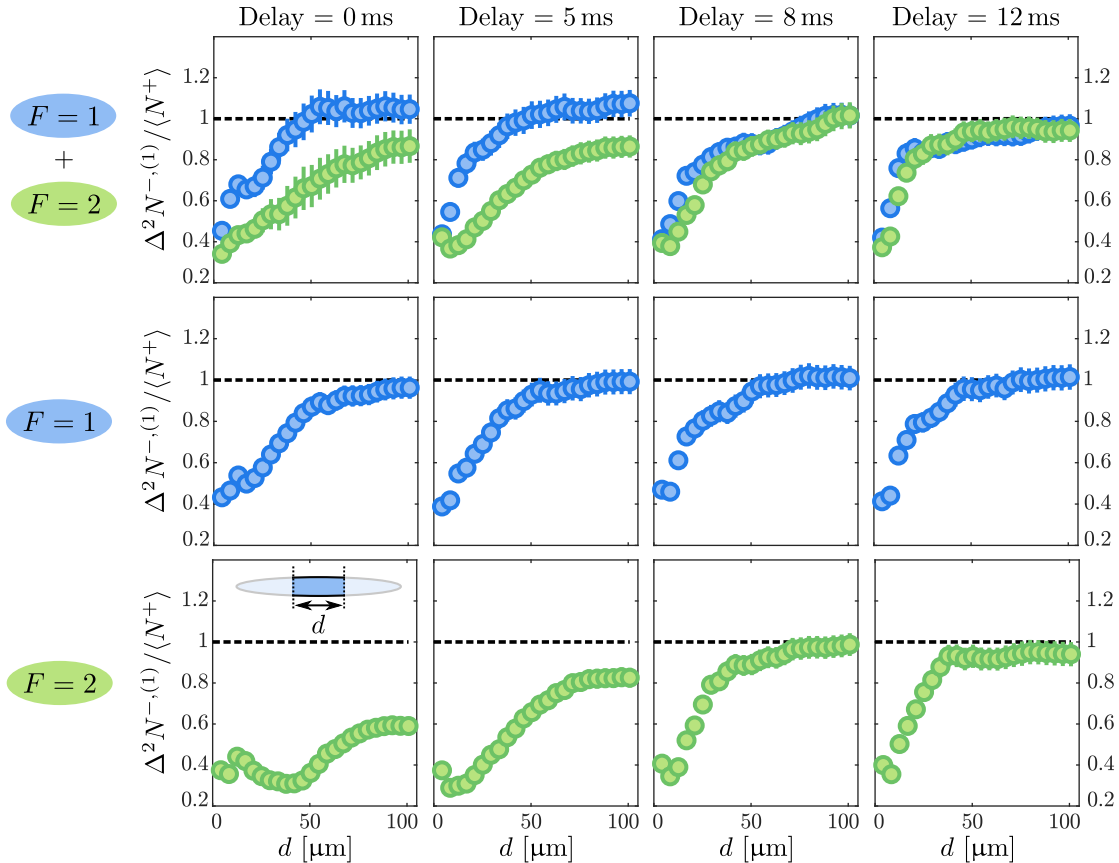


Figure A.7.: Correlation lengths after expansion: We systematically increase the evaluation region starting symmetrically around the middle of the atomic cloud (see inset in the left down corner). In each region of size d we evaluate $\Delta^2 N_F^{-(1)} / \langle N_F \rangle$. If the readout pulses are applied at the end of the expansion (column on the right), we recover the classical correlations induced by the imaging. In the case where only the states $(2, \pm 2)$ are populated we find a long correlation length. Thus, the interactions in $F = 2$ lead to considerable spin-spin correlations during expansion which is modified as soon as also atoms in $F = 1$ are present.

A.4. Technical stability of the rf pulse

To assess the technical stability of the rf pulse we load the BEC in an optical lattice potential similar to the imaging calibration measurement mentioned before. After the preparation we have again ≈ 35 independent BECs in the state $(1, -1)$. We then apply an rf $\pi/2$ pulse to generate a state with equal probability of $p_{-1} = p_{+1} = 0.25$ to measure a particle in each state $(1, \pm 1)$. Including technical fluctuations the variance of the population difference N^- between the two states is given by

$$\begin{aligned}
 \Delta^2 N^- &= \langle N^+ \rangle + \Delta^2[N(p_{+1} - p_{-1})] \\
 &= \langle N^+ \rangle + \langle N \rangle^2 \Delta^2[\cos(\Omega_{\text{rf}} \cdot t_{\pi/2})] + \overbrace{\langle p_{+1} - p_{-1} \rangle^2}^{=0} \Delta^2 N \\
 &\approx \langle N^+ \rangle + \underbrace{\sin(\Omega_{\text{rf}} \cdot t_{\pi/2}) t_{\pi/2}^2}_{=1} \Delta^2 \Omega_{\text{rf}} 4 \langle N^+ \rangle^2.
 \end{aligned} \tag{A.4}$$

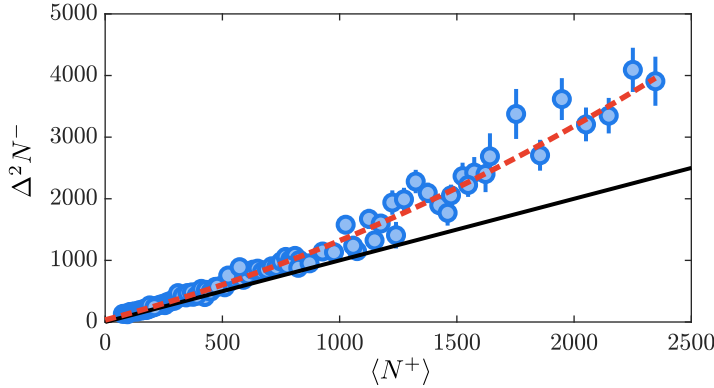


Figure A.8.: **Technical stability of the rf pulse:** By combining different lattice sites for the evaluation, we assess the variance of the population difference for up to $\approx 2,500$ atoms. We then fit a polynomial function up to second order (red dashed line) to the data and extract a quadratic term of $(2.87 \pm 0.15) \cdot 10^{-4}$. For reference we include a line with slope 1 (black solid line).

The first term are statistical fluctuations which are calculated from a multinomial distribution. The additional fluctuations can be divided in two terms; one term corresponds to the variance of the total atom number. This contribution, however, is negligible as long as the mean populations in $(1, \pm 1)$ are approximately equal. Finally, we obtain the technical noise contribution from the rf pulse which is proportional to the square of the atom number. To extract this term we combine multiple lattice sites to get higher mean atom numbers. Together with the results from the single lattice sites we obtain the data shown in Fig. A.8. We fit a polynomial function up to second order to the data, where we fixed the linear slope to one. Out of this fit we extract a quadratic prefactor of $(2.87 \pm 0.15) \cdot 10^{-4}$. For a pulse length of $t_{\pi/2} = 47 \mu\text{s}$, this corresponds to shot-to-shot fluctuations of the rf Rabi frequency of $\Delta\Omega_{\text{rf}} = 2\pi \cdot (29 \pm 1) \text{ Hz}$ or relative fluctuations of $\sigma_{\text{rf}} = \Delta\Omega_{\text{rf}}/\Omega_{\text{rf}} = (0.54 \pm 0.02)\%$.

A.5. Technical stability of the mw pulse

Similarly we determine the technical stability of the mw pulse that has been generated with the I/Q mixer. Starting from the state $(1, -1)$ we use a $\pi/2$ pulse coupling the states $(1, -1) \leftrightarrow (2, 0)$ directly followed by a π pulse coupling the states $(2, 0) \leftrightarrow (1, +1)$ to transfer half of the population to the state $(1, +1)$. Neglecting the noise contribution from the π pulse the variance of the population difference is given by

$$\Delta^2 N^- = \langle N^+ \rangle + t_{\pi/2}^2 \Delta^2 \Omega_{\text{mw}} \cdot \langle N^+ \rangle^2. \quad (\text{A.5})$$

The second term differs by a factor of four from the one in Eq. (A.4). This is because after the preparation all atoms are in the states $(1, \pm 1)$ and as a consequence $\langle N \rangle = \langle N^+ \rangle$. Analogously to the previous measurement we combine multiple wells and extract the quadratic part of the fluctuations (see Fig.A.9). In this case, we find a value of $(1.26 \pm 0.08) \cdot 10^{-4}$. For a pulse length of $t_{\pi/2} = 155 \mu\text{s}$, this corresponds to fluctuations of the mw Rabi frequency of $\Delta\Omega_{\text{mw}} = 2\pi \cdot (11.5 \pm 0.4) \text{ Hz}$ or relative fluctuations of $\sigma_{\text{mw}} = \Delta\Omega_{\text{mw}}/\Omega_{\text{mw}} = (0.72 \pm 0.02)\%$.

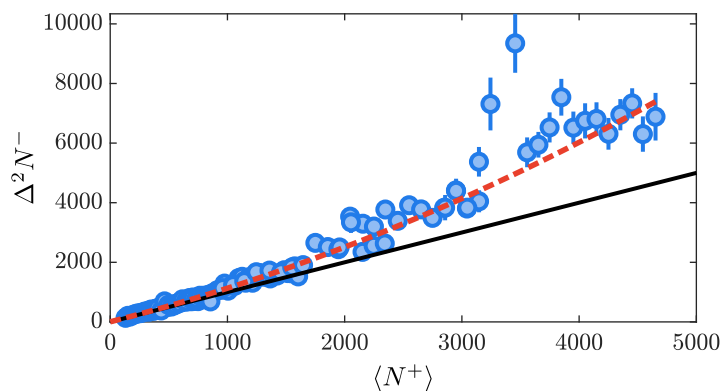


Figure A.9.: **Technical stability of the mw pulse:** By combining different lattice sites for the evaluation, we assess the variance of the population difference for up to $\approx 5,000$ atoms. We then fit a polynomial function up to second order (red dashed line) to the data and extract a quadratic term of $(1.26 \pm 0.08) \cdot 10^{-4}$. For reference we include a line with slope 1 (black solid line).

B. Simultaneous readout of conjugate spin observables

Here, we provide further details to two readout sequences detailed in Ch. 6, namely for the simultaneous extraction of all spin directions without spin rotations in $F = 2$ (see Sec. 6.4) and for the proposed simultaneous readout of \hat{S}_x and \hat{Q}_{yz} with an additional spin rotation in the $F = 2$ manifold (see Sec. 7.1.5). In the end we give a possible informationally complete readout sequence for a pseudo-spin-1/2 system.

B.1. Readout of all spin directions with arbitrary splitting ratio

In the main text we described a sequence to simultaneously read out all three spin directions by using the $F = 2$ manifold as a kind of storage and just employ spin rotations in the $F = 1$ manifold (see Sec. 6.4). There, detuned $\pi/2$ pulses are used to initially transfer a quarter of the population from the states $(1, \pm 1)$ to $(2, \pm 1)$. In the following we will give the measurement operators for this sequence for an arbitrary splitting ratio of η . The rest of the sequence remains the same as described in the main text, i.e. after the first splitting we use $\pi/2$ spin rotation around S_y after which we transfer half of the remaining population to the $F = 2$ and finally apply another $\pi/2$ rotation around S_x . The measurement operators for the final projective measurement are then given as

$$\begin{aligned}
\hat{N}_{1,-1} &= (1 - \eta) \left(\frac{1}{6} \hat{N} - \frac{1}{16} \hat{Q}_{zz} \right) + \sqrt{1 - \eta} \left(-\frac{1}{4} \hat{\mathcal{S}}_y + \frac{1}{8} \hat{V}_x \right) \\
\hat{N}_{1,0} &= (1 - \eta) \left(\frac{1}{6} \hat{N} + \frac{1}{8} \hat{Q}_{zz} \right) + \sqrt{1 - \eta} \frac{1}{4} \hat{V}_x \\
\hat{N}_{1,+1} &= (1 - \eta) \left(\frac{1}{6} \hat{N} - \frac{1}{16} \hat{Q}_{zz} \right) + \sqrt{1 - \eta} \left(\frac{1}{4} \hat{\mathcal{S}}_y + \frac{1}{8} \hat{V}_x \right) \\
\hat{N}_{2,+2} &= (1 - \eta) \left(\frac{1}{6} \hat{N} - \frac{1}{16} \hat{Q}_{zz} \right) + \sqrt{1 - \eta} \left(-\frac{1}{4} \hat{\mathcal{S}}_x + \frac{1}{8} \hat{V}_x \right) \\
\hat{N}_{2,+1} &= \eta \left(\frac{1}{3} \hat{N} + \frac{1}{2} \hat{\mathcal{S}}_z + \frac{1}{4} \hat{Q}_{zz} \right) \\
\hat{N}_{2,0} &= (1 - \eta) \left(\frac{1}{6} \hat{N} + \frac{1}{8} \hat{Q}_{zz} \right) - \sqrt{1 - \eta} \frac{1}{4} \hat{V}_x \\
\hat{N}_{2,-1} &= \eta \left(\frac{1}{3} \hat{N} - \frac{1}{2} \hat{\mathcal{S}}_z + \frac{1}{4} \hat{Q}_{zz} \right) \\
\hat{N}_{2,-2} &= (1 - \eta) \left(\frac{1}{6} \hat{N} - \frac{1}{16} \hat{Q}_{zz} \right) + \sqrt{1 - \eta} \left(\frac{1}{4} \hat{\mathcal{S}}_x + \frac{1}{8} \hat{V}_x \right).
\end{aligned} \tag{B.1}$$

Here, we omitted the terms containing operators from the initially unoccupied $F = 2$ manifold. The three spin directions are extracted via the linear combinations

$$\begin{aligned}\hat{S}_x &= \frac{2}{\sqrt{1-\eta}} (\hat{N}_{2,-2} - \hat{N}_{2,+2}) \\ \hat{S}_y &= \frac{2}{\sqrt{1-\eta}} (\hat{N}_{1,+1} - \hat{N}_{1,-1}) \\ \hat{S}_z &= \frac{1}{\eta} (\hat{N}_{2,+1} - \hat{N}_{2,-1}).\end{aligned}\quad (\text{B.2})$$

Moreover, this measurement contains information about two additional quadrupole operators that are obtained via

$$\begin{aligned}\hat{Q}_{zz} &= \frac{2}{\eta} (\hat{N}_{2,+1} + \hat{N}_{2,-1}) - \frac{4}{3} \hat{N} \\ \hat{V}_x &= \frac{2}{\sqrt{1-\eta}} (\hat{N}_{1,+1} + \hat{N}_{1,-1} - \hat{N}_{1,0}) - \frac{\sqrt{1-\eta}}{3} \hat{N}.\end{aligned}\quad (\text{B.3})$$

B.2. Alternative readout sequence for \hat{S}_x and \hat{Q}_{yz}

In Sec. 7.1.5 we proposed an alternative sequence to simultaneously readout \hat{S}_x and \hat{Q}_{yz} which mitigates the influence of magnetic field fluctuations. For this readout three mw pulses are used to transfer half of the population from $(1, m)$ to $(2, m)$ with $m \in \{0, \pm 1\}$, where the pulse coupling the states $(1, 0) \leftrightarrow (2, 0)$ has a $\pi/2$ phase shift compared to the other two pulses. Afterwards, we would use two selective $\pi/2$ spin rotation in $F = 1$ and $F = 2$ around S_y and $S_y^{F=2}$, respectively. The unitary transformation describing this pulse sequence is

$$\hat{U} = e^{-i\pi/2\hat{S}_y^{F=2}} e^{-i\pi/2\hat{S}_y} e^{-i\pi/2\hat{C}_x^{00}} e^{-i\pi/2\hat{C}_y^{11}} e^{-i\pi/2\hat{C}_y^{-1-1}}. \quad (\text{B.4})$$

With this unitary transformation, the measurement operators read

$$\begin{aligned}\hat{N}_{1,-1} &= \frac{1}{6} \hat{N} + \frac{1}{4} \hat{S}_x - \frac{1}{16} \hat{Q}_{zz} + \frac{1}{8} \hat{V}_x \\ \hat{N}_{1,0} &= \frac{1}{6} \hat{N} + \frac{1}{8} \hat{Q}_{zz} - \frac{1}{4} \hat{V}_x \\ \hat{N}_{1,+1} &= \frac{1}{6} \hat{N} - \frac{1}{4} \hat{S}_x - \frac{1}{16} \hat{Q}_{zz} + \frac{1}{8} \hat{V}_x \\ \hline \hat{N}_{2,+2} &= \frac{7}{48} \hat{N} + \frac{\sqrt{3}}{8} \hat{Q}_{yz} - \frac{1}{32} \hat{Q}_{zz} + \frac{1}{8} \hat{V}_x \\ \hat{N}_{2,+1} &= \frac{1}{12} \hat{N} + \frac{1}{16} \hat{Q}_{zz} - \frac{1}{8} \hat{V}_x \\ \hat{N}_{2,0} &= \frac{1}{24} \hat{N} - \frac{1}{16} \hat{Q}_{zz} \\ \hat{N}_{2,-1} &= \frac{1}{12} \hat{N} + \frac{1}{16} \hat{Q}_{zz} - \frac{1}{8} \hat{V}_x \\ \hat{N}_{2,-2} &= \frac{7}{48} \hat{N} - \frac{\sqrt{3}}{8} \hat{Q}_{yz} - \frac{1}{32} \hat{Q}_{zz} + \frac{1}{8} \hat{V}_x.\end{aligned}\quad (\text{B.5})$$

Again, we neglected the contribution from operators of the initially empty $F = 2$ manifold. After such a measurement the two operators of interest are extracted via the linear combinations

$$\begin{aligned}\hat{S}_x &= 2 \left(\hat{N}_{1,-1} - \hat{N}_{1,+1} \right) \\ \hat{Q}_{yz} &= \frac{4}{\sqrt{3}} \left(\hat{N}_{2,+2} - \hat{N}_{2,-2} \right).\end{aligned}\tag{B.6}$$

Additionally, we can extract the following operators

$$\begin{aligned}\hat{Q}_{zz} &= -16\hat{N}_{2,0} + \frac{2}{3}\hat{N} \\ \hat{V}_x &= 4 \left(\hat{N}_{2,+2} + \hat{N}_{2,-2} - \hat{N}_{2,0} \right) - \hat{N}.\end{aligned}\tag{B.7}$$

Since the operator \hat{Q}_{zz} is connected to $\hat{Q}_0 = -\hat{Q}_{zz} - 1/3\hat{N}$, we can use such a measurement to directly measure the spin-mixing dynamics on a spin-nematic sphere spanned by the operators $\{\hat{Q}_{yz}, \hat{S}_x, \hat{Q}_0\}$.

B.2.1. Entanglement detection using this readout

Eq. (B.6) means that the atom number difference $N_2^- = N_{2,+2} - N_{2,-2}$ in $F = 2$ contains information about the operator $\sqrt{3}/4\hat{Q}_{yz}$. In contrast, the readout sequence used in the experiment which measured the operator $1/2\hat{Q}_{yz}$. Thus, we have to check whether the arguments used for the entanglement criterion still remain valid for this readout sequence. In Fig. 7.3 we have seen that this particular readout has the same sensitivity to detect spin-nematic squeezing as the sequence introduced in Sec. 6.5. To detect this squeezing, we evaluate for both sequences the measured atom number difference $N_F^- = N_{F,+F} - N_{F,-F}$ (with $F = 1, 2$) and compare it to the shot noise limit given in each manifold by $N_F^+ = N_{F,+F} - N_{F,-F}$. For simplicity let us assume that the squeezed axis is aligned with the Q_{yz} direction. Then the maximal squeezing that can be measured with the sequence proposed here is

$$\frac{\Delta^2 N_2^-}{\langle N_2^+ \rangle} \approx \frac{\Delta^2 N_2^-}{\langle 3N/8 \rangle} = 0.5.\tag{B.8}$$

Here we have used that in the undepleted pump approximation the mean atom number $\langle N_2^+ \rangle = \langle N_{2,+2} + N_{2,-2} \rangle \approx \langle 3N/8 \rangle$. As explained above, the atom number difference N_2^- gives us information about the observable $\sqrt{3}/4\hat{Q}_{yz}$. For the entanglement criterion as in Eq. (7.14) we need to quantify the variance

$$\frac{\Delta^2(Q_{yz}/2)}{\langle N/2 \rangle} \rightarrow \frac{\Delta^2(2N_2^-/\sqrt{3})}{\langle N/2 \rangle} = \frac{4}{3} \frac{\Delta^2 N_2^-}{\langle N/2 \rangle} = \frac{\Delta^2 N_2^-}{\langle 3N/8 \rangle} = 0.5.\tag{B.9}$$

The variance of the S_x measurement is the same for both readout sequences. Thus, even though we gain additional information about \hat{Q}_0 , this readout technique has the same potential to detect entanglement as the sequence used in the experiment.

B.3. Informationally complete sequence in a pseudo-spin-1/2

Here, we provide details about a possible informationally complete readout of a pseudo-spin-1/2 system. Such a measurement could be realized by just using the initially empty magnetic substates of the $F = 1$ manifold. Here, we present a possible readout sequence to implement such an informationally complete measurement. In a first step, one uses a mw-pulse coupling the states $(2, -1) \leftrightarrow (1, 0)$ followed by another mw pulse coupling the states $(2, -1) \leftrightarrow (1, -1)$ with a relative phase of $\pi/2$. The remaining population in $(2, -1)$ contains the information about the spin in z -direction. The length of the two mw pulses can be adjusted to tune the transferred population and thus the measurement statistics. With a spin rotation in the $F = 1$ manifold one maps the two remaining spin directions onto the population differences of the magnetic substates in this manifold. For arbitrary rotation angles θ_1 and θ_2 of the two mw pulses the spin observables are extracted by evaluating

$$\begin{aligned} N^{J_x} &= \frac{2}{\sin(\theta_1/2)}(N_{1,+1} - N_{1,-1}) \\ N^{J_y} &= \frac{2}{\sin(\theta_2/2) \cos(\theta_1/2)}[N_{1,0} - (N_{1,+1} + N_{1,-1}) - \frac{1}{2} \tan^2(\theta_2/2) N_{2,-1}] \\ N^{J_z} &= \frac{1}{\cos^2(\theta_1/2) \cos^2(\theta_2/3)} N_{2,-1} - \frac{1}{2}(N_{2,-1} + N_{1,+1} + N_{1,0} + N_{1,-1}). \end{aligned} \quad (\text{B.10})$$

C. Spin-1 operators

Even though we have given the definitions of the operators in the main text, we will provide here a compact overview of the relevant operators in matrix form and second-quantization. Additionally, we will give the commutation relations for the different SU(2) subspaces.

Matrix notation:

$$\hat{S}_x = \frac{1}{\sqrt{2}} \begin{pmatrix} 0 & 1 & 0 \\ 1 & 0 & 1 \\ 0 & 1 & 0 \end{pmatrix}$$

$$\hat{S}_y = \frac{1}{\sqrt{2}} \begin{pmatrix} 0 & -i & 0 \\ i & 0 & -i \\ 0 & i & 0 \end{pmatrix}$$

$$\hat{S}_z = \begin{pmatrix} 1 & 0 & 0 \\ 0 & 0 & 0 \\ 0 & 0 & -1 \end{pmatrix}$$

Second-quantization:

$$\hat{S}_x = \frac{1}{\sqrt{2}} \hat{a}_0^\dagger (\hat{a}_{+1} + \hat{a}_{-1}) + \frac{1}{\sqrt{2}} (\hat{a}_{+1}^\dagger + \hat{a}_{-1}^\dagger) \hat{a}_0$$

$$\hat{S}_y = \frac{i}{\sqrt{2}} \hat{a}_0^\dagger (\hat{a}_{+1} - \hat{a}_{-1}) - \frac{i}{\sqrt{2}} (\hat{a}_{+1}^\dagger - \hat{a}_{-1}^\dagger) \hat{a}_0$$

$$\hat{S}_z = \hat{a}_{+1}^\dagger \hat{a}_{+1} - \hat{a}_{-1}^\dagger \hat{a}_{-1}$$

$$\hat{Q}_{yz} = \frac{1}{\sqrt{2}} \begin{pmatrix} 0 & -i & 0 \\ i & 0 & i \\ 0 & -i & 0 \end{pmatrix}$$

$$\hat{Q}_{yz} = \frac{i}{\sqrt{2}} \hat{a}_0^\dagger (\hat{a}_{+1} + \hat{a}_{-1}) - \frac{i}{\sqrt{2}} (\hat{a}_{+1}^\dagger + \hat{a}_{-1}^\dagger) \hat{a}_0$$

$$\hat{Q}_{xz} = \frac{1}{\sqrt{2}} \begin{pmatrix} 0 & 1 & 0 \\ 1 & 0 & -1 \\ 0 & -1 & 0 \end{pmatrix}$$

$$\hat{Q}_{xz} = \frac{1}{\sqrt{2}} \hat{a}_0^\dagger (\hat{a}_{+1} - \hat{a}_{-1}) + \frac{1}{\sqrt{2}} (\hat{a}_{+1}^\dagger - \hat{a}_{-1}^\dagger) \hat{a}_0$$

$$\hat{Q}_{zz} = \begin{pmatrix} \frac{2}{3} & 0 & 0 \\ 0 & -\frac{4}{3} & 0 \\ 0 & 0 & \frac{2}{3} \end{pmatrix}$$

$$\hat{Q}_{zz} = \frac{2}{3} (\hat{a}_{+1}^\dagger \hat{a}_{+1} + \hat{a}_{-1}^\dagger \hat{a}_{-1}) - \frac{4}{3} \hat{a}_0^\dagger \hat{a}_0$$

$$\hat{V}_x = \frac{1}{2} (\hat{Q}_{xx} - \hat{Q}_{yy}) = \begin{pmatrix} 0 & 0 & 1 \\ 0 & 0 & 0 \\ 1 & 0 & 0 \end{pmatrix}$$

$$\hat{V}_x = \hat{a}_{+1}^\dagger \hat{a}_{-1} + \hat{a}_{-1}^\dagger \hat{a}_{+1}$$

$$\hat{V}_y = \hat{Q}_{xy} = \begin{pmatrix} 0 & 0 & -i \\ 0 & 0 & 0 \\ i & 0 & 0 \end{pmatrix}$$

$$\hat{V}_y = i \hat{a}_{+1}^\dagger \hat{a}_{-1} - i \hat{a}_{-1}^\dagger \hat{a}_{+1}$$

Additional operators

$$\hat{\mathcal{N}} = \mathbb{1}_3 = \begin{pmatrix} 1 & 0 & 0 \\ 0 & 1 & 0 \\ 0 & 0 & 1 \end{pmatrix}$$

$$\hat{N} = \hat{a}_{+1}^\dagger \hat{a}_{+1} + \hat{a}_0^\dagger \hat{a}_0 + \hat{a}_{-1}^\dagger \hat{a}_{-1}$$

$$\hat{Q}_0 = -\hat{Q}_{zz} - \frac{1}{3}\hat{\mathcal{N}} = \begin{pmatrix} -1 & 0 & 0 \\ 0 & 1 & 0 \\ 0 & 0 & -1 \end{pmatrix}$$

$$\hat{Q}_0 = \hat{a}_0^\dagger \hat{a}_0 - (\hat{a}_{+1}^\dagger \hat{a}_{+1} + \hat{a}_{-1}^\dagger \hat{a}_{-1})$$

$$\hat{\mathcal{N}}^+ = \begin{pmatrix} 1 & 0 & 0 \\ 0 & 0 & 0 \\ 0 & 0 & 1 \end{pmatrix}$$

$$\hat{N}^+ = \hat{a}_{+1}^\dagger \hat{a}_{+1} + \hat{a}_{-1}^\dagger \hat{a}_{-1}$$

C.1. SU(2) subspaces

$$\{\hat{S}_x, \hat{S}_y, \hat{S}_z\}$$

$$\left. \begin{aligned} [\hat{S}_z, \hat{S}_x] &= i\hat{S}_y \\ [\hat{S}_y, \hat{S}_z] &= i\hat{S}_x \end{aligned} \right\} \longleftrightarrow \hat{S}_\perp(\phi_L) = \cos(\phi_L)\hat{S}_x + \sin(\phi_L)\hat{S}_y$$

$$[\hat{S}_x, \hat{S}_y] = i\hat{S}_z$$

Since a rotation around S_z corresponds to a change of the Larmor phase ϕ_L , the first two commutation relations are equivalent to the statement that the operators \hat{S}_x and \hat{S}_y are connected via a change of the Larmor phase. The commutation relation in the last line ensures that also rotations around S_x and S_y can be visualized on a sphere.

$$\{\hat{Q}_{yz}, -\hat{Q}_{xz}, \hat{S}_z\}$$

$$\left. \begin{aligned} [\hat{S}_z, \hat{Q}_{yz}] &= -i\hat{Q}_{xz} \\ [-\hat{Q}_{xz}, \hat{S}_z] &= i\hat{Q}_{yz} \end{aligned} \right\} \longleftrightarrow \hat{Q}_\perp(\phi_L) = \cos(\phi_L)\hat{Q}_{yz} - \sin(\phi_L)\hat{Q}_{xz}$$

$$[\hat{Q}_{yz}, -\hat{Q}_{xz}] = i\hat{S}_z$$

$$\{\hat{V}_x, \hat{V}_y, \hat{S}_z\}$$

$$\left. \begin{aligned} [\hat{S}_z, \hat{V}_x] &= 2i\hat{V}_y \\ [\hat{V}_y, \hat{S}_z] &= 2i\hat{V}_x \end{aligned} \right\} \longleftrightarrow \hat{V}_\perp(\phi_L) = \cos(2\phi_L)\hat{V}_x + \sin(2\phi_L)\hat{V}_y$$

$$[\hat{V}_x, \hat{V}_y] = 2i\hat{S}_z$$

C.2. Spin-nematic subspaces

$$\{\hat{Q}_{yz}, \hat{S}_x, \hat{Q}_0\}$$

$$\left. \begin{aligned} [\hat{Q}_0, \hat{Q}_{yz}] &= 2i\hat{S}_x \\ [\hat{S}_x, \hat{Q}_0] &= 2i\hat{Q}_{yz} \end{aligned} \right\} \longleftrightarrow \hat{F}(\phi_S) = \cos(\phi_S)\hat{S}_x + \sin(\phi_S)\hat{Q}_{yz}$$

$$\langle [\hat{Q}_{yz}, \hat{S}_x] \rangle_Q = 2i\langle \hat{Q}_0 \rangle_Q \quad \text{for all states with} \quad \langle \hat{N}^+ \rangle_Q = \langle \hat{V}_x \rangle_Q$$

As before, a rotation generated by \hat{Q}_0 corresponds to a change of the spinor phase ϕ_S . Thus, the first two commutation relations are equivalent to the statement that \hat{S}_x and \hat{Q}_{yz} are connected via a change of the spinor phase irrespective of the state. Only for the visualization of the other rotations on a spin-nematic sphere, one requires that the uncertainty relation in the last line is fulfilled.

For general Larmor phases the spin-nematic subspace is given by

$$\{\hat{Q}_\perp, \hat{S}_\perp, \hat{Q}_0\}$$

$$\left. \begin{aligned} [\hat{Q}_0, \hat{Q}_\perp] &= 2i\hat{S}_\perp \\ [\hat{S}_\perp, \hat{Q}_0] &= 2i\hat{Q}_\perp \end{aligned} \right\} \longleftrightarrow \hat{F}_\perp(\phi_L, \phi_S) = \cos(\phi_S)\hat{S}_\perp(\phi_L) + \sin(\phi_S)\hat{Q}_\perp(\phi_L)$$

$$\langle [\hat{Q}_\perp, \hat{S}_\perp] \rangle_Q = 2i\langle \hat{Q}_0 \rangle_Q \quad \text{for all states with} \quad \langle \hat{N}^+ \rangle_Q = \langle \hat{V}_\perp \rangle_Q$$

Publication list

- **Active SU(1,1) atom interferometry**
D. Linnemann, J. Schulz, W. Muessel, P. Kunkel, M. Prüfer, A. Frölian, H. Strobel and M. K. Oberthaler
Quantum Science and Technology **2**, 044009 (2017)
- **Spatially distributed multipartite entanglement enables EPR steering of atomic clouds***
P. Kunkel, M. Prüfer, H. Strobel, D. Linnemann, A. Frölian, T. Gasenzer, M. Gärttner and M. K. Oberthaler
Science **360**, 413–416 (2018)
- **Observation of universal dynamics in a spinor Bose gas far from equilibrium**
M. Prüfer, P. Kunkel, H. Strobel, S. Lannig, D. Linnemann, C.-M. Schmied, J. Berges, T. Gasenzer and M. K. Oberthaler
Nature **563**, 217–220 (2018)
- **Simultaneous Readout of Noncommuting Collective Spin Observables beyond the Standard Quantum Limit***
P. Kunkel, M. Prüfer, S. Lannig, R. Rose-Medina, A. Bonnin, M. Gärttner, H. Strobel and M. K. Oberthaler
Phys. Rev. Lett. **123**, 063603 (2019)
- **Experimental extraction of the quantum effective action for a non-equilibrium many-body system**
M. Prüfer, T. V. Zache, P. Kunkel, S. Lannig, A. Bonnin, H. Strobel, J. Berges and M. K. Oberthaler
arXiv:1909.05120 (2019)

The publications marked with * are used within this thesis

Bibliography

- [1] A. Peres. *Quantum theory: concepts and methods*, vol. 57 (Springer Science & Business Media, 2006).
- [2] P. A. M. Dirac. On the Theory of Quantum Mechanics. *Proceedings of the Royal Society A: Mathematical, Physical and Engineering Sciences* **112**, 661–677 (1926).
- [3] K. Eckert, J. Schliemann, D. Bruß & M. Lewenstein. Quantum correlations in systems of indistinguishable particles. *Ann. Phys.* **299**, 88–127 (2002).
- [4] T. Ichikawa, T. Sasaki, I. Tsutsui & N. Yonezawa. Exchange symmetry and multipartite entanglement. *Physical Review A* **78** (2008).
- [5] T.-C. Wei. Exchange symmetry and global entanglement and full separability. *Physical Review A* **81** (2010).
- [6] G. Ghirardi & L. Marinatto. General criterion for the entanglement of two indistinguishable particles. *Phys. Rev. A* **70** (2004).
- [7] C. Gross, T. Zibold, E. Nicklas, J. Estève & M. K. Oberthaler. Nonlinear atom interferometer surpasses classical precision limit. *Nature* **464**, 1165–1169 (2010).
- [8] M. F. Riedel, P. Böhi, Y. Li, T. W. Hänsch, A. Sinatra & P. Treutlein. Atom-chip-based generation of entanglement for quantum metrology. *Nature* **464**, 1170–1173 (2010).
- [9] L. Pezzè, A. Smerzi, M. K. Oberthaler, R. Schmied & P. Treutlein. Quantum metrology with nonclassical states of atomic ensembles. *Rev. Mod. Phys.* **90**, 035005 (2018).
- [10] M. Kitagawa & M. Ueda. Squeezed spin states. *Phys. Rev. A* **47**, 5138–5143 (1993).
- [11] G. Tóth, C. Knapp, O. Gühne & H. J. Briegel. Spin squeezing and entanglement. *Phys. Rev. A* **79**, 042334 (2009).
- [12] J. Peise, I. Kruse, K. Lange, B. Lücke, L. Pezzè, J. Arlt, W. Ertmer, K. Hammerer, L. Santos, A. Smerzi & C. Klempt. Satisfying the Einstein-Podolsky-Rosen criterion with massive particles. *Nat. Commun.* **6**, 8984 (2015).
- [13] R. Schmied, J.-D. Bancal, B. Allard, M. Fadel, V. Scarani, P. Treutlein & N. Sangouard. Bell correlations in a bose-einstein condensate. *Science* **352**, 441–444 (2016).
- [14] H. M. Wiseman & J. A. Vaccaro. Entanglement of indistinguishable particles shared between two parties. *Phys. Rev. Lett.* **91**, 097902 (2003).
- [15] P. Hyllus, L. Pezzé, A. Smerzi & G. Tóth. Entanglement and extreme spin squeezing for a fluctuating number of indistinguishable particles. *Phys. Rev. A* **86**, 012337 (2012).

- [16] N. Killoran, M. Cramer & M. B. Plenio. Extracting entanglement from identical particles. *Phys. Rev. Lett.* **112**, 150501 (2014).
- [17] S. L. Braunstein & P. van Loock. Quantum information with continuous variables. *Rev. Mod. Phys.* **77**, 513–577 (2005).
- [18] N. Gisin, G. Ribordy, W. Tittel & H. Zbinden. Quantum cryptography. *Rev. Mod. Phys.* **74**, 145 (2002).
- [19] B. Morris, B. Yadin, M. Fadel, T. Zibold, P. Treutlein & G. Adesso. Entanglement between identical particles is a useful and consistent resource. *arXiv preprint arXiv:1908.11735* (2019).
- [20] M. Reid, P. Drummond, W. Bowen, E. G. Cavalcanti, P. K. Lam, H. Bachor, U. L. Andersen & G. Leuchs. Colloquium: the einstein-podolsky-rosen paradox: from concepts to applications. *Rev. Mod. Phys.* **81**, 1727 (2009).
- [21] R. Raussendorf & H. J. Briegel. A one-way quantum computer. *Phys. Rev. Lett.* **86**, 5188 (2001).
- [22] M. Prüfer, P. Kunkel, H. Strobel, S. Lannig, D. Linnemann, C.-M. Schmied, J. Berges, T. Gasenzer & M. K. Oberthaler. Observation of universal dynamics in a spinor Bose gas far from equilibrium. *Nature* **563**, 217–220 (2018).
- [23] J. J. Sakurai & J. Napolitano. *Modern Quantum Mechanics* (Addison-Wesley, 2011).
- [24] C. D. Hamley, C. S. Gerving, T. M. Hoang, E. M. Bookjans & M. S. Chapman. Spin-nematic squeezed vacuum in a quantum gas. *Nat. Phys.* **8**, 305–308 (2012).
- [25] E. Majorana. Atomi orientati in campo magnetico variabile. *Il Nuovo Cimento (1924-1942)* **9**, 43–50 (1932).
- [26] Y. Kawaguchi & M. Ueda. Spinor bose-einstein condensates. *Phys. Rep.* **520**, 253–381 (2012).
- [27] I. Carusotto & E. J. Mueller. Imaging of spinor gases. *J. Phys. B* **37**, S115–S125 (2004).
- [28] Y. Di, Y. Wang & H. Wei. Dipole-quadrupole decomposition of two coupled spin 1 systems. *J. Phys. A* **43**, 065303 (2010).
- [29] N. F. Ramsey. *Nuclear Moments* (Wiley, 1953).
- [30] M. Gell-Mann. Symmetries of baryons and mesons. *Phys. Rev.* **125**, 1067–1084 (1962).
- [31] H. M. Bharath, M. Boguslawski, M. Barrios, L. Xin & M. S. Chapman. Singular loops and their non-Abelian geometric phases in spin-1 ultracold atoms. *arXiv preprint arXiv:1801.00586* (2018).
- [32] P. Jordan. Der Zusammenhang der symmetrischen und linearen Gruppen und das Mehrkörperproblem. *Zeitschrift für Physik* **94**, 531–535 (1935).
- [33] J. Schwinger. On angular momentum (1952).

- [34] M. A. Nielsen & I. L. Chuang. *Quantum Computation and Quantum Information: 10th Anniversary Edition* (Cambridge University Press, New York, NY, USA, 2011), 10th edn.
- [35] S. T. Flammia, A. Silberfarb & C. M. Caves. Minimal informationally complete measurements for pure states. *Foundat. Phys.* **35**, 1985–2006 (2005).
- [36] H. P. Robertson. The uncertainty principle. *Phys. Rev.* **34**, 163–164 (1929).
- [37] U. Leonhardt, P. Knight & A. Miller. *Measuring the Quantum State of Light*. Cambridge Studies in Modern Optics (Cambridge University Press, 1997).
- [38] E. Wigner. On the quantum correction for thermodynamic equilibrium. *Phys. Rev.* **40**, 749–759 (1932).
- [39] J. P. Dowling, G. S. Agarwal & W. P. Schleich. Wigner distribution of a general angular-momentum state: Applications to a collection of two-level atoms. *Physical Review A* **49**, 4101–4109 (1994).
- [40] G. S. Agarwal. *Quantum Optics* (Cambridge University Press, 2009).
- [41] T. Kiesel, W. Vogel, S. L. Christensen, J.-B. Béguin, J. Appel & E. S. Polzik. Atomic nonclassicality quasiprobabilities. *Phys. Rev. A* **86** (2012).
- [42] J. Bertrand & P. Bertrand. A tomographic approach to wigner’s function. *Foundations of Physics* **17**, 397–405 (1987).
- [43] A. Kenfack & K. yczkowski. Negativity of the wigner function as an indicator of non-classicality. *J. Opt. B: Quantum Semiclassical Opt.* **6**, 396–404 (2004).
- [44] A. I. Lvovsky & M. G. Raymer. Continuous-variable optical quantum-state tomography. *Rev. Mod. Phys.* **81**, 299 (2009).
- [45] K. Husimi. Some formal properties of the density matrix. *Proceedings of the Physics Mathematical Society of Japan* **22**, 264–314 (1940).
- [46] M. O. Scully & M. S. Zubairy. *Quantum optics* (Cambridge University Press, 1997).
- [47] E. Schrödinger. Discussion of probability relations between separated systems. *Math. Proc. Cambridge Philos. Soc.* **31**, 555–563 (1935).
- [48] E. Schrödinger. Die gegenwärtige situation in der quantenmechanik. *Naturwissenschaften* **23**, 807–812 (1935).
- [49] A. Einstein, B. Podolsky & N. Rosen. Can quantum-mechanical description of physical reality be considered complete? *Phys. Rev.* **47**, 777–780 (1935).
- [50] J. P. Dowling & G. J. Milburn. Quantum technology: the second quantum revolution. *Philosophical Transactions of the Royal Society of London. Series A: Mathematical, Physical and Engineering Sciences* **361**, 1655–1674 (2003).
- [51] R. Feynman. *The Character of Physical Law* (The M.I.T. Press, 1967).
- [52] S. Popescu & D. Rohrlich. Quantum nonlocality as an axiom. *Found. Phys.* **24**, 379–385 (1994).

- [53] J. S. Bell. On the einstein podolsky rosen paradox. *Physics* **1**, 195–200 (1964).
- [54] A. Aspect, P. Grangier & G. Roger. Experimental tests of realistic local theories via bell's theorem. *Phys. Rev. Lett.* **47**, 460–463 (1981).
- [55] M. Giustina, M. A. Versteegh, S. Wengerowsky, J. Handsteiner, A. Hochrainer, K. Phelan, F. Steinlechner, J. Kofler, J.-Å. Larsson, C. Abellán, W. Amaya, V. Pruneri, M. W. Mitchell, J. Beyer, T. Gerrits, A. E. Lita, L. K. Shalm, S. W. Nam, T. Scheidl, R. Ursin, B. Wittmann & A. Zeilinger. Significant-loophole-free test of bell's theorem with entangled photons. *Phys. Rev. Lett.* **115** (2015).
- [56] B. Hensen, H. Bernien, A. E. Dréau, A. Reiserer, N. Kalb, M. S. Blok, J. Ruitenberg, R. F. L. Vermeulen, R. N. Schouten, C. Abellán, W. Amaya, V. Pruneri, M. W. Mitchell, M. Markham, D. J. Twitchen, D. Elkouss, S. Wehner, T. H. Taminiau & R. Hanson. Loophole-free bell inequality violation using electron spins separated by 1.3 kilometres. *Nature* **526**, 682–686 (2015).
- [57] J. Bowles, T. Vértesi, M. T. Quintino & N. Brunner. One-way einstein-podolsky-rosen steering. *Phys. Rev. Lett.* **112** (2014).
- [58] C. H. Bennett, G. Brassard, C. Crépeau, R. Jozsa, A. Peres & W. K. Wootters. Teleporting an unknown quantum state via dual classical and einstein-podolsky-rosen channels. *Phys. Rev. Lett.* **70**, 1895 (1993).
- [59] R. F. Werner. Quantum states with einstein-podolsky-rosen correlations admitting a hidden-variable model. *Phys. Rev. A* **40**, 4277–4281 (1989).
- [60] R. Horodecki, P. Horodecki, M. Horodecki & K. Horodecki. Quantum entanglement. *Rev. Mod. Phys.* **81**, 865–942 (2009).
- [61] O. Gühne & G. Tóth. Entanglement detection. *Phys. Rep.* **474**, 1 – 75 (2009).
- [62] D. J. Wineland, J. J. Bollinger, W. M. Itano & D. Heinzen. Squeezed atomic states and projection noise in spectroscopy. *Phys. Rev. A* **50**, 67 (1994).
- [63] V. Giovannetti, S. Lloyd & L. Maccone. Quantum-enhanced measurements: Beating the standard quantum limit. *Science* **306**, 1330–1336 (2004).
- [64] W. Muessel, H. Strobel, D. Linnemann, T. Zibold, B. Juliá-Díaz & M. K. Oberthaler. Twist-and-turn spin squeezing in Bose-Einstein condensates. *Phys. Rev. A* **92** (2015).
- [65] L. K. Shalm, D. R. Hamel, Z. Yan, C. Simon, K. J. Resch & T. Jennewein. Three-photon energy-time entanglement. *Nat. Phys.* **9**, 19–22 (2012).
- [66] P. van Loock & A. Furusawa. Detecting genuine multipartite continuous-variable entanglement. *Phys. Rev. A* **67**, 052315 (2003).
- [67] S. Armstrong, M. Wang, R. Y. Teh, Q. Gong, Q. He, J. Janousek, H.-A. Bachor, M. D. Reid & P. K. Lam. Multipartite Einstein–Podolsky–Rosen steering and genuine tripartite entanglement with optical networks. *Nat. Phys.* **11**, 167–172 (2015).

- [68] G. Tóth, W. Wieczorek, R. Krischek, N. Kiesel, P. Michelberger & H. Weinfurter. Practical methods for witnessing genuine multi-qubit entanglement in the vicinity of symmetric states. *New J. Phys.* **11**, 083002 (2009).
- [69] W. Wieczorek, R. Krischek, N. Kiesel, P. Michelberger, G. Tóth & H. Weinfurter. Experimental entanglement of a six-photon symmetric dicke state. *Phys. Rev. Lett.* **103**, 020504 (2009).
- [70] S. Wengerowsky, S. K. Joshi, F. Steinlechner, H. Hübel & R. Ursin. An entanglement-based wavelength-multiplexed quantum communication network. *Nature* **564**, 225 (2018).
- [71] R. Raussendorf, D. E. Browne & H. J. Briegel. Measurement-based quantum computation on cluster states. *Phys. Rev. A* **68**, 022312 (2003).
- [72] P. Walther, K. J. Resch, T. Rudolph, E. Schenck, H. Weinfurter, V. Vedral, M. Aspelmeyer & A. Zeilinger. Experimental one-way quantum computing. *Nature* **434**, 169 (2005).
- [73] M. Hein, J. Eisert & H. J. Briegel. Multiparty entanglement in graph states. *Phys. Rev. A* **69**, 062311 (2004).
- [74] A. Weller. *Dynamics and Interaction of Dark Solitons in Bose-Einstein Condensates*. Ph.D. thesis, Heidelberg University (2009).
- [75] C. Groß. *Spin squeezing and non-linear atom interferometry with Bose-Einstein condensates*. Ph.D. thesis, Heidelberg University (2010).
- [76] T. Zibold. *Classical Bifurcation and Entanglement Generation in an Internal Bosonic Josephson Junction*. Ph.D. thesis, Heidelberg University (2012).
- [77] E. Nicklas. *A new tool for miscibility control: Linear coupling*. Ph.D. thesis, Heidelberg University (2013).
- [78] W. Müssel. *Scalable Spin Squeezing for Quantum-Enhanced Magnetometry with Bose-Einstein Condensates*. Ph.D. thesis, Heidelberg University (2014).
- [79] H. Strobel. *Fisher information and entanglement of non-Gaussian spin states*. Ph.D. thesis, Heidelberg University (2015).
- [80] W. Petrich, M. H. Anderson, J. R. Ensher & E. A. Cornell. Stable, tightly confining magnetic trap for evaporative cooling of neutral atoms. *Phys. Rev. Lett.* **74**, 3352–3355 (1995).
- [81] G. Reinaudi, T. Lahaye, Z. Wang & D. Guéry-Odelin. Strong saturation absorption imaging of dense clouds of ultracold atoms. *Opt. Lett.* **32**, 3143 (2007).
- [82] W. Muessel, H. Strobel, M. Joos, E. Nicklas, I. Stroescu, J. Tomkovič, D. B. Hume & M. K. Oberthaler. Optimized absorption imaging of mesoscopic atomic clouds. *Appl. Phys. B* **113**, 69–73 (2013).
- [83] C. F. Ockeloen, A. F. Tauschinsky, R. J. C. Spreeuw & S. Whitlock. Detection of small atom numbers through image processing. *Phys. Rev. A* **82**, 061606(R) (2010).

- [84] P. A. Murthy, D. Kedar, T. Lompe, M. Neidig, M. G. Ries, A. N. Wenz, G. Zürn & S. Jochim. Matter-wave fourier optics with a strongly interacting two-dimensional fermi gas. *Phys. Rev. A* **90** (2014).
- [85] Y. Castin & R. Dum. Bose-Einstein condensates in time dependent traps. *Phys. Rev. Lett.* **77**, 5315 (1996).
- [86] C. Cohen-Tannoudji, J. Dupont-Roc & G. Grynberg. *Atom—Photon Interactions* (Wiley, 1998).
- [87] D. C. Burnham & D. L. Weinberg. Observation of simultaneity in parametric production of optical photon pairs. *Phys. Rev. Lett.* **25**, 84 (1970).
- [88] P. G. Kwiat, K. Mattle, H. Weinfurter, A. Zeilinger, A. V. Sergienko & Y. Shih. New High-Intensity Source of Polarization-Entangled Photon Pairs. *Phys. Rev. Lett.* **75**, 4337–4341 (1995).
- [89] D. Dehlinger & M. Mitchell. Entangled photons, nonlocality, and bell inequalities in the undergraduate laboratory. *Am. J. Phys* **70**, 903–910 (2002).
- [90] D. Bouwmeester, J.-W. Pan, K. Mattle, M. Eibl, H. Weinfurter & A. Zeilinger. Experimental quantum teleportation. *Nature* **390**, 575 (1997).
- [91] D. M. Stamper-Kurn & M. Ueda. Spinor bose gases: Symmetries, magnetism, and quantum dynamics. *Rev. Mod. Phys.* **85**, 1191–1244 (2013).
- [92] F. Dalfovo, S. Giorgini, L. P. Pitaevskii & S. Stringari. Theory of Bose-Einstein condensation in trapped gases. *Rev. Mod. Phys.* **71**, 463 (1999).
- [93] K. Huang & C. N. Yang. Quantum-mechanical many-body problem with hard-sphere interaction. *Phys. Rev.* **105**, 767–775 (1957).
- [94] E. G. M. van Kempen, S. J. J. M. F. Kokkelmans, D. J. Heinzen & B. J. Verhaar. Interisotope determination of ultracold rubidium interactions from three high-precision experiments. *Phys. Rev. Lett.* **88** (2002).
- [95] C. K. Law, H. Pu & N. P. Bigelow. Quantum spins mixing in spinor bose-einstein condensates. *Phys. Rev. Lett.* **81**, 5257–5261 (1998).
- [96] C. Gross, H. Strobel, E. Nicklas, T. Zibold, N. Bar-Gill, G. Kurizki & M. K. Oberthaler. Atomic homodyne detection of continuous-variable entangled twin-atom states. *Nature* **480**, 219–223 (2011).
- [97] D. Linnemann, H. Strobel, W. Muessel, J. Schulz, R. J. Lewis-Swan, K. V. Kheruntsyan & M. K. Oberthaler. Quantum-enhanced sensing based on time reversal of nonlinear dynamics. *Phys. Rev. Lett.* **117**, 013001 (2016).
- [98] D. Linnemann, J. Schulz, W. Muessel, P. Kunkel, M. Prüfer, A. Frölian, H. Strobel & M. K. Oberthaler. Active SU(1,1) atom interferometry. *Quantum Science and Technology* **2**, 044009 (2017).
- [99] J. Stenger, S. Inouye, D. M. Stamper-Kurn, H.-J. Miesner, A. P. Chikkatur & W. Ketterle. Spin domains in ground-state bose-einstein condensates. *Nature* **396**, 345–348 (1998).

- [100] F. Gerbier, A. Widera, S. Fölling, O. Mandel & I. Bloch. Resonant control of spin dynamics in ultracold quantum gases by microwave dressing. *Phys. Rev. A* **73**, 041602 (2006).
- [101] P. B. Blakie†, A. S. Bradley†, M. J. Davis, R. J. Ballagh & C. W. Gardiner. Dynamics and statistical mechanics of ultra-cold Bose gases using c-field techniques. *Adv. Phys.* **57**, 363–455 (2008).
- [102] A. Sinatra, C. Lobo & Y. Castin. The truncated wigner method for bose-condensed gases: limits of validity and applications. *J. Phys. B: At., Mol. Opt. Phys.* **35**, 3599–3631 (2002).
- [103] R. J. Lewis-Swan, M. K. Olsen & K. V. Kheruntsyan. Approximate particle number distribution from direct stochastic sampling of the wigner function. *Phys. Rev. A* **94** (2016).
- [104] T. Hoang. *Quantum Control Of A Many-body System In A Spin-1 Bose-einstein Condensate*. Ph.D. thesis, Georgia Institute of Technology (2013).
- [105] H. Strobel, W. Muessel, D. Linnemann, T. Zibold, D. B. Hume, L. Pezze, A. Smerzi & M. K. Oberthaler. Fisher information and entanglement of non-Gaussian spin states. *Science* **345**, 424–427 (2014).
- [106] C. Klempert, O. Topic, G. Gebreyesus, M. Scherer, T. Henninger, P. Hyllus, W. Ertmer, L. Santos & J. J. Arlt. Multiresonant spinor dynamics in a Bose-Einstein condensate. *Phys. Rev. Lett.* **103**, 195302 (2009).
- [107] M. Scherer, B. Lücke, G. Gebreyesus, O. Topic, F. Deuretzbacher, W. Ertmer, L. Santos, J. J. Arlt & C. Klempert. Spontaneous breaking of spatial and spin symmetry in spinor condensates. *Phys. Rev. Lett.* **105**, 135302 (2010).
- [108] M. Scherer, B. Lücke, J. Peise, G. Gebreyesus, F. Deuretzbacher, W. Ertmer, L. Santos, C. Klempert, J. J. Arlt *et al.* Spontaneous symmetry breaking in spinor Bose-Einstein condensates. *Phys. Rev. A* **88**, 053624 (2013).
- [109] B. Allard, M. Fadel, R. Schmied & P. Treutlein. Sideband rabi spectroscopy of finite-temperature trapped bose gases. *Phys. Rev. A* **93** (2016).
- [110] R. Rosa-Medina. *Probing Long-Time Spin Dynamics in a ⁸⁷Rb Bose-Einstein Condensate*. Master’s thesis, Universität Heidelberg (2018).
- [111] K. Lange, J. Peise, B. Lücke, I. Kruse, G. Vitagliano, I. Apellaniz, M. Kleinmann, G. Tóth & C. Klempert. Entanglement between two spatially separated atomic modes. *Science* **360**, 416–418 (2018).
- [112] C. Weedbrook, S. Pirandola, R. García-Patrón, N. J. Cerf, T. C. Ralph, J. H. Shapiro & S. Lloyd. Gaussian quantum information. *Rev. Mod. Phys.* **84**, 621 (2012).
- [113] D. Smithey, M. Beck, J. Cooper & M. Raymer. Measurement of number-phase uncertainty relations of optical fields. *Phys. Rev. A* **48**, 3159 (1993).
- [114] W. Grice & I. A. Walmsley. Homodyne detection in a photon counting application. *J. Mod. Opt.* **43**, 795–805 (1996).

- [115] R. G. Miller. The jackknife-a review. *Biometrika* **61**, 1–15 (1974).
- [116] P. Kunkel, M. Prüfer, H. Strobel, D. Linnemann, A. Frölian, T. Gasenzer, M. Gärttner & M. K. Oberthaler. Spatially distributed multipartite entanglement enables epr steering of atomic clouds. *Science* **360**, 413–416 (2018).
- [117] A. Sørensen, L.-M. Duan, J. Cirac & P. Zoller. Many-particle entanglement with bose-einstein condensates. *Nature* **409**, 63 (2001).
- [118] M. D. Reid. Monogamy inequalities for the Einstein-Podolsky-Rosen paradox and quantum steering. *Phys. Rev. A* **88**, 062108 (2013).
- [119] S. Armstrong, J.-F. Morizur, J. Janousek, B. Hage, N. Treps, P. K. Lam & H.-A. Bachor. Programmable multimode quantum networks. *Nat. Commun.* **3**, 1026 (2012).
- [120] M. Fadel, T. Zibold, B. Décamps & P. Treutlein. Spatial entanglement patterns and einstein-podolsky-rosen steering in bose-einstein condensates. *Science* **360**, 409–413 (2018).
- [121] Q. Y. He & M. D. Reid. Genuine multipartite einstein-podolsky-rosen steering. *Phys. Rev. Lett.* **111** (2013).
- [122] M. A. Joffe, W. Ketterle, A. Martin & D. E. Pritchard. Transverse cooling and deflection of an atomic beam inside a Zeeman slower. *J. Opt. Soc. Am. B* **10**, 2257–2262 (1993).
- [123] P. Kunkel, M. Prüfer, S. Lannig, R. Rosa-Medina, A. Bonnin, M. Gärttner, H. Strobel & M. K. Oberthaler. Simultaneous Readout of Noncommuting Collective Spin Observables beyond the Standard Quantum Limit. *Phys. Rev. Lett.* **123** (2019).
- [124] C. W. Helstrom. Cramér-rao inequalities for operator-valued measures in quantum mechanics. *Int. J. Theor. Phys.* **8**, 361–376 (1973).
- [125] J. Bae & L.-C. Kwek. Quantum state discrimination and its applications. *J. Phys. A: Math. Theor.* **48**, 083001 (2015).
- [126] E. Prugovečki. Information-theoretical aspects of quantum measurement. *Int. J. Theor. Phys.* **16**, 321–331 (1977).
- [127] P. Busch & P. J. Lahti. The determination of the past and the future of a physical system in quantum mechanics. *Found. Phys.* **19**, 633–678 (1989).
- [128] J. M. Renes, R. Blume-Kohout, A. J. Scott & C. M. Caves. Symmetric informationally complete quantum measurements. *J. Math. Phys.* **45**, 2171–2180 (2004).
- [129] A. J. Scott & M. Grassl. Symmetric informationally complete positive-operator-valued measures: A new computer study. *J. Math. Phys.* **51**, 042203 (2010).
- [130] A. Smith, B. E. Anderson, H. Sosa-Martinez, C. A. Riofrío, I. H. Deutsch & P. S. Jessen. Quantum control in the cs $6S_{1/2}$ ground manifold using radio-frequency and microwave magnetic fields. *Phys. Rev. Lett.* **111**, 170502 (2013).

- [131] M. Prüfer, T. V. Zache, P. Kunkel, S. Lannig, A. Bonnin, H. Strobel, J. Berges & M. K. Oberthaler. Experimental extraction of the quantum effective action for a non-equilibrium many-body system. *arXiv preprint arXiv:1909.05120* (2019).
- [132] H. Sosa-Martinez, N. K. Lysne, C. H. Baldwin, A. Kalev, I. H. Deutsch & P. S. Jessen. Experimental study of optimal measurements for quantum state tomography. *Phys. Rev. Lett.* **119**, 150401 (2017).
- [133] L.-M. Duan, G. Giedke, J. I. Cirac & P. Zoller. Inseparability criterion for continuous variable systems. *Phys. Rev. Lett.* **84**, 2722–2725 (2000).
- [134] E. Arthurs & J. Kelly. Bstj briefs: On the simultaneous measurement of a pair of conjugate observables. *The Bell System Technical Journal* **44**, 725–729 (1965).
- [135] C. Spengler, M. Huber, S. Brierley, T. Adaktylos & B. C. Hiesmayr. Entanglement detection via mutually unbiased bases. *Phys. Rev. A* **86**, 022311 (2012).
- [136] J. Schwinger. Unitary operator bases. *Proc. Natl. Acad. Sci. U.S.A.* **46**, 570 (1960).
- [137] P. Erker, M. Krenn & M. Huber. Quantifying high dimensional entanglement with two mutually unbiased bases. *Quantum* **1**, 22 (2017).
- [138] J. Bavaresco, N. H. Valencia, C. Klöckl, M. Pivoluska, P. Erker, N. Friis, M. Malik & M. Huber. Measurements in two bases are sufficient for certifying high-dimensional entanglement. *Nat. Phys.* **14**, 1032 (2018).
- [139] N. Friis, G. Vitagliano, M. Malik & M. Huber. Entanglement certification from theory to experiment. *Nature Reviews Physics* **1** (2018).
- [140] Y. S. Weinstein, M. Pravia, E. Fortunato, S. Lloyd & D. G. Cory. Implementation of the quantum fourier transform. *Phys. Rev. Lett.* **86**, 1889 (2001).
- [141] N. V. Vitanov. Synthesis of arbitrary su (3) transformations of atomic qutrits. *Phys. Rev. A* **85**, 032331 (2012).
- [142] D. Tasca, Ł. Rudnicki, R. Gomes, F. Toscano & S. Walborn. Reliable entanglement detection under coarse-grained measurements. *Phys. Rev. Lett.* **110**, 210502 (2013).
- [143] E. Paul, S. Walborn, D. Tasca & Ł. Rudnicki. Mutually unbiased coarse-grained measurements of two or more phase-space variables. *Phys. Rev. A* **97**, 052103 (2018).
- [144] F. Toscano, D. Tasca, Ł. Rudnicki & S. Walborn. Uncertainty relations for coarse-grained measurements: An overview. *Entropy* **20**, 454 (2018).
- [145] P. J. Coles, M. Berta, M. Tomamichel & S. Wehner. Entropic uncertainty relations and their applications. *Rev. Mod. Phys.* **89**, 015002 (2017).
- [146] Y. Lai & H. Haus. Characteristic functions and quantum measurements of optical observables. *Quantum Optics: Journal of the European Optical Society Part B* **1**, 99 (1989).
- [147] S. L. Braunstein, C. M. Caves & G. Milburn. Interpretation for a positive p representation. *Phys. Rev. A* **43**, 1153 (1991).

- [148] S. Stenholm. Simultaneous measurement of conjugate variables. *Ann. Physics* **218**, 233–254 (1992).
- [149] A. Papoulis & S. U. Pillai. *Probability, Random Variables and Stochastic Processes* (McGraw-Hill Higher Education, 2002).
- [150] H. Gould & J. Quaintance. Double Fun with Double Factorials. *Mathematics Magazine* **85**, 177–192 (2012).
- [151] H. Yuen & J. Shapiro. Optical communication with two-photon coherent states—part III: Quantum measurements realizable with photoemissive detectors. *IEEE Transactions on Information Theory* **26**, 78–92 (1980).
- [152] U. Leonhardt & H. Paul. Measuring the quantum state of light. *Prog. Quantum Electron.* **19**, 89–130 (1995).
- [153] J. Řeháček, Y. S. Teo, Z. Hradil & S. Wallentowitz. Surmounting intrinsic quantum-measurement uncertainties in gaussian-state tomography with quadrature squeezing. *Sci. Rep.* **5** (2015).
- [154] C. R. Müller, C. Peuntinger, T. Dirmeier, I. Khan, U. Vogl, C. Marquardt, G. Leuchs, L. L. Sánchez-Soto, Y. S. Teo, Z. Hradil & J. Řeháček. Evading Vacuum Noise: Wigner Projections or Husimi Samples? *Phys. Rev. Lett.* **117**, 070801 (2016).
- [155] Y. S. Teo, C. R. Müller, H. Jeong, Z. Hradil, J. Řeháček & L. L. Sánchez-Soto. Superiority of heterodyning over homodyning: An assessment with quadrature moments. *Phys. Rev. A* **95**, 042322 (2017).
- [156] Y. S. Teo, C. R. Müller, H. Jeong, Z. Hradil, J. Řeháček & L. L. Sánchez-Soto. Joint measurement of complementary observables in moment tomography. *Int. J. Quantum Inf.* **15**, 1740002 (2017).
- [157] M.-S. Chang, Q. Qin, W. Zhang, L. You & M. S. Chapman. Coherent spinor dynamics in a spin-1 Bose condensate. *Nat. Phys.* **1**, 111 (2005).
- [158] S. Erne, R. Bücker, T. Gasenzer, J. Berges & J. Schmiedmayer. Universal dynamics in an isolated one-dimensional Bose gas far from equilibrium. *Nature* **563**, 225–229 (2018).
- [159] L. A. Williamson & P. B. Blakie. Universal coarsening dynamics of a quenched ferromagnetic spin-1 condensate. *Phys. Rev. Lett.* **116**, 025301 (2016).
- [160] N. Friis, O. Marty, C. Maier, C. Hempel, M. Holzäpfel, P. Jurcevic, M. B. Plenio, M. Huber, C. Roos, R. Blatt & B. Lanyon. Observation of entangled states of a fully controlled 20-qubit system. *Phys. Rev. X* **8**, 021012 (2018).
- [161] M. H. Devoret & R. J. Schoelkopf. Superconducting circuits for quantum information: an outlook. *Science* **339**, 1169–1174 (2013).
- [162] M. A. Nielsen. Cluster-state quantum computation. *Rep. Math. Phys.* **57**, 147–161 (2006).

- [163] O. Mandel, M. Greiner, A. Widera, T. Rom, T. W. Hänsch & I. Bloch. Controlled collisions for multi-particle entanglement of optically trapped atoms. *Nature* **425**, 937 (2003).
- [164] I. Bloch. Quantum coherence and entanglement with ultracold atoms in optical lattices. *Nature* **453**, 1016–1022 (2008).
- [165] S. Lloyd & S. L. Braunstein. Quantum computation over continuous variables. *Phys. Rev. Lett.* **82**, 1784–1787 (1999).
- [166] N. C. Menicucci, P. van Loock, M. Gu, C. Weedbrook, T. C. Ralph & M. A. Nielsen. Universal quantum computation with continuous-variable cluster states. *Phys. Rev. Lett.* **97**, 110501 (2006).
- [167] R. Ukai, S. Yokoyama, J. ichi Yoshikawa, P. van Loock & A. Furusawa. Demonstration of a controlled-phase gate for continuous-variable one-way quantum computation. *Phys. Rev. Lett.* **107** (2011).
- [168] R. Ukai, N. Iwata, Y. Shimokawa, S. C. Armstrong, A. Politi, J. ichi Yoshikawa, P. van Loock & A. Furusawa. Demonstration of unconditional one-way quantum computations for continuous variables. *Phys. Rev. Lett.* **106** (2011).
- [169] X. Su, S. Hao, X. Deng, L. Ma, M. Wang, X. Jia, C. Xie & K. Peng. Gate sequence for continuous variable one-way quantum computation. *Nat. Commun.* **4**, 2828 (2013).
- [170] J.-I. Yoshikawa, S. Yokoyama, T. Kaji, C. Sornphiphatphong, Y. Shiozawa, K. Makino & A. Furusawa. Generation of one-million-mode continuous-variable cluster state by unlimited time-domain multiplexing. *APL Photonics* **1**, 060801 (2016).
- [171] S. Takeda & A. Furusawa. Universal quantum computing with measurement-induced continuous-variable gate sequence in a loop-based architecture. *Phys. Rev. Lett.* **119** (2017).
- [172] J. Zhang & S. L. Braunstein. Continuous-variable gaussian analog of cluster states. *Phys. Rev. A* **73** (2006).
- [173] P. van Loock, C. Weedbrook & M. Gu. Building gaussian cluster states by linear optics. *Phys. Rev. A* **76**, 032321 (2007).
- [174] M. Yukawa, H. Benichi & A. Furusawa. High-fidelity continuous-variable quantum teleportation toward multistep quantum operations. *Phys. Rev. A* **77**, 022314 (2008).
- [175] N. C. Menicucci, S. T. Flammia & O. Pfister. One-way quantum computing in the optical frequency comb. *Phys. Rev. Lett.* **101**, 130501 (2008).
- [176] R. Pooser & J. Jing. Continuous-variable cluster-state generation over the optical spatial mode comb. *Phys. Rev. A* **90** (2014).
- [177] M. Chen, N. C. Menicucci & O. Pfister. Experimental realization of multipartite entanglement of 60 modes of a quantum optical frequency comb. *Phys. Rev. Lett.* **112** (2014).
- [178] A. Frölian. *Implementation of local addressability in a Bose-Einstein condensate*. Master's thesis, Heidelberg University (2017).

Danksagung

Eine solche Arbeit ist nur möglich geworden durch die Hilfe von vielen wundervollen Menschen, bei denen ich mich an dieser Stelle bedanken möchte.

Mein erster und tiefer Dank gilt Markus. Auf dem langen Weg der Doktorarbeit stand er mir stets als wertvoller Ratgeber, Wegweiser und Inspirator zur Seite. Dass ich mich überhaupt auf diesen Weg gewagt habe, ist ebenfalls sein großer Verdienst. Bereits mit seiner ersten Vorlesung hat er es geschafft, mein Interesse für ultrakalte Atome zu wecken und seine Begeisterung war über die vielen Jahre hinweg ein steter Quell der Motivation. Ebenfalls außergewöhnlich war seine konsequente Unterstützung des internationalen wissenschaftlichen Austauschs, wodurch er mir den Besuch einiger wichtiger Konferenzen ermöglicht hat.

Ein großer Dank gebührt auch Selim Jochim für die Übernahme des Zweitgutachtens und den stets bereichernden fachlichen Austausch.

Die vielen Stunden im Labor wären sicherlich nicht möglich gewesen ohne tolle Kollegen im BEC Team, mit denen man auch schwierigere Zeiten am Experiment meistern konnte. Die vielen konstruktiven Diskussionen im Team haben maßgeblich zu den Ergebnissen dieser Arbeit beigetragen. Besonders erwähnen möchte ich Max, der in vielfacher Hinsicht diese Arbeit bereichert hat und auf dessen Engagement und Zuverlässigkeit ich immer zählen konnte – nicht zuletzt bei dem Ausfindigmachen kleiner MOTs oder dem Suchen herumstreunender Magnetfelder.

Helmut danke ich für seine unermüdliche Bereitschaft, sich in alle möglichen (und unmöglichen) Probleme und Fragen hineinzudenken. Sein Talent, komplexe Themen anschaulich und nachvollziehbar darstellen zu können, hat mir selbst zu zahlreichen neuen Einsichten in die Physik verholfen.

Der deutsch-amerikanische Psychologe Kurt Lewin soll einmal gesagt haben: "Es gibt nichts Praktischeres als eine gute Theorie." Als Experimentalphysiker würde ich diesen Satz leicht abwandeln und sagen: Es gibt nichts Praktischeres als einen guten Theoretiker. Um diesen Titel hat sich Martin mehr als verdient gemacht, der mir in unzähligen Diskussionen dabei geholfen hat, die Brücke zwischen Theorie und Experiment zu schlagen.

Overall a huge thanks is dedicated to the whole SynQS and matterwave team for the many discussions and the opportunity to share all the positive and negative experiences in the lab. The many activities such as the weekly breakfast and the countless BBQs provided a special and precious atmosphere.

Ein herzlicher Dank gebührt auch Dagmar und Christiane, die das organisatorische Rückgrat der Gruppe bilden und mit unermüdlichem Einsatz dabei helfen, jedes administrative Problem unkompliziert zu lösen.

Bei der Studienstiftung des deutschen Volkes möchte ich mich für die finanzielle Unterstützung des letzten Jahres der Promotion bedanken.

Auch außerhalb der SynQS Gruppe gibt es viele Menschen, die zum Gelingen dieser Arbeit beigetragen habe. Caro und Luca haben mich nicht nur durch das ganze Studium sowie durch China und Taiwan begleitet, sondern waren auch auf dem Weg der Doktorarbeit immer an meiner Seite. Meinen Freunden aus Aschaffenburg danke ich dafür, dass sie mir immer ein offenes Ohr schenken und bei Besuchen in der Heimat für willkommene Abwechslung vom Physikalltag sorgen.

Ein großer Dank gilt meiner Familie, die mir Kraft gegeben und an mich geglaubt hat. Meinen Eltern gebührt mein tiefster Dank für ihre bedingungslose Bereitschaft, mich in allen Vorhaben zu unterstützen und immer für mich da zu sein.

Zu guter Letzt bleibt noch ein ganz besonderer Mensch übrig, der mich durch alle Hochs und Tiefs dieser Arbeit begleitet hat und jeden Tag meines Lebens unendlich bereichert. Mein lieber Tobias, danke, dass du an meiner Seite bist.